SOME ASPECTS OF THE MAGNETIC PROPERTIES OF AMORPHOUS MAGNETIC MATERIALS

THESIS SUBMITTED FOR THE DEGREE OF
DOCTOR OF PHILOSOPHY (SCIENCE)
OF THE
JADAVPUR UNIVERSITY

SUMAN SINHA

SATYENDRANATH BOSE NATIONAL CENTRE
FOR BASIC SCIENCES
BLOCK - JD, SECTOR III, SALT LAKE CITY
KOLKATA 700 098, INDIA

2010

CERTIFICATE FROM THE SUPERVISOR(S)

This is to certify that the thesis entitled **"Some Aspects of the Magnetic Properties of Amorphous Magnetic Materials"** submitted by **Sri Suman Sinha**, who got his name registered on **8th June, 2006** for the award of **Ph.D. (Science) degree** of **Jadavpur University**, is absolutely based upon his own work under the supervision of **Dr. Kalyan Mandal** and that neither this thesis nor any part of it has been submitted for either any degree/diploma or any other academic award anywhere before.

DATE :   DR. KALYAN MANDAL
                          ASSOCIATE PROFESSOR,
                          DEPARTMENT OF MATERIAL SCIENCES,
                          SATYENDRA NATH BOSE NATIONAL
                          CENTRE FOR BASIC SCIENCES,
                          BLOCK-JD, SECTOR-III, SALT LAKE,
                          KOLKATA - 700098,
                          INDIA.

Dedicated to my parents

ACKNOWLEDGEMENTS

List of Publications

Publications in refereed journals :

1. **S. Sinha**, B. Das and K. Mandal..
   Magnetoimpedance of a glass-coated amorphous microwire.
   Journal of Applied Physics, 105, 07A311 (2009).

2. **S. Sinha**, K. Mandal and B. Das.
   Magnetization dynamics in wire-shaped amorphous magnetic materials as probed by Barkhausen noise measurement.
   Journal of Physics D : Applied Physics, 40, 2710 (2007).

3. **S. Sinha** and K. Mandal.
   Study of magnetic barkhausen noise from amorphous $Fe_{70}Ni_8Si_{10}B_{12}$ and $Fe_{40}Ni_{40}B_{20}$ Ribbons.
   Journal of Non destructive Testing and Evaluation, 5, 49 (2006).

4. **S. Sinha**, K. Mandal and M. Vazquez.
   Giant magnetoimpedance in amorphous $(Co_{0.93}Fe_{0.07})_{63}Ni_{10}Si_{11}B_{16}$ glass-coated microwire.
   Journal of Magnetism and Magnetic Materials, 302, 223 (2006).

5. K. Mandal, **S. Sinha** and P. Anil Kumar.
   Contributions to giant magnetoimpedance from different domain regions of $Co_{68.15}Fe_{4.35}Si_{12.5}B_{15}$ amorphous wire.
   Journal of Applied Physics, 99, 033901 (2006).

6. Subarna Mitra, K. Mandal, **Suman Sinha**, P M G nambissan and S. Kumar.
   Size and temperature dependent cationic redistribution in $NiFe_2O_4(SiO_2)$ nanocomposites : positron annihilation and Mössbauer studies.
   Journal of Physics D : Applied Physics, 39, 4228 (2006).

7. **S. Sinha** and K. Mandal.
   Effect of tensile stress on the magnetic Barkhausen noise in amorphous $Fe_{70}Ni_8Si_{10}B_{12}$ ribbon.
   Indian Journal of Physics, 79(9), 991 (2005).

Preprints :

8. **S. Sinha**, B. Das and K. Mandal.
   Effect of short duration heat treatment on magnetoimpedance in positive magnetostrictive glass-coated amorphous microwires.
   Submitted to Japanese Journal of Applied Physics.

9. **S. Sinha** and K. Mandal.
   Study of magnetization processes in ferromagnetic amorphous ribbons using magnetic barkhausen noise technique.
   Submitted to Journal of Applied Physics.

10. **S. Sinha** and K. Mandal.
    Giant magnetoimpedance modelling in wire-shaped amorphous magnetic materials.
    To be submitted to Journal of Magnetism and Magnetic Materials.

Papers presented in Symposia/Conferences :

1. **S. Sinha** and K. Mandal.
   Magnetoimpedance of a Glass Coated Amorphous Microwire
   53rd **Annual Conference on Magnetism and Magnetic Materials**, November 10 - 14, 2008, Austin, Texas, USA.

2. **S. Sinha** and K. Mandal.
   Study of Giant magnetoimpedance of $Co_{68.15}Fe_{4.35}Si_{12.5}B_{15}$ amorphous wires.
   Proceedings of Condensed Matter days-2005.

3. **S. Sinha** and K. Mandal.
   Study of magnetic Barkhausen noise from amorphous $Fe_{70}Ni_8Si_{10}B_{12}$ and $Fe_{40}Ni_{40}B_{20}$ ribbons.
   Proceedings of National seminar on NDT & E (NDE-2005).

4. **S. Sinha** and K. Mandal.
   Study of magnetic Barkhausen noise from polycrystalline and amorphous ferromagnetic materials .
   Proceedings of Condensed Matter days-2004.

Important Project Report :

1. *Characterization of Magnetic Materials by Non-Destructive Barkhausen Noise Measurement.*
   Funded by Board of Research in Nuclear Science (Department of Atomic Energy, Government of India), BRNS Sanction No. 2003/37/13/BRNS, 2003 - 2007.

Contents

Chapter 1

INTRODUCTION

1.1 Ferromagnetic Disordered Alloys

The term "disordered alloys" in general and "amorphous alloys" in particular way include liquid, vapour or plasma quenched materials as well as alloys obtained by solid state synthesis, whose x-ray diffraction patterns show characteristic broad rings. Among them the term "etallic glass" is used to denote only liquid quenched products. Amorphous magnetic materials mainly belong to this subcategory. These alloys lack long-range atomic order and consequently exhibit high metallic resistivity (100 - 200 $\mu ohm - cm$) and no macroscopic magnetocrystalline anisotropy due to the absence of crystal structure. As a result, ferromagnetic metallic glasses based on 3d transition metals are generally good "soft" magnetic materials with both low dc hysteresis loss and low eddy current dissipation. In addition, they are characterized by high elastic limit (i.e. they resist plastic deformation) and for certain compositions, they show good corrosion resistance. Amorphous magnetic alloys containing appreciable fractions of rare earth metals show magnetic anisotropy and magnetostriction that can be varied almost continuously with compositions upto very large values. These characteristics combined with the expectation that metallic glasses can be economically mass fabricated, has led to a broad commercial interest. To physicists, the attraction lies in seeing how the absence of crystal structure modifies the collective magnetic phenomena, which are mainly governed by short-range interactions.

Because of the lack of atomic ordering it was believed for many years that ferromagnetism could not exist in amorphous solids. However in 1960 Gubanov [1] predicted, on the basis

of theoretical analysis, that amorphous solids would be ferromagnetic. This was based on the evidence that the electronic band structure of crystalline solids did not change in any fundamental way on transition to the liquid state. This implies that the band structure and hence ferromagnetism depends on short-range atomic order and should not be destroyed in the corresponding amorphous solid. In 1950, Brenner et. al. [2] first reported the amorphous metallic alloy of nickel phosphorus prepared by electro-deposition. The present great interest in amorphous metal research stems from reports by Duwez et. al. [3] in 1960 on the preparation and properties of amorphous metallic alloys. In 1967 Duwez and Lin [4] reported a liquid quenched Fe-P-C alloy exhibiting a saturation magnetization of 7 kG, low coercivity (3 Oe), rather high Curie temperature and good stability at room temperature against crystallization. Luborsky et. al. [5] first demonstrated the reduction of coercivity in Fe-Ni-P-B alloys down to less than 10 mOe by suitable annealing and showed that the changes in properties correlated with the relief of internal strain.

Amorphous states for pure metals like Fe, Co, Ni etc. are obtained only at low temperature whereas this state is stable for above alloys at room temperature. The stability increases with the number of components in alloys. Two important classes of amorphous magnetic materials are being studied intensively in recent times. They are the transition metal metalloid (TM-M) glass and the rare-earth transition metal glass (RE-TM) [6], [7]. TM-M glasses are stable for composition around 75-80 % of TM (Fe, Ni, Co etc. or in combination of them). Typical composition for RE-TM glass is $RE_{33} - TM_{67}$ where the RE's are heavior rare-earth metal like Gd, Tb, Dy etc. and TM's are Fe, Co etc. Later metalloids in TM-M glasses are replaced by non-magnetic metals [8] like Zr, Hf and are being studied for the last several years.

Many good reviews of amorphous alloys are available, covering a variety of physical properties [9] - [17]. Among those, the review by Moorjani and Coey [14] presents a wealth of information on metallic as well as on insulating magnetic systems. Wohlfarth [10] examines many aspects of magnetism in light of itinerant theory. Kaneyoshi [13] reviews theoretical issues related to exchange and moment fluctuations as well as spin- wave state. Luborsky treats anisotropy, moment variations, coercivity and losses. O'Handley reviewed the recent development in the physics of ferromagnetic amorphous alloys in details [17].

1.2   Preparation of Ferromagnetic Amorphous Alloy

The basic principle to prepare an amorphous alloy is that the molten alloy must be cooled very rapidly so that it must pass quickly enough through the temperature range where nucleation can occur. The cooling rate is of the order of $10^{5\circ}Cs^{-1}$ or higher [18],[19]. A wide variety of different processes with low cost production techniques have been reported. The most widely used technique to prepare TM-M metallic glass is the liquid-quenching method [20]. In this method, a rapidly spinning copper or steel wheel is used to conduct the heat away rapidly and continuously from the melt. This method is suitable to produce metallic glass in the form of ribbons. The typical dimension of the ribbon is few cm in width and 20 - 60 μm in thickness. The other methods are splat cooling, sputtering, irradiation by energetic neutron, vapour or electrodeposition [20]. RE-TM glasses are normally prepared by sputtering or vapour deposition techniques [20]. Some new techniques to obtain metallic glass are still under development. These are laser glazing [21], electric field emission of ions from the melt [22] and spark erossion technique [23].

Glassy metal in the form of amorphous wires with diameter of about 100 μm are fabricated by in-rotating-water quenching technique by squirting a jet of molten liquid into a rotating bowl of water [14], [25]. The first successful method to produce amorphous wires, based on a process of liquid solidification into water, was developed by Kavesh [26]. Further development of quenching technique into rotating water was subsequently achieved by Ohnaka et al. and Masumoto, Ohnaka, Inoue and Hagiwara in Japan [27], [28].

Microwires are manufactured by means of a modified Taylor-Utilovsky process based on direct casting from the melt [29] - [36]. Glass-coated microwires are fabricated by quenching and drawing method. They are composite materials formed by an amorphous metallic nucleus (1 -20 μm in diameter) covered by Pyrex-like insulating coating (2 -20 μm thick). In this method a few grams of the master alloy with the desired composition is put into a pyrex-like glass tube and placed within a high frequency inductor heater. The alloy is heated up to its melting point forming a droplet. While the metal melts, the portion of the glass tube adjacent to the melting metal softens, enveloping the metal droplet. A glass capillary is then drawn from the softened glass portion and wound on a rotating coil. At suitable drawing conditions, the molten metal fills the glass capillary and a microwire
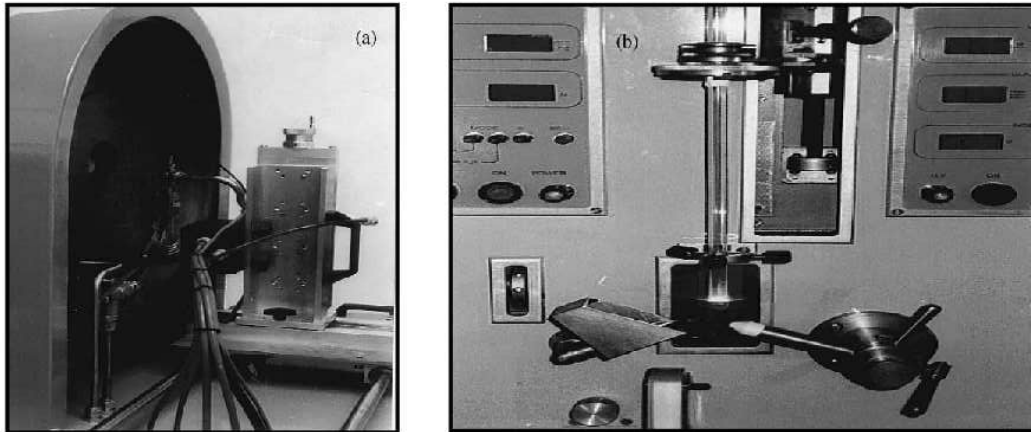
Figure 1.1: In-rotating-water-quenching unit (a) and the Quenching and drawing unit (b) for the fabrication of wires and microwires respectively (at the ICMM/CSIC Laboratories).

is thus formed where the metal core is completely covered by a glass shell. Fig. 1.1 shows the in-rotating-water-quenching unit (a) and the quenching and drawing unit for the fabrication of wires and microwires respectively (at the ICMM/CSIC Laboratories) [34]. During fabrication, glass-coated microwires undergo large internal stresses, stronger than in the case of in-water-quenched wires due to additional stresses coming from the coating. These stresses determine their magnetic properties.

1.3 Magnetic properties of wire-shaped amorphous magnetic materials

Recently, amorphous wires and microwires with a metallic nucleus covered by an insulating glass coating has attracted considerable interest because of their outstanding soft magnetic properties. Due to their amorphous character, only magnetoelastic anisotropy coming from frozen-in stresses has to be considered together with the shape anisotropy to determine the magnetic behaviour. Due to their ferromagnetic behaviour, the largest energy term among magnetic interactions to be considered is exchange coupling. Since they are structurally amorphous in character, magnetocrystalline anisotropy can be neglected so that magnetoelstic anisotropy plays the dominating role. Lastly, their cylindrical sym-
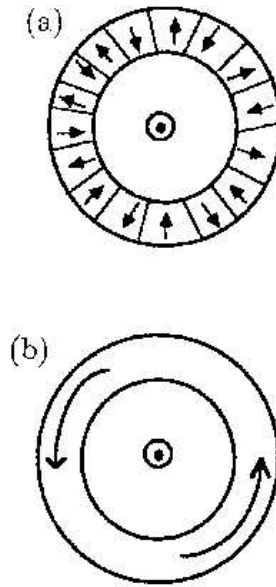
Figure 1.2: A cross section of an amorphous wire showing a schematic view of the domain structure in the middle part (determined by the distribution of internal stresses) of wires with (a) positive and (b) negative magnetostriction.

metry induces a very characteristic magnetic shape anisotropy [24] - [25], [34].

The above factors determining the magnetic behaviour of these wire-shaped samples are influenced by the rapid solidification method employed in the fabrication. Firstly, the alloy composition determines the magnetostriction constant (λ). Secondly, the quenching technique introduces unique distribution of strong internal mechanical stresses (σ). Thus magnetostriction and stresses determine the strength of magnetoelastic anisotropy. The magnetoelastic energy density ($E_{me} \approx \lambda\sigma$) determines the magnetic behaviour i.e., domain structure and hysteresis loop of these materials. The sign and value of the magnetostriction is decisive. Positive and negative magnetostriction result respectively in radial and circumferential easy axis at the shell, while a vanishing magnetostriction (order of magnitude of 0.1 ppm and less) destroys the single inner domain structure to built up new domain walls. Magnetostriction is directly correlated to alloy composition. Fig. 1.2 shows the cross section of an amorphous wire showing the domain structure in the middle part with positive and negative magnetostriction [35].
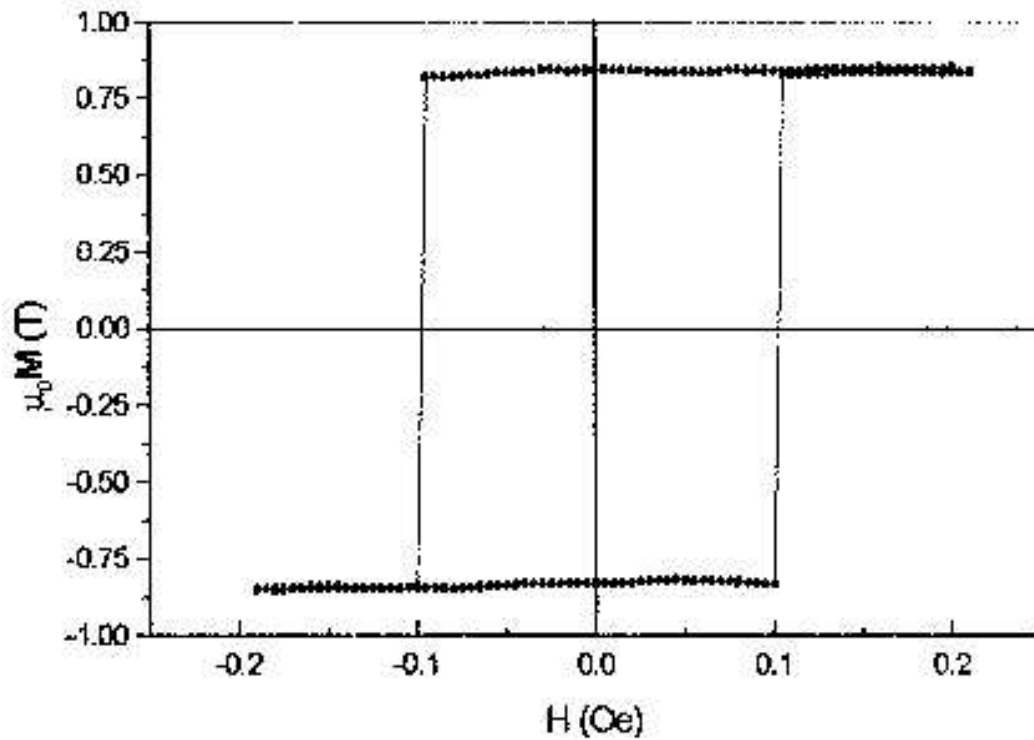
Figure 1.3: Longitudinal hysteresis loop of a 10 cm long FeSiB in-water-quenched amorphous wire

Magnetostrictive wires are characterized by a single Barkhausen jump that results in square-shaped hysteresis loops. This behaviour is due to the particular domain structure with a quite large single domain with axial easy magnetization direction. Non-magnetostrictive wires are among the softest magnetic materials ever found and exhibit giant magnetoimpedance effect due to their ultra-soft magnetic behaviour. Fig. 1.3 shows the longitudinal hysteresis loop of a 10 cm long FeSiB in-water-quenched amorphous wire [34]. This bistable magnetic behaviour is a consequence of the magnetization reversal process which proceeds by depinning of a single wall from the closure domain structure at one end and propagates towards the other end.

As mentioned earlier, the hysteretic magnetic properties of glass-coated microwires are rather different from those of conventional amorphous wires mostly because of additional magnetoelastic energy related with strong internal stresses induced during the rapid solid-

ification of the thin wire surrounded by the glas coating [25],[37]. Significant mechanical stresses appear inside the metallic nucleus and glass coating as a result of the difference in thermal expansion coefficients of metal and glass. The value of such stresses depends on ratio between metallic nucleus diameter and total microwire diameter [36].

The magnetic behaviour of microwires can be classified into the folowing groups according to their magnetostriction [24]:

(i) FeSiB alloys with large and positive magnetostriction ($\sim 1 - 3 \times 10^{-5}$).

(ii) CoFeSiB alloys with balanced magnetostriction for the Fe/Co rate at around 5%.

(iii) CoSiB alloys with negative and slightly reduced magnetostriction ($\approx -1 \times 10^{-6}$).

Typical hysteresis loops with different magnetostriction : (a) negative , (b) vanishing but negative and (c) positive CoMnSiB microwires is shown in Fig. 1.4 [36]. In case of negative magnetostriction, constant mechanical stresses give rise to the easy axis direction perpendicular to the microwire axes. Where the negative values of the magnetostriction constant are large the magnetoelastic energy exceeds the magnetostatic energy and the magnetization aligns perpendicular (circumferentially) to the microwire axis. With the application of an axial magnetic field the magnetization rotates from circular to axial orientation exhibiting minimal hysteresis (Fig. 1.4(a)).

For vanishing but negative value of magnetostriction, the magnetoelastic energy is of the same order as the magnetostatic energy. The magnetization process takes place first by domain wall movement and then by magnetization orientation (Fig. 1.4(b)). In case of positive magnetostrictive microwire, the magnetoelastic anisotropy results in axial easy axes, thereby reinforcing the shape anisotropy. Single or quassi-single domain structure is observed typically with a single or only few large Barkhausen jumps (Fig. 1.4(c)).

1.4 Characterization

The physical, chemical and magnetic characteristic of amorphous magnetic materials have been studied by various techniques. Since the magnetic properties of these materials will be discussed in the following chapters, their physical and chemical aspects will be discussed in brief.
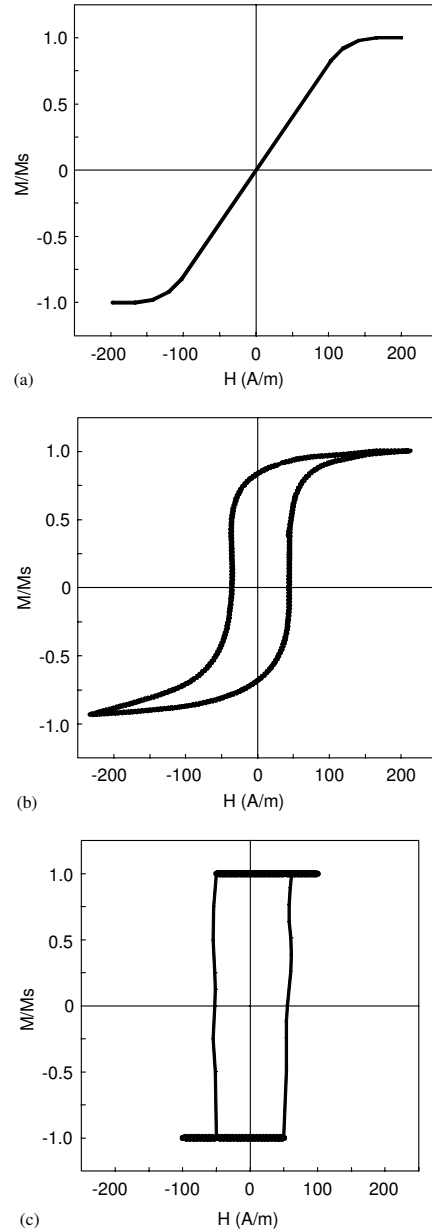
Figure 1.4: Typical hysteresis loops corresponding to CoMnSiB microwires with different magnetostriction : (a) negative , (b) vanishing but negative and (c) positive.

1.4.1   Atomic Structure

X-ray, electron or neutron diffraction pattern is the simplest way of deciding whether a material is amorphous or crystalline. In contrast to crystalline materials, the diffraction pattern consists of diffuse rings which sharpen as the material transforms, on heating, into polycrystalline phase. The atomic position in an amorphous solid are far from completely random in the sense that positions of atoms in a gas are random. The atoms in a solid, imposes some regularity on the local environment of each of them. Atomic positions are strongly correlated in nearest neighbour shell, yet uncorrelated beyond a few inter-atomic-spacings. This is the meaning of the statement that amorphous solids possess no long range order but short-range order that resembles those of liquids. Methods such as extended x-ray absorption fine structure and nuclear magnetic resonance [38] have been employed to examine the short-range order in amorphous metals, specifically the distribution of inter-atomic distances and co-ordination numbers. The accepted approach to modelling the atomic arrangements in metallic glasses is based on the structure formed by the dense random packing of hard spheres (DRPHS). Such model qualitatively accounts for the major features in the radial distribution functions of metallic glasses.

1.4.2   Chemical Composition

Generally, the percentage of the constituents, used during the preparation of alloy is taken as the composition of the metallic glass sample.

After the preparation, chemical composition of amorphous alloys are determined by various techniques. One of the most commonly used method is the atomic absorption spectroscopy where the substance is ignited to dissociate the material into its atomic constituents and they are then identified by their characteristic optical absorption. This method is appropriate for most light and heavy elements. Other commonly employed methods are X-ray photoelectron spectroscopy and auger spectroscopy etc.

1.4.3 Density

The amorphous alloys are generally about 2 % less dense than their corresponding equilibrium crystalline mixtures though materials which are upto 40 % less dense than the corresponding crystalline metals have also been reported [39]. Density of these materials can be measured easily by measuring their mass and volume.

Considering the structure of this metallic glasses formed by the dense random packing of hard spheres, their densities can be calculated. Taking the 12 coordinated Goldschmidt radii for the metal atoms and tetrahedral covalent radii for the metalloid atoms [40] the calculated densities were found to be within $\pm$ 5 % of the measured densities.

1.4.4 Resistivity

The resistivities of the amorphous alloys are generally 2 to 4 times larger than the corresponding transition metal crystalline alloys without the glass formers. This results in smaller eddy current contributions to the permeability and losses, especially at high frequencies. This is one of the many advantages of the amorphous metallic alloys for application in devices.

The low temperature resistivity of amorphous materials exhibit an anomalous minimum with a logarithmic increase below the minimum which, Cochrane et. al. [41] have shown to be nonmagnetic in origin and to be associated with the amorphous structure.

1.4.5 Thermal Stability

A glassy state being a metastable state, the metallic glasses tend to transform continuously towards more stable states. Two broad classes of transformation exist i.e. structural relaxation and crystallization. During the rapid quenching from the melt, some internal stresses are frozen-in within the sample which can be relaxed by structural relaxation through short or long duration heat treatment. This crystallization processes depend on a number of kinetic and thermodynamic factors. For a homogeneous crystallization process, the time for the onset of crystallization, τ_c follows an Arrhenius relation, $\tau_c = \tau_0 e^{\Delta E/kT}$, where τ_0 is the characteristic time and ΔE is the activation energy.

At the temperature for rapid crystallization, T_x the most physical properties (eg. restivity, remanence, coercivity) of the alloys change drastically and the device features based on these properties may deteriorate rapidly [46]. So, by judicious annealing it is possible to minimize internal stress and the accompanying anisotropy thereby achieving improved device characteristics. The useful lifetime of a device based on amorphous alloys ends at T_x , but for T_x in the range 400 K to 800 K (found for all most all the transition metal metalloid alloys) and ΔE in the range $26eV$ as have been reported for transition metal metalloid alloys in the vicinity of the eutectic [20], $\tau_C \simeq 10^{10}$ years so that amorphous alloys are stable against homogeneous crystallization for all practical purposes.

1.4.6   Effect of Disorder

Different types of disorder are observed in disordered magnetic materials [14]. Among them bond disorder is perhaps the simplest variety which is characterized by bonds of different length making different angles with each other in a monatomic crystal. A much stronger disruption of periodicity is the topological disorder where the crystal network includes different membered rings distributed at random within the solid. Chemical disorder is found in alloys having two or more constituents where atoms of a particular constituent have different chemical environment at different places within the solid. All these disorders are observed in amorphous ferromagnetic alloys which affect their magnetic properties by (i) changing the moment of an atom (ii) producing a distribution of exchange interaction between moments and (iii) altering local energy of atoms, i.e., anisotropy energy. Each of these effects will be discussed briefly in the following paragraphs.

Magnetic moment variations in amorphous alloys

The magnetic moment of most amorphous alloys are lower than those of the pure crystalline transition metals which they contain. Normally structural disorder in alloy causes little change in average magnetic moment/atom. The moments are mainly reduced by the change in the local chemical environment caused by the presence of metalloids. Slater-Pauling like plots of magnetic moment variation with composition was interpreted

earlier by charge transfer from the glass former to the 3d band [15]. From this consideration the magnetic moment of transition metal atoms in the general amorphous alloy $(TM)_{1-z-y}F_zG_y$ can be expressed as [20],

$$\mu = [m(1-z-y)fz - gy]/(1-z-y) \tag{1.1}$$

or for the moment per atom of alloy as

$$\mu = m(1-z-y)fz - gy \tag{1.2}$$

where F and G represent the metalloid or glass forming atomic species, m is the original number of unpaired spins in the transition metal alloy and f and g are the number of electrons transferred from F and G atoms respectively.

Later, a more realistic understanding of compositional effects was introduced in terms of (sp) d bonding [20], [42]. This chemical bonding are of covalent or polar bond type. In a covalent bond, charge is delocalized from each of the atomic sites and builds up between the atoms having similar electronegativities. Bonding and antibonding hybrid orbitals are created. The d-states become more delocalized as a result of covalent bonding. The delocalizatopn results in loss of d character and hence weaker intra-atomic exchange which weakens moment formation.

Polar bonds are formed between orbitals that differ significantly in their electronegativity. Here charge is transferred from the orbital of lower electronegativity to that of higher electronegativity. If a polar bond is formed in a metal, the conduction electrons will redistribute themselves to screen the charge transfer and maintain some degree of local charge neutrality. This bond formation will affect the magnetic properties if one of the orbitals involved contributes to the magnetism (eg. a 3d orbital).

Some models have been developed to describe trends in magnetic property variation with alloy content. Magnetic valence model is one of them which is based on Freidels concept of virtual bound states and generalized by Terakura and Kanamori [17]. It accounts for the variation of average magnetic moment with alloy content by defining an atom averaged magnetic valence

$$V_m = 2N_d^\uparrow - V \tag{1.3}$$

where V is the average electronic valence $V = N_d^\uparrow + N_d^\downarrow + N_{sp}^\uparrow + N_{sp}^\downarrow$ and $N_d^\uparrow$ is the number of majority-spin d-electrons. Substitution of the definition for V in the previous

equation leads to the relation

$$V_m = \mu_{av} - 2N_{sp}^{\uparrow} \tag{1.4}$$

which demonstrates the Slater-Pauling like behavior. ($|d\mu_{av}/dx| \simeq 1$ with the x intercept determined by the average number of conduction electrons). This model is applicable to a wide range of TE-TL (early transition metal late transition metal) and T-M (transition metal metalloid) alloy.

Coordination bonding model is developed in the local environment spirit and sheds light on the role of co-ordination in the interesting variations of magnetic moment. According to the model, suppression of host magnetization in a transition metal metalloid $T_{1-x}M_x$ alloy depends upon how strongly M is bonded with T and the extent of p-d bonding is assumed to be proportional to the number of T atoms surrounding an M atom. Hence, the magnitude of the average magnetic moment μ per T atom in the alloy is suppressed below that in the pure host n_B by an amount proportional to $Z^T{}_M$, the T co-ordination about the metalloid:

$$\mu_T = n_B[1 - Z^T{}_M N_M/5N_T] \tag{1.5}$$

where N_M/N_T (more commonly written as $x/(1-x)$ is the ratio of the number of M atoms). This model is applicable to metallic glasses as to crystalline solid solutions based on a strongly magnetic host like cobalt and nickel.

To explain magnetic moment variation in a large number of dilute alloys, Jaccarino and Walker [43] introduced a simple phenomenological model based on local environment effect. In this model the influence of more distant neighbours are neglected which are thought to be unimportant by the damping of "magnetic interactions" by the finite electron mean free path. The variation in the saturation magnetization in binary Ni-Cu, Ni-Rh alloys can be described well with this model. Buschow et. al. [44] have used this approach to fit the moment variation in amorphous Co-Y alloys.

Exchange Interactions

The appearance of a magnetically ordered structure such as ferromagnetism requires an interaction to couple the magnetic moments together. It has been found that exchange interactions between two electronic spins usually tend to allign them parallel or antipar-

allel. This tendency is represented by the isotropic Heisenberg interaction for a pair of localized moments $g\mu_B S$ [45]

$$H_{ij} = -2J_{ij}\vec{S}_i.\vec{S}_j \tag{1.6}$$

J_{ij} is the exchange constant between spins at site i and site j. It is positive for ferromagnetic coupling and negative for antiferromagnetic coupling.

The origin of exchange coupling lies in the electrostatic interaction between electrons of different spins on different sites [46]. Various exchange mechanisms exist [47] such as direct exchange, super exchange via ligands, indirect exchange via conduction electrons (RKKY interaction) [48] - [50]. All these interactions depend sensitively on the distance between interacting electrons. To a first approximation J_{ij} in above equation depends on interatomic distances (r_{ij}), even changes sign depending on r_{ij}. For the 4f series, S in above equation must be replaced by J. This equation is not directly applicable to 3d transition metals because their magnetic moments are not due to an integral number of localized d electrons on each atom. Nevertheless, an effective value of S can be obtained by equating the atomic moment to $g\mu_B S$. Other interactions exist which favour a perpendicular configuration for the pair of spins represented by the antisymmetric Dzloshinskii-Moriya (DM) term, which are weak in comparison with the Heisenberg interaction.

In an amorphous solid the distribution of interatomic separations leads to a distribution of exchange interactions which may sometimes include interactions of either sign. The same is true for other exchange mechanisms also. Superexchange is negative for a 180° metal-ligand-metal bond, but a weaker positive for bond angles near 90° [51]. RKKY interaction oscillates in sign as a function of r. It arises from the interaction of a localized spin with the polarization of the conduction band induced by other localized spins. It is the major sources of exchange coupling between 4f shells and it is also important in dilute 3d alloys where direct exchange can not operate.

The probability of finding an exchange interaction of a given magnitude and sign may be represented on a P(J) diagram. For a crystal the diagram consists of one or more delta functions, but the disorder in an amorphous solid will broaden the peaks even to the extent that interactions of both sign may be included in the distribution.

Because of this distribution of exchange interaction, some alloys have competing ferromagnetic and antiferromagnetic exchange interactions and exhibit "re-entrant" magnetic

behaviour. This means, upon cooling from high temperature, the system first undergoes para to ferromagnetic transition at a temperature T_{C1}. But this ferro-phase becomes unstable at a much lower temperature. Infact, the ferromagnetism vanishes ata temperature T_{C2} ($<$ T_{C1}) and the system enters into a glass-like phase. This re-entrant magnetic behaviour is observed in transition metal based glasses eg. Fe-Mn glasses [13], crystalline dilute alloys eg. Au-Fe, Pd-Mn [52] and in some compounds eg. $Eu_xSr_{1-x}S$ [53] - [54].

Anisotropy Energy and Magnetization Process

The macroscopic behaviour of magnetization in a ferromagnetic material is determined by anisotropy energy. In crystalline system, the anisotropy energy is mainly magnetocrystalline in origin. The structure of amorphous metal consists of random array of atoms and is normally considered to be isotropic on a long range scale. As a result, one expects the symmetry of the crystal field to be low enough to remove orbital degeneracy completely from the ground state of magnetic ions. So, in case of amorphous transition metal based alloys, the magnetization vector, which is mainly due to spin degrees of freedom, is supposed to be free from any spatial anisotropy. But during the fabrication process, the microstructural defects are frozen-in, originating internal stress field and giving rise to magneto-elastic anisotropy. Anisotropy energy in amorphous material is, therefore, determined only by magneto-elastic interaction, which is normally small. This anisotropy determines the process of magnetization. If this anisotropy energy is small, the macroscopic moment can be induced with a small field resulting large initial susceptibility (χ_i). The coercive field (H_c) is also reduced as it is directly determined by anisotropy energy. When the anisotropy energy is dominantly magnetoelastic in nature due to the presence of internal stress, the macroscopic magnetic properties are found to be a sensitive function of thermal history and external stress [55]. Thermal treatment can reduce internal stress. The removal of stress depends on the temperature and duration of annealing. The magnetic properties of the materials improve by annealing under mechanical stress and in presence of magnetic field. The stress relief process is related to the existence of local minima of potential energy and occurs through thermal activation. Due to disorder, the activation barrier forms a spectrum. The structure of this spectrum can be obtained from the study of annealing behaviour of anisotropy. The response of magnetic properties to

external stress facilitates to determine the nature and magnitude of anisotropy energy.

The local anisotropy also plays an important role in determining the magnetic state of RE-TM amorphous system. In this system the local easy axis of magnetic moment is considered to be random in nature. The consequence of local random anisotropy of magnetic system have been examined by assuming uniform exchange interaction between magnetic moments [56]. It is found that the strong disorder in anisotropy direction results a magnetic state with no long range order but frozen moment.

The family of soft magnetic materials has been considerably enriched by the discovery of nanocrystalline alloys [57], [58]. Yoshizawa, Oguma and Yamauchi reported for the first time, a new class of iron-based alloys exhibiting excellent soft magnetic behaviour [59]. The materials revealed an ultrafine microstructure of bcc Fe-Si with grain sizes of 10-15 nm (after this named *nanocrystalline*) embedded in an amorphous matrix. This particular microstructure provided excellent magnetic properties such as low losses, high permeability and low magnetostriction achieved by permalloys and Co-based amorphous alloys, but with a high saturation magnetization upto 1.3 T, much higher than either of these materials [60] - [62]. These materials also known by their trade names $FINEMET^R$ (this name derives from the combination of FINE and METAL) [63] and $VITROPERM^R$ [64], has great potential use as core material, magnetic components as saturable reactors, choke coils, transformers and can also be used for superior electromagnetic noise suppression for electric and electronic devices.

The precursor of $FINEMET^R$ is amorphous ribbon (non-crystalline) obtained by rapid quenching at $\sim 1 million°$C/second from the molten metal consisting of Fe, Si, B and small amounts of Cu and Nb. The soft magnetic properties of $FINEMET^R$ result from its two phase nanocomposite microstructure where nanocrystalline grains of an α-Fe-Si phase is embedded in the amorphous matrix. This fine microstructure has been shown to depend on Cu atoms (which are not soluble in bcc-Fe or the derivative DO3 structure of α-Fe-Si clustering and aiding nucleation for nanocrystallization of Fe-Si grains [65]-[67]. The alloy with composition $Fe_{73.5}Cu_1Nb_3Si_{13.5}B_9$ at% can be considered as a typical FeSiB metallic glass with additions of Cu and Nb. This material produced by rapid solidification is subsequently annealed above its crystallization temperature. Annealing of $Fe_{73.5}Cu_1Nb_3Si_{13.5}B_9$ at temperatures between $\sim 500°$C to $600°$C leads to the

primary crystallization of of ultrafine bcc $Fe_{\sim 80}Si_{\sim 20}$ grains with typical grain sizes of 10-15 nm. The bcc grains are randomly oriented and embedded in a residual amorphous matrix which occupies about 20-30 % of the volume and separates the crystallites at a distance of about 1-2 nm. This nanocrystalline structure is the basis for the excellent soft magnetic properties indicated by the high values of initial permeability of $\sim 10^5$ and correspondingly low coercivities of less than 1 A/m. The only drawback of this nanocrystalline material is that it becomes brittle upon crystallization.

1.4.7   Giant magnetoimpedance and Magnetic Barkhausen noise

Giant magnetoimpedance (GMI) is the huge change in both the real and imaginary components of total impedance of a metallic conductor upon the application of an external static magnetic field. When an alternating current is applied to these conductors, their impedance $Z = R + j\omega L$ changes sensitively with the change in biasing dc magnetic field, where R and L are the resistance and inductance of the conductor and $j = \sqrt{-1}$. This externally applied magnetic field induces changes in the effective complex magnetic permeability of the material and hence on the material's complex impedance. GMI effect depends sensitively on the frequency of the alternating current flowing through the sample. It is also strongly dependent on the magnetic anisotropies and domain configuration of the sample. The common experimental method for evaluating GMI is measured through the four-points technique by which the voltage at the ends of the sample is measured as a function of the ac current flowing along the sample. Change in the impedance is observed when the sample is subjected to a static magnetic field. The percentage change of MI with applied magnetic field is calculated by using the expression,

$$\frac{\Delta Z}{Z} = 100[\frac{Z(H) - Z(H_{max})}{Z(H_{max})}] \tag{1.7}$$

where$Z(H)$ and $Z(H_{max})$ are the magnetoimpedance for any magnetic field (H) and for the maximum applied magnetic field (H_{max}) respectively.

First reports of this effect by Harrison et. al. [68], [69], attracted much attention in 1990's until its rediscovery by Panina and Mohri and Beach and Berkowitz [70] - [73]. Since then GMI effect has been studied extensively in various materials for its wide range of technological applications [74] - [76].

The application of a varying magnetic field to a ferromagnetic material induces small discontinuous changes in the magnetization of the material. These sudden localized changes in magnetization are produced by the abrupt motion of domain walls from one pinning site to the next. The corresponding voltages induced in a pick-up coil on the sample are referred to as Magnetic Barkhausen noise (MBN) [77], [78]. This effect known as Barkhausen effect was discovered by Heinrich Barkhausen in 1919 [79]. MBN is caused by jerky domain-wall motion in ferromagnetic materials and is a fundamental proof of the existence of magnetic domains in these materials. The magnetization process in ferromagnetic materials mainly consists of the reversible and irreversible displacement of domain walls and irreversible rotation of local domain magnetization. MBN is primarily associated with the depinning and discontinuous motion of 180° domain walls and has been used as a tool for the estimation of residual stress, determination of magnetic easy axis and characterization of microstructure and particle size [80].

1.5 Summary and Organization of the Thesis

To study the magnetic properties of amorphous magnetic materials, in the form of wire, microwire and ribbon, some experimental set up have been developed and described in Chapter 2 of this dissertation. For generating highly homogeneous magnetic field, air-core solenoid and Helmholtz coil has been fabricated. An experimental facility has been developed to measure the stress and temperature dependence of magnetic properties of soft magnetic materials using fluxmetric method. For the measurement of magnetoimpedance of amorphous wires and microwires at different values of external stress, an experimental set-up has been assembled. Magnetic barkhausen noise from different amorphous magnetic materials were measured by a home-fabricated sensitive experimental set-up. An arrangement has been made for short duration heat treatment of these samples. Here heat treatment was performed by sending current pulses (square wave) each of duration of ~ 12 seconds. These current pulses were generated by a 555-timer IC.

The frequency dependence of magnetoimpedance of amorphous wire with composition $Co_{68.15}Fe_{4.35}Si_{12.5}B_{15}$ has been studied in the presnce of various tensile stresses up to 285 MPa and the results are presented in Chapter 3. The contribution to giant magne-

toimpedance were found to be different from different domain regions of the wire. The external stress affects the MI of these materials to a large extent as magnetocrystalline anisotropy is absent and magnetoelastic anisotropy is the main source of anisotropy in these materials. At a particular frequency, a stress-induced anisotropy changes the domain structure, magnetization dynamics and hence the MI. Single peak MI characteristics obtained at lower frequencies ($\sim$ a few kHz) were changed to a double-peak behaviour with the application of a tensile stress or increase in frequency. Asymmetry between the two peaks were also developed by sending a dc current of 5 mA. For a better understanding of the MI results, hysteresis loop measurements of the amorphous wire (by fluxmetric method) at various frequencies and tensile stresses were performed. We have also developed a model to investigate the stress dependent GMI effect in amorphous $Co_{68.15}Fe_{4.35}Si_{12.5}B_{15}$ wire. The effect of stress was incorporated by changing the IC and OS volume. This model qualitatively describes well the GMI response to the external axial stress at different exciting frequencies.

The domain structure of wire-shaped amorphous magnetic material can also be predicted from the measurements of magnetoimpedance of glass-coated amorphous microwires, which has been described in Chapter 4. The effect of external stress and heat treatment (by different forms of current annealing) in glass-coated amorphous microwires with compositions $Co_{83.2}Mn_{7.6}Si_{5.8}B_{3.3}$ and $(Co_{0.93}Fe_{0.07})_{63}Ni_{10}Si_{11}B_{16}$ are studied in this chapter. In amorphous $Co_{83.2}Mn_{7.6}Si_{5.8}B_{3.3}$ microwire, GMI effect has been studied upto a frequency, $f \sim 12.85$ MHz . The GMI of this sample is also very stress sensitive and decreases from 53% to 24% due to the application of an axial tensile stress of 566 MPa. Two-peak GMI characteristic observed at high frequency reduces to one peak when sufficient high stress was applied. GMI in this microwire was increased from 66% to 129% on short duration heat treatment by passing four current pulses of amplitude of 100 mA and each of 12 seconds duration. GMI effect was studied in amorphous $(Co_{0.93}Fe_{0.07})_{63}Ni_{10}Si_{11}B_{16}$ microwire upto a frequency of 11 MHz. This sample showed single peak GMI characteristics within the whole range of frequency. A maximum change of 8.85% in MI of the as-quenched sample reduced to 3.92% on application of an external stress (603 MPa), whereas heat treatment (by passing a dc current of 50 mA for 25 minutes) enhanced the MI value to 18.74%.

In Chapter 5, we have studied the magnetization processes in ferromagnetic amorphous magnetic materials using Magnetic Barkhausen noise technique. A theoretical model has been developed to estimate the direction of magnetic easy axis in amorphous $Fe_{40}Ni_{40}B_{20}$ ribbon. We have also studied the effect of tensile stress on MBN in amorphous $Fe_{40}Ni_{40}B_{20}$ and $Fe_{70}Ni_8Si_{10}B_{12}$ ribbons. Influence of heat treatment on MBN has also been done in amorphous $Fe_{40}Ni_{40}B_{20}$ ribbon to investigate the amorphous structural changes. The hysteresis loops of amorphous $Fe_{40}Ni_{40}B_{20}$ and $Fe_{70}Ni_8Si_{10}B_{12}$ ribbons, measured under different axial tensile stresses by induction method gives a better understanding of the MBN results. MBN from the as-quenched and annealed (heated at 540°C for 1 hour) $Fe_{73.5}Cu_1Nb_3Si_{13.5}B_9$ ribbon was studied to investigate the amorphous to crysatlline phase transformation. To get a clear understanding of the domain structure and magnetization processes in wire-shaped amorphous magnetic materials, we have studied stress dependent MBN on $Co_{68.15}Fe_{4.35}Si_{12.5}B_{15}$ amorphous wire.

So, from the above study, it is clear that magnetoelastic anisotropy mainly governs the magnetic properties in ferromagnetic amorphous materials, which originates from the internal stress frozen-in during preparation. It has been found that different forms of heat treatment can be a useful method to improve the magnetic properties of these materials by reducing internal stresses. Relaxation of internal stress or application of external stress causes a change in the magnetoelastic energy, a feature that has been exploited to improve the magnetic responses, which is presented in this thesis.

Chapter 2

DEVELOPMENT OF EXPERIMENTAL SET-UP

2.1 Magnetization measurement set-up

2.1.1 Construction of an air-core Solenoid

For low field magnetic measurement (below 1000 G), air-core solenoid is very suitable and can be constructed easily by winding insulated copper or aluminium wire on a cylinder made of any insulator. The field (in Oe) produced at any point on the axis can be calculated using the expression,

$$H = \frac{2\pi n I}{10}(cos\theta_1 - cos\theta_2) \tag{2.1}$$

where n and I are the number of turns/cm and current (in ampere) respectively. The angle θ_1 and θ_2 have been shown in Fig. 2.1(a). Magnitude of the field can be increased
(a) by increasing the number of turns/cm and the layers which are limited by the power supply available in the laboratory and
(b) by increasing the current through the wire, which is limited by the heat generated because this can damage the insulated coating of the wire.
So, all these parameters should be optimised. On the other hand, for a solenoid of finite length, homogeneity falls off rapidly on both sides of the centre which can be increased by increasing length and decreasing the diameter. But longer solenoid results higher resistance which is unwanted. So, the homogeneity of a sufficiently short solenoid ($\sim$ 20 cm) can be increased by using compensating coil at the two ends of the solenoid. Considering the above facts a solenoid along with the compensating colis at the two ends, have been constructed by winding copper wire on an insulator as shown in the Fig. 2.2
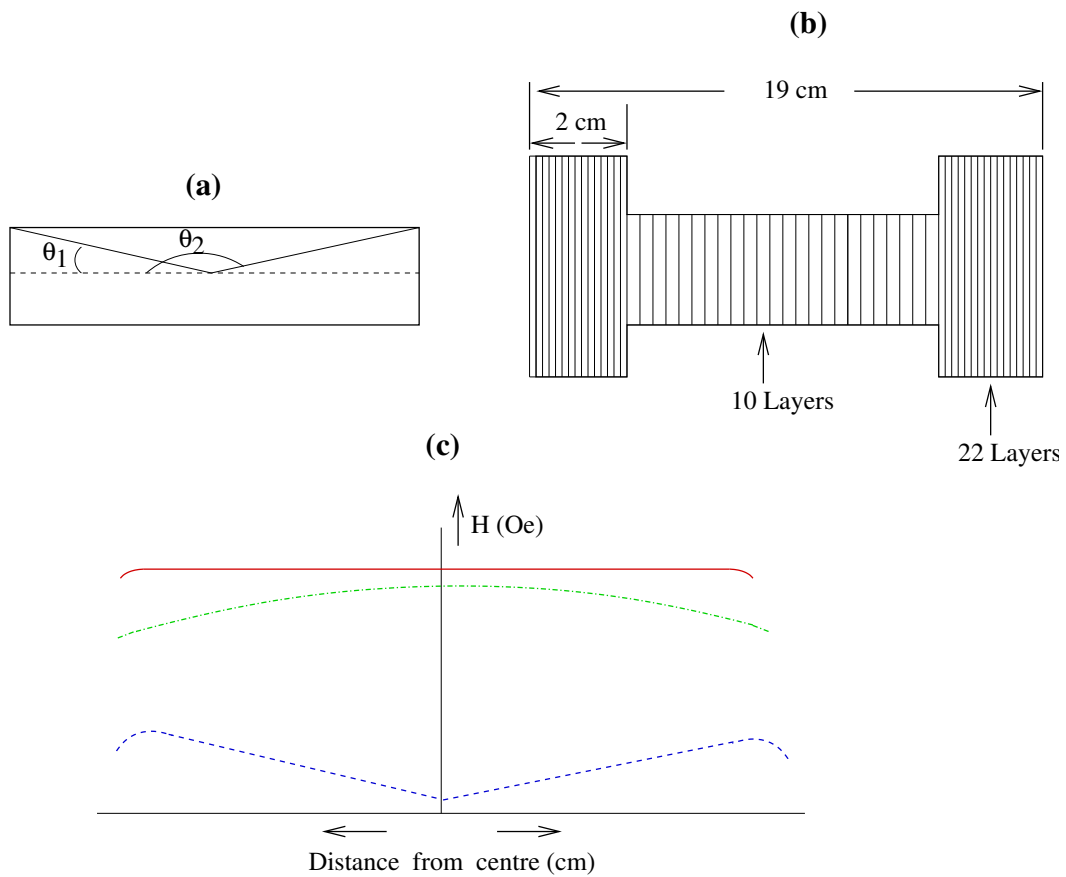
(b)

(a)

(c)

Figure 2.1: (a) Figure for solenoid field calculation (b) Geometry and dimensions of the main and compensating coil of the solenoid (c) Magnetic field due to the main coil (green dash and dot line), the compensating coil (blue dotted line) and the resultant of the above two (red solid line).

with the indicated dimensions (Fig. 2.1(b)).

The magnetic field due to the main coil, the compensating coil and the resultant of the above two have been shown in Fig. 2.1(c). A maximum of 0.2 % field inhomogeneity has been observed within 10 cm central zone of the solenoid.
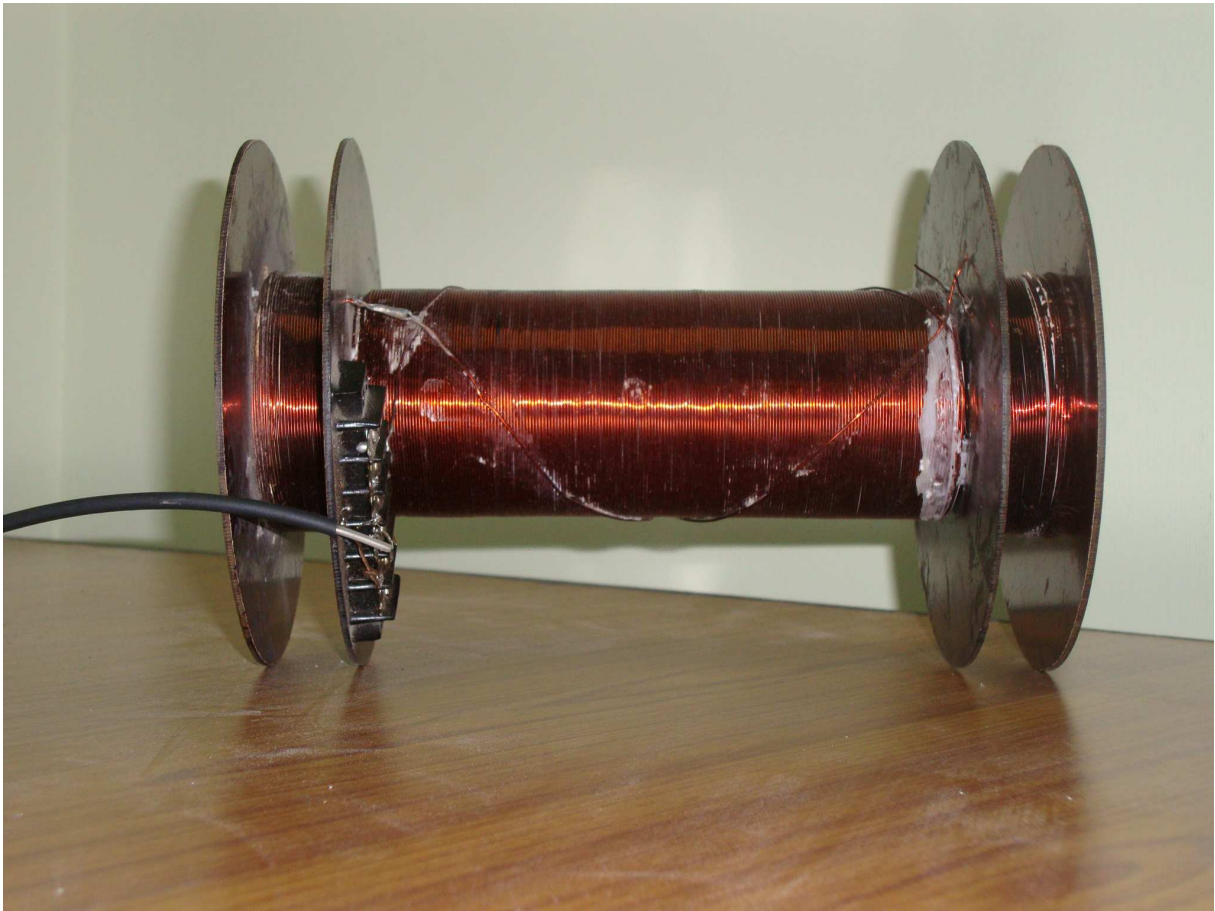
Figure 2.2: Photograph of the constructed solenoid along with the compensating coils at the two ends.

2.1.2   Construction of a Helmholtz coil

A Helmholtz coil has been constructed for producing a homogeneous magnetic field in its centre as shown in Fig. 2.3 with the indicated dimensions. The magnetic field is directly proportional to the number of turns in the coils and the current applied to them. Here the parallel pair of identical circular coils are spaced one radius (r =25 cm) apart and wound in such a manner so that the current flows through the coils in the same direction. This winding gives a very uniform magnetic field between the coils with the primary component parallel to the axes of the two coils. This uniform field is the resultant of the addition of the two field components parallel to the axes of the two coils. The magnetic
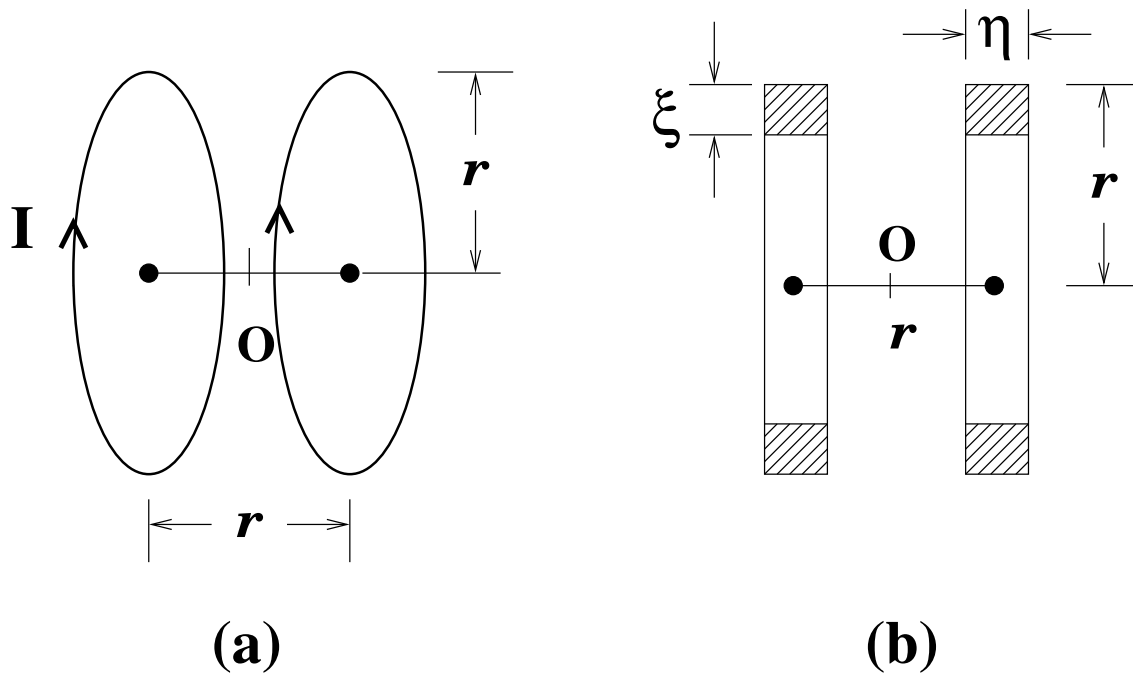
Figure 2.3: (a) Geometry and (b) dimensions of the constructed Helmholtz coil.

field strength, H along the axis, generated by a given AC or DC current through the pair of coils is given by

$$H = 0.899\frac{NI}{R} \qquad (2.2)$$

where, H is in oersteds, N is the number of turns per coil, I is the coil current in amperes and R is the coil radius in centimeters. For Helmholtz coil with extended cross-section, the dimensions ξ (here it is 2.15 cm) and η (here it is 2.0 cm) should be in the ratio of $\xi/\eta = 1.0776$ for maximum field uniformity. The magnetic field generated by this Helmholtz coil is 10.55 Oe/ampere. Only 0.1% inhomogeneity in magnetic field within the central portion of the coils ($\sim$ 10 cm) has been observed.

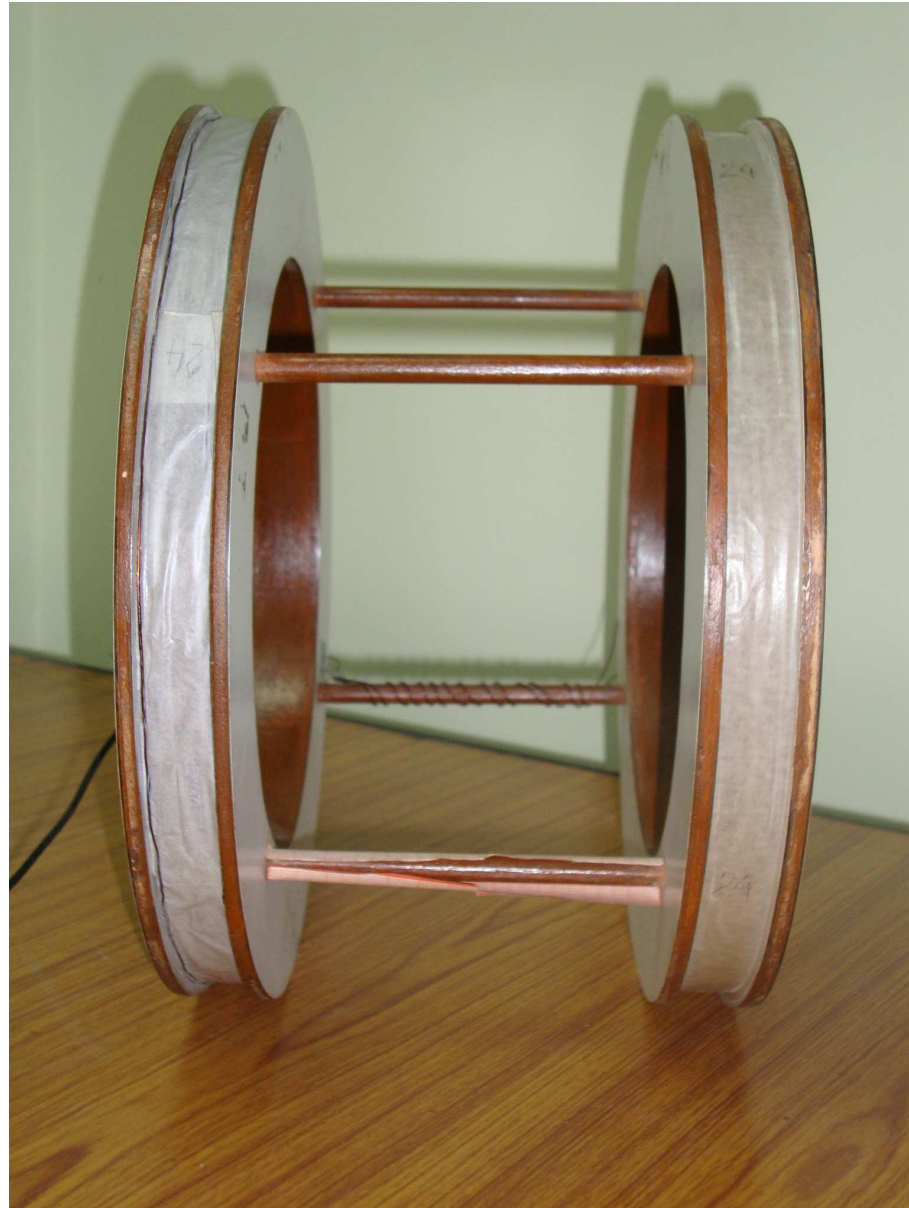The photograph of the constructed Helmholtz coil is shown in Fig. 2.4.

Figure 2.4: Photograph of the constructed Helmholtz coil.

2.1.3   Experimental set up for measuring different magnetic properties of soft magnetic materials

The magnetic properties of a material is mainly characterized by measuring the quantities like initial susceptibility, coercive field, saturation magnetization, anisotropy energy, remanent magnetization etc. and they can be determined if we can plot the anhysteretic or normal M vs H curve and hysteresis loop of that material. The usual methods of measuring magnetization can be divided into three classes: (1) measurement of the force acting on the magnetic specimen, (2) measurement of the magnetic field produced by the sample and (3) measurement of the voltage or current induced by electromagnetic induction. Most of the results on magnetic properties, given later in this dissertation, have been measured by fluxmetric method which belong to the third category and is very suitable for measuring various magnetic propertis of soft ferromagnetic materials.

The magnetization value of amorphous magnetic materials were measured as a function of dc magnetic field H and at different external tensile stresses σ by fluxmetric method. Fig.2.5 shows the block diagram of the experimental set-up for measuring both a.c. and d.c. M-H curves. The sample is placed symmetrically in one of two identical secondary coils which are in series opposition for the cancellation of signal in absence of any sample. The coils were located coaxially within a long solenoid producing a homogeneous field along the length of the sample. The flux in presence of the sample is measured with an integrating fluxmeter (Walker Scientific MF-3D). The MF-3D is a precision electronic integrating fluxmeter which measures the magnetic flux coupling within a coil or loop of wire. It integrates the volt-second signals induced across a coil, by the flux coupling to the coil. The output is representative of the change in flux coupling during the integrating period. Each magnetic line (Maxwell), in linking a conductor induces in it a 10^{-8} volt-second impulse. For a coil of N turns, the signal input received is $N\phi$ Maxwell-turns or $N\phi10^{-8}$ volt-seconds. Therefore the induced voltage in presence of the sample is

$$V = N\frac{d\phi}{dt}10^{-8} \tag{2.3}$$

The flux can be expressed as AB where A is the area of the coil in which a flux density B is experienced, and the input impulse becomes, $NAB10^{-8}$ volt-seconds. By virtue of the heavy feedback employed in the integrator, its input impedance appears as the resistance
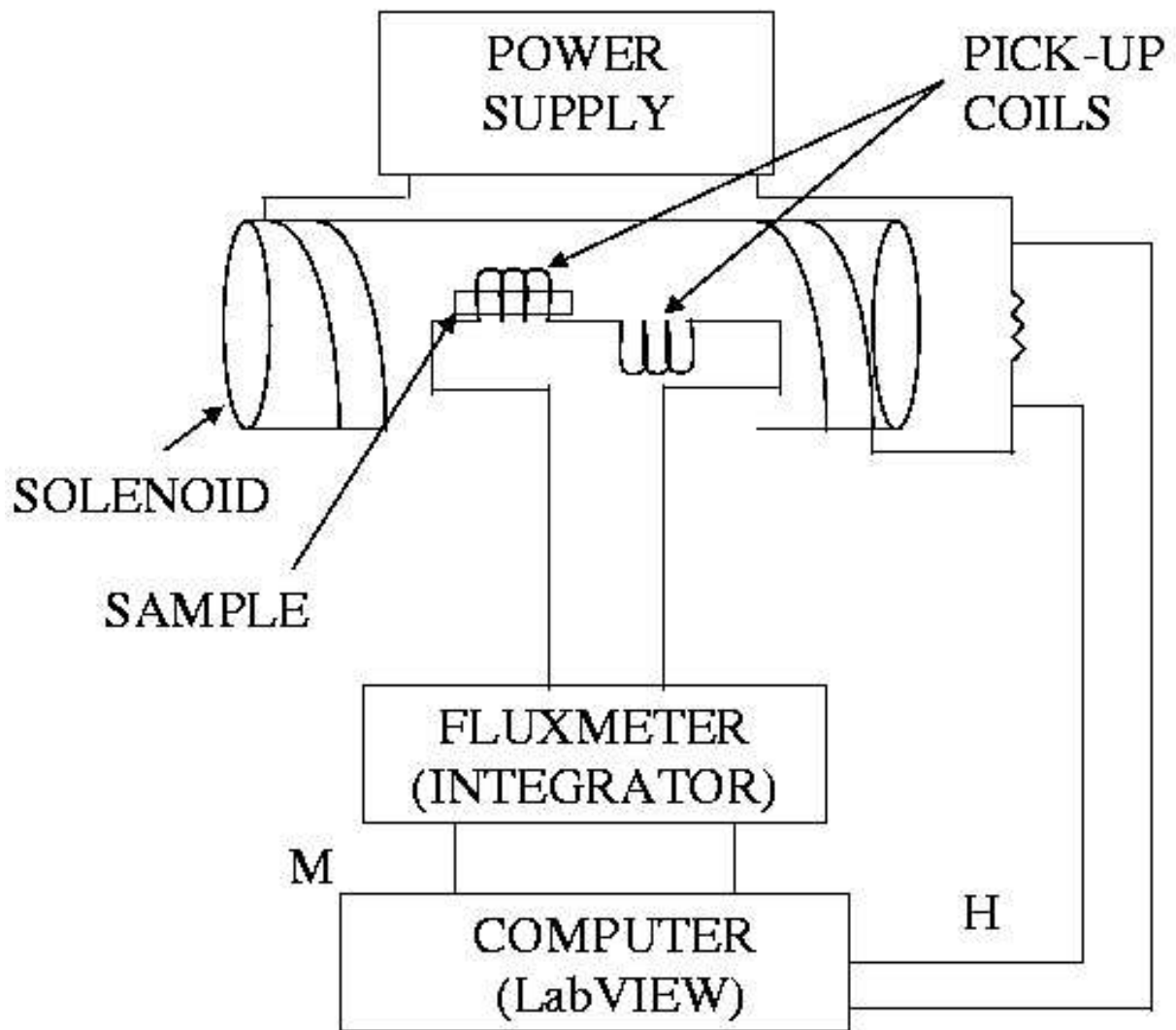
Figure 2.5: Block diagram of the experimental set-up for measuring a.c. and d.c. hysteresis loops.

Figure 2.6: Photograph of the experimental set-up for measuring hysteresis loops.

value set in on the decade dial. A current, $\frac{NAB}{R}10^{-8}$ ampere-seconds flows in this resistor and is constrained by the feedback to flow solely into the integrating capacitor which is free to move in voltage only at the output terminal. From the relationship, voltage equals charge (ampere-seconds) divided by capacitance, we obtain the output voltage (in volts)

$$V = \frac{N\phi}{RC}10^{-8} = \frac{NAB}{RC}10^{-8} \tag{2.4}$$

The value of R (Ω) is 100 times the setting of the decade dial, and the value of C (farad) is 10^{-7}, 10^{-6} or 10^{-5}, depending on the range selected. This integrated voltage which is proportional to the magnetization of the sample was recorded as a function of the voltage proportional to the magnetic field produced by the uniform solenoid. These voltages corresponding to M and H are recorded in two respective Digital Multimeters (Agilent, 34401A) and then plotted in the computer using a program in Labview. M-H curve of the sample is finally obtained after calibrating the values of these voltages. Fig. 2.6 shows the photograph of the experimental set-up for measuring hysteresis loops.

Figure 2.7: Photograph of the experimental set-up for studying stress dependent magnetization measurements.

Stress dependent hysteresis loops were studied by applying external tensile stress, by loading one end of the sample and keeping the other end fixed as shown in Fig.2.7. For investigating the effect of stress in GMI and MBN study, tensile stresses were applied along the length of the samples as shown in Fig.2.8. The magnetic properties of the sample such as coercive field, anisotropy field, saturation magnetization, remanent magnetization were measured from the hysteresis loop.
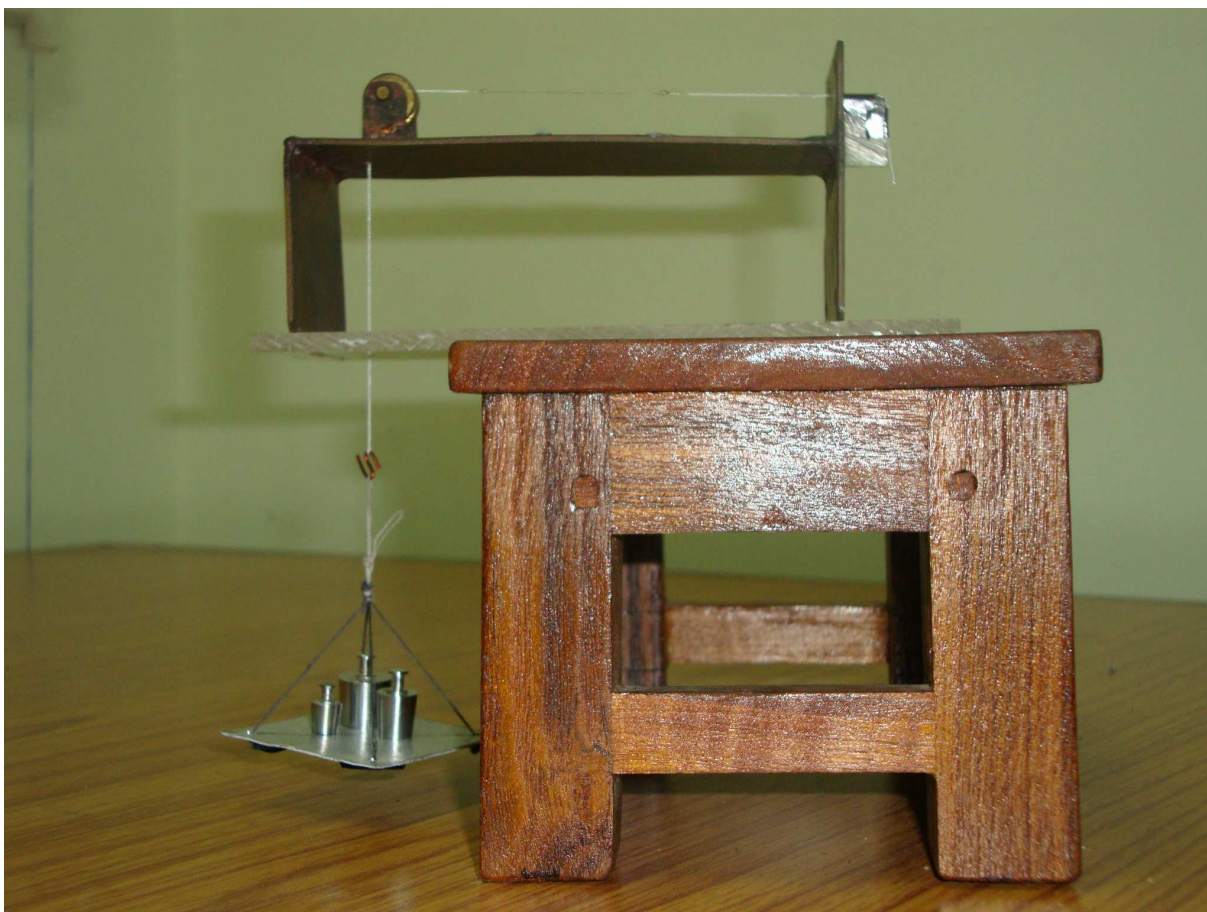
Figure 2.8: Photograph of the experimental set-up for applying stress to various amorphous samples used in stress dependent GMI and MBN study.

Figure 2.9: Photograph of the experimental set-up for measuring giant magnetoimpedance.

2.2 Giant magnetoimpedance measurement set-up

The impedance of the samples were measured by a Precision Impedance Analyzer (Agilent 4294A, 40 Hz 110 MHz) as shown in Fig.2.9 The frequency of the ac current was varied up to 12 MHz and its magnitude was kept fixed at 1 mA. A Helmholtz coil system was used to apply a dc magnetic field (maximum value ∼ 140 Oe) along the axis of the sample during impedance measurement. The axis of the sample as well as that of the Helmholtz coil was kept perpendicular to the direction of the earths magnetic field. Axial tensile stresses were applied to the samples (by loading one end of the sample and keeping the

other end fixed) for studying the effect of stress on magnetoimpedance. The percentage change of MI with applied magnetic field was calculated from Eqn. 1.7

The asymmetry between the two peaks of GMI profile in the amorphous $Co_{68.15}Fe_{4.35}Si_{12.5}B_{15}$ wire has been developed by passing a dc current I_{dc}=5 mA through the sample during GMI measurement. For investigating the effect of heat treatment in presence of a circular magnetic field in glass-coated amorphous $(Co_{0.93}Fe_{0.7})_{63}Ni_{10}Si_{11}B_{16}$ microwire, a dc current with amplitude, $I_{an} = 50$mA has been passed through the sample for various time duration, T_{an} starting from 5 minutes to 35 minutes. To study the effect of short duration heat treatment, current pulses (square wave) f amplitude ~ 100 mA and each of duration of ~ 12 seconds (generated by 555-timer IC) were sent through glass-coated amorphous $Co_{83.2}Mn_{7.6}Si_{5.8}B_{3.3}$ microwire.

2.3 Magnetic Barkhausen Noise set-up

Generation, detection and analysis of Barkhausen noise were accomplished using a home-fabricated Barkhausen noise experimental set-up as shown in Fig.2.10 The instrument consists of a Helmholtz coil for applying a time varying magnetic field to the sample to generate Barkhausen noise. The signal to the Helmholtz coil was produced by a 15 MHz Function/Arbitrary Waveform Generator (Agilent-33120A) and amplified by a Bipolar Operational Power Supply/Amplifier (Kepco, BOP 72-3M). The sweep field frequency was set at various frequencies from the waveform generator (4 Hz and 12Hz). Barkhausen noise was detected using a pick-up coil wound around the sample located at the centre of the Helmholtz coil, with the sample aligned parallel to the direction of the magnetic field. The signal from the pick-up coil was amplified by the Low-noise preamplifier (Stanford Research Systems, Model SR560), passed through a band-pass filter and then collected to a personal computer. Fig. 2.11 shows the photograph of the experimental setup for measuring MBN.
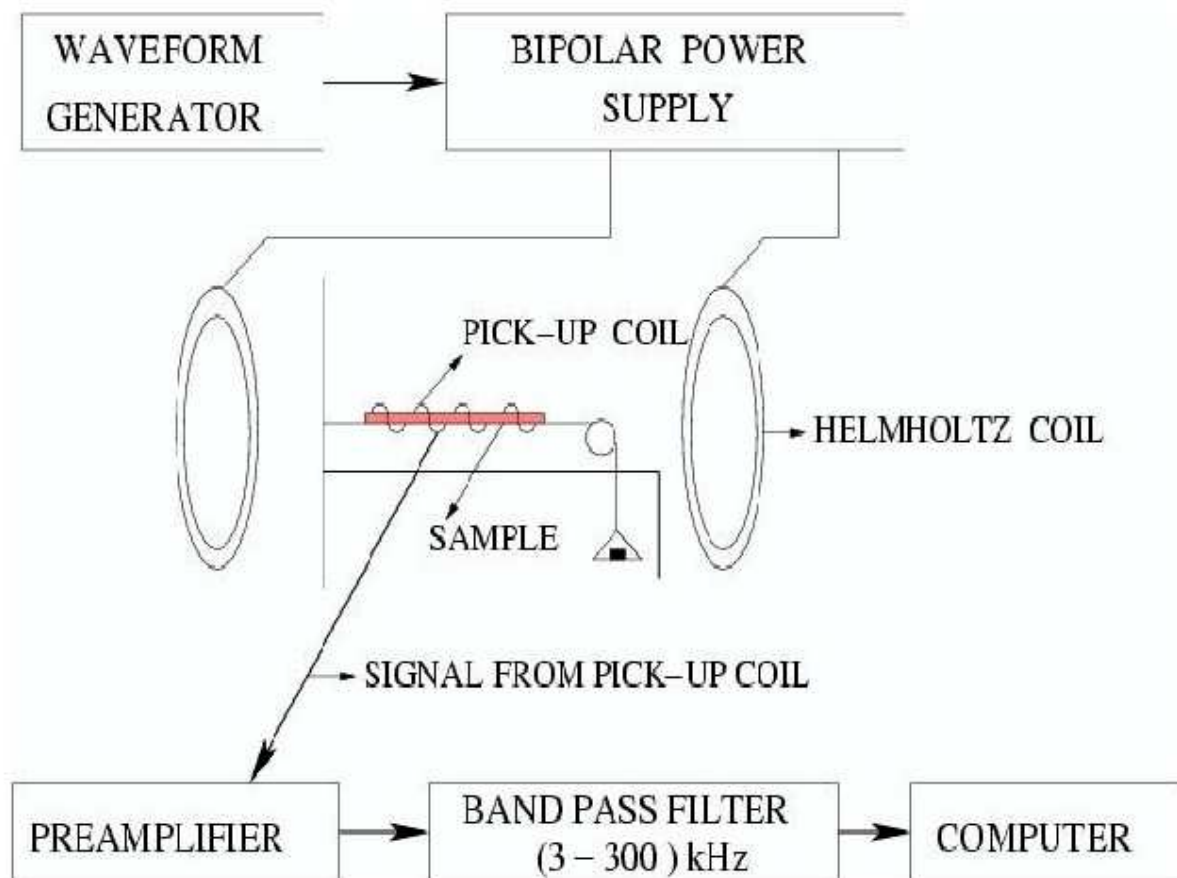
Figure 2.10: Block diagram of the experimental set-up for measuring Magnetic Barkhausen noise.

Figure 2.11: Photograph of the experimental set-up for measuring Magnetic Barkhausen noise.
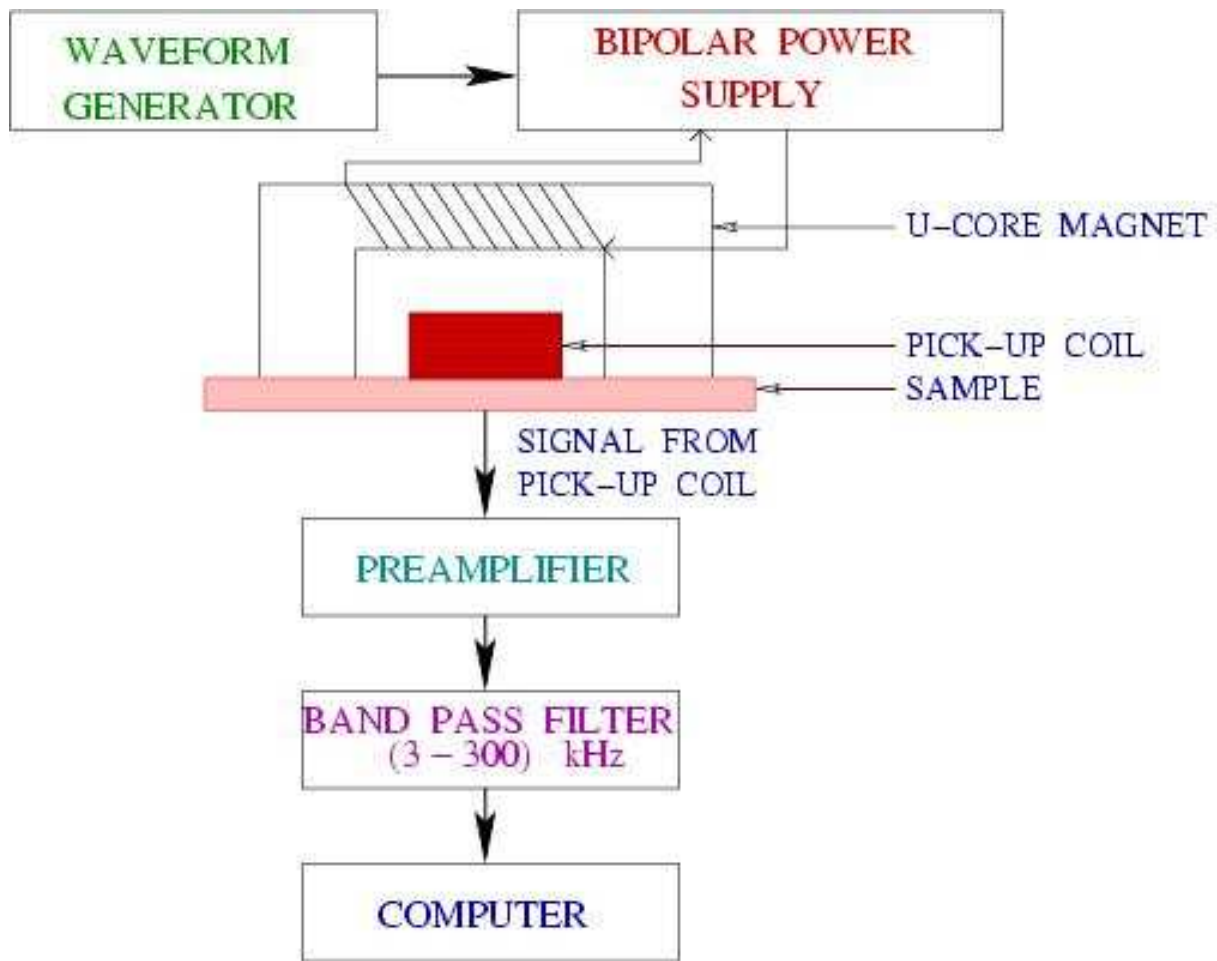
Figure 2.12: Block diagram of the experimental set-up for measuring surface Magnetic Barkhausen noise.

The block diagram of the experimental setup developed for the surface MBN measurement is shown in Fig. 2.12. A magnetic field, which is sufficient for the technical saturation of the sample, is generated by passing a 4 Hz or 12 Hz sinusoidal current through a U-shaped ferrite core. A small pick-up coil is placed between the two pole pieces of the U-core magnet to detect the MBN signals. Fig. 2.13 shows the photograph of a U-shaped ferrite core along with the pick-up coil placed between the pole pieces of the core. The signal from the coil is preamplified, filtered using a bandpass filter and then fed into a personal computer.

Figure 2.13: Photograph of a U-shaped ferrite core with the pick-up coil placed between the pole pieces of the U-core magnet used for measuring surface Magnetic Barkhausen noise.

Only those voltage signals above a certain threshold were considered in the analysis. The MBN energy denoted by E_{MBN} is calculated by integrating the square of these voltages w.r.to time i.e.,

$$E_{MBN} = \sum_{i=1}^{n} \int V_i^2 dt \qquad (2.5)$$

where the time integral is over each event and the summation is taken over all N measured events. For this purpose, a computer program has been developed.

For investigating the effect of stress, tensile stresses were applied along the length of the samples, where tensile stress was applied by hanging various loads from one end keeping

the other end fixed. Angular dependent MBN measurements were performed by varying the orientation of the magnetic field w.r.to the axis of the sample from 0° to 360° at intervals of 10°.

2.4 Set-up for Flash annealing

The physical properties of metallic glasses are very sensitive to the thermal tratment because of their metastable state. The extent of change in these magnetic materials depend on both the temperature and duration of annealing. It has been observed that a short duration heat treatment can be used more effectively than the prolonged one to relieve the internal stress of the samples. The short duration heat treatments can be given either by allowing an electric current of large amplitude to pass through the sample for a very short duration of time called flash annealing or by irradiating the sample by infrared light pulses.

The experimental set-up for flash annealing has been shown in Fig. 2.14. The one-shot square wave pulse is generated by the 555 timer IC. It triggers itself and work as a free run multivibrator. When power is first applied to the circuit, the external capacitor (C) will be uncharged, therefore both the trigger and threshold inputs will be near zero volts. The lower comprator sets the control flip-flop (built inside 555 timer IC) causing the output to switch high. That also turns off transistor T1 (built inside 555 timer IC) This allows the capacitor to begin charging through R_1 and R_2. As soon as the charge on the capacitor reaches 2/3 of the supply voltage the upper comparatorwill trigger causing the flip-flop to reset. That causes the output to switch low. Transistor T1 also conducts. The effect of T1 conducting causes resistor R_2 to be connected across the external capacitor. Resistor R_2 is effectively connected to ground through internal transistor T1. The result of it is that the capacitor now begins to discharge through R_2. As soon as the voltage across the capacitor reaches 1/3 of the supply voltage, the lower comparator is triggered. That again causes the control flip-flop to set and the output to go high. Transistor T1 cuts off and again the capacitor begins to charge. This cycle continues to repeat with the capacitor alternately charging and discharging, as the comparators cause the flip-flop to be repeatedly set and reset. The resulting output is a continuous stream of rectangular
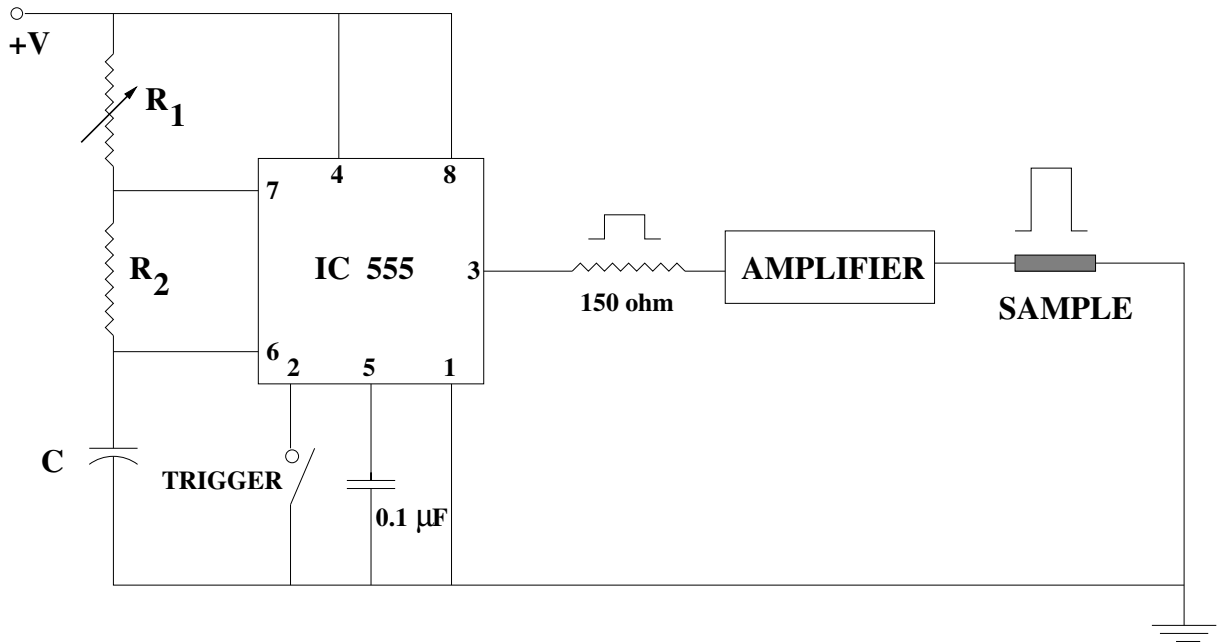
Figure 2.14: Block diagram of the experimental set-up for flash annealing.

pulses.

The charging time (output high) is given by

$$t_1 = 0.693(R_1 + R_2)C \tag{2.6}$$

and the discharging time (output low) is given by

$$t_2 = 0.693 R_2 C \tag{2.7}$$

The duration of the pulse can be varied from the fraction of a second to a few seconds by changing the resistance R_1 and external capacitor C and the amplitude can be changed by varying the supply voltage V_{CC}. The current pulse was amplified by a Bipolar Operational Power Supply/Amplifier (Kepco, BOP 72-3M) and finally sent through the sample. Fig. 2.15 shows the photograph of the experimental set-up for flash annealing.

Figure 2.15: Photograph of the experimental set-up for flash annealing.

Chapter 3

GIANT MAGNETOIMPEDANCE IN AMORPHOUS MAGNETIC MATERIALS

3.1 Introduction

Magnetoimpedance (MI) is the change of both the real and imaginary components of total impedance of a magnetic conductor (usually ferromagnetic) upon the application of an external static magnetic field, H_{dc}. When an alternating current is applied to these conductors, their impedance $Z = R + j\omega L$ changes sensitively with the change in biasing dc magnetic field (H_{dc}), where R and L are the resistance and inductance of the conductor and $j = \sqrt{-1}$. Giant magnetoimpedance (GMI) is the huge change in the material's complex impedance under the application of an external magnetic field. This externally applied magnetic field induces drastic variations in the effective complex magnetic permeability of the material. This variation in the effective complex permeability within the material causes variations in the internal fields and electrical current density and hence on the material's complex impedance. GMI effect depends sensitively on the frequency of the alternating current flowing through the sample. It is also strongly dependent on the magnetic anisotropies and domain configuration of the sample. The percentage change of MI with applied magnetic field is calculated by using the expression

$$\frac{\Delta Z}{Z} = 100[\frac{Z(H) - Z(H_{max})}{Z(H_{max})}] \tag{3.1}$$

where$Z(H)$ and $Z(H_{max})$ are the magnetoimpedance for any magnetic field (H) and for the maximum applied magnetic field (H_{max}) respectively.

Magnetic field dependence of the complex impedance of a ferromagnetic wire was first observed long time back by Harrison et. al. [68], [69]. Giant magnetoresistance effect (GMR) was observed in amorphous $Co_{68.1}Fe_{4.4}Si_{12.5}B_{15}$ wire which was enhanced in the presence of stress by Mandal et.al. [81]. Panina et. al. observed giant magnetoinductive (at low frequencies, 1 -10 kHz) and giant magnetoimpedance (at high frequencies, 0.1 - 10 MHz) effects in FeCoSiB amorphous wires[70],[71]. GMI measurements as functions of axial magnetic field and ac frequencies for $Fe_{4.3}Co_{68.2}Si_{12.5}B_{15}$ wire and ribbon were studied extensively by Beach et. al. Panina and Mohri and Beach and Berkowitz [72],[73] explained GMI effect using classical skin effect. Machado et. al. observed similar effect in FeCoSiB thin films [82] during that period. Since then GMI effect has been studied extensively in amorphous wires. A maximum change in magnetoimpedance of 180% for the former and 300% for the latter wire is reported here [83]. Vazquez et. al. have reported the field dependence of GMI in amorphous $Co_{68.1}Fe_{4.4}Si_{12.5}B_{15}$ wire after current annealing (1 minute, 0.5 A) under different values of stress [84]. Knobel et. al. [85]have studied the effect of stress on GMI in positive and negative magnetostrictive amorphous wires of compositions $Fe_{4.9}Co_{71.8}Nb_{0.8}Si_{7.5}B_{15}$ and $Co_{68.1}Fe_{4.4}Si_{12.5}B_{15}$ respectively for two different frequencies ($f = 5$ kHz and 100 kHz). Chen et. al. [86] have calculated the impedance of a metallic soft magnetic wire with periodic circular domains related to domain-wall displacements and compared with the classical model relevant to domain magnetization rotations. Frequency dependence of GMI in amorphous $Co_{68.15}Fe_{4.35}Si_{12.5}B_{15}$ wire in presence of external stress is studied extensively by Mandal et. al. [87] to understand the contributions to GMI from two different domain regions i.e. inner core (IC) and outer shell (OS). Here it is shown that the OS with transversely oriented magnetization contributes mainly to GMI.

Giant magnetoimpedance effect is studied extensively in microwires [88] - [91], thin films [92] - [94], ribbons [93],[95],[96], sandwich structures [97],[98], nanocrystalline materials [99],[100], commercial materials such as mumetal [101] among others. The study of GMI effect in these varied materials is due to its potential technological applications in the design of tiny magnetic recording heads and micromagnetic sensors [84],[95], [102].

The origin of GMI is different in various frequency regions of the exciting alternating current [75],[104]. For a conductor in an external magnetic field with a varying frequency,

ω, the magnetic field penetrates into the conductor and induces in it a variable electric field. This field creates current in the conductor known as Eddy currents. The magnetic field penetrates into the conductor to a distance δ, given by,

$$\delta = \sqrt{\frac{c^2}{2\pi\sigma\omega\mu}} \qquad (3.2)$$

where σ and μ are the electrical conductivity and circumferential permeability of the conductor . From Maxwell's equations of electromagnetic field we can write for a varible magnetic field with frequency ω,

$$\nabla^2\vec{H} = -\frac{4\pi i\sigma\omega\vec{H}}{c^2} \qquad (3.3)$$

For two limiting cases of penetration depth, δ :

(a) When δ is very large (i.e. for low frequencies) then to a first approximation we can write,

$$\nabla^2\vec{H} = 0 \qquad (3.4)$$

Therefore the magnetic field distribution will be same as it would be in the steady state.

(b) When δ is very small (i.e. for high frequencies) the magnetic field penetrates only into a thin surface layer of the conductor. This phenomenon is known as the skin effect.

Therefore depending on the frequency of the exciting alternating current through the samples, the origin of GMI can be broadly classified in three different regions.

(i)**Low frequency region ($\sim$ kHz)** :

The change in magnetoimpedance is only due to the inductive part which is known as magnetoinductance [70]. When an alternating current $I = I_0\exp{(-i\omega t)}$ flows through a circular wire of length l, a circular magnetic field H_ϕ is developed within the wire which magnetizes the wire in circular direction. This circular magnetization affects the voltage across the wire ends. When the skin effect is negligible i.e. at low frequencies this voltage across the ends of the wire is given by,

$$V_\phi = RI+ < E_z(r) > l \qquad (3.5)$$

where R is the resistance of the wire and $< E_z(r) >$ is the averaged electric field due to the change in the circular magnetization from the circular magnetic field,

$$H_\phi = \frac{2Ir}{ca^2} \qquad (3.6)$$

The averaged electric field is given by,

$$E_z(r) = -\frac{j\omega I}{c^2} \int_0^r \frac{2r'\mu_\phi(r')}{a^2} \, dr' \qquad (3.7)$$

where a is the radius of the wire. $\mu_\phi = dB_\phi/dH_\phi$ is the circular differential permeability. Writing $V = Z(\omega)I$ and averaging $< E_z(r) > l$ over the cross section of the wire, Eq. 3.5 reduces to

$$Z(\omega) = R - i(\frac{\omega}{c^2})L_i \qquad (3.8)$$

where $Z(\omega)$ is the the complex impedance and L_i the internal inductance of the wire given by,

$$L_i = 2l < \int_0^r \frac{\mu_\phi r'}{a^2} \, dr' > \qquad (3.9)$$

ω is the angular frequency of the alternating current, c is the velocity of light and $i = \sqrt{-1}$. When an additional dc magnetic field is applied along the wire axis the circular component of magnetization and the circular permeability changes giving rise to a large change in the total voltage and $Z(\omega)$ changes accordingly. Therefore it follows from above that at low frequencies, the field dependence of the impedance is attributed to its inductive part which is simply proportional to the circumferential differential permeability.

(ii)**High frequency region ($\sim$ MHz)** :

Huge change in magnetoimpedance i.e. GMI is observed which is due to the change in magnetic penetration depth in the sample caused by the changes in the effective magnetic permeability in presence of an externally applied magnetic field [70], [72]. In the high frequency region (500 kHz to a few MHz) the change in the impedance of the sample in presence of an external magnetic field depends on its skin depth which in turn depends on the permeability of the sample. The origin of GMI in this frequency range can be explained with the help of classical electomagnetism. When the frequency of the alternating current flowing through the sample is quite high ($\sim$ MHz), the cross-section through which the current flows is reduced due to the generation of eddy current and consequently the current flows through a thin sheath near the surface of the sample due to skin effect. From classical Maxwell's equations of electrodynamics, the ac impedance Z for any frequency of a straight wire of radius a and electrical conductivity σ can be obtained as follows [105]. For this linear circuit containing a variable emf, $\varepsilon(t)$, resistance R and inductance, L the total power can be divided into two parts. From the law of conservation of energy, the

total power, $\varepsilon(t)J$ is equal to the change in the magnetic field energy outside the wire and the other is the total energy consumed inside the wire (it is the total energy flux entering the wire through its surface per unit time), where J is the current density.

$$\varepsilon(t)J = \frac{d}{dt}\left(\frac{L_e J^2}{2c^2}\right) + \frac{c}{4\pi}[EH2\pi al] \tag{3.10}$$

where, L_e, a and l are the external part of the self inductance, radius and length of the wire respectively. E and H are the electric and magnetic fields at the surface of the wire. Solving above equation we get,

$$
\begin{aligned}
\varepsilon J &= \frac{L_e}{c^2}J\frac{dJ}{dt} + \frac{1}{2}EHcal \\
&= \frac{L_e}{c^2}J\frac{dJ}{dt} + \frac{1}{2}E\left(\frac{2J}{ca}\right)cal \\
&= \frac{L_e}{c^2}J\frac{dJ}{dt} + EJl \\
\varepsilon &= \frac{L_e}{c^2}\frac{dJ}{dt} + El
\end{aligned}
\tag{3.11}
$$

putting $J = J_0 e^{-i\omega t}$ and $\varepsilon = ZJ$, we get

$$
\begin{aligned}
\varepsilon &= \frac{L_e}{c^2}\frac{d}{dt}(J_0 e^{-i\omega t}) + El \\
ZJ &= \frac{L_e}{c^2}(-i\omega)J + El \\
Z &= -i\omega\frac{L_e}{c^2} + \frac{El}{J} \\
&= -i\omega\frac{L_e}{c^2} + \frac{2El}{Hca}
\end{aligned}
\tag{3.12}
$$

where, $H = \frac{2J}{ca}$.

Let us now calculate the electric field, $\vec{E}$ and magnetic field, $\vec{H}$ when current flows through the wire. The electric field is parallel to the axis and the magnetic field is in a plane perpendicular to the axis of the wire. From Maxwell's equations,

$$\vec{\nabla} \times \vec{E} = \frac{-1}{c}\left(\frac{\partial \vec{B}}{\partial t}\right) = \frac{-1}{c}\mu\left(\frac{\partial \vec{H}}{\partial t}\right) \tag{3.13}$$

$$\vec{\nabla} \times \vec{H} = \frac{4\pi \vec{J}}{c} = \frac{4\pi\sigma \vec{E}}{c} \tag{3.14}$$

$$\tag{3.15}$$

Therefore, from above two equations,

$$\vec{\nabla} \times (\vec{\nabla} \times \vec{E}) = \frac{-\mu}{c}\frac{\partial}{\partial t}(\vec{\nabla} \times \vec{H}) = \frac{-\mu}{c}\frac{\partial}{\partial t}(\frac{4\pi\sigma \vec{E}}{c})$$

Since $\vec{\nabla}.\vec{E} = 0$, therefore

$$\nabla^2 \vec{E} = \frac{4\pi\sigma}{c^2}(\frac{\partial \vec{E}}{\partial t})$$

Since in a variable field with frequency ω, all quantities depend on time through a factor $e^{-i\omega t}$, therefore above equation becomes,

$$\nabla^2 \vec{E} = -\frac{4\pi i\sigma\omega \vec{E}}{c^2}$$

In cylindrical polar coordinates with z-axis along the axis of the wire, the only non zero component of $\vec{E}$ is E_z which depends only on r. For a periodic field with frequency ω we can write,

$$\frac{1}{r}\frac{\partial}{\partial r}(r\frac{\partial \vec{E}}{\partial r}) + k^2\vec{E} = 0$$

where, $k = \frac{1+i}{\delta}$ and $\delta = \frac{c}{\sqrt{2\pi\sigma\omega}}$.
The solution of this equation which remains finite at $r = 0$ is,

$$E = E_z = AJ_0(kr)e^{-i\omega t} \tag{3.16}$$

where J_0 is the zero order Bessel function and A a constant.
The circumferential magnetic field, $H_\phi = H$ is calculated from the electric field by Eq.3.13
,

$$\frac{i\omega H}{c} = (\vec{\nabla} \times \vec{E})_\phi = -\frac{\partial E_z}{\partial r} \tag{3.17}$$

since $J_0'(x) = -J_1(x)$, we get

$$H = A\frac{ck}{i\omega}J_1(kr)e^{-i\omega t} \tag{3.18}$$

$$H = -Ai\sqrt{\frac{4\pi\sigma i}{\omega}}J_1(kr)e^{-i\omega t} \tag{3.19}$$

putting these values of E (Eq.1.16) and H (Eq.1.19) in the expression of Z we get,

$$Z = \frac{-i\omega L_e}{c^2} + 2l\left[\frac{AJ_0(kr)e^{-i\omega t}}{-Ai\sqrt{\frac{4\pi\sigma i}{\omega}}J_1(kr)e^{-i\omega t}}\right] \tag{3.20}$$

solving further above equation reduces to

$$Z = \frac{-i\omega L_e}{c^2} + R_{dc}[kaJ_0(ka)/2J_1(ka)] \tag{3.21}$$

At high frequencies where L_e can be neglected the impedance of the wire is given by,

$$Z = R_{dc}[kaJ_0(ka)/2J_1(ka)] \tag{3.22}$$

where R_{dc} is the dc resistance of the wire, J_i is the ith order Bessel function and δ is the skin effect penetration depth.Here f and μ_ϕ are the frequency and circumferential permeability respectively. At a particular frequency, application of an external dc magnetic field changes the circumferential permeability, μ_ϕ and therefore the penetration depth which in turn changes the magnetoimpedance untill the value of δ reaches the radius of the sample. In the case of strong skin effect ($a/\delta >> 1$), the high frequency expansion of Eq.1.4 gives $Z \propto (f\mu_\phi)^{1/2}$. Therefore in the high frequency region, when skin effect cannot be ignored , the impedance of the wire is proportional to the sqare root of circumferential permeability. GMI effect can be achieved when the penetration depth is very small in absence of any external magnetic field which though can be increased with application of a dc magnetic field. High value of current density, large circumferential permeability and low value of resistivity gives small penetration depth in absence of any external magnetic field and hence to a large change in MI.

(iii) **Very high frequency region ($\sim$GHz)** :

Noticeable change in impedance of the sample is observed because of a large increase in circumferential permeability due to ferromagnetic resonance (FMR) [106] - [108], [110] - [112]. FMR occurs when samples are simultaneously subjected to a longitudinal static magnetic field and a perpendicular oscillating magnetic field. The frequency for ferromagnetic resonance for cylindrical (wire-shaped) samples is given as [113]

$$\omega_r = \gamma(H + M_s/2\mu_0) \tag{3.23}$$

where γ and M_s are the gyromagnetic constant and saturation magnetization respectively. Considering $H = H_0 + H(t)$ where H_0 and $H(t)$ are the static and oscillating magnetic field, the resonant frequency for a thin ferromagnetic film can be written as [108]

$$\omega_r = \gamma\mu_0\sqrt{H_0(H_0 + M_s)} \tag{3.24}$$

At this resonant frequency permeability increases drastically with a corresponding decrease in skin depth. For a particular angular frequency, ω and magnetic field, H around resonance, changing the applied magnetic field reduces the permeability resulting in a corresponding change in GMI.

Considering the permeability to be a tensor quantity, the electric field (which determines the voltage) and the magnetic field (which determines the current) is defined through the surface impedance tensor. The voltage induced from a ferromagnetic sample in terms of tangential electric field, $\mathbf{e}$ and magnetic field $\mathbf{h}$ at the surface can be written as [109],

$$\mathbf{e} = \hat{\varsigma}(\mathbf{h} \times \mathbf{n}) \tag{3.25}$$

where $\hat{\varsigma}$ is the surface impedance tensor and $\mathbf{n}$ is a unit vector along the inward normal to the surface. The components of the surface impedance tensor can be determined from the above equation as [123],

$$e_\phi = -\varsigma_{\varphi\varphi}h_z + \varsigma_{\varphi z}h_\varphi \tag{3.26}$$

$$e_z = -\varsigma_{z\varphi}h_z + \varsigma_{zz}h_\varphi \tag{3.27}$$

The voltage determining the GMI can be measured either across the wire ends (V_z) or in the external coil wound around the wire (V_c) as given below

$$V_z = e_z l = (-\varsigma_{z\varphi}h_z + \varsigma_{zz}\frac{2i}{ca})l \tag{3.28}$$

$$V_c = (-\varsigma_{\varphi\varphi}h_z + \varsigma_{\varphi z}\frac{2i}{ca})2\pi nal \tag{3.29}$$

where $h_\varphi = \frac{2i}{ca}$ is the induced field due to the alternating current, $i = i_0 exp(-j\omega t)$ in the wire, c is the velocity of light, l and a are the length and radius of the wire respectively and n is the number of coil turns per unit length. The longitudinal diagonal component ς_{zz} defines the voltage drop along the wire and corresponds to the impedance defined in the classical model,

$$\varsigma_{zz} = \frac{V_z(ca)}{2il} \tag{3.30}$$

The off-diagonal components $\varsigma_{z\varphi}$ and $\varsigma_{\varphi z}$ and the circumferential diagonal component $\varsigma_{\varphi\varphi}$ arise from cross-sectional magnetization processes. The off-diagonal components $\varsigma_{z\varphi}$ and $\varsigma_{\varphi z}$ determined by measuring the coil voltage when the wire is excited by ac current or measuring the wire voltage in presence of ac axial magnetic field are responsible for asymmetric GMI.

Asymmetric GMI behaviour in magnetic materials is being studied extensively because it can be very useful in sensor devices. In principle, asymmetric GMI (AGMI) effect can be studied by using a dc bias field or by passing a dc current through the sample. Other mechanisms of AGMI can be due to ac bias field and due to exchange bias. The resultant of circular magnetic field due to the ac current and the applied dc magnetic field generates a helical induced anisotropy giving rise to the asymmetry in GMI peaks. There are several reports on asymmetric GMI in microwires, wires, twisted wires and ribbons biassed by dc current [114], [87],[115],[116],[117]. The comination of the external static magnetic field and dc biased current applied along the wire generates an effective helical field on the sample. This leads to asymmetric GMI with respect to the sign of the static aplied field. Panina et. al. have analyzed the mechanism of asymmetric GMI in wires and twisted wires using surface impedance tensor[124] - [125]. They have shown that the diagonal component of surface impedance tensor i.e. ς_{zz} (responsible for GMI) becomes asymmetric when a circumferential dc magnetic field is applied to the sample.

Soft ferromagnetic materials such as Co or Co-Fe rich amorphous or nanocrystalline alloys have been studied in great detail for their use in GMI applications. These materials are characterized with high permeability and low coercivity which makes them most applicable for developing magnetic read heads, storage devices, magnetic sensors etc. Due to the absence of crystal structure, magnetoelastic anisotropy is the main source of aniosotropy in these amorphous magnetic materials. During the preparation of these materials by rapid quenching from the molten alloy, internal stresses are generated, which in turn develop magnetoelastic anisotropy energy. Therefore these frozen-in internal stresses developed during their preparation or the application of an external stress affect the magnetic properties of these materials to a significant extent.

Amorphous wires produced by in-rotating-water quenching technique has an unique distribution of internal stress. When the molten alloy hits the water, the outer shell solidifies

first as the surface layer has maximum contact with water. Later, when the inner core solidifies, a radial tension is developed due to shrinking of the core. Due to this differential cooling process, the radial tension thus created increases towards the center of the wire resulting in axial tensile stress at the inner region. Thus the internal stress distribution produces two distinct regions in the amorphous wires - one is the inner core where a tensile stress exists and the other is an outer core where a radial directional stress is present. The transition from longitudinal to transverse stress distribution is expected to occur gradually over a few atomic layers. the volume of the inner and outer core regions depend very much on the magneto-elastic coupling of the sample. These two internal stresses are long range in character and plays a predominant role in determining the domain structure.

For a positive magnetostrictive system like $Fe_{77.5}Si_{7.5}B_{15}$ the axial tensile stress produces an axial domain (inner core) whose magnetization orients almost parallel to the axis. Similarly, the radial stress produces a domain structure where the magnetization is perpendicular to the axis. In order to reduce the magnetostatic energy, the domain structure in as-quenched amorphous wire should be such that the direction of magnetization within each domain is either parallel to the wire axis in case of positive magnetostrictive sample or perpendicular to it in case of negative magnetostrictive sample. So, it is expected that a wire with a very small negative magnetostrictive coefficient ($Co_{68.15}Fe_{4.35}Si_{12.5}B_{15}$) has a bamboo shaped domain structure and the direction of magnetization is circumferential in each domain and opposite to each other in consecutive two domains. In case of wire shaped samples with vanishing magnetostriction, the domain structure consists of a single-domain core (termed as inner core, IC) having magnetization direction close to the wire axis and a multidomain external shell (termed as outer shell, OS) with transversely oriented magnetization (radial and circular for positive and negative magnetostrictive samples respectively) [70], [126] - [128] . The predicted domain structures of a positive and a negative magnetostrictive sample are shown in Fig. 3.1 and Fig. 3.2 respectively.
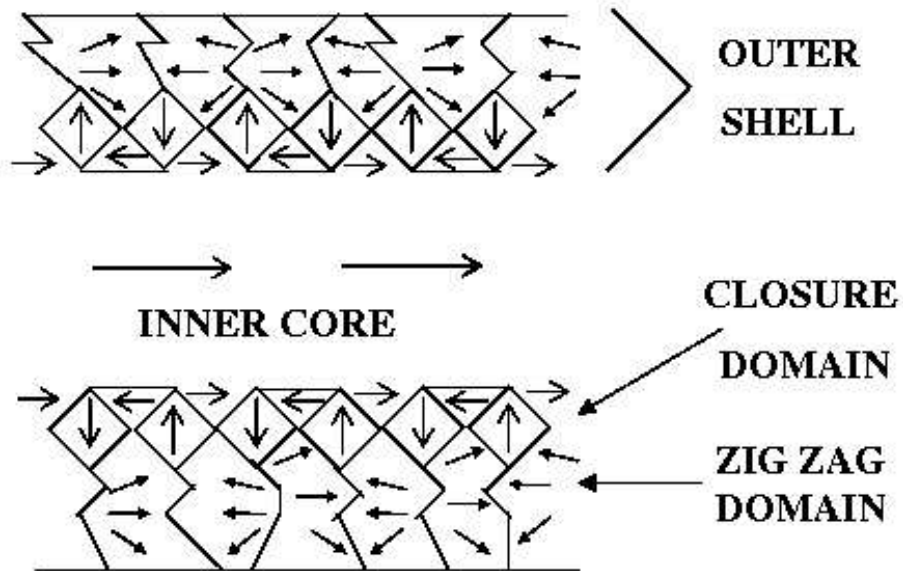
Figure 3.1: Possible domain structure of a positive magnetostrictive wire-shaped amorphous magnetic material.
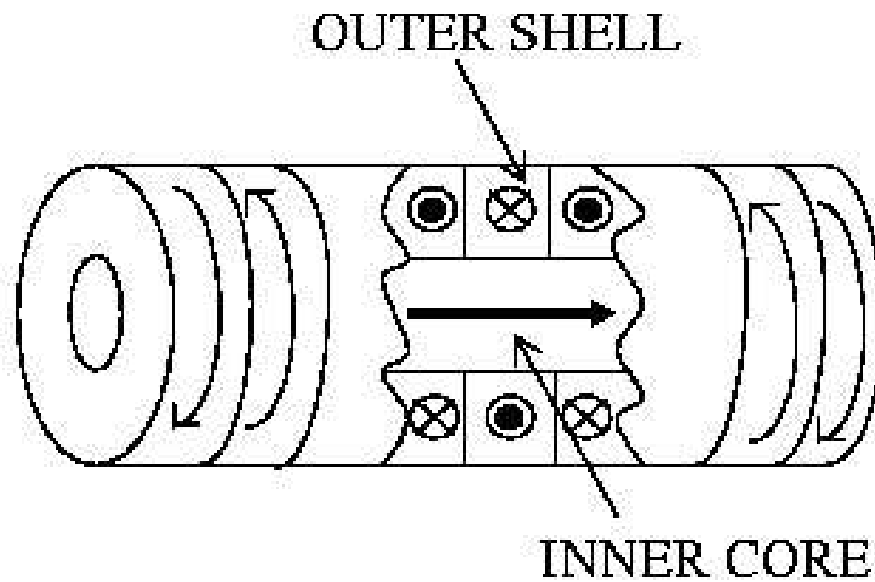

Figure 3.2: Possible domain structure of a negative magnetostrictive wire-shaped amorphous magnetic material.

Interesting properties exhibited by wire-shaped amorphous materials depend on their domain structures as well as on the volume fraction of IC and OS of these domains. In the present chapter, we have therefore, studied the frequency dependence of magnetoimpedance of amorphous $Co_{68.15}Fe_{4.35}Si_{12.5}B_{15}$ wire in presence of various tensile stress to understand the contributions to GMI from different domain regions.

3.2 Giant magnetoimpedance in amorphous $Co_{68.15}Fe_{4.35}Si_{12.5}B_{15}$ wire

3.2.1 Experimental Details

The sample used in the measurement of magnetoimpedance is an amorphous wire with composition $Co_{68.15}Fe_{4.35}Si_{12.5}B_{15}$ having a diameter of 125 μm and length 12 cm. Fig. 3.3 shows the Scanning Electron Microscopy (SEM) image of amorphous $Co_{68.15}Fe_{4.35}Si_{12.5}B_{15}$ wire. The impedance of the sample was measured by Precision Impedance Analyzer (Agilent, 4294A, 40 Hz - 110 MHz) (as described in Chapter 2) . The frequency of the ac current was varied up to 11 MHz and its magnitude was kept fixed at 1 mA. A Helmholtz coil system was used to apply a dc magnetic field (maximum value $\sim$ 140 Oe) along the axis of the sample during impedance measurement. The axis of the sample as well as that of the Helmholtz coil were kept perpendicular to the direction of the earth's magnetic field. Axial tensile stresses up to 285 MPa were applied to the wire for studying the effect of stress on magnetoimpedance. The percentage change of MI with applied magnetic field is calculated by using Eq.(1.7) and the maximum applied magnetic field is 140 Oe. The asymmetry between the two peaks of GMI has been developed by passing a dc current, $I_{dc} = 5$ mA through the sample during GMI measurement. The hysteresis loops of the sample have been measured under different axial tensile stresses and at different frequencies by induction method using an integrating flux meter (as described in Chapter 2 in detail).
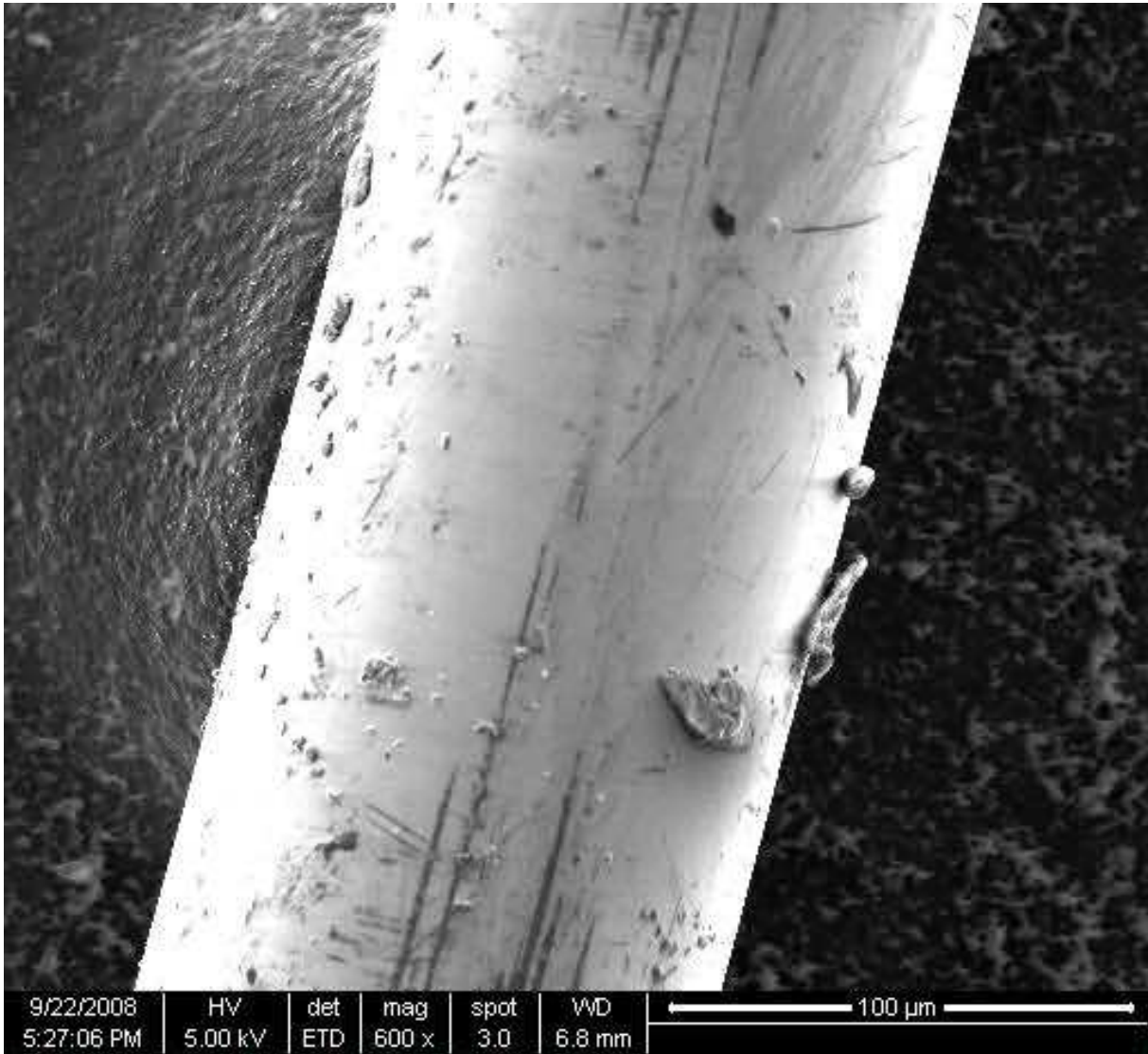
Figure 3.3: Scanning Electron Microscopy (SEM) image of amorphous $Co_{68.15}Fe_{4.35}Si_{12.5}B_{15}$ wire.

3.2.2 Results and Discussions

Stress dependence of giant magnetoimpedance (GMI) is studied for negative magnetostrictive amorphous wire of composition $Co_{68.15}Fe_{4.35}Si_{12.5}B_{15}$ with frequencies upto 11 MHz. Here we have reported the frequency dependent GMI of the wire in absence of any external stress as well as for stresses 48 MPa and 285 MPa applied along the length of the wire.

Fig. 3.4 shows the field dependence of percentage change of magnetoimpedance of $Co_{68.15}Fe_{4.35}Si_{12.5}B_{15}$ amorphous wire at 0.0325, 0.1825, 0.8725, 5.05 and 11.0 MHz in the absence of any external stress. A sharp rise in GMI is observed for H_{dc} close to 0 when the frequency is less than 1 MHz. Field sensitivity of GMI is given as,

$$s = (1/\Delta H)(\Delta Z/Z) \tag{3.31}$$

where $2(\Delta H)$ is the full width of the magnetic field at half maximum of $\Delta Z/Z(\%)$. At 0.0325 MHz the maximum field sensitivity of GMI is 130 %/Oe, and at 0.8725 MHz, it is 70 %/Oe. For better understanding, the GMI value at low field has been taken at very small intervals of H_{dc} and shown in Fig. 3.5 for the five above-mentioned frequencies. At 0.0325 MHz, only one peak is observed at $H_{dc} \sim 0$, whereas at 0.1825 MHz, two peaks are observed at $H_{dc} = \pm 0.27$ Oe (termed as H_p). The position of peaks shifts towards higher values with increase in frequencies. H_p increases from ± 0.45 Oe to ± 0.78 Oe due to a change in frequency from 0.8725 MHz to 5.05 MHz. At higher frequency (11 MHz), in addition to the two broad peaks at $H_p \sim 50$ Oe, an additional peak is observed at $H_{dc} \sim 0$.

The GMI properties change sensitively with stress. Fig. 3.6 shows the field dependence of percentage change of magnetoimpedance of $Co_{68.15}Fe_{4.35}Si_{12.5}B_{15}$ amorphous wire at 0.0325, 0.1825, 0.8725, 5.05 and 11.0 MHz in the presence of an external stress, $\sigma = 48$ MPa. Fig. 3.7 shows the low field GMI characteristics of the wire in the presence of an external stress, $\sigma = 48$ MPa. In the presence of an external tensile stress, the peak value of GMI decreases. Emergence of two peak characteristics in GMI are observed for a stress, $\sigma = 48$ MPa (Fig. 3.7) in contrast to the single-peak behaviour for $\sigma = 0$ (Fig. 3.5) at a frequency of 0.0325 MHz. Fig. 3.8 shows the field dependence of percentage change of magnetoimpedance of the wire at frequencies 0.0325, 0.1825, 0.8725, 5.05 and 11 MHz
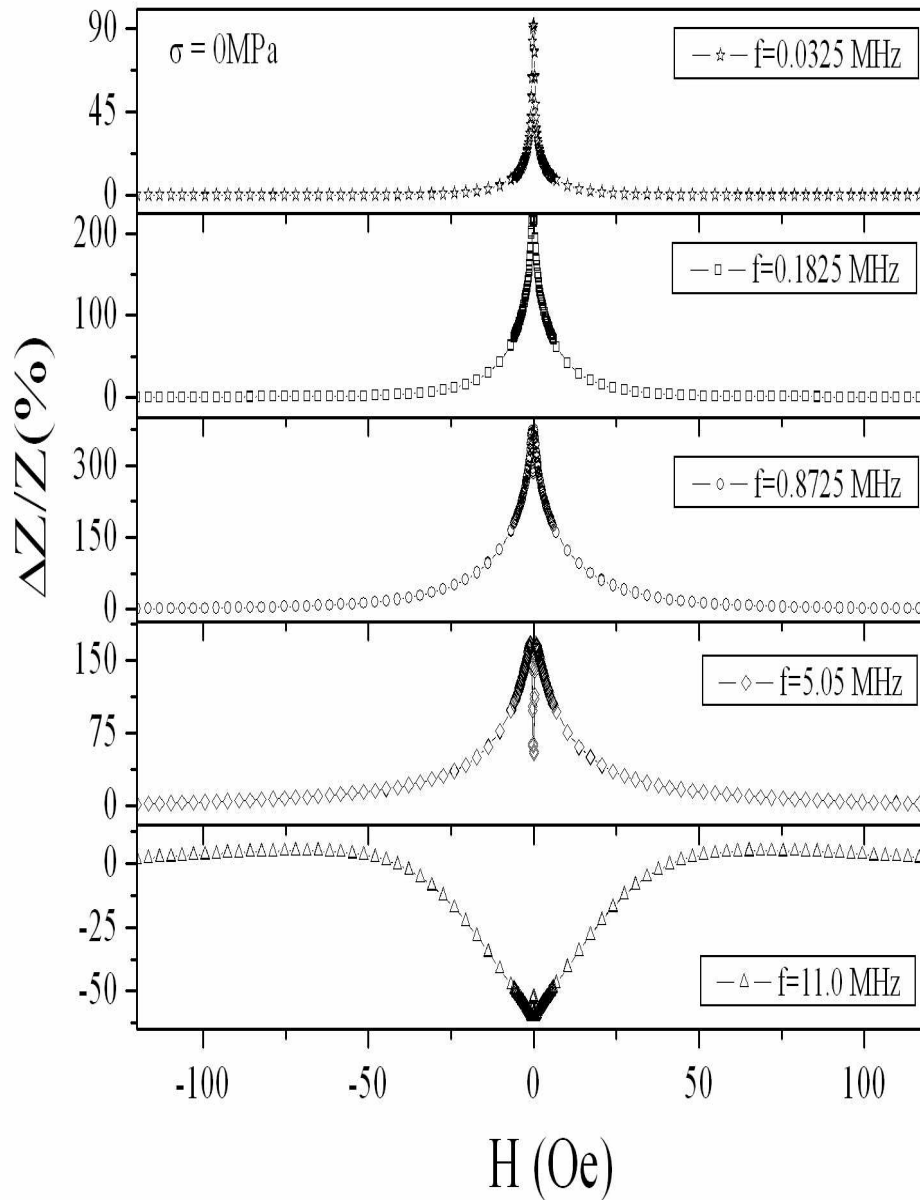
Figure 3.4: The variation of percentage change of magnetoimpedance $\Delta Z/Z(\%)$ with dc magnetic field H_{dc} of $Co_{68.15}Fe_{4.35}Si_{12.5}B_{15}$ amorphous wire in the absence of any stress at frequencies 0.0325 MHz, 0.1825 MHz, 0.8725 MHz, 5.05MHz and 11 MHz.
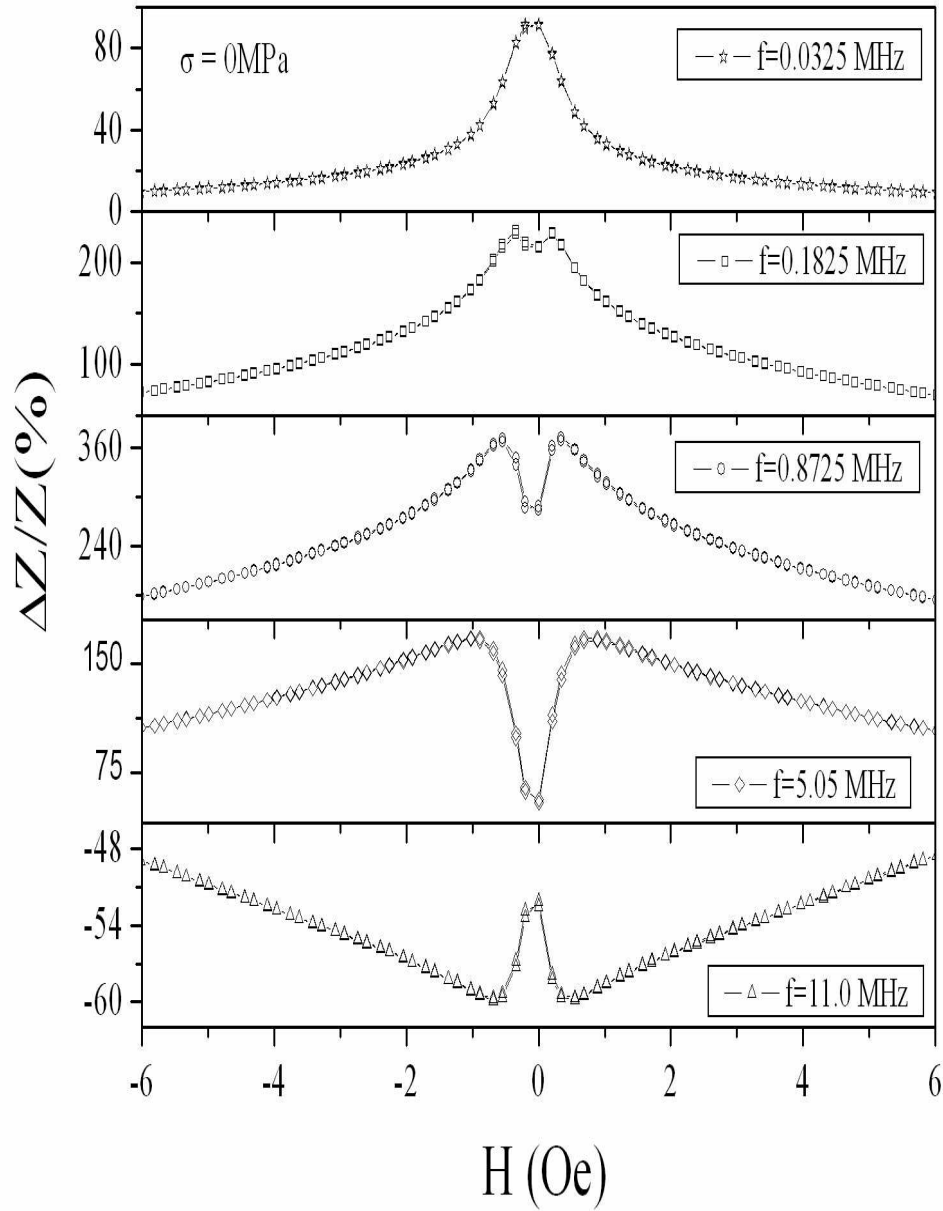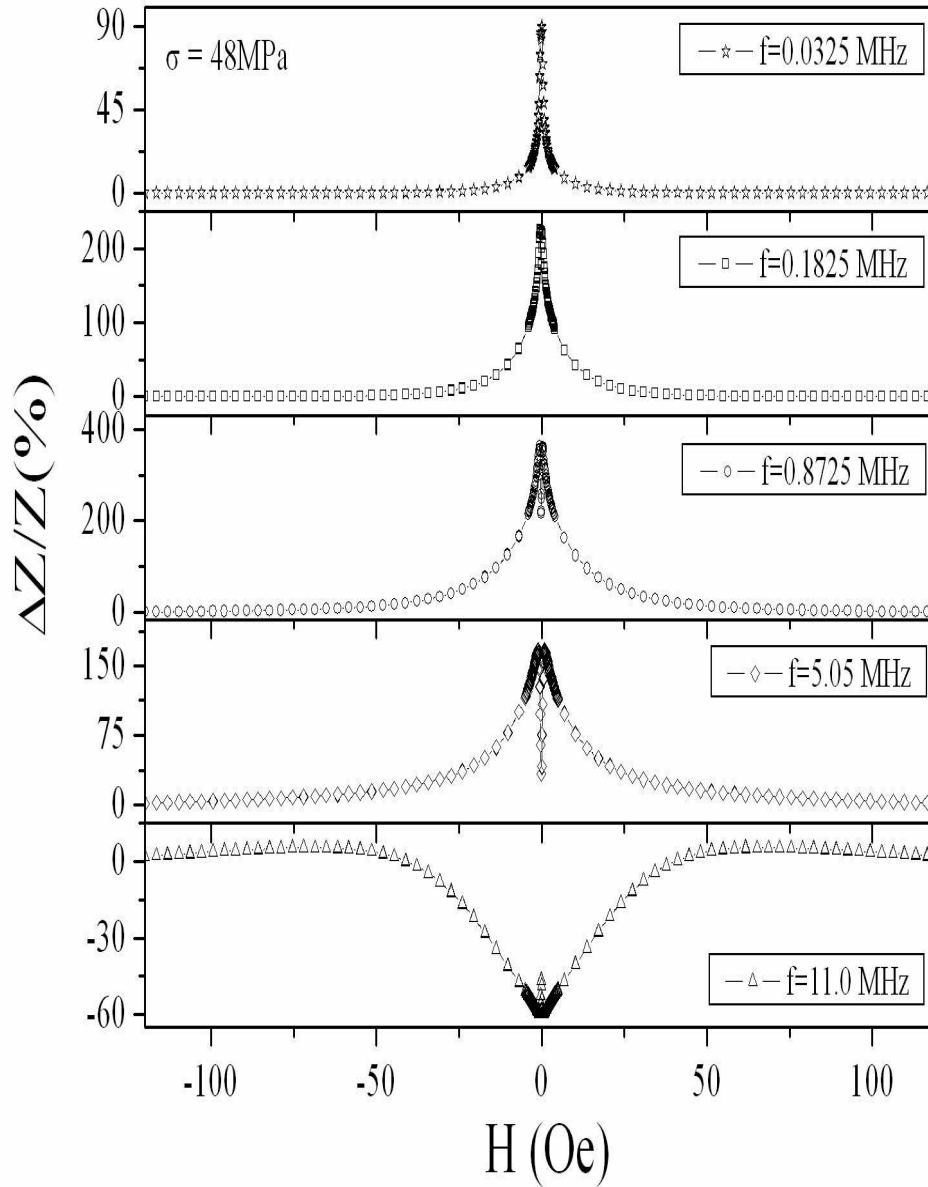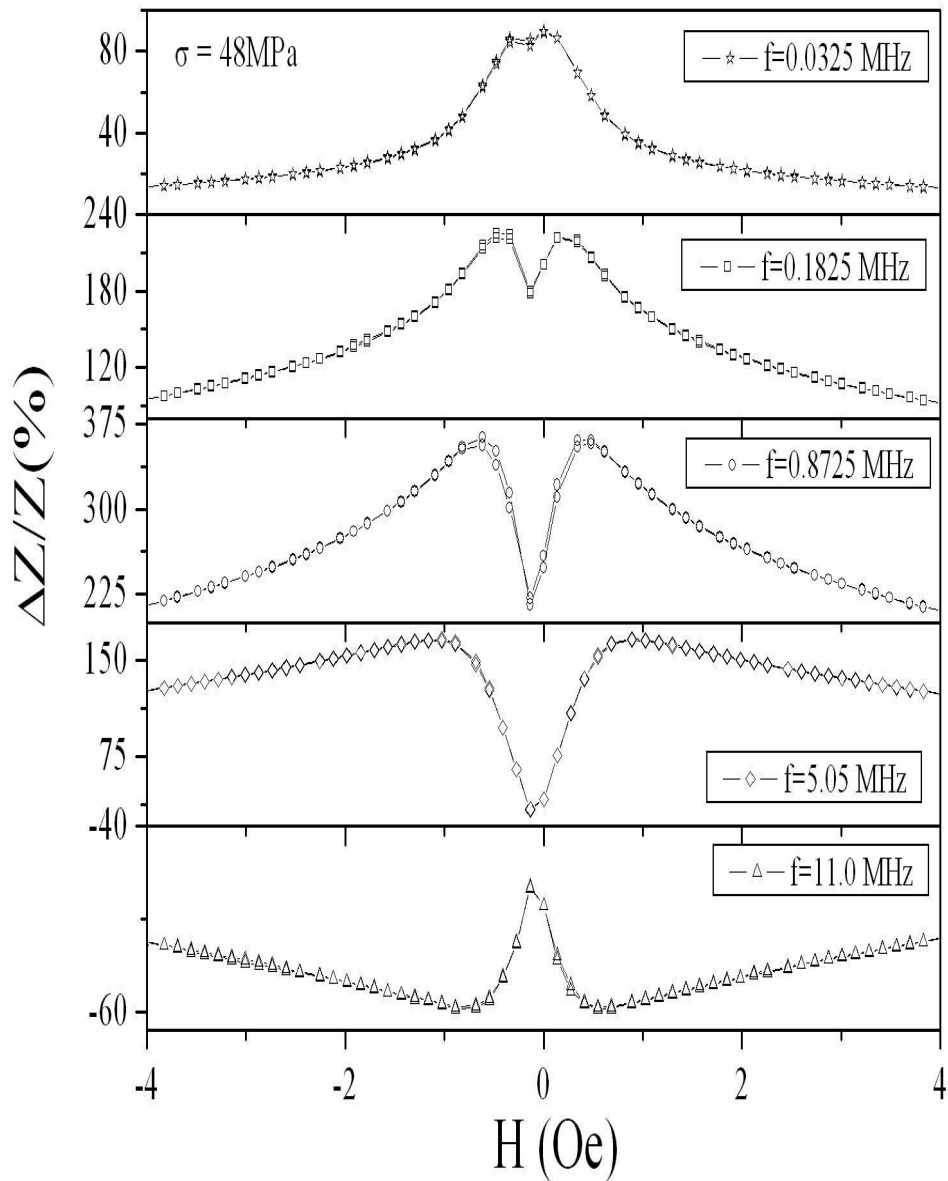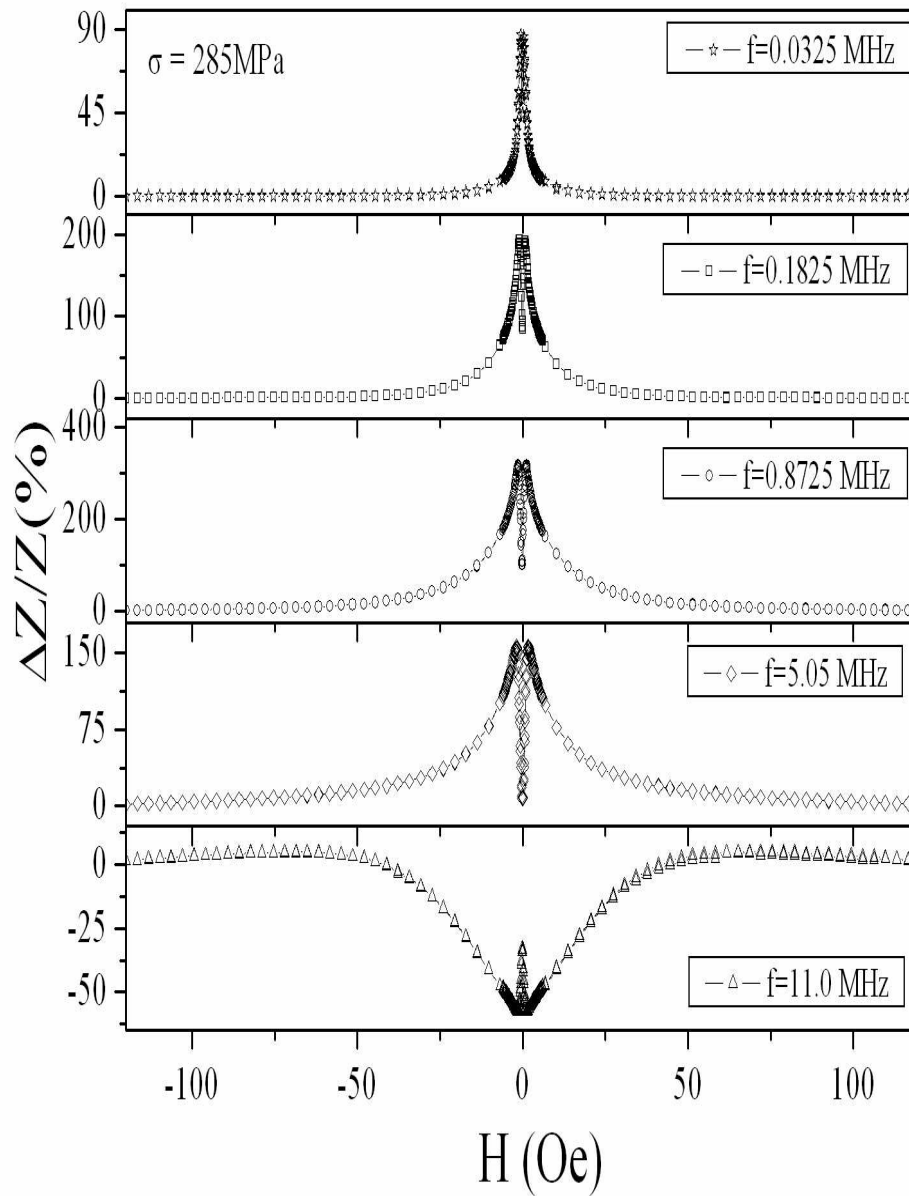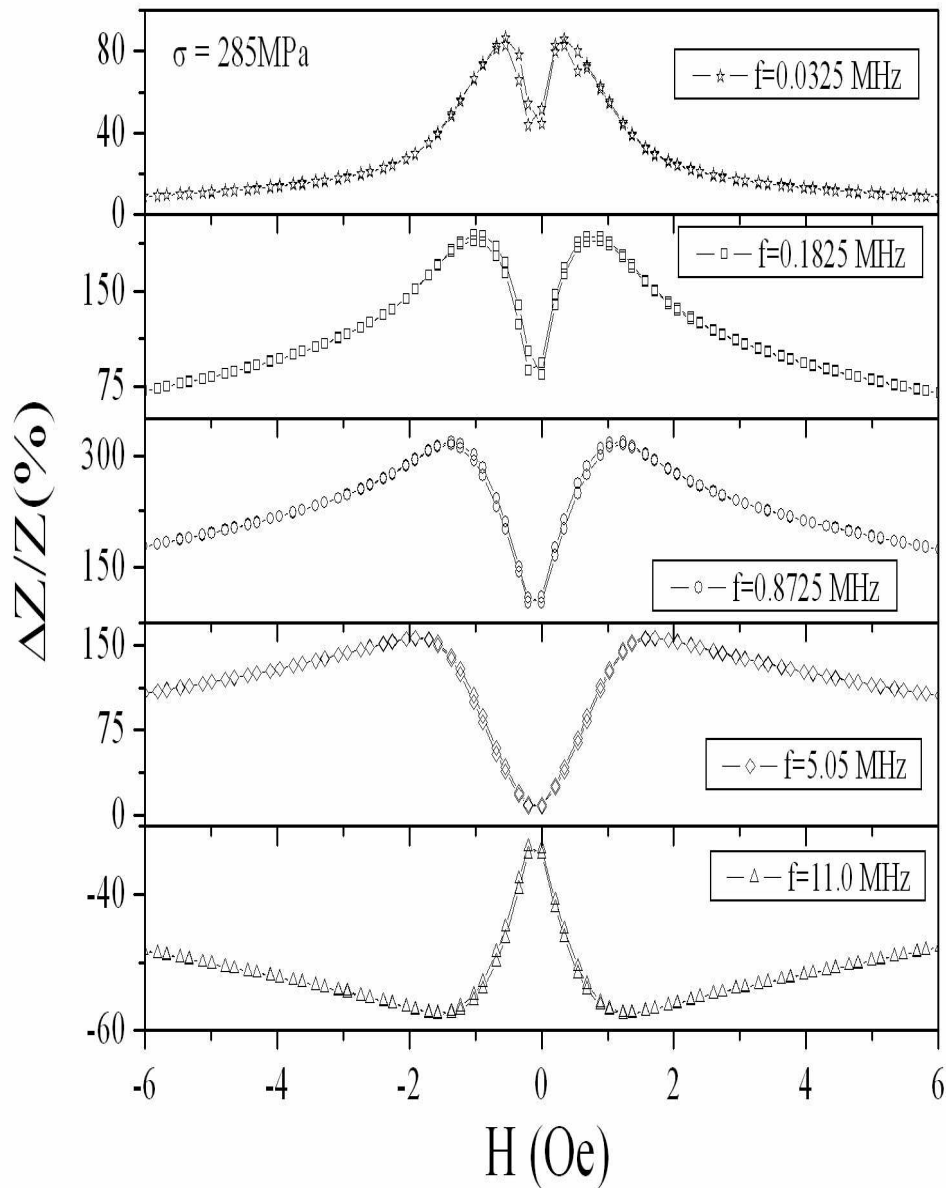
Figure 3.5: The variation of percentage change of magnetoimpedance $\Delta Z/Z(\%)$ with low values of dc magnetic field H_{dc} of $Co_{68.15}Fe_{4.35}Si_{12.5}B_{15}$ amorphous wire in the absence of any stress at frequencies 0.0325 MHz, 0.1825 MHz, 0.8725 MHz, 5.05MHz and 11 MHz.

Figure 3.6: The variation of percentage change of magnetoimpedance $\Delta Z/Z(\%)$ with dc magnetic field H_{dc} of $Co_{68.15}Fe_{4.35}Si_{12.5}B_{15}$ amorphous wire in the presence of 48 MPa stress at frequencies 0.0325 MHz, 0.1825 MHz, 0.8725 MHz, 5.05MHz and 11 MHz.

Figure 3.7: The variation of percentage change of magnetoimpedance $\Delta Z/Z(\%)$ with low values of dc magnetic field H_{dc} of $Co_{68.15}Fe_{4.35}Si_{12.5}B_{15}$ amorphous wire in the presence of 48 MPa stress at frequencies 0.0325 MHz, 0.1825 MHz, 0.8725 MHz, 5.05MHz and 11 MHz.

Figure 3.8: The variation of percentage change of magnetoimpedance $\Delta Z/Z(\%)$ with low values of dc magnetic field H_{dc} of $Co_{68.15}Fe_{4.35}Si_{12.5}B_{15}$ amorphous wire in the presence of 285 MPa stress at frequencies 0.0325 MHz, 0.1825 MHz, 0.8725 MHz, 5.05MHz and 11 MHz.

Figure 3.9: The variation of percentage change of magnetoimpedance $\Delta Z/Z(\%)$ with low values of dc magnetic field H_{dc} of $Co_{68.15}Fe_{4.35}Si_{12.5}B_{15}$ amorphous wire in the presence of 285 MPa stress at frequencies 0.0325 MHz, 0.1825 MHz, 0.8725 MHz, 5.05MHz and 11 MHz.

in the presence of an external stress, $\sigma = 285$ MPa. Two peak behaviour in GMI is distinctly visible for the wire under a stress of $\sigma = 285$ MPa at a frequency of 0.0325 MHz (Fig. 3.9). At 0.1825 MHz or higher frequencies, the value of H_p increases due to the application of tensile stress. The third peak observed at $f = 11$ MHz and in the presence of $\sigma = 285$ MPa is much higher than the corresponding peak for $\sigma = 0$.

The frequency dependence of maximum values of percentage change in GMI, $[\Delta Z/Z(\%)]_{peak}$, has been plotted in Fig. 3.10 for two extreme values of stresses $\sigma = 0$ and 285 MPa. The
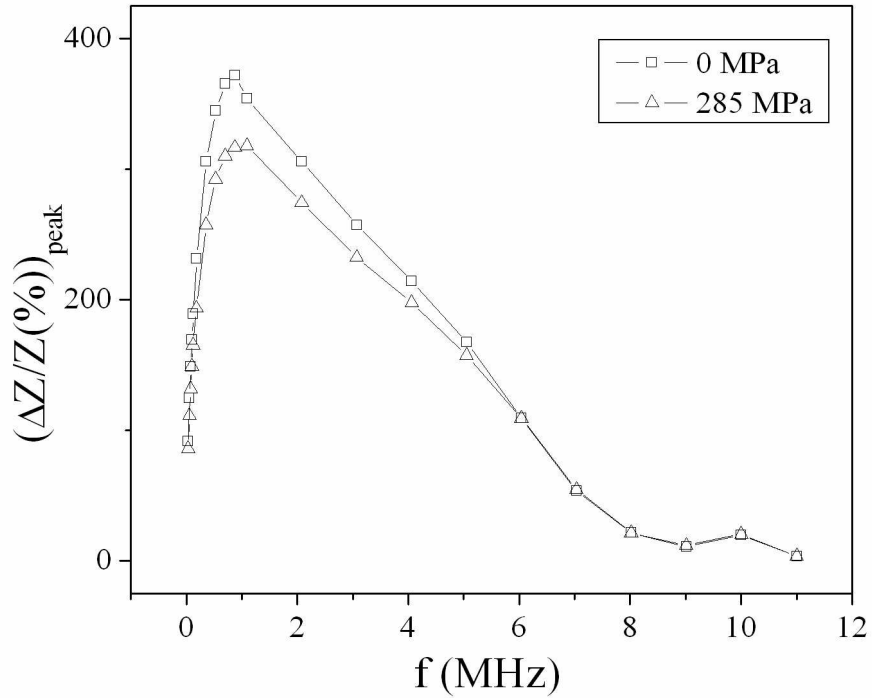
Figure 3.10: Frequency dependence of maximum values of percentage change in GMI $[\Delta Z/Z(\%)]_{peak}$ for two values of stresses $\sigma = 0$ and 285 MPa.

maximum value of $[\Delta Z/Z(\%)]_{peak}$ is observed around 1.5 MHz frequency. The difference between the $[\Delta Z/Z(\%)]_{peak}$ values at $\sigma = 0$ and 285 MPa vanishes above 6 MHz. Figure 3.11 shows the position of peaks in MI curves of $Co_{68.15}Fe_{4.35}Si_{12.5}B_{15}$ amorphous wire, H_p with frequency in absence and in presence of 285 MPa stress. The effect of stress on
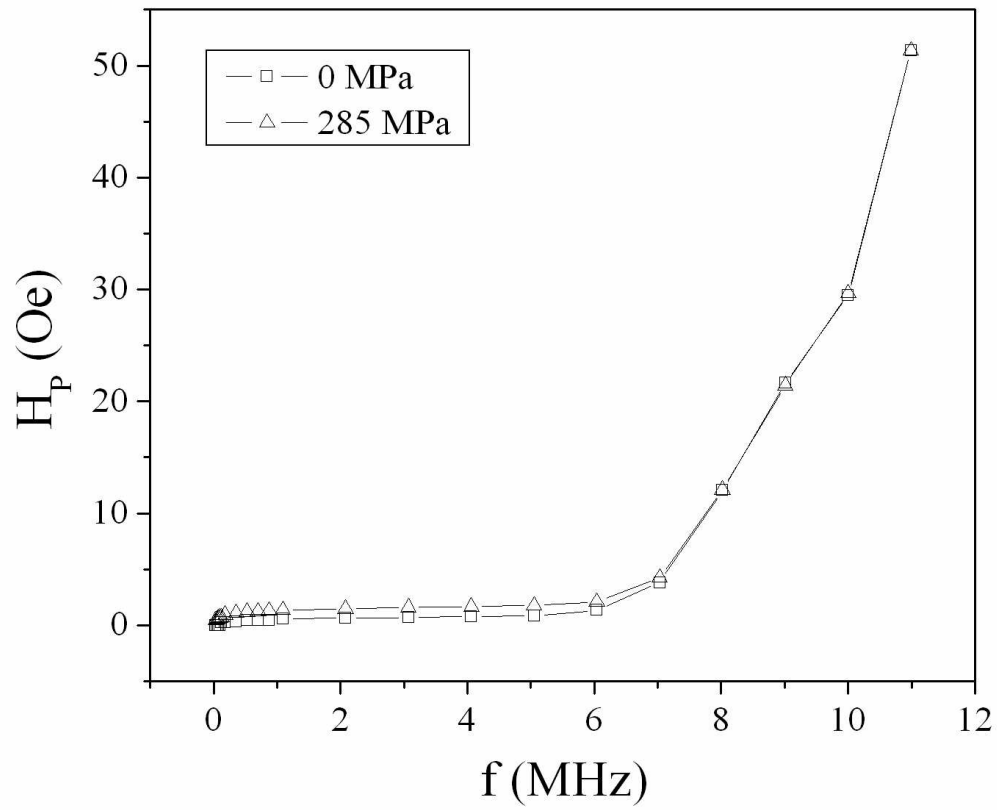
Figure 3.11: The position of peaks in MI curves, H_p with frequency in absence ($\sigma = 0$) and in presence of external stress ($\sigma = 285$ MPa) of $Co_{68.15}Fe_{4.35}Si_{12.5}B_{15}$ amorphous wire.
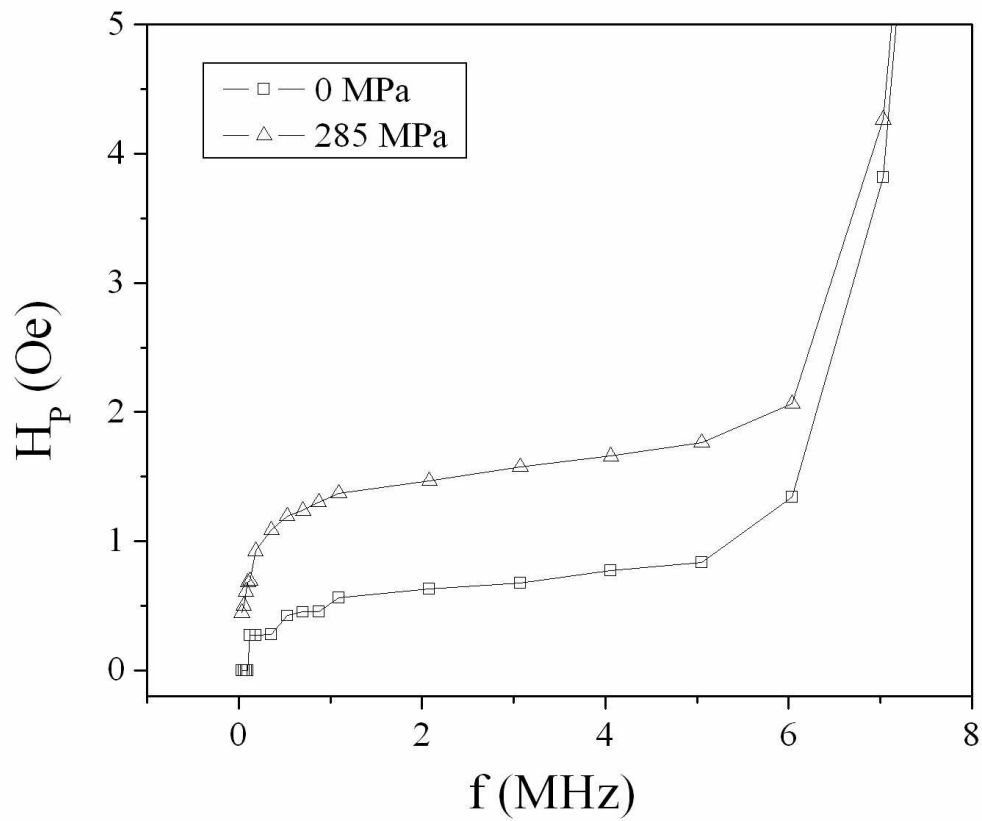
Figure 3.12: The position of peaks in MI curves, H_p with stress $\sigma = 0$ and 285 MPa of $Co_{68.15}Fe_{4.35}Si_{12.5}B_{15}$ amorphous wire upto a frequency of 8 MHz.

H_p is insignificant beyond 6 MHz as observed in the case of H_p versus the frequency curve [Fig. 3.11]. For a better understanding, peak positions of GMI for the wire is shown upto a frequency of $8MHz$ (Fig. 3.12).

Asymmetry between the two peaks in magnetoimpedance has been developed by passing a dc, $I_{dc} = 5$ mA through the length of the wire along with the ac current I_{ac}. Figures 3.13, 3.14, 3.15 and 3.16 show the asymmetric magnetoimpedance of the $Co_{68.15}Fe_{4.35}Si_{12.5}B_{15}$ amorphous wire at frequencies 0.0325 MHz, 0.1825 MHz, 0.5275 MHz and 0.8725 MHz respectively. Percentage change in the difference between the two MI peak heights is calculated as,

$$[\Delta(Z_{peak})]\% = 100[\frac{Z_{peak1} - Z_{peak2}}{Z_{peak2}}] \tag{3.32}$$

where Z_{peak1} and Z_{peak2} represent the two MI peak heights at a particular frequency of I_{ac}. Fig. 3.17 shows the frequency dependence of the percentage change in the difference between the two MI peak heights. The difference between the two peak heights is maximum at 0.0325 MHz indicating asymmetry is more prominent at the lower frequency region.Fig. 3.18 shows the frequency dependence of the peak positions in asymmetric GMI of $Co_{68.15}Fe_{4.35}Si_{12.5}B_{15}$ amorphous wire.

The combination of the external static magnetic field (H_{dc}) and the dc biassed current applied along the wire (I_{dc}) generates an effective helical field acts on the wire. This is shown by a schematic of the experimental set-up in fig.3.19. This results in the asymmetric GMI with regard to the sign of the static field applied [114],[124].

The magnetization of the amorphous wire at various frequencies and at different tensile stresses have been studied to get a better insight of the domain stucture and hence in explaining the magnetoimpedance results.
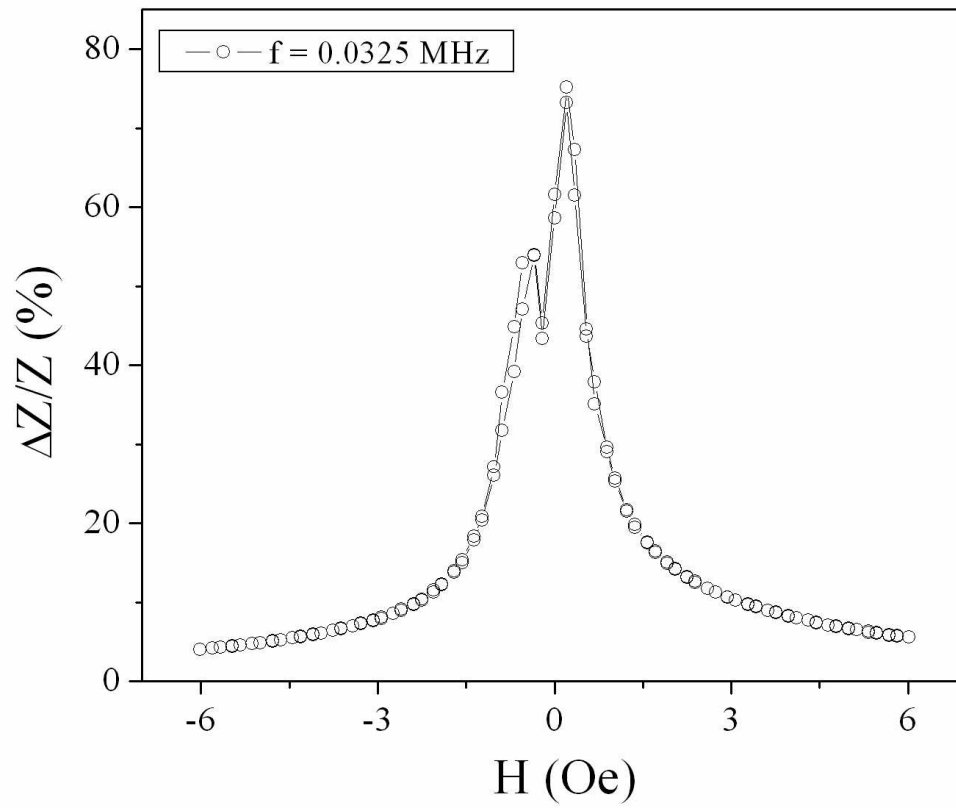
Figure 3.13: Asymmetric GMI of $Co_{68.15}Fe_{4.35}Si_{12.5}B_{15}$ amorphous wire with $I_{dc} = 5$ mA at a frequency of 0.0325 MHz
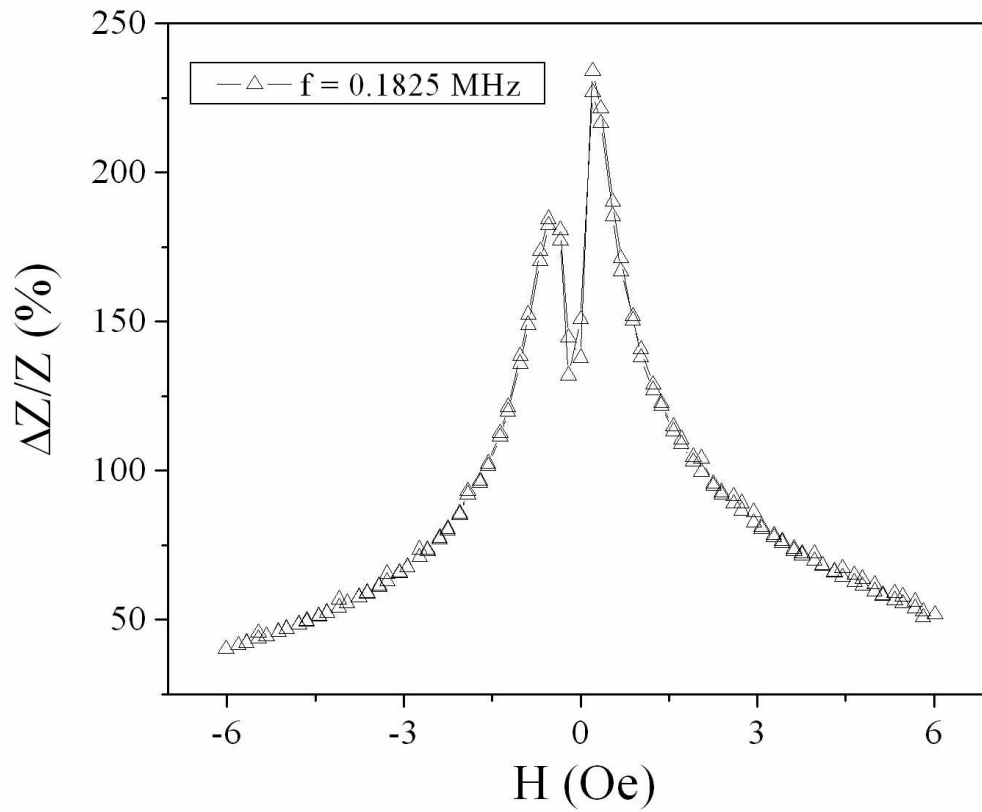
Figure 3.14: Asymmetric GMI of $Co_{68.15}Fe_{4.35}Si_{12.5}B_{15}$ amorphous wire with $I_{dc} = 5$ mA at a frequency of 0.1825 MHz
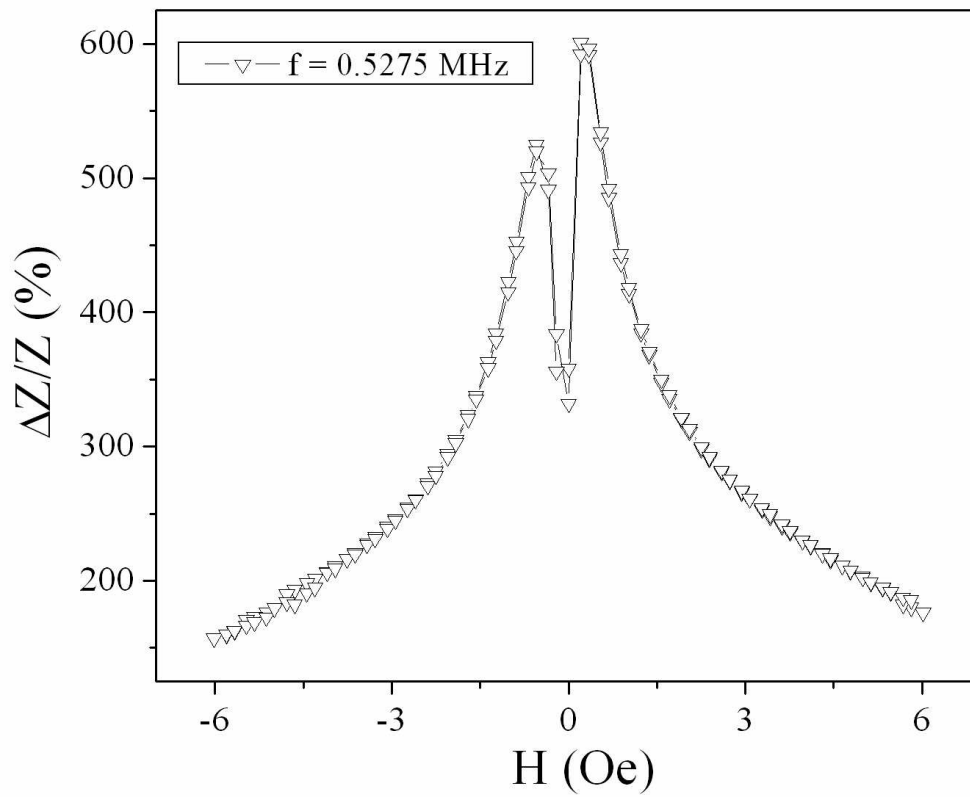
Figure 3.15: Asymmetric GMI of $Co_{68.15}Fe_{4.35}Si_{12.5}B_{15}$ amorphous wire with $I_{dc} = 5$ mA at a frequency of 0.5275 MHz
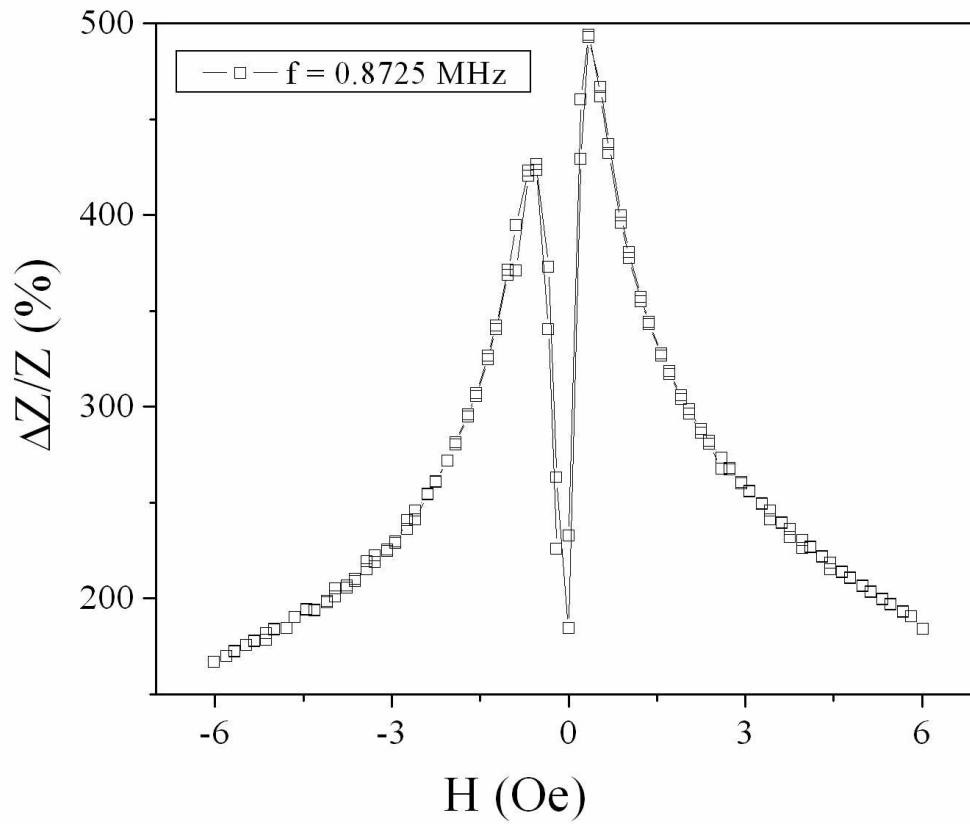
Figure 3.16: Asymmetric GMI of $Co_{68.15}Fe_{4.35}Si_{12.5}B_{15}$ amorphous wire with $I_{dc} = 5$ mA at a frequency of 0.8725 MHz
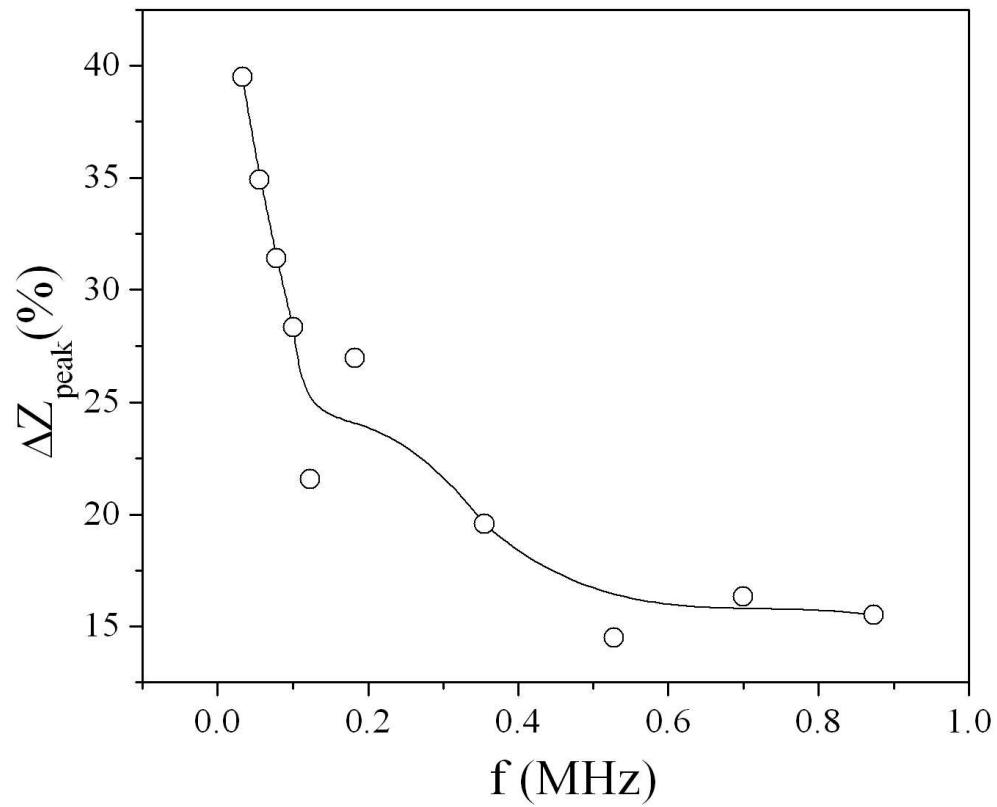
Figure 3.17: Frequency dependence of the percentage change in the difference between two MI peak heights in case of asymmetric GMI of $Co_{68.15}Fe_{4.35}Si_{12.5}B_{15}$ amorphous wire
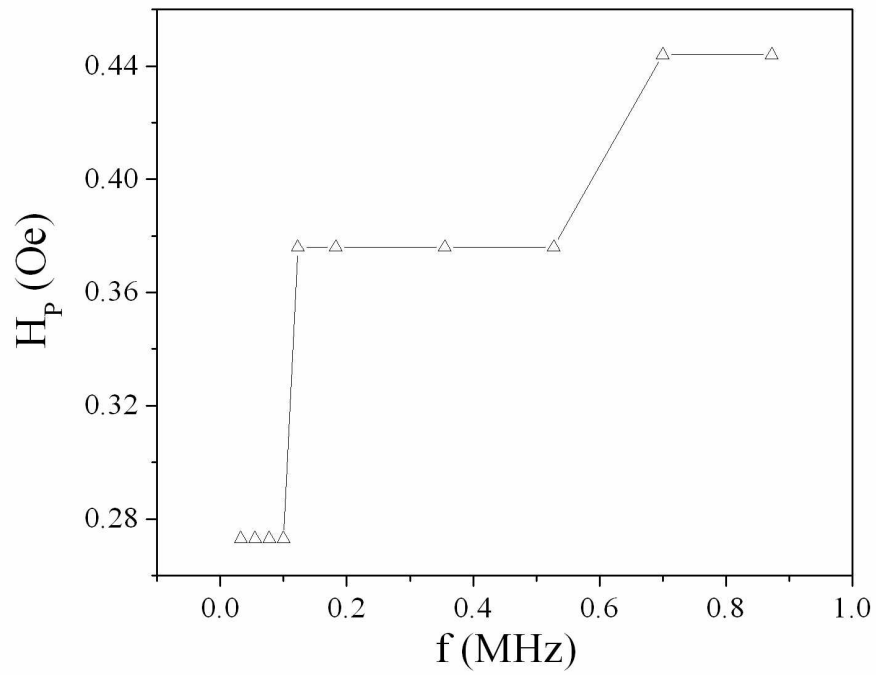
Figure 3.18: Frequency dependence of the peak positions in asymmetric GMI of $Co_{68.15}Fe_{4.35}Si_{12.5}B_{15}$ amorphous wire
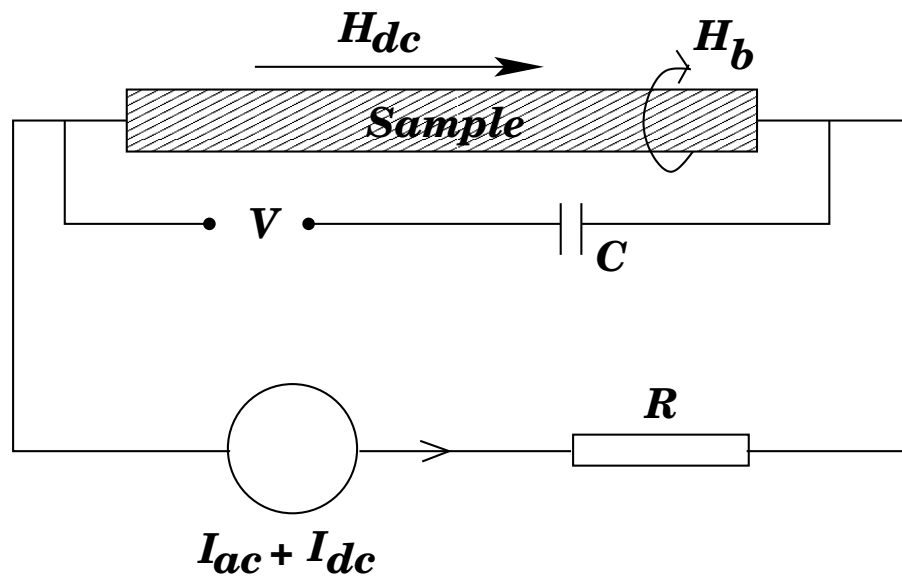

Figure 3.19: The schematic of the experimental set-up for measuring asymmetric GMI
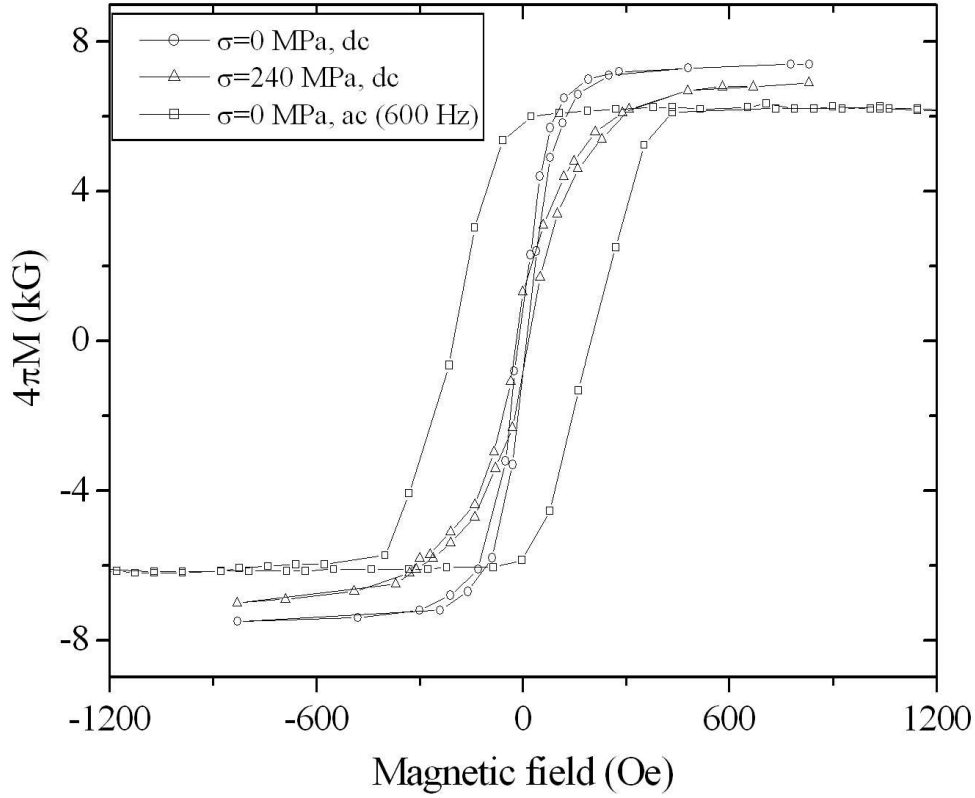
Figure 3.20: The dc hysteresis loops of $Co_{68.15}Fe_{4.35}Si_{12.5}B_{15}$ amorphous wire in the absence and in presence of $\sigma = 240$ MPa and ac hysteresis loop at a frequency of 600 Hz

The dc magnetic hysteresis loops with $\sigma = 0$ MPa and $\sigma = 240$ MPa and ac hysteresis loop at a frequency of 600 Hz is shown in Fig. 3.20. It is observed from Fig. 3.20 that the coercivity as well as the anisotropy field increases with frequency. Fig. 3.21 shows the variation of coercivity with applied tensile sress of $Co_{68.15}Fe_{4.35}Si_{12.5}B_{15}$ amorphous wire. This figure clearly depicts the increase of coercivity with external tensile stress. The amorphous wire with composition $Co_{68.15}Fe_{4.35}Si_{12.5}B_{15}$ is slightly negative magnetostrictive in nature [83]. It consists of a cylindrical axial inner-core (IC) domain surrounded by an outer shell (OS) with a circumferential easy axis. The impedance of the wire is given by Eqn.(1.22). The impedance changes sensitively with magnetic field
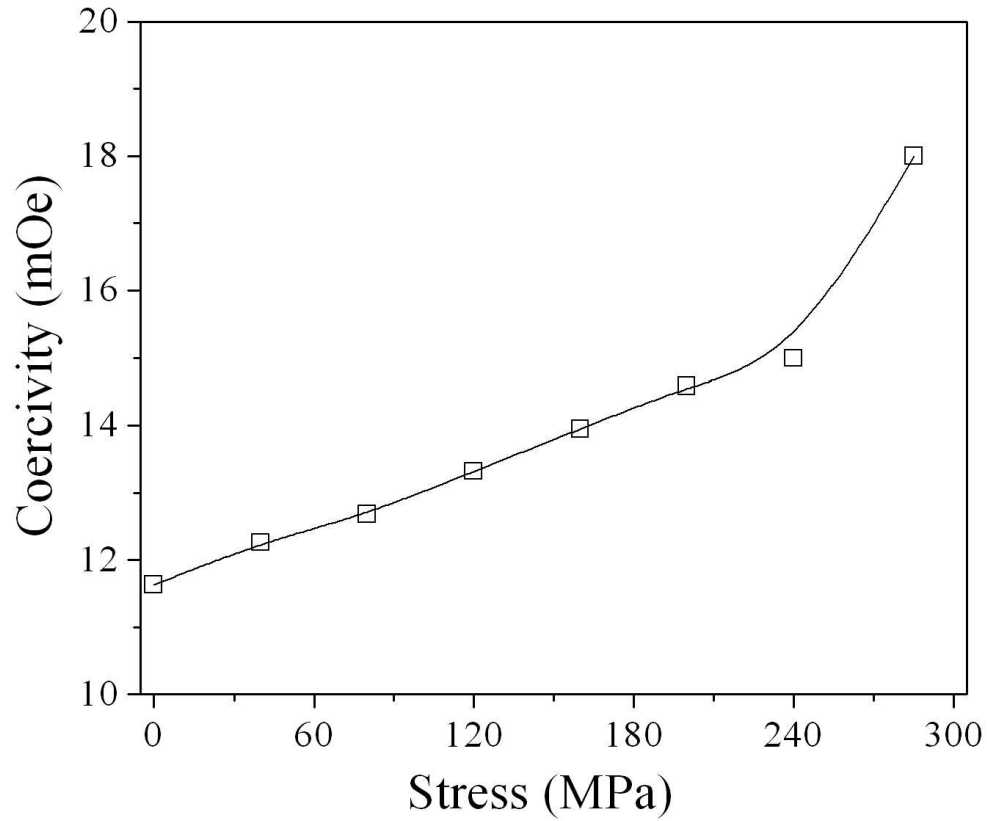
Figure 3.21: The variation of coercivity with applied tensile sress of $Co_{68.15}Fe_{4.35}Si_{12.5}B_{15}$ amorphous wire

when circumferential permeability (μ_ϕ) and hence the skin penetration depth (δ) change significantly with magnetic field. From the relation between δ and f ($=\omega/2\pi$), we can calculate the frequency at which the skin depth, δ becomes comparable to the radius, a of the wire. We know that (in S.I.)

$$\delta = \frac{1}{\sqrt{\pi\sigma\mu f}} \tag{3.33}$$

therefore at $\delta = a$ with $\mu \sim 10^3$ we have

$$f = \frac{1}{\pi\sigma\mu a^2} \tag{3.34}$$

giving $f \sim 0.06$ MHz ($\sigma \sim 1061571$ /ohm-metre, $\mu = 4\pi 10^{-7} \times 10^3$, a $= 60$ μ metre) where the wire started showing GMI effect around this frequency.

The magnetization processes and anisotropy fields in the IC domain and OS of the wire are different due to the two different domain structures. As a result of it, the field dependence of MI of IC and OS does not follow the same characteristics. The circumferential permeability, μ_ϕ from the IC is due to the rotation of domain magnetization by the circular ac magnetic field generated by the ac current and reaches its maximum value when the applied dc magnetic field nearly compensates the axial magnetic anisotropy in the IC. The peak value of MI due to IC is observed at the anisotropy field of IC, which is very small, a few millioersted. On the other hand, circular magnetic field changes magnetization in OS by domain-wall displacement. As the anisotropy field of the outer shell along the wire axis is larger compared to that of IC, the peak value of μ_ϕ of OS is also developed at higher magnetic field resulting MI peak of OS at higher H_{dc}.

At comparatively low frequency (Fig. 3.4), the peaks of MI originated from IC and OS are very close to $H_{dc} = 0$ and therefore a single peak is observed with a peak around $H_{dc} \sim 0$ as the peaks on both sides of $H_{dc} = 0$ and those from IC and OS are hardly distinguishable. Rotational relaxation is a faster process than the domain-wall relaxation. As the circumferential permeability of IC is originated by rotation of magnetization only, the GMI contribution from IC is not affected much by the increase in frequency but MI from OS is changed drastically due to the increase in frequency. Zhukov et. al. [129] have shown that the coercivity of $Co_{68.1}Fe_{4.4}Si_{12.5}B_{15}$ amorphous wire increases with square root of frequency ($f^{1/2}$) for depinned domain walls due to the development of microeddy current. The peak position of MI of OS shifts towards higher field due to the increase in anisotropy field with frequency. As the contribution from IC is much less than due to OS, only the two-peak GMI pattern dominated by OS is observed. In this frequency region, the peak value of MI increases with frequency as δ reduces with f. At very high frequency of the alternating current (beyond 2 MHz) the domain wall motion in OS is strongly damped owing to eddy currents causing reduction in MI contribution from OS as observed above 2 MHz in Fig. 3.10 [71]. The peak positions of MI from OS are also shifted further towards the higher values of H_{dc} reducing its contributions at low field. As a result, the third peak at $H_{dc} = 0$ from IC is observed [Fig. 3.4].

The application of an external tensile stress induces a transverse anisotropy in this negative magnetostrictive sample. This induced anisotropy enlarges the fractional volumes of domains with circular magnetization. The stress anisotropy energy (which is the magnetoelastic energy) is given as [155],

$$E_{SA} = \frac{3}{2}\lambda_s \sigma \sin^2 \theta \qquad (3.35)$$

where, λ, σ and θ are the linear magnetostriction coefficient, applied tensile stress and angle between saturation magnetization (M_s) and applied stress respectively. E_{SA} will be a minimum i.e. equal to zero when saturation magnetization and applied stress are parallel for a positive magnetostrictive sample. Whereas for a negative magnetostrictive sample E_{SA} will be a minimum i.e. equal to $-\frac{3}{2}\lambda_s\sigma$ when M_s is perpendicular to σ. Application of tensile stress along the length of this sample (which is negative magnetostrictive in nature) will cause domain walls to move in such a way so as to increase the volume of domains magnetized at right angle to stress, thus minimizing the anisotropy energy. The value of transverse permeability reduces as a result of which the MI value decreases with the increase in stress at a particular frequency [Fig. 3.10]. Due to the stress-induced transverse anisotropy, the longitudinal anisotropy field of OS is shifted towards the higher values (since higher magnetic field is required to saturate the sample) giving rise to a double-peak nature in the presence of a stress instead of a single-peak behavior as observed in the absence of any stress at the same frequency [Fig. 3.4 and Fig. 3.5]. At 11 MHz, the magnitude of central peak with $\sigma = 285$ MPa is much larger compared to that in the absence of any stress as the contribution to MI from OS around $H_{dc} \sim 0$ is much reduced by the application of stress. It is clear from Fig. 3.4 and Fig. 3.6 that the contributions to MI from IC is much less than that from the OS. The linear magnetostriction coefficient, λ_s, can be estimated from the change in anisotropy field ΔH_P due to the change in stress, $\Delta\sigma = 285$ MPa, using the expression

$$\lambda_s = (\mu_0 M_s \Delta H_P / 3\Delta\sigma) \qquad (3.36)$$

The estimated value is $\sim -2.36 \times 10^{-8}$ at 0.0325 MHz with $\mu_0 M_s \sim 0.75$ T. The resultant of circular magnetic field due to the ac current and the applied dc magnetic field generates a helical-induced anisotropy giving rise to the asymmetry in the two GMI peaks [Fig.

3.13 - Fig. 3.16].

The longitudinal coercivity of the sample, H_c, increases with the increase in longitudinal tensile stress [Fig. 3.21] indicating a transverse-induced anisotropy in the presence of the stress. This induced anisotropy hinders the domain wall motion of OS due to the longitudinal magnetic field resulting the decrease in transverse permeability μ_ϕ and hence the MI and supports our earlier explanation. The coercivity and anisotropy field of the sample also increase with frequeny, f as observed in Fig. 3.20. The coercivity of this amorphous wire is found to increase with $f^{1/2}$ due to the development of micro-eddy current and is in agreement with the increase in ΔH_P.

3.2.3 Model

Amorphous wires display GMI effect due to their peculiar domain structures determined by stress distribution caused primarily by their fabrication method [118]. The domain structure of wire-shaped sample consists of an inner core (IC) domain having a magnetization direction closely parallel to the wire axis and a multidomain outer shell (OS) with transversely oriented magnetization (radial and circumferential for positive and negative magnetostrictive samples, respectively) as mentioned earlier. Magnetic properties as well as GMI of these amorphous magnetic materials depend on their domain structure and volume fraction of IC and OS which are best understood by studying their magnetization dynamics in presence of different applied stresses [[72], [83], [85]]. For a better understanding of the experimental results and in pursuit of better GMI materials, several theoretical models of GMI have been developed [86], [119] - [123], [131]. These models find an expression for the circumferential permeability and hence GMI using the structure of domains, domain wall motion and magnetization rotation etc ([120], [122]-[131]).

Magnetic hysteresis in thin ferromagnetic films has been described by Nowak [132], introducing an additional internal field (originating from the domain structure) to the existing Stoner-Wolfarth model. A simple model has already been developed by Menard et.al. [131] to describe GMI effects in amorphous $Co_{68.15}Fe_{4.35}Si_{12.5}B_{15}$ wire using the concept proposed by Nowak. In the present paper, we have used this model to investigate the stress dependent GMI effect in amorphous $Co_{68.15}Fe_{4.35}Si_{12.5}B_{15}$ wire. The effect of stress

is incorporated by changing the IC and OS volume. This model qualitatively describes well the GMI response to the external axial stress at different exciting frequencies. For the estimation of circumferential permeability and its field dependence, the model considers a core-shell domain structure of the amorphus $Co_{68.15}Fe_{4.35}Si_{12.5}B_{15}$ wire. An additional internal field having two components parallel and perpendicular to the external applied magnetic field is taken into consideration. The magnetization of the IC and OS domains depending on the longitudinal applied magnetic field is given by [131],

$$M_j(H) = M_s cos[\gamma_j(H) + k\pi] \tag{3.37}$$

where $\gamma_j(H)$ is the angle between the external magnetic field and the direction of local magnetization expressed as,

$$\gamma_j(H) = tan^{-1}(\frac{T_j}{H + L_j}) \tag{3.38}$$

Here M_s is the saturation magnetization and k = 0, 1 is taken to select the appropriate argument of the cosine function. L_j and T_j are the components of internal field longitudinal and transverse to the direction of the applied axial magnetic field. The suffix j for L and T denotes two different domain regions i.e. IC and OS. The circumferential permeability of the wire is given by,

$$\mu_\phi = 1 + 4\pi\frac{\partial M_\gamma}{\partial H_\gamma} \tag{3.39}$$

where,

$$M_{\gamma_j}(H) = M_s sin[\gamma_j(H) + k\pi] \tag{3.40}$$

The final expression of circumferential permeability used to calculate the skin depth and hence the field dependence of the impedance of the wire is,

$$\mu_\phi = 1 + 4\pi M_s cos[\gamma_j(H)][\frac{H + L_j}{(H + L_j)^2 + T_j^2}] \tag{3.41}$$

where H is the applied external magnetic field along the axis of the wire. The parameters L_j and T_j are estimated from the hysteresis loops of the sample at different stresses. Using these parameters the impedance is evaluated individually for both the IC and OS regions

of the sample. The total impedance of the wire is the sum of the contributions from the IC and OS domains from which we finally calculate the variation of percentage change of magnetoimpedance (MI) with applied dc magnetic field. In this model the effect of stress is taken into account by incorporating the increase in fractional volume of the OS at the cost of IC and the changes in the parameters L_j and T_j.

Fig. 3.22 shows the dc hysteresis loops of $Co_{68.15}Fe_{4.35}Si_{12.5}B_{15}$ amorphous wire in absence and in presence of a stress (σ) of 285 MPa. This figure shows an increase of coercivity
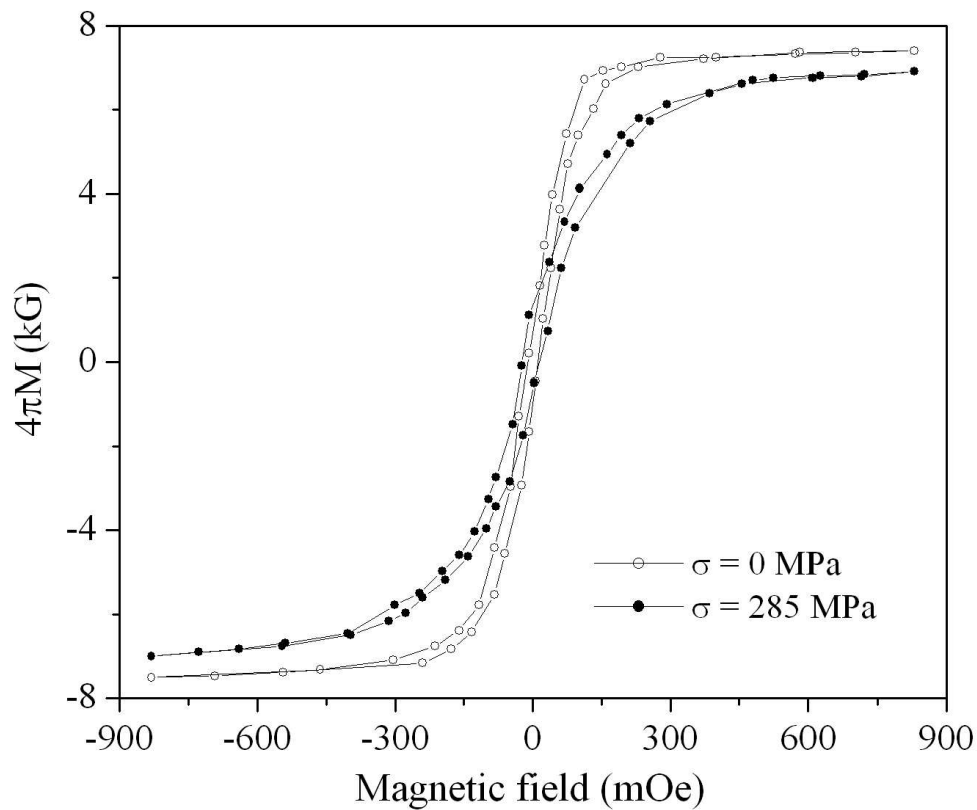
Figure 3.22: The dc hysteresis loops of $Co_{68.15}Fe_{4.35}Si_{12.5}B_{15}$ amorphous wire in absence and in presence of $\sigma = 285$ MPa.

from ∼12 mOe to ∼16 mOe and anisotropy field due to $\sigma = 285$ MPa. The parameters L_{IC} and T_{OS} related respectively to the coercive field H_C of IC region and the anisotropy

field H_K of OS region are calculated from the hysteresis loops of the wire in absence and in presence of various tensile stresses [131]. Fig. 3.23(a) shows the percentage change of
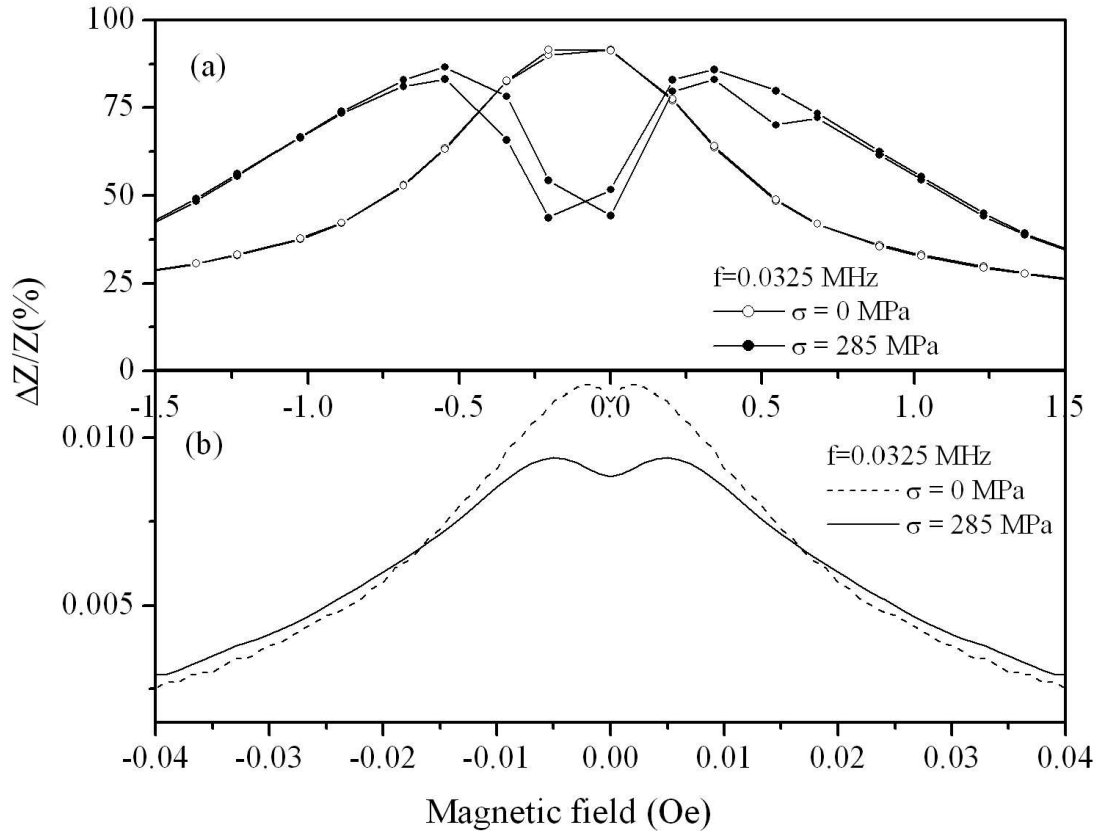

Figure 3.23: (a) Experimental (Upper Panel) and (b) simulated results (Lower Panel) of the variation of percentage change of magnetoimpedance $[\Delta Z/Z(\%)]$ for $Co_{68.15}Fe_{4.35}Si_{12.5}B_{15}$ amorphous wire in absence and in presence of a stress, $\sigma =285$ MPa at a frequency of 0.0325 MHz.

MI ($[\Delta Z/Z(\%)]$) of the wire at low values of dc magnetic field in absence and in presence of a tensile stress, $\sigma = 285$ MPa, at a frequency of 0.0325 MHz. A single peak is observed at Hdc ~ 0 Oe in absence of any stress, whereas a two-peak characteristic is observed in presence of the stress. The peak value of GMI, $[\Delta Z/Z(\%)]_{peak}$ decreases with the application of an external tensile stress. In Fig. 3.23(b) we have plotted the simulated curve of

the variation of percentage change of MI with magnetic field in absence and in presence of a tensile stress ($\sigma = 285$ MPa) using the proposed model. Here the GMI values have been taken at low field with very small intervals of the magnetic field in order to get a more precise picture of the GMI peaks. In the simulated curves, two-peak behaviour is observed for the wire in absence as well as in presence of any external tensile stress. The figure also shows a decrease in GMI peak value and a peak shift towards higher magnetic field with stress as observed from the experimental data (Fig. 3.23(a)) also.

As the sample is negative magnetostrictive in nature, the applied longitudinal stress develops an anisotropy in a direction perpendicular to the stress. As a result, the fractional volume of OS with domains having circular magnetization, enlarges and the anisotropy field, when measured in the longitudinal direction, shifts towards higher values of magnetic field. The theoretical results on stress dependent GMI effect are obtained by incorporating the change in volumes of IC and OS due to stress. Relative volume of inner core is estimated from the reduced remanent magnetization i.e. $(r_{IC}{}^2/a^2) = M_r/M_s$ where r_{IC} and M_r represent respectively the radius and remanence of IC [14]. Application of stress reduces the IC volume and we have calculated impedance with reduced IC radius of the wire in presence of tensile stress as compared to that of the wire in absence of any stress. Applied longitudinal tensile stress increases the coercive field and anisotropy field along the length of the negative magnetostrictive wire. In the calculation, L_{IC} (corresponding to the coercive field H_C of IC region) and T_{OS} (corresponding to the anisotropy field H_K of OS region) are increased for the wire in presence of stress for calculating its impedance. The experimental and simulated results on MI at f = 0.8725 MHz in absence and in presence of $\sigma = 285$ MPa is shown in Fig. 3.24(a) and Fig. 3.24(b) respectively. The figure shows a two-peak GMI characteristic in absence and in presence of a stress from both the experimental as well as for the theoretical data. A decrease in GMI peak value and a peak shift towards higher magnetic field is observed for the sample under stress. Fig. 3.25(a) and Fig. 3.25(b) show respectively the experimental and theoretical curves on the variation of percentage change of MI with and without stress at a frequency of 11 MHz.
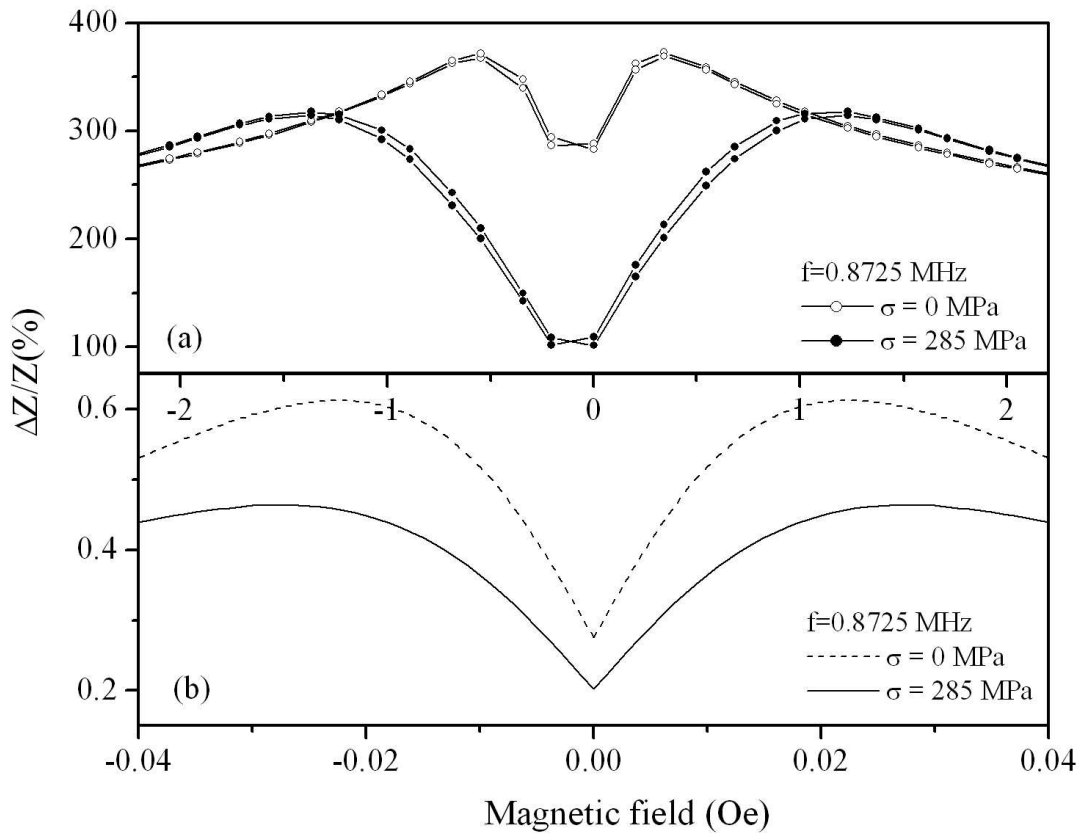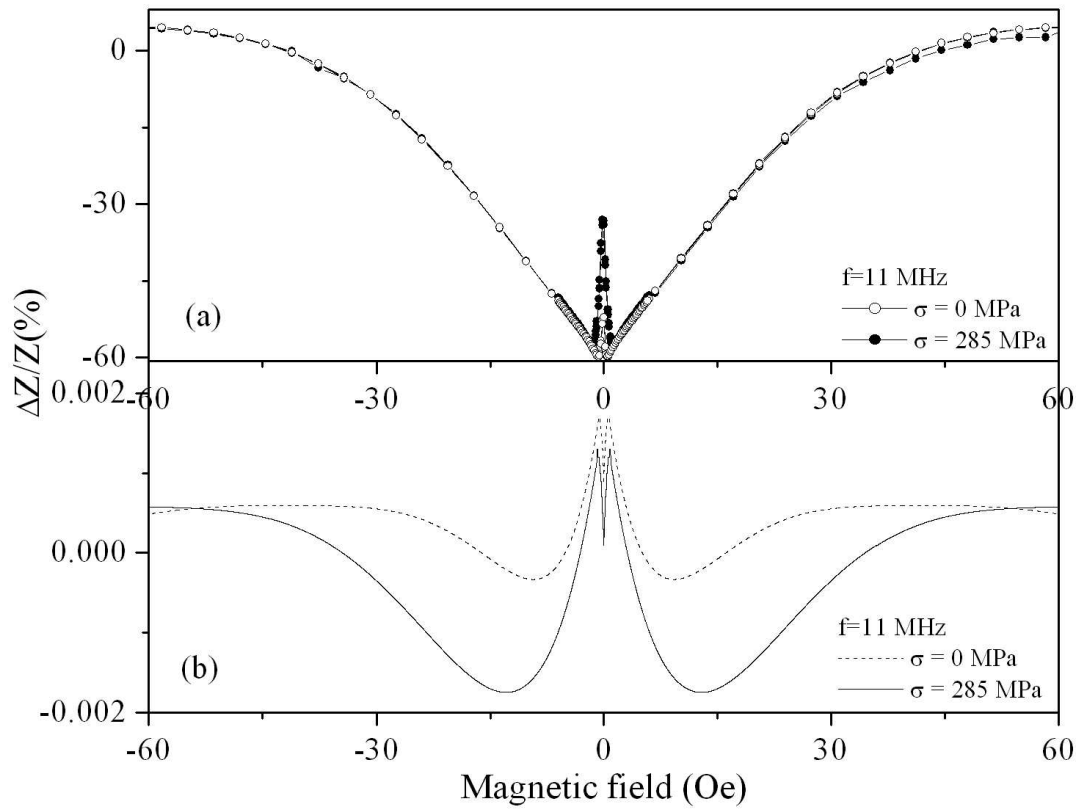
Figure 3.24: (a) Experimental (Upper Panel) and (b) simulated results (Lower Panel) of the variation of percentage change of magnetoimpedance $[\Delta Z/Z(\%)]$ for $Co_{68.15}Fe_{4.35}Si_{12.5}B_{15}$ amorphous wire in absence and in presence of a stress, $\sigma = 285$ MPa at a frequency of 0.8725 MHz.

Figure 3.25: (a) Experimental (Upper Panel) and (b) simulated results (Lower Panel) of the variation of percentage change of magnetoimpedance $[\Delta Z/Z(\%)]$ for $Co_{68.15}Fe_{4.35}Si_{12.5}B_{15}$ amorphous wire in absence and in presence of a stress, $\sigma =285$ MPa at a frequency of 11 MHz.

An additional peak around $H_{dc} \sim 0$ is observed along with the peaks at higher values of magnetic field in absence and in presence of an external stress (Fig. 3.25(a)). Using the model a two-peak characteristic at low field values ($H_{dc} \sim 0$ Oe) is observed due to IC along with the peaks at higher H_{dc} values due to OS in absence as well as in presence of an external stress.

From the above study, it is clearly visible that the impedance of the wire depends not only on the frequency of the driving current and the effective permeability but also on

the anisotropies present in the sample. The total magnetic permeability can be separated into contributions from magnetic moment rotation and domain wall motion in IC and OS domain regions of the wire respectively. The peak values of MI from the IC and OS regions occur at their respective anisotropy fields. Since the anisotropy field of the OS is larger compared to that of the IC and the contribution to MI from OS is much higher than that from IC, the resultant peaks in MI are observed at the anisotropy field of OS. However at low frequency and in absence of any stress, the peaks of MI originating from IC and OS are very close to $H_{dc} = 0$ and are not distinguishable resulting in a single peak at $H_{dc} = 0$ (Fig. 3.23(a)). Two-peak behaviour in MI could be seen experimentally by studying GMI at very small intervals of the field as observed from the theoretical curve derived from the model [Fig. 3.23(b)]. It is also observed from the above study that GMI is strongly dependent on the driving frequency of the current. GMI contribution from OS is greater than that from IC with increasing frequency. The anisotropy field and hence MI peaks shift towards higher values with frequency. At lower frequencies (∼kHz), the peak value of MI increases with frequency as the skin penetration depth decreases with increasing frequency. The increase in peak value and shifting of MI peaks towards higher field values with increased frequency is also observed using the proposed model [Fig. 3.24(b)]. But at a very high frequency region the domain wall motion is strongly damped due to eddy currents causing a reduction in peak value of MI. The peak positions of MI from OS are shifted towards higher values of magnetic field and therefore additional peaks at H_{dc} 0 is observed [Fig. 3.25] due to the IC.

The longitudinal external tensile stress promotes the development of transverse domains in this negative magnetostrictive sample. Due to this stress induced transverse anisotropy, the anisotropy field is shifted towards higher values, which gives a two-peak behaviour in presence of stress at all frequencies. Stress induced transverse anisotropy also increases the volume of domains with circular magnetization. With the increase in stress the value of transverse permeability reduces and hence MI peak value decreases. This explains the stress dependent GMI behaviour as observed in Fig. 3.23(a), Fig. 3.24(a) and Fig. 3.25(a) which can be qualitatively explained using the model [Fig. 3.232(b), Fig. 3.24(b) and Fig. 3.25(b)]. In case of positive magnetostrictive wires and microwires [20], reverse trend is observed, i.e., the GMI peaks comes closer on application of tensile stress. These

characteristics can also be explained using this model with proper modifications as described above.

3.3   Conclusions

Since magnetoelastic anisotropy is the main source of anisotropy in this wire-shaped sample the stress-induced anisotropy changes the domain structure and hence the GMI effect to a large extent. The MI contributions from IC and OS of the wire are different. MI study at higher frequency and under the application of stress confirms much higher contribution of MI from OS than IC. Asymmetry between the two peaks in MI can be developed by sending a dc current through the sample. The coercivity of the sample increases with the increase in longitudinal tensile stress applied to the sample.

Here we have described the stress dependent GMI behaviour of amorphous $Co_{68.15}Fe_{4.35}Si_{12.5}B_{15}$ wire at various frequencies using a simple model. Due to the absence of crystal structure, the magnetization processes of amorphous ferromagnetic wires depend on magnetoelastic anisotropy. Therefore quenched-in and applied stresses determine their domain structure. The model assumes a core-shell domain structure consisting of an inner core and outer shell region. Considering separate contributions from these two regions, stress dependent GMI results at various frequencies is well understood qualitatively. Results obtained using the model shows a two-peak behaviour in unstressed condition of the wire even at low frequencies which is yet to be studied experimentally. Another important aspect of this model is that we can use this simple model with required modifications to explain stress dependent GMI phenomena in case of positive magnetostrictive wires at various frequencies.

Chapter 4

EFFECT OF STRESS AND HEAT TREATMENT ON MAGNETOIMPEDANCE IN GLASS-COATED AMORPHOUS MICROWIRES

4.1 Introduction

In the previous chapter we have studied the frequency dependent GMI in amorphous $Co_{68.15}Fe_{4.35}Si_{12.5}B_{15}$ wire (negative magnetostrictive) in presence of various tensile stresses to understand the contributions to GMI from different domain regions. The MI study at high frequency and stress confirmed much higher contribution of MI from outer shell (OS) than inner core (IC) domains. We were interested to verify the effect of stress and heat treatment in positive magnetostrictive wire-shaped samples, which would show the opposite behaviour as compared to that of the negative magnetostrictive wire. There are many experimental and theoretical studies indicating that the OS with transversely oriented magnetization contributes mainly to GMI. Different kinds of heat treatment play an important role in modifying the domain structure and hence the GMI values. Heat treatments by passing dc currents is an effective method in enhancing the MI by increasing the OS volume. This motivated us to conduct a study of the effect of heat treatment (by passing short duration current pulses and dc current with various duration) on GMI and hence to increase its value of positive magnetostrictive microwires. Therefore, in the present chapter frequency dependent GMI of glass coated amorphous microwire with composition $Co_{83.2}Mn_{7.6}Si_{5.8}B_{3.3}$ and glass coated amorphous microwire with composition $(Co_{0.93}Fe_{0.07})_{63}Ni_{10}Si_{11}B_{16}$ has been studied in detail in presence of different tensile

stress and various heat treatments (by sending current pulses of amplitude ~ 100 mA and each of duration 12 seconds for the former microwire and a dc current with amplitude I_{an} = 50 mA for various time duration for the latter respectively).

4.2 Giant magnetoimpedance in positive magnetostrictive glass coated amorphous $Co_{83.2}Mn_{7.6}Si_{5.8}B_{3.3}$ microwire

4.2.1 Experimental Details

Glass coated amorphous microwire with composition $Co_{83.2}Mn_{7.6}Si_{5.8}B_{3.3}$ were used in the measurement of magnetoimpedance. Fig. 4.1 shows the Scanning Electron Microscopy (SEM) image of the glass coated amorphous $Co_{83.2}Mn_{7.6}Si_{5.8}B_{3.3}$ microwire. The diameter of the metallic part of the sample is about 18 μm and the thickness of the insulating glass coating is approximately 6 μm. Length of the sample used in the experiment is 12 cm. The glass-coating was removed at the two ends of the microwire, by etching carefully with a sand paper, for the impedance measurements. The impedance of the sample was measured by Precision Impedance Analyzer (Agilent, 4294A, 40 Hz - 110 MHz). Here we have studied both the stress dependendence and effect of heat treatment (by sending square wave current pulses of amplitude ~ 100 mA and each of duration 12 seconds through the microwire) of GMI at various frequencies in glass coated amorphous $Co_{83.2}Mn_{7.6}Si_{5.8}B_{3.3}$ microwire. The frequency of the ac current was varied up to 10.9 MHz and 12.85 MHz respectively (with its magnitude fixed at 1 mA) for stress and heat-treated dependence of GMI for the sample. A Helmholtz coil system was used to apply a dc magnetic field (maximum value ~ 140 Oe) along the axis of the sample during impedance measurement. The axis of the sample as well as that of the Helmholtz coil were kept perpendicular to the direction of the earth's magnetic field. Axial tensile stresses up to 566 MPa were applied to the wire for studying the effect of stress on magnetoimpedance. To study the effect of heat treatment, current pulses (square wave) of amplitude ~ 100 mA and each of duration 12 seconds was sent along the length of the sample. The current pulses were generated by a 555-timer IC. The duration of the generated pulse was fixed to ~ 12 seconds by adjusting the values of external resistance and capacitance to the 555-timer IC. The amplitude of the pulse was amplified by Kepco Bipolar Power Supply and fixed at
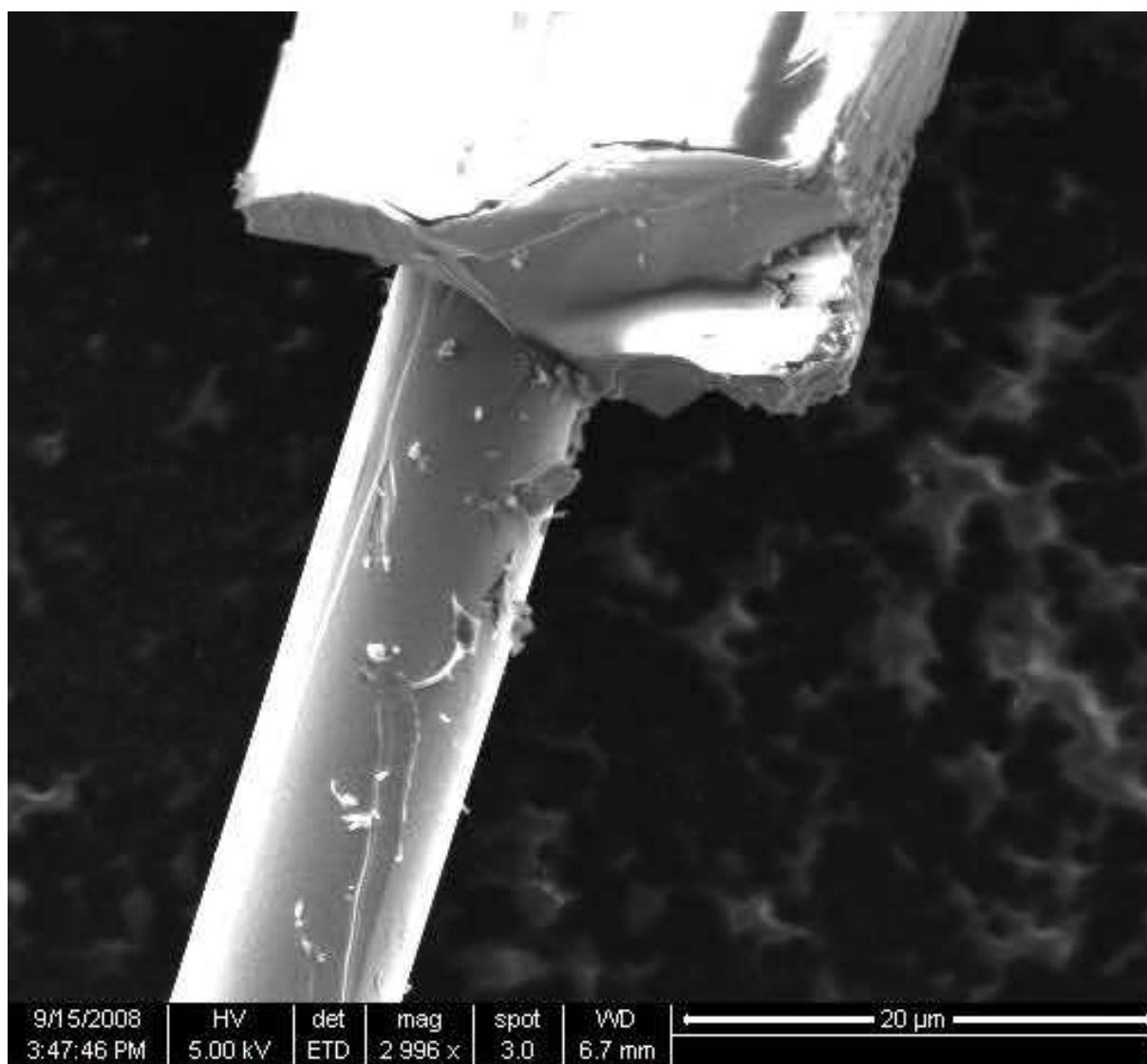
Figure 4.1: Scanning Electron Microscopy (SEM) image of glass coated amorphous $Co_{83.2}Mn_{7.6}Si_{5.8}B_{3.3}$ microwire.

~ 100 mA. The sample was heat treated by passing different number of current pulses with amplitude ~ 100 mA and each of duration 12 seconds. The percentage change of MI with applied magnetic field is calculated by using Eq.(1.7) and the maximum applied magnetic field is 140 Oe.

4.2.2   Results and Discussions

Frequency dependence of giant magnetoimpedance (GMI) in absence and in the presence of stresses 110 MPa, 221 MPa, 331 MPa, 426 MPa and 566 MPa is studied for positive magnetostrictive glass coated amorphous $Co_{83.2}Mn_{7.6}Si_{5.8}B_{3.3}$ microwire with frequencies upto 10.9 MHz. Fig. 4.2 shows the field dependence of percentage change of magnetoimpedance of glass coated amorphous $Co_{83.2}Mn_{7.6}Si_{5.8}B_{3.3}$ microwire at a frequency of 1.9 MHz in absence and in the presence of stresses 110 MPa, 221 MPa, 331 MPa, 426 MPa and 566 MPa.
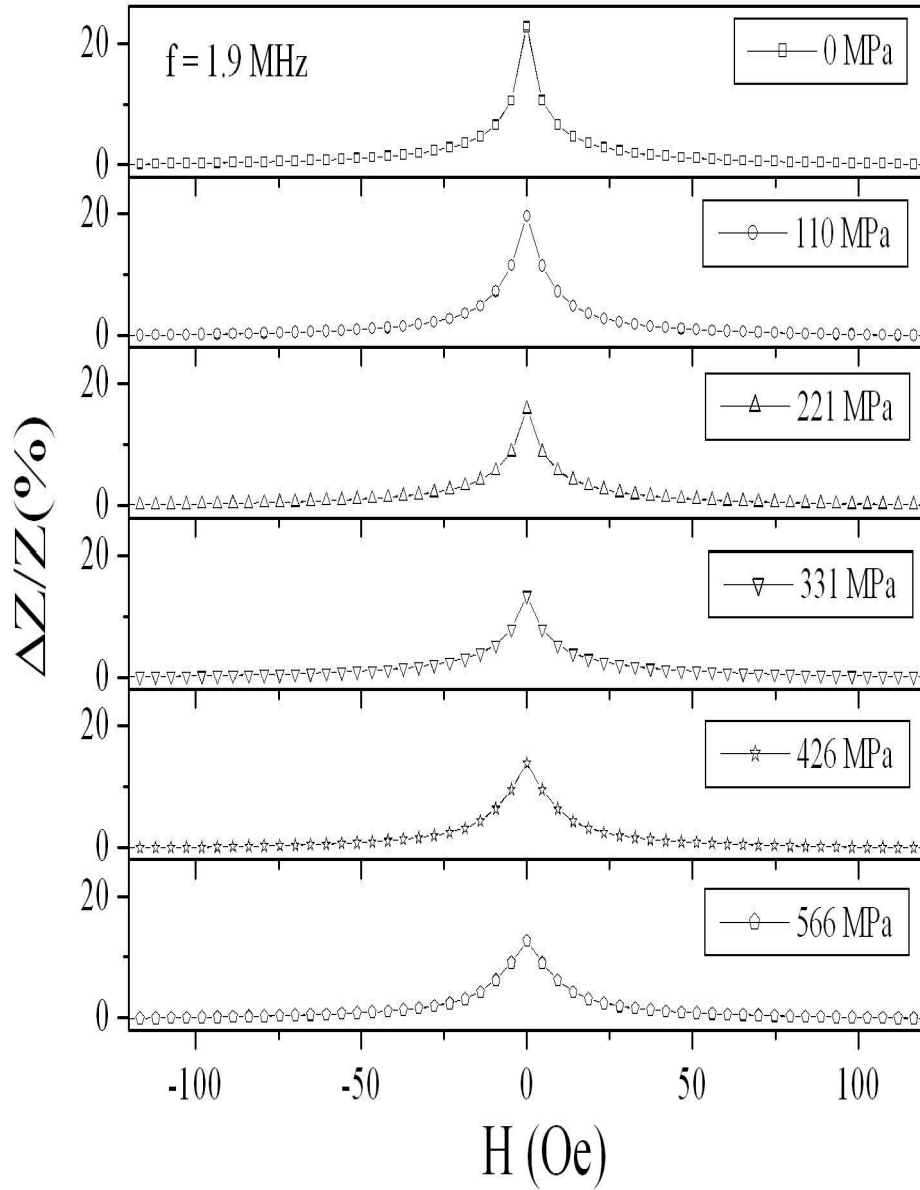
Figure 4.2: The variation of percentage change of magnetoimpedance, $\Delta Z/Z(\%)$ with dc magnetic field H of glass coated amorphous $Co_{83.2}Mn_{7.6}Si_{5.8}B_{3.3}$ microwire at a frequency of 1.9 MHz in absence and in the presence of stresses 110 MPa, 221 MPa, 331 MPa, 426 MPa and 566 MPa.

At this frequency the maximum value of GMI is observed at $H_{dc} = 0$, thus giving single-peak characteristic for the sample in absence as well as in presence of different tensile stresses. The value of $\Delta Z/Z(\%)$ decreass with increase of applied dc magnetic field. $[\Delta Z/Z(\%)]_{peak}$ decreases from 23% at $\sigma = 0$ MPa to 13% at $\sigma = 566$ MPa. At a higher frequency, $f = 4.6$ MHz, single peak behaviour of GMI as a function of magnetic field is observed for the microwire in absence as well as in presence of stress (Fig. 4.3). The peak value of $\Delta Z/Z(\%)$ decreases from 51% at $\sigma = 0$ MPa to 26% at $\sigma = 566$ MPa. Single peak GMI characteristic is observed at lower frequencies i.e. upto ~ 6 MHz. Two-peak GMI behaviour appears at a higher frequency (above 6 MHz). Fig. 4.4 shows the field dependence of percentage change of magnetoimpedance of the microwire at a frequency of 7.3 MHz in absence and in the presence of external tensile stress. Two peak GMI behaviour is seen for the sample in absence of any stress as well as for $\sigma = 110$ MPa, 221 MPa and 331 MPa. The dip at $H_{dc} = 0$ gradually diminishes with stress and finally it vanishes at $\sigma = 426$ MPa and 566 MPa at this frequency. At a more higher frequency, $f = 10$ MHz double-peak GMI is observed for the microwire in absence as well as in presence of external stress (Fig. 4.5). The shift in GMI peak values with magnetic field is most prominent in case of $\sigma = 0$ MPa, which gradually reduces with increasing stress. The peak value of $\Delta Z/Z(\%)$ decreases with increasing values of applied tensile stress at all frequencies of the ac current.

The variation of maximum values of percentage change in magnetoimpedance ($[\Delta Z/Z(\%)]_{peak}$) with frequency under different axial tensile stresses is shown in Fig. 4.6. It is clear from the figure that the peak value of GMI decreases with increasing stress. Maximum value of $[\Delta Z/Z(\%)]_{peak} \sim 53\%$ is observed at a frequency of 3.7 MHz for the sample in absence of any stress. The maximum value of $[\Delta Z/Z(\%)]_{peak}$ reduces to 26% for $\sigma = 566$ MPa at $f = 4.6$ MHz. The frequency dependence of GMI peak positions (ΔH_p) for different values of axial tensile stress is studied in Fig. 4.7. Single peak GMI characteristic ($\Delta H_p = 0$) is seen for the sample at various values of stress till a frequency of 5.5 MHz. With further increase in frequency two-peak GMI with increasing peak shift is observed for the sample in absence of any stress. Single peak GMI changes to double-peak at $f = 6.4$ MHz for $\sigma = 221$ MPa and at $f = 7.3$ MHz for $\sigma = 566$ MPa respectively. The stress dependence of maximum percentage change in magnetoimpedance at different frequencies is shown in

Fig. 4.8. From the figure it is clear that $[\Delta Z/Z(\%)]_{peak}$ decreases with increasing stress. We have also verified the influence of the magnitude of the alternating current on the value of magnetoimpedance upto a frequency of 10.9 MHz. The magnitude of the alternating current sent along the length of the microwire were 0.2 mA, 1.0 mA and 5.0 mA (Fig. 4.9). There was almost no change in the GMI values with change in magnitude of the alternating current for the whole frequency range. We have studied the stress and heat-treated dependence of GMI for the microwire for 1 mA ac current.

The magnetization of the sample have been measured in presence of different tensile stresses to understand the domain structure and magnetoimpedance results. Fig. 4.10 shows the dc hysteresis loops of glass coated amorphous $Co_{83.2}Mn_{7.6}Si_{5.8}B_{3.3}$ microwire under 0 MPa, 220 MPa and 440 MPa axial tensile stresses. The hysteresis loops suggest two kinds of magnetization processes corresponding to two different domain structures within the sample. There is a sudden large change in magnetization at very low field and a slow variation in magnetization at higher field. The magnetization reversal in the axial inner core domain at the switching field gives rise to large jump at low field and the change in magnetization in the outer shell is responsible for the slow variation of magnetization. Stress dependence of the large jump in magnetization due to inner core ($jump_{IC}$) and the change in magnetization from the outer shell ($jump_{OS}$) is shown in Fig. 4.11. It is observed that jump in magnetization due to inner core ($jump_{IC}$) increases with increasing tensile stress with a corresponding decrease in variation of magnetization due to outer shell ($jump_{OS}$). Stress dependence of coercivity of the microwire is shown in Fig. 4.12. The figure clearly shows that the application of tensile stress decreases the coercivity i.e. increases the magnetic softness of the material. The coercivity, H_c decreases from $\sim$ 70 mOe at $\sigma = 0$ MPa to $\sim$ 50 mOe at $\sigma = 440$ MPa. Due to the application of this tensile stress the anisotropy field, H_k reduces from $\sim$ 3.8 Oe to $\sim$ 2.7 Oe. An estimation of the linear magnetostriction coefficient, λ can be calculated from the change in the anisotropy field from $\sim$ 3.8 Oe to $\sim$ 2.7 Oe due to the change in applied tensile stress of $\sigma = 440$ MPa by using the following formula,

$$\lambda = (\mu_0 M_s H_k/3\sigma) \times (M_s/\Delta M) \tag{4.1}$$

where M_s is the saturation magnetization and ΔM is the contribution to magnetization from the outermost shell as shown in Fig. 4.10. Considering the fact that the anisotropy

field mainly changes the magnetization in the outermost shell of the microwire an additional factor $M_s/\Delta M$ has been incuded in the usual expression of λ. Taking $\mu_0 M_s \sim 0.7$ T, the estimated value of $\lambda \sim 1.0 \times 10^{-7}$ indicating that the sample is very low positive magnetostrictive in nature.
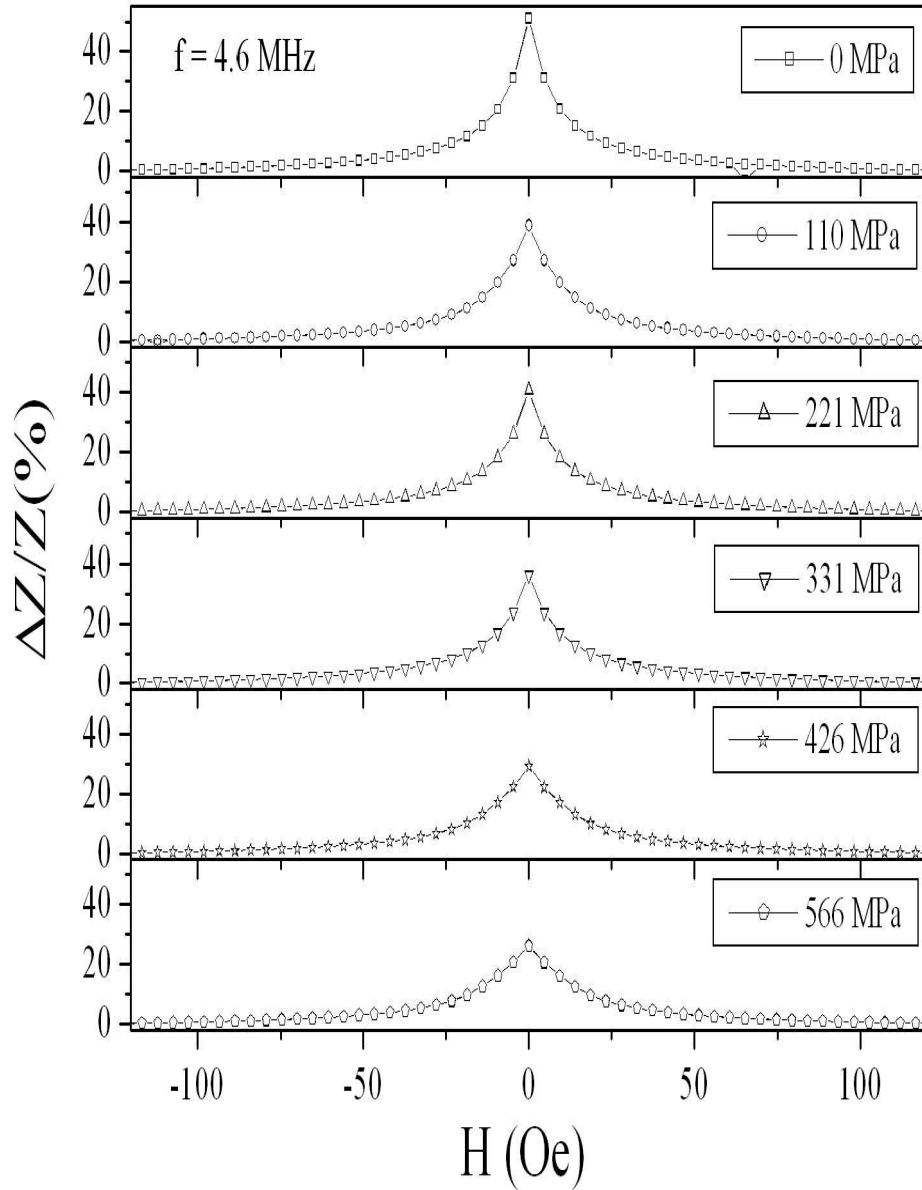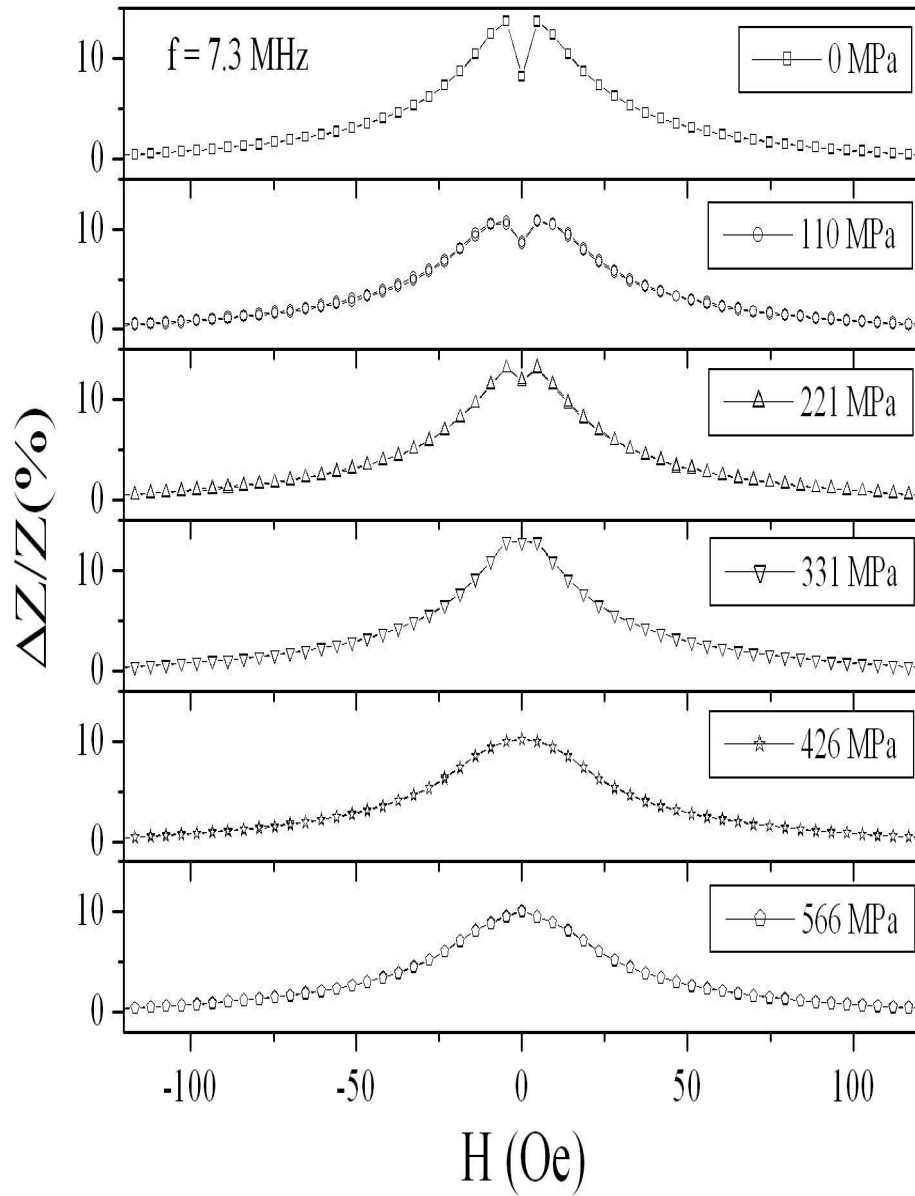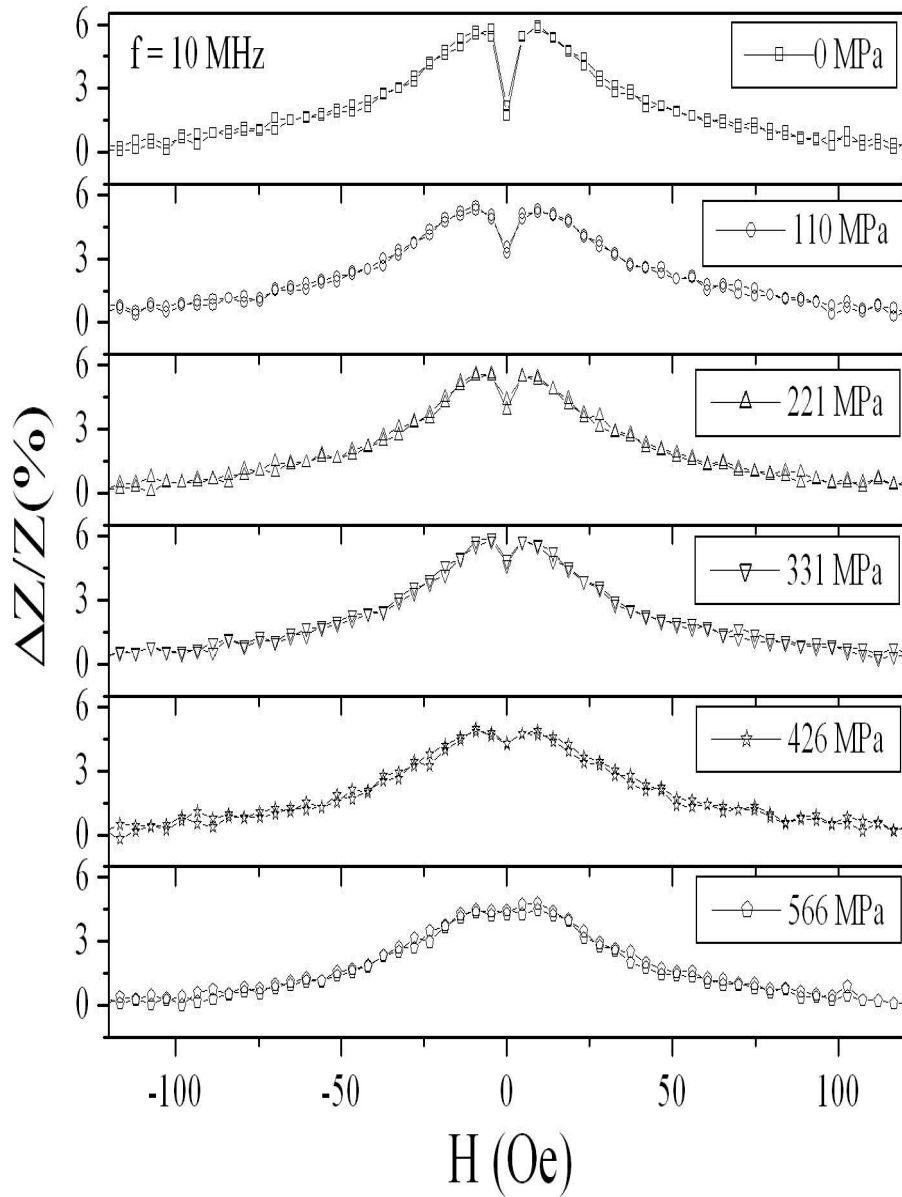
Figure 4.3: The variation of percentage change of magnetoimpedance, $\Delta Z/Z(\%)$ with dc magnetic field H of glass coated amorphous $Co_{83.2}Mn_{7.6}Si_{5.8}B_{3.3}$ microwire at a frequency of 4.6 MHz in absence and in the presence of stresses 110 MPa, 221 MPa, 331 MPa, 426 MPa and 566 MPa.

Figure 4.4: The variation of percentage change of magnetoimpedance, $\Delta Z/Z(\%)$ with dc magnetic field H of glass coated amorphous $Co_{83.2}Mn_{7.6}Si_{5.8}B_{3.3}$ microwire at a frequency of 7.3 MHz in absence and in the presence of stresses 110 MPa, 221 MPa, 331 MPa, 426 MPa and 566 MPa.

Figure 4.5: The variation of percentage change of magnetoimpedance, $\Delta Z/Z(\%)$ with dc magnetic field H of glass coated amorphous $Co_{83.2}Mn_{7.6}Si_{5.8}B_{3.3}$ microwire at a frequency of 10 MHz in absence and in the presence of stresses 110 MPa, 221 MPa, 331 MPa, 426 MPa and 566 MPa.
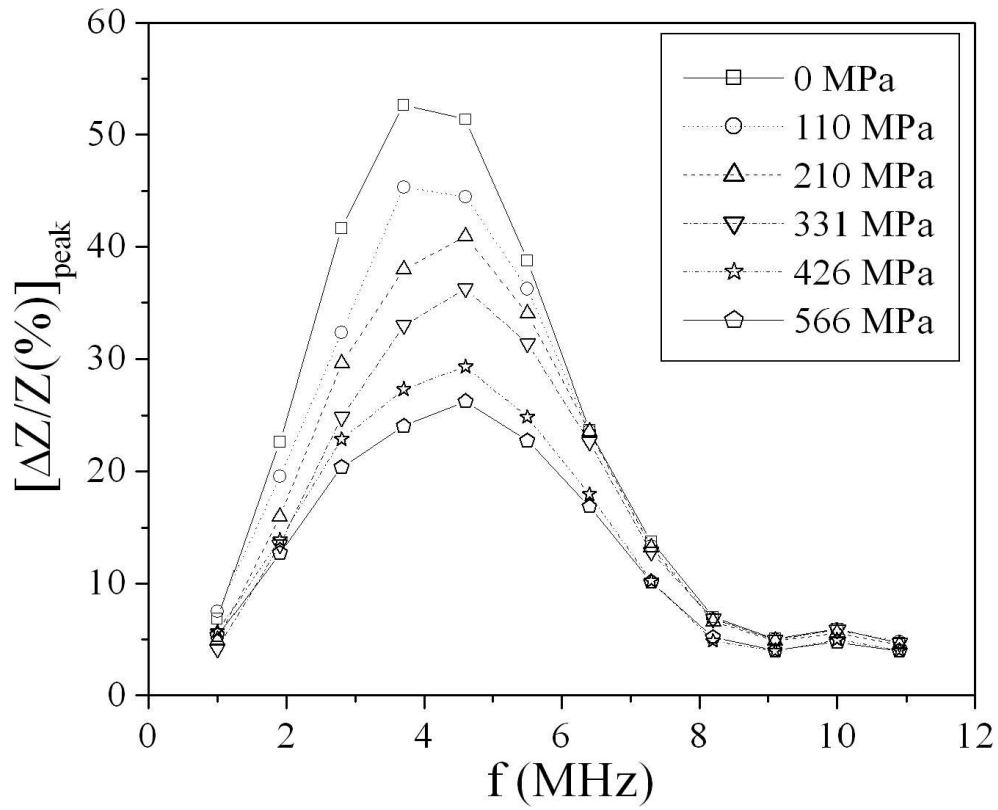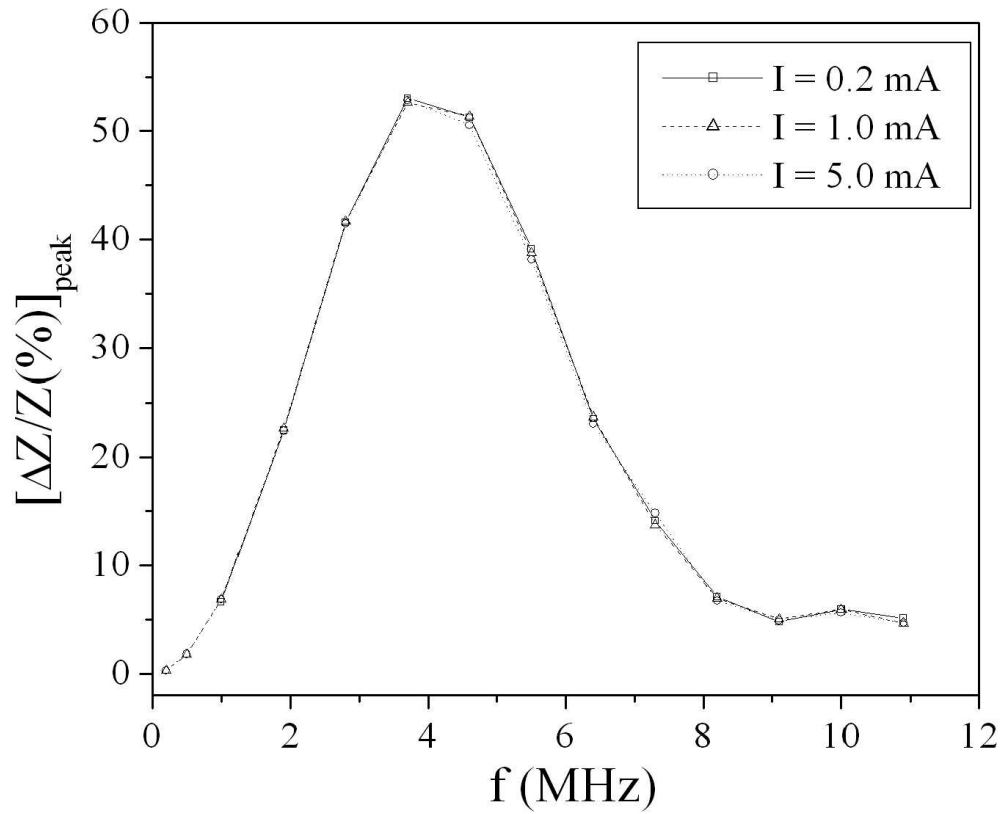
Figure 4.6: The variation of maximum percentage change of magnetoimpedance, $[\Delta Z/Z(\%)]_{peak}$ with frequency under different axial tensile stresses of glass coated amorphous $Co_{83.2}Mn_{7.6}Si_{5.8}B_{3.3}$ microwire.
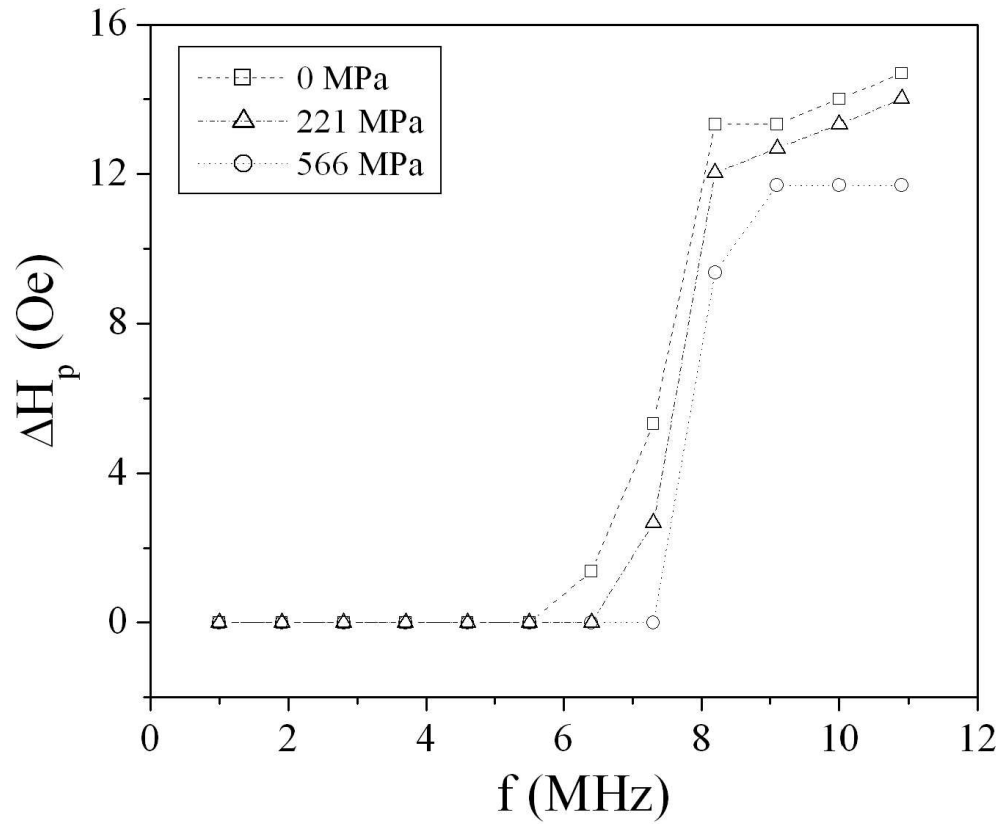
Figure 4.7: The frequency dependence of the peak positions of GMI in presence of different axial tensile stresses of glass coated amorphous $Co_{83.2}Mn_{7.6}Si_{5.8}B_{3.3}$ microwire.
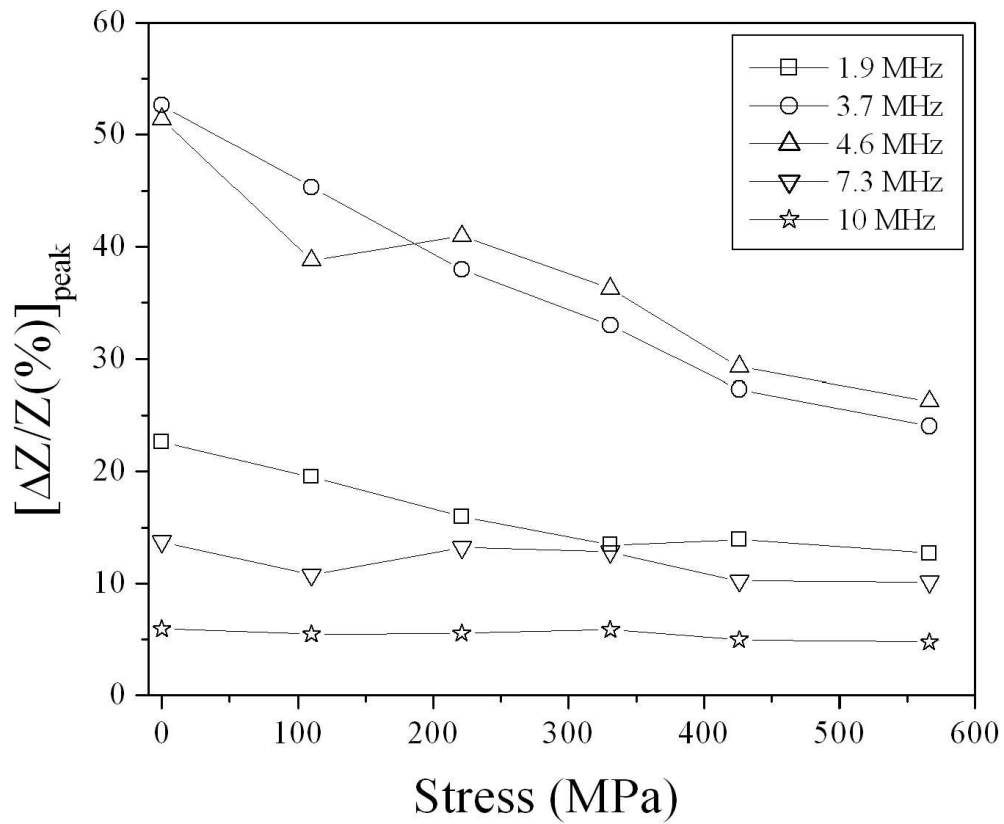
Figure 4.8: The stress dependence of maximum percentage change in magnetoimpedance at different frequencies of glass coated amorphous $Co_{83.2}Mn_{7.6}Si_{5.8}B_{3.3}$ microwire.

Figure 4.9: The variation of maximum percentage change of magnetoimpedance, $[\Delta Z/Z(\%)]_{peak}$ with frequency for different magnitudes of alternating current of glass coated amorphous $Co_{83.2}Mn_{7.6}Si_{5.8}B_{3.3}$ microwire.
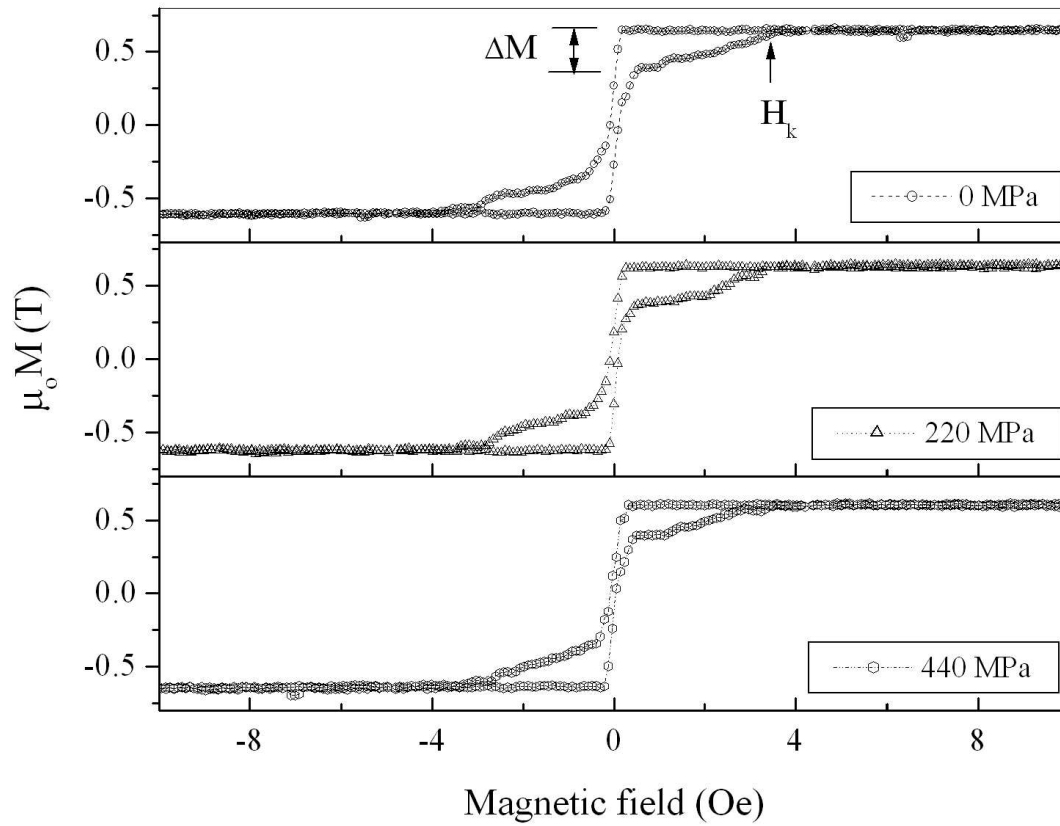
Figure 4.10: The dc hysteresis loops of glass coated amorphous $Co_{83.2}Mn_{7.6}Si_{5.8}B_{3.3}$ microwire under 0 MPa, 220 MPa and 440 MPa axial tensile stresses.
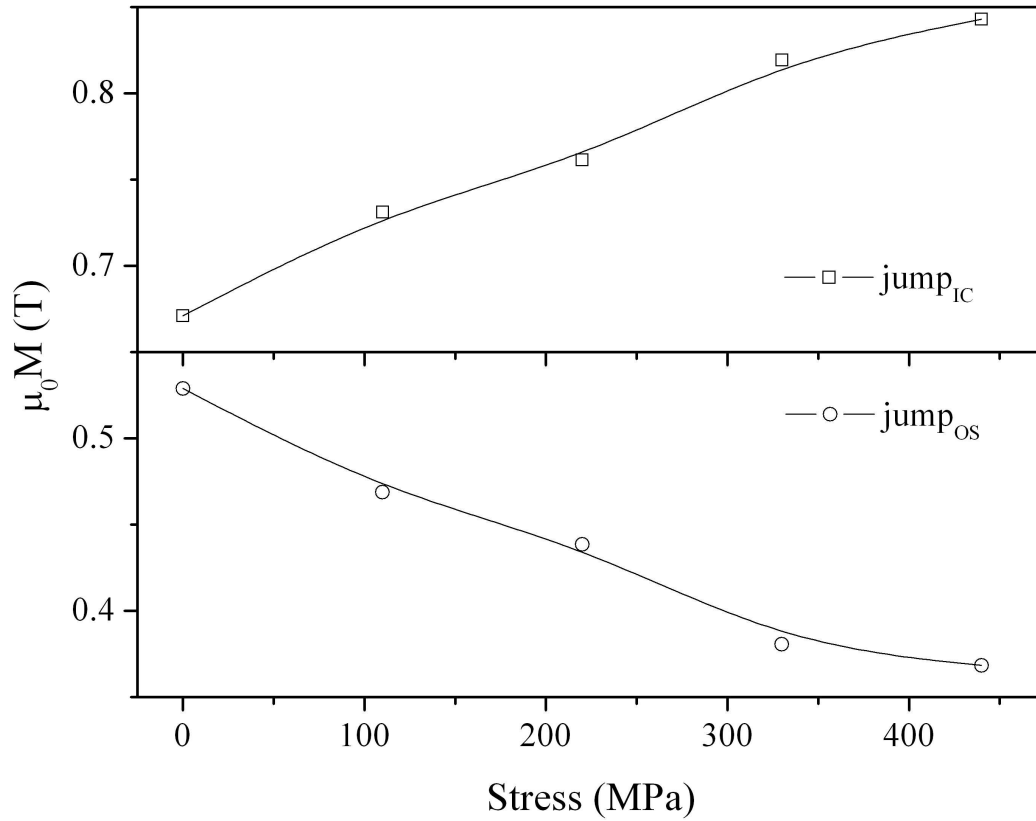
Figure 4.11: The variation of jump in magnetization due to inner core ($jump_{IC}$) and the change in magnetization from the outer shell ($jump_{OS}$) of glass coated amorphous $Co_{83.2}Mn_{7.6}Si_{5.8}B_{3.3}$ microwire under different axial tensile stresses.
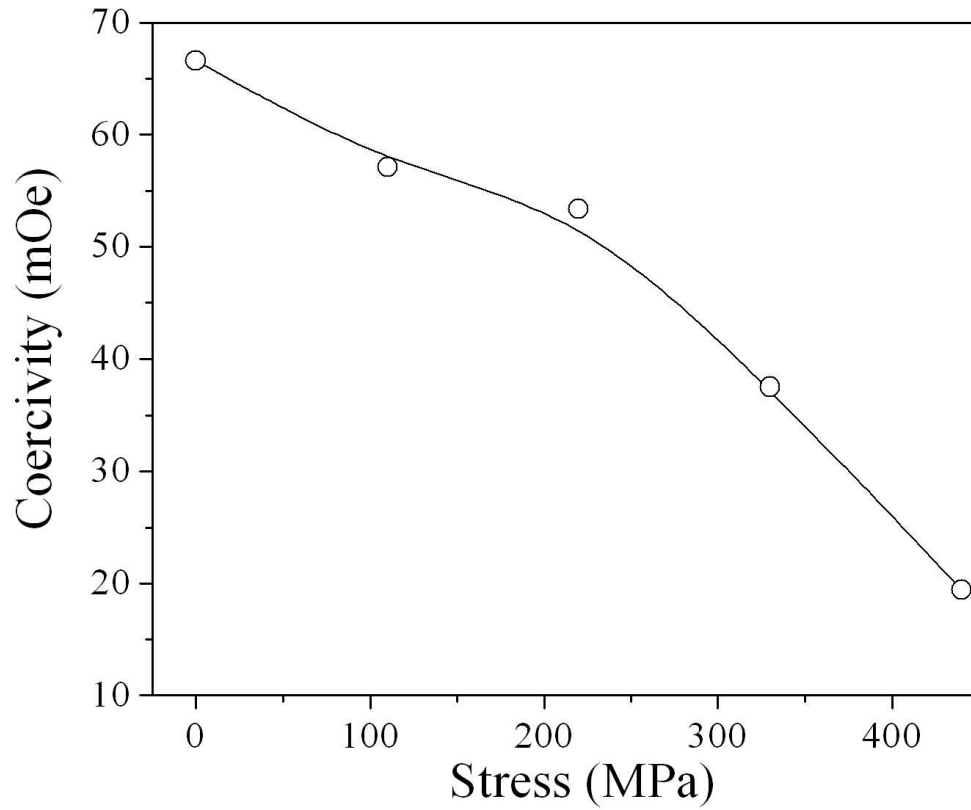
Figure 4.12: The variation of coercivity as a function of applied tensile stress in glass coated amorphous $Co_{83.2}Mn_{7.6}Si_{5.8}B_{3.3}$ microwire.

The variation of magnetoimpedance of the as-quenched and heat treated (annealing done by sending one, two, three and four current pulses respectively) microwires as a function of dc magnetic field is shown in Fig. 4.13 for 1 mA ac current with a frequency, $f = 0.95$ MHz. Single peak GMI characteristics with peak value $[\Delta Z/Z(\%)]_{peak}$ at H_{dc} ~ 0 Oe is observed for both the as-quenched and heat treated microwires. The value of $[\Delta Z/Z(\%)]_{peak}$ increases drastically from $\sim 4\%$ for the as-quenched sample to $\sim 47\%$ when the microwire is annealed by sending four pulses. Fig. 4.14 shows the variation of $[\Delta Z/Z(\%)]$ with H_{dc} of the as-quenched and heat treated microwires for 1 mA ac current with a frequency, $f = 3.5$ MHz. As-quenched sample shows a single peak GMI characteristic with a peak value, $[\Delta Z/Z(\%)]_{peak} \sim 48\%$ at $H_{dc} \sim 0$ Oe. However, two-peak behaviour with increasing GMI values is observed for successive current-pulse annealed microwires at this frequency. The maximum peak value of GMI appear at $H_{dc} = \pm 2.12$ Oe (termed as ΔH_p) with $[\Delta Z/Z(\%)]_{peak} \sim 129\%$ for the four pulse annealed microwire. The magnetic field sensitivity of GMI for the four pulse annealed sample is equal to $14.7\%/Oe$ at $f = 3.5$ MHz. Fig. 4.15 and Fig. 4.16 show the field dependence of GMI for the as-quenched and heat treated microwires for 1 mA ac current with frequencies 7.75 MHz and 12.85 MHz respectively. Two-peak GMI characteristic is observed for the as-quenched and heat treated microwires at $f = 7.75$ MHz. The MI peak positions (ΔH_p) shift towards higher H_{dc} for successive heat treated sample with respect to the as-quenched one. At $f = 12.85$ MHz, an additional peak at $H_{dc} \sim 0$ Oe is observed along with the two peaks at higher H_{dc} for the heat treated sample. The frequency dependence of maximum percentage change in magnetoimpedance is shown in Fig. 4.17 for the as-quenched and heat treated samples. The field response of GMI increases gradually w.r.to frequency with a maximum of $\sim 66\%$ at $f = 5.2$ MHz and then decreases for higher frequencies for the as-quenched microwire. The maximum value of $[\Delta Z/Z(\%)]_{peak}$ for the annealed microwires is observed at $f = 3.5$ MHz. There is a negligible variation in $[\Delta Z/Z(\%)]_{peak}$ at $f = 3.5$ MHz for the heat treated samples, annealed with one, two and three current pulses. There is a noticeable increase in GMI value, $[\Delta Z/Z(\%)]_{peak} \sim 129\%$ on heat treatment of the sample by sending four pulses of amplitude 100 mA and duration of 12 seconds. Fig. 4.18 shows the change in MI peak positions, ΔH_p with frequency of the as-quenched and heat treated microwires. Two peak behaviour for the as-quenched sample appears after

6.9 MHz but heat treated microwires show two peak characteristic from a much lower frequency. The value of ΔH_p increases with frequency i.e. shifts toward higher values of magnetic field for the as-quenched and annealed microwires. Heat treatment of the sample with increasing current pulses increases the value of ΔH_p.

The dc hysteresis loops of the as-quenched and heat treated samples (Fig. 4.19) was studied to understand the domain structure and magnetoimpedance of the microwire. The as-quenched sample shows a sharp change in magnetization at low magnetic field due to the change in magnetization in the IC with a slow rise at higher fields due to the contribution from the OS. On gradual heat treatment with current pulses, volume of OS increases at the cost of IC which is reflected in the hysteresis loop measurements (the initial jump in magnetization is reduced significantly).
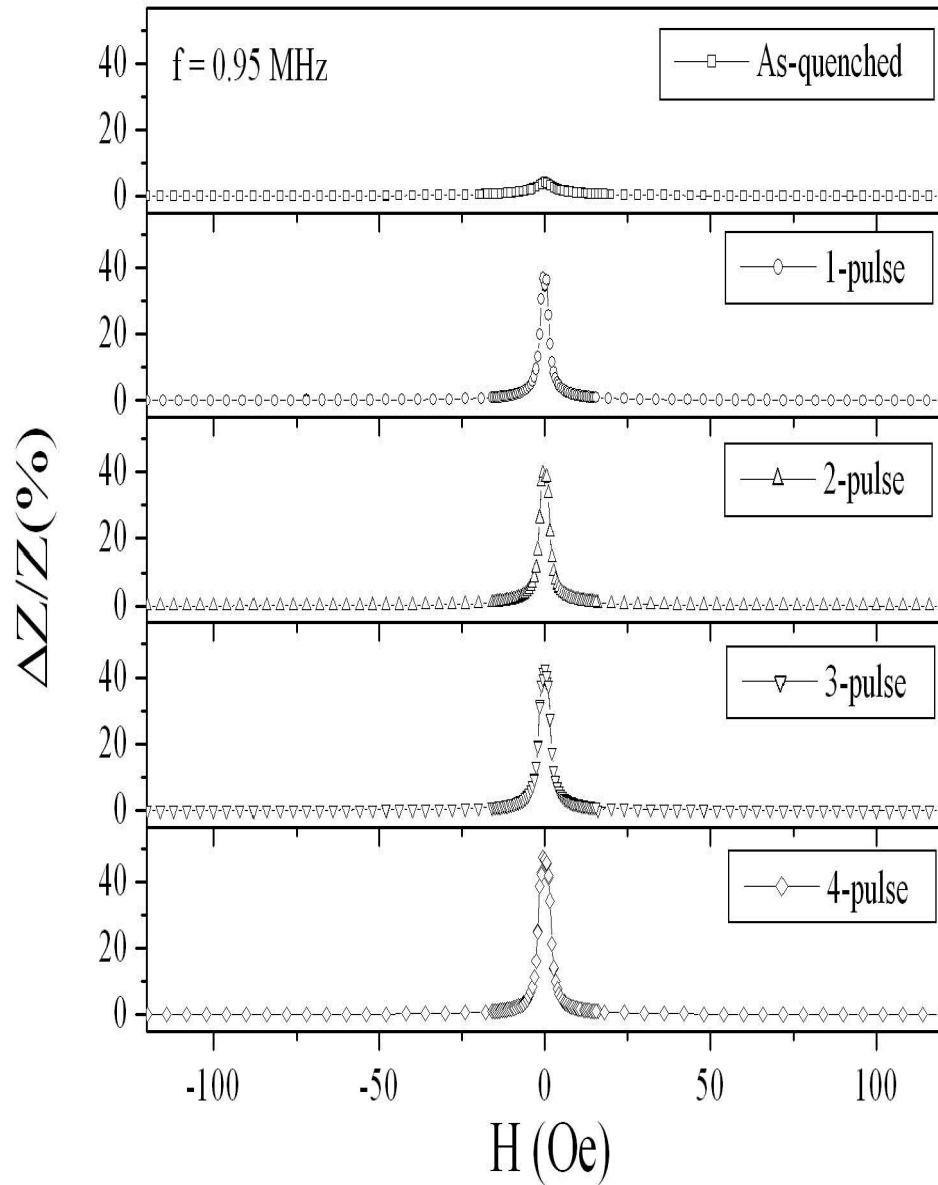
Figure 4.13: The variation of percentage change of magnetoimpedance, $\Delta Z/Z(\%)$ with dc magnetic field H of the as quenched and heat treated glass coated amorphous $Co_{83.2}Mn_{7.6}Si_{5.8}B_{3.3}$ microwires at a frequency of 0.95 MHz.
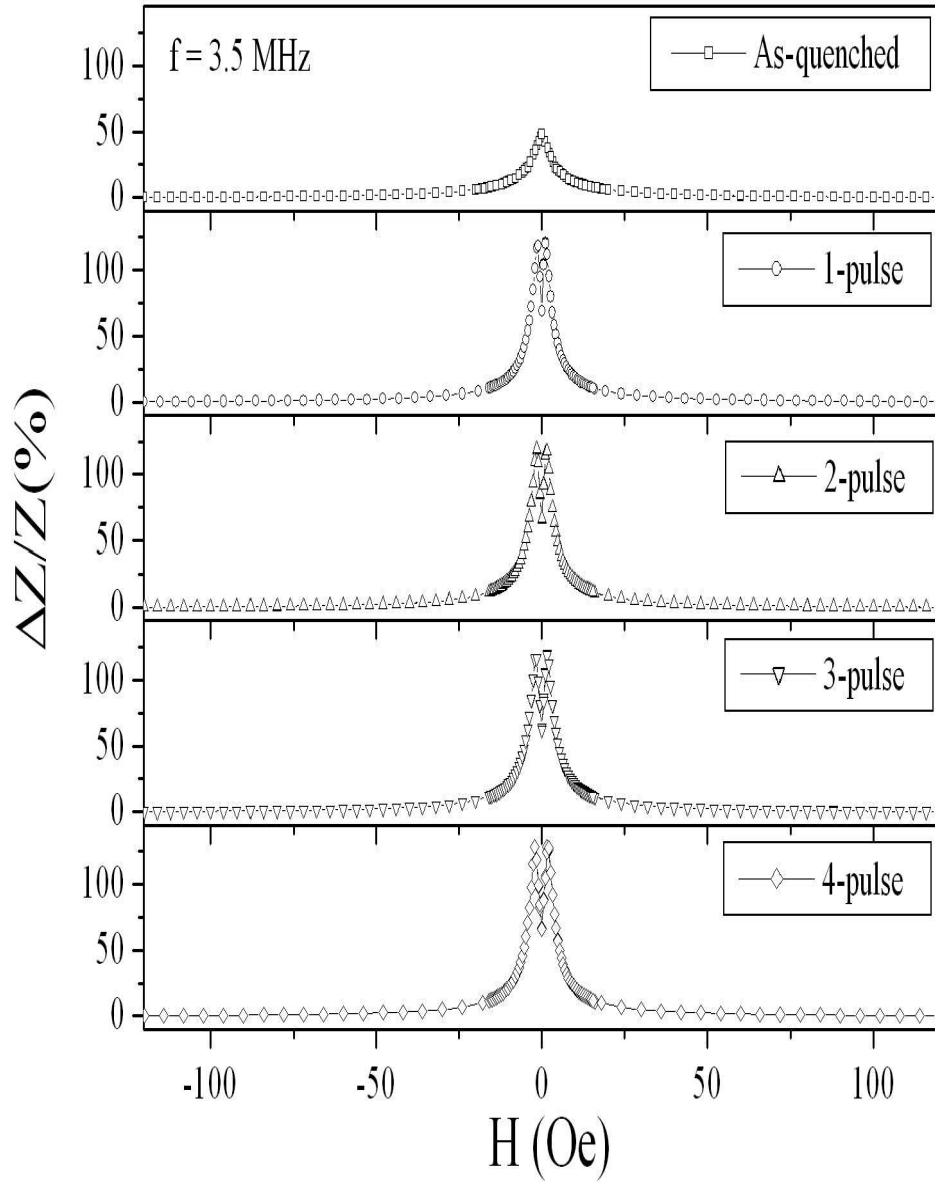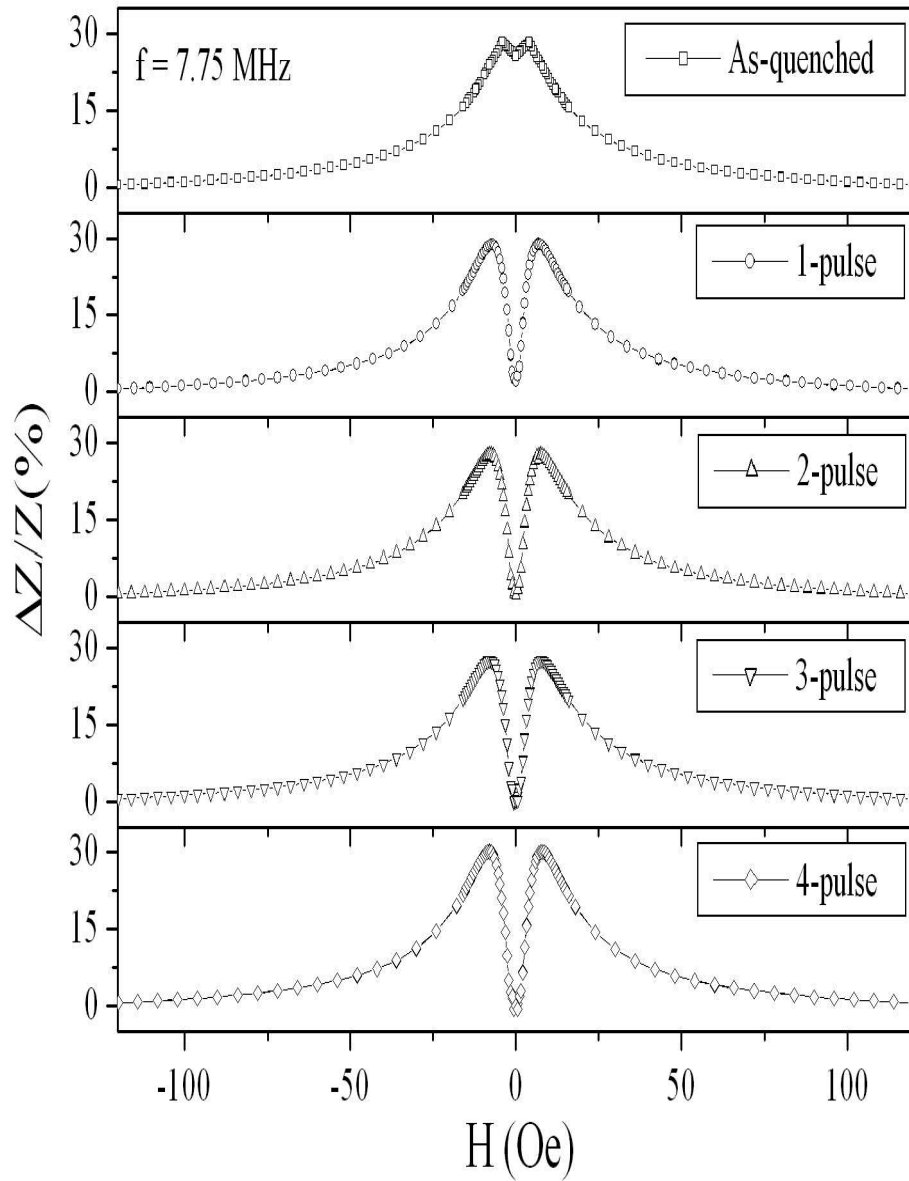
Figure 4.14: The variation of percentage change of magnetoimpedance, $\Delta Z/Z(\%)$ with dc magnetic field H of the as quenched and heat treated glass coated amorphous $Co_{83.2}Mn_{7.6}Si_{5.8}B_{3.3}$ microwires at a frequency of 3.5 MHz.

Figure 4.15: The variation of percentage change of magnetoimpedance, $\Delta Z/Z(\%)$ with dc magnetic field H of the as quenched and heat treated glass coated amorphous $Co_{83.2}Mn_{7.6}Si_{5.8}B_{3.3}$ microwires at a frequency of 7.75 MHz.
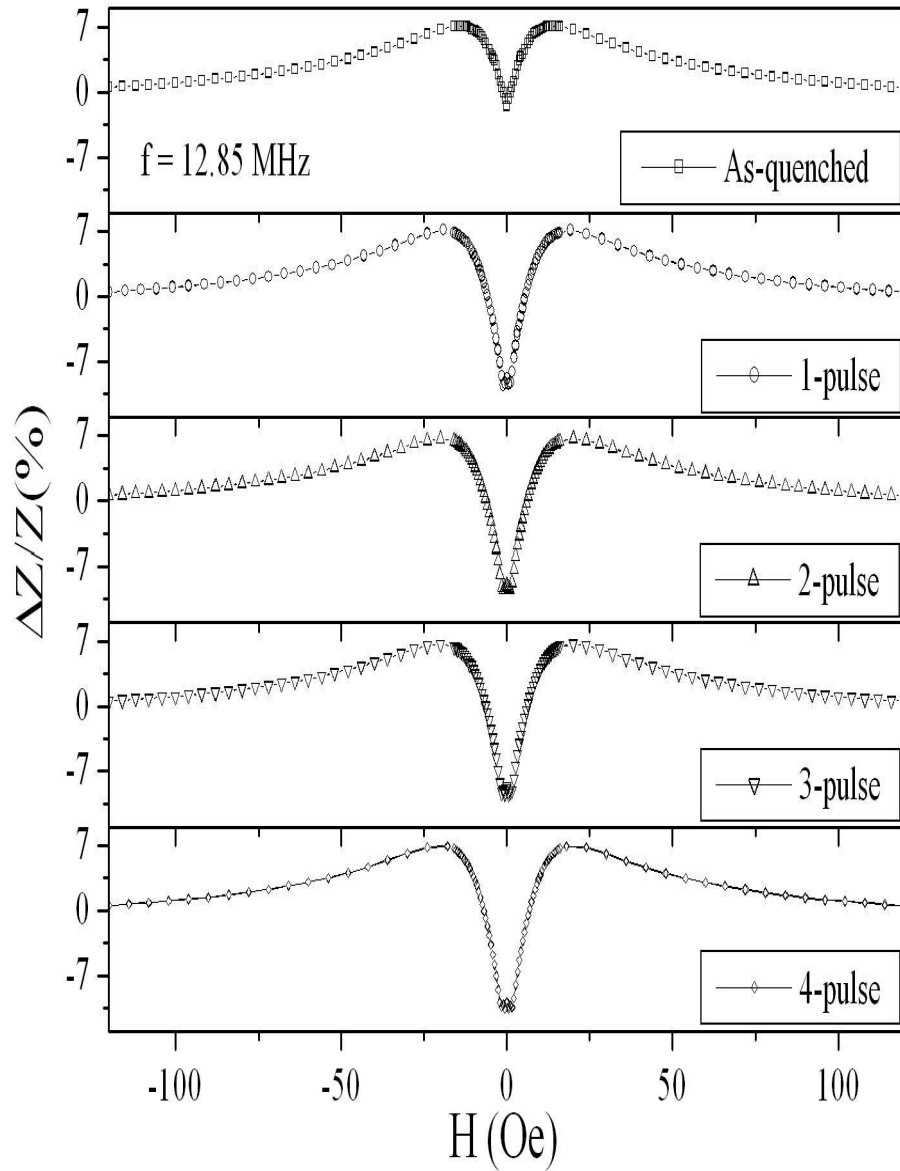
Figure 4.16: The variation of percentage change of magnetoimpedance, $\Delta Z/Z(\%)$ with dc magnetic field H of the as quenched and heat treated glass coated amorphous $Co_{83.2}Mn_{7.6}Si_{5.8}B_{3.3}$ microwires at a frequency of 12.85 MHz.
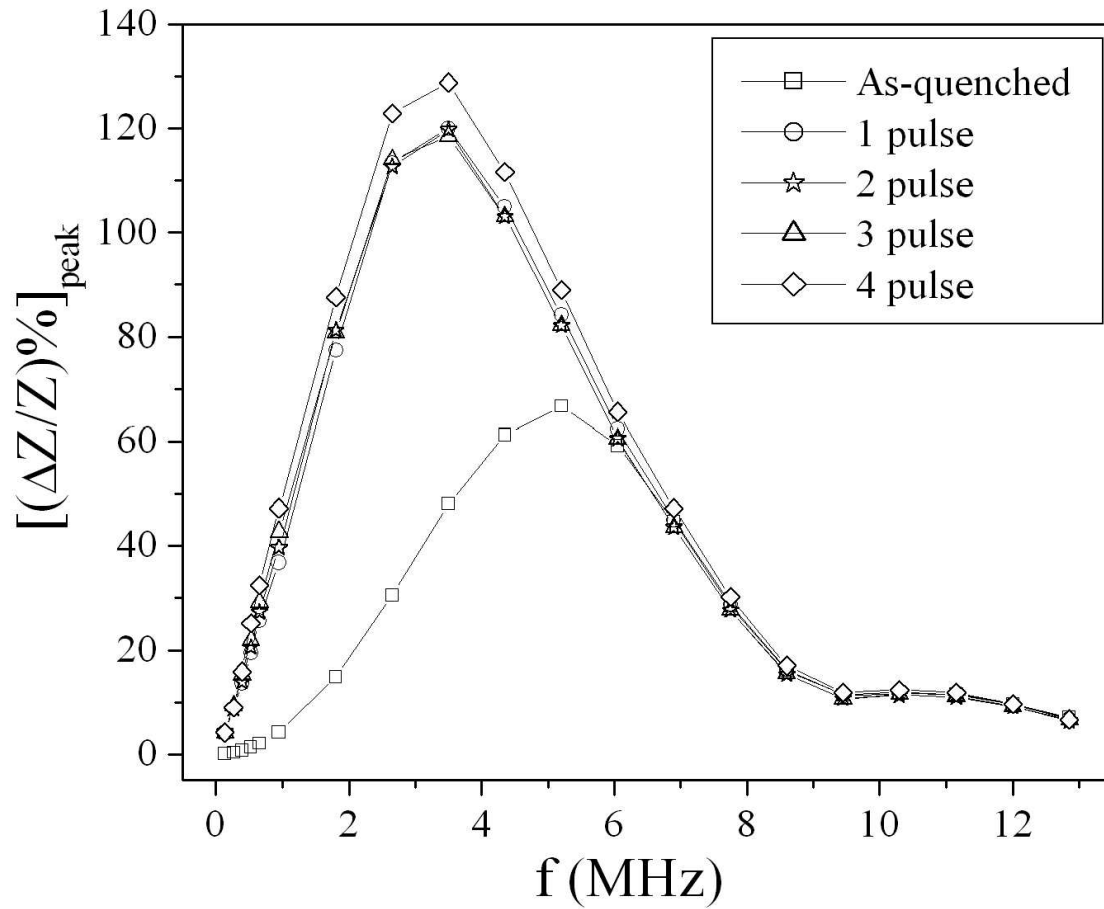
Figure 4.17: The variation of maximum percentage change of magnetoimpedance, $[\Delta Z/Z(\%)]_{peak}$ with frequency of the as quenched and heat treated glass coated amorphous $Co_{83.2}Mn_{7.6}Si_{5.8}B_{3.3}$ microwires.
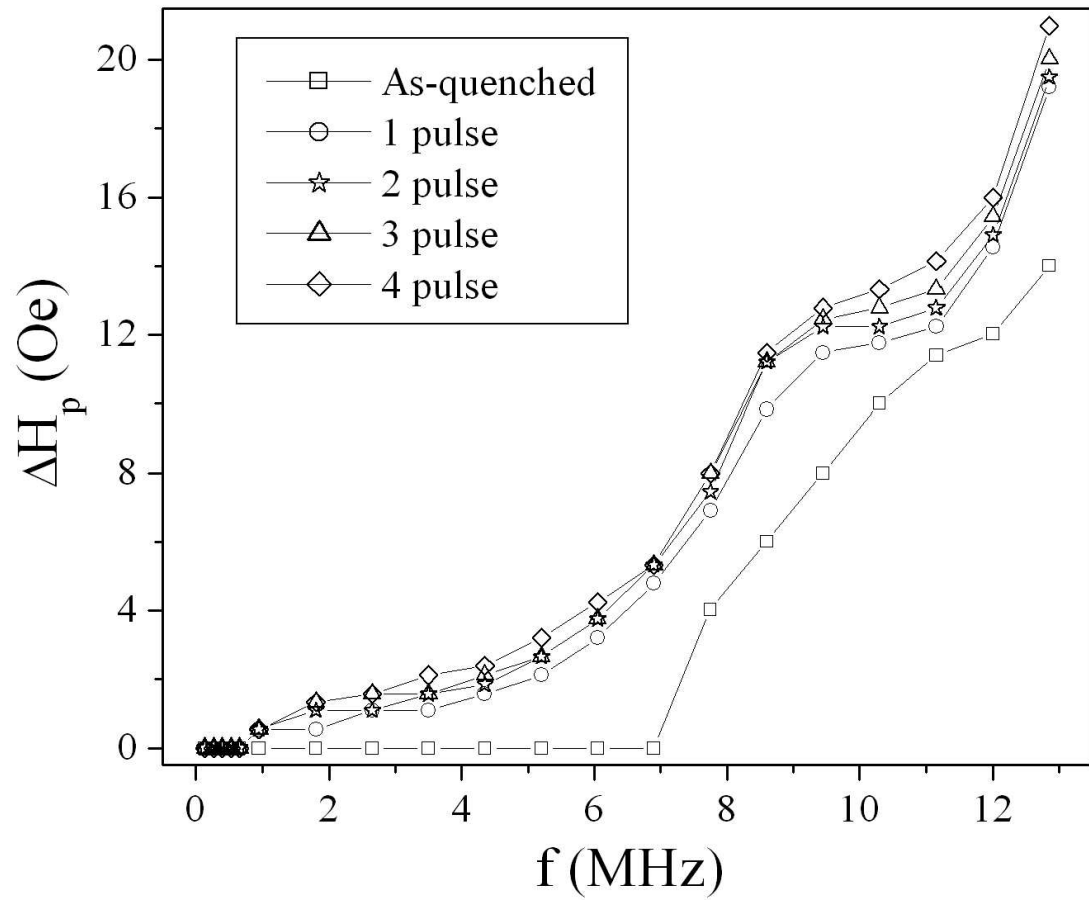
Figure 4.18: Frequency dependence of the peak positions of GMI of the as quenched and heat treated glass coated amorphous $Co_{83.2}Mn_{7.6}Si_{5.8}B_{3.3}$ microwires.
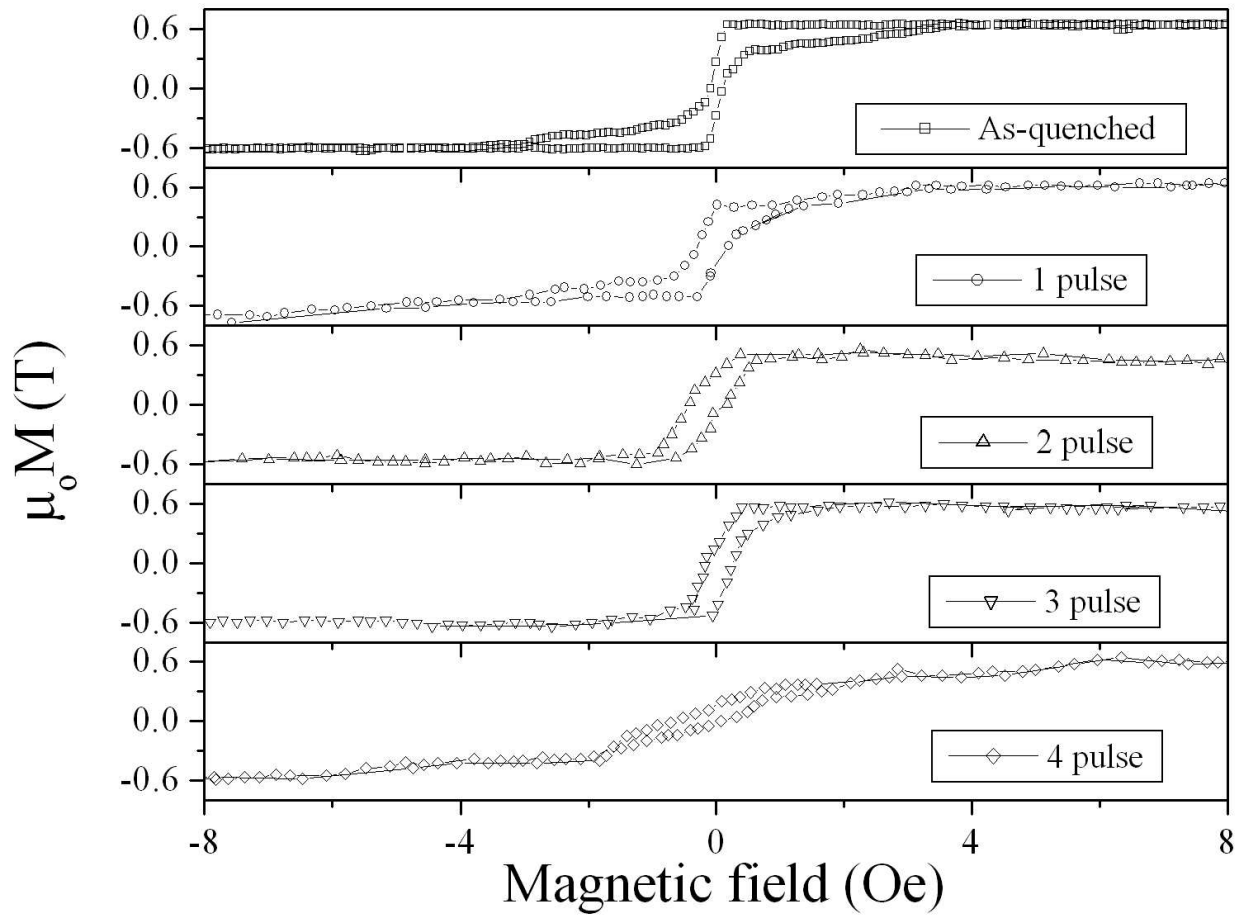
Figure 4.19: Axial hysteresis loops of the as-quenched and heat treated glass coated amorphous $Co_{83.2}Mn_{7.6}Si_{5.8}B_{3.3}$ microwires.

Asymmetry between the two peaks in magnetoimpedance has been developed by passing dc currents of magnitude, $I_{dc} = 1$ mA and 2 mA for a duation of $t_{an} = 25$ minutes through the length of the microwire along with the ac current $I_{ac} = 1$ mA. Figures 4.20, 4.21, 4.22 and 4.23 show the asymmetric magnetoimpedance of the glass coated amorphous $Co_{83.2}Mn_{7.6}Si_{5.8}B_{3.3}$ microwires at frequencies 0.66 MHz, 0.79 MHz, 1.8 MHz and 3.5 MHz respectively where annealing was done with $I_{dc} = 1mA$ for a duration of $t_{an} = 25min$. Percentage change in the difference between the two MI peak heights is calculated as,

$$[\Delta(Z_{peak})]\% = 100[\frac{Z_{peak1} - Z_{peak2}}{Z_{peak2}}] \tag{4.2}$$

where Z_{peak1} and Z_{peak2} represent the two MI peak heights at a particular frequency of I_{ac}. Frequency dependence of the percentage change in the difference between two MI peak heights in case of asymmetric MI of glass coated amorphous $Co_{83.2}Mn_{7.6}Si_{5.8}B_{3.3}$ microwires obtained with $I_{ac} = 1mA$ and $I_{dc} = 1mA$ is shown in Fig.4.24.

Figures 4.25, and 4.26 show the asymmetric magnetoimpedance of the glass coated amorphous $Co_{83.2}Mn_{7.6}Si_{5.8}B_{3.3}$ microwires at frequencies 0.92 MHz and 3.5 MHz respectively where annealing was done with $I_{dc} = 2mA$ for a duration of $t_{an} = 25min$. Fig.4.27 show the frequency dependence of the percentage change in the difference between two MI peak heights in case of AGMI of glass coated amorphous $Co_{83.2}Mn_{7.6}Si_{5.8}B_{3.3}$ microwires obtained with $I_{ac} = 1mA$ and $I_{dc} = 2mA$. The combination of the external static magnetic field (H_{dc}) and the dc biassed current applied along the microwire (I_{dc}) generates an effective helical field that acts on the microwire resulting in asymmetric GMI (discussed in detail in Chapter 3).

Figure 4.20: Asymmetric magnetoimpedance of glass coated amorphous $Co_{83.2}Mn_{7.6}Si_{5.8}B_{3.3}$ microwires with $I_{ac} = 1mA$ at a frquency of 0.66 MHz. Annealing was done with $I_{dc} = 1mA$ for a duration of $t_{an} = 25$ min.
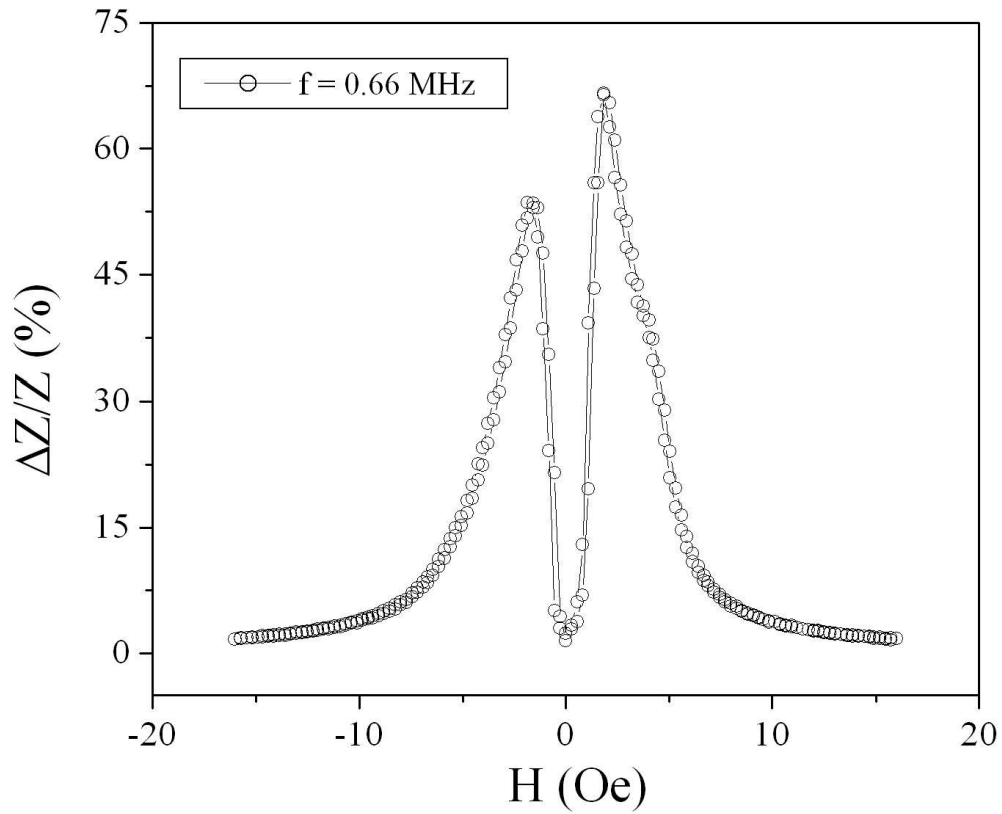
Figure 4.21: Asymmetric magnetoimpedance of glass coated amorphous $Co_{83.2}Mn_{7.6}Si_{5.8}B_{3.3}$ microwires with $I_{ac} = 1mA$ at a frquency of 0.79 MHz. Annealing was done with $I_{dc} = 1mA$ for a duration of $t_{an} = 25$ min.
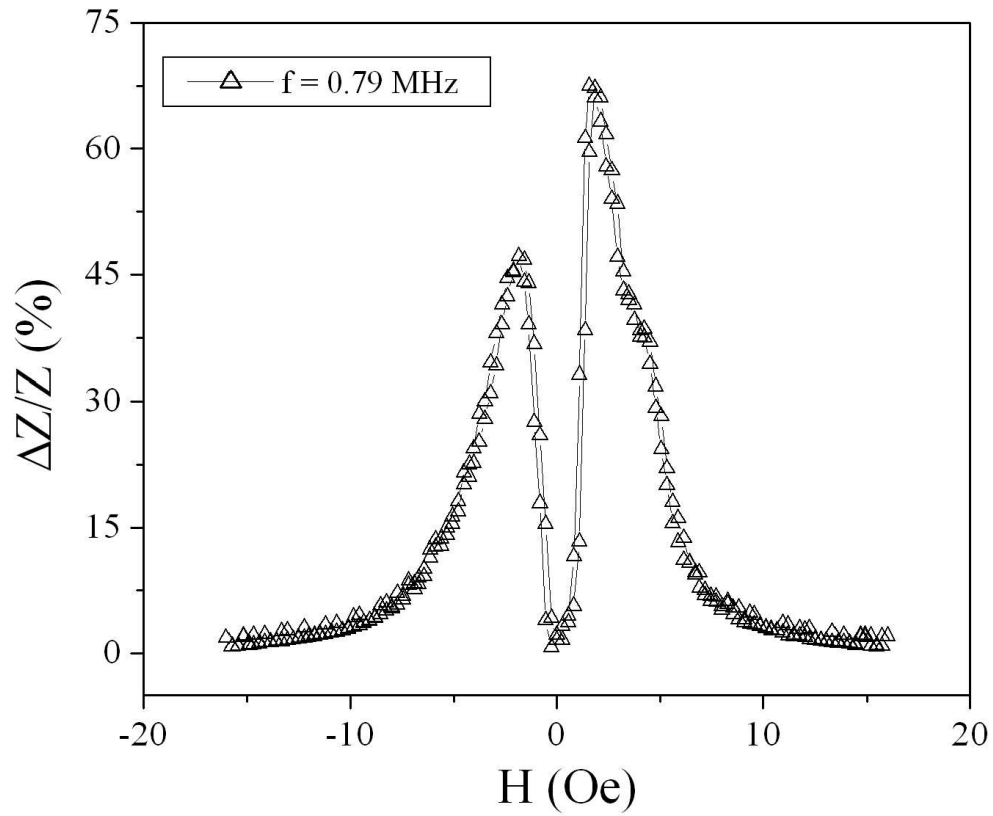
Figure 4.22: Asymmetric magnetoimpedance of glass coated amorphous $Co_{83.2}Mn_{7.6}Si_{5.8}B_{3.3}$ microwires with $I_{ac} = 1mA$ at a frquency of 1.8 MHz. Annealing was done with $I_{dc} = 1mA$ for a duration of $t_{an} = 25$ min.
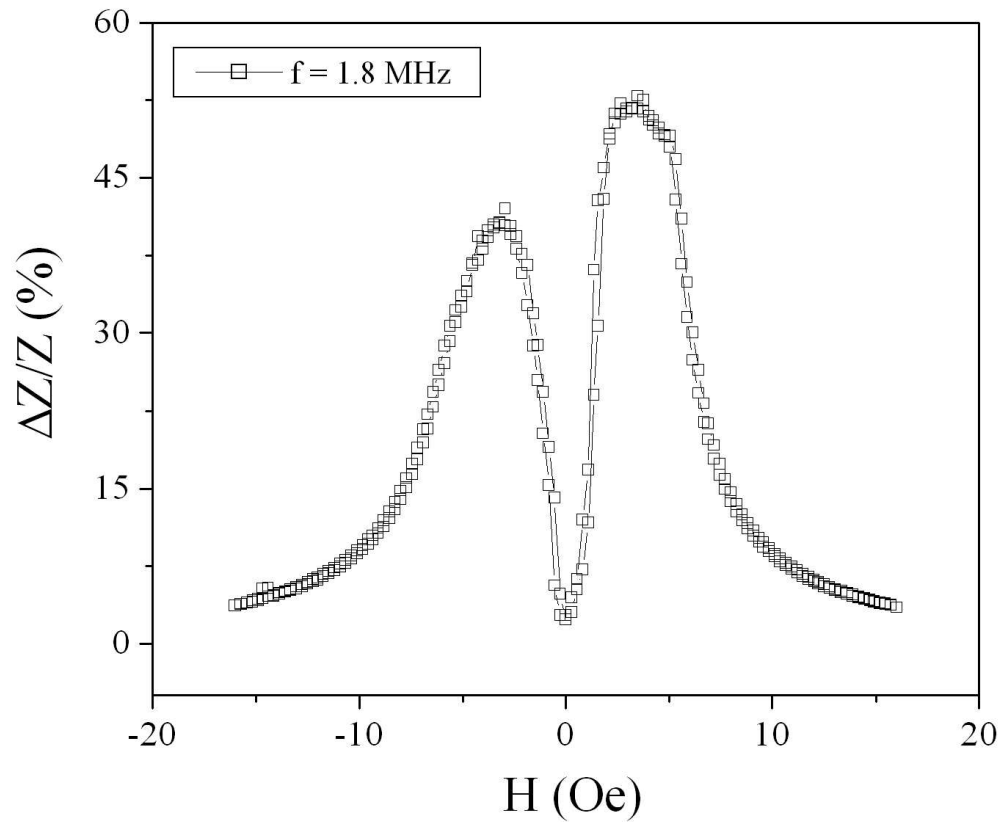
Figure 4.23: Asymmetric magnetoimpedance of glass coated amorphous $Co_{83.2}Mn_{7.6}Si_{5.8}B_{3.3}$ microwires with $I_{ac} = 1mA$ at a frquency of 3.5 MHz. Annealing was done with $I_{dc} = 1mA$ for a duration of $t_{an} = 25$ min.

Figure 4.24: Frequency dependence of the percentage change in the difference between two MI peak heights in case of asymmetric MI of glass coated amorphous $Co_{83.2}Mn_{7.6}Si_{5.8}B_{3.3}$ microwires obtained with $I_{ac} = 1mA$ and $I_{dc} = 1mA$.
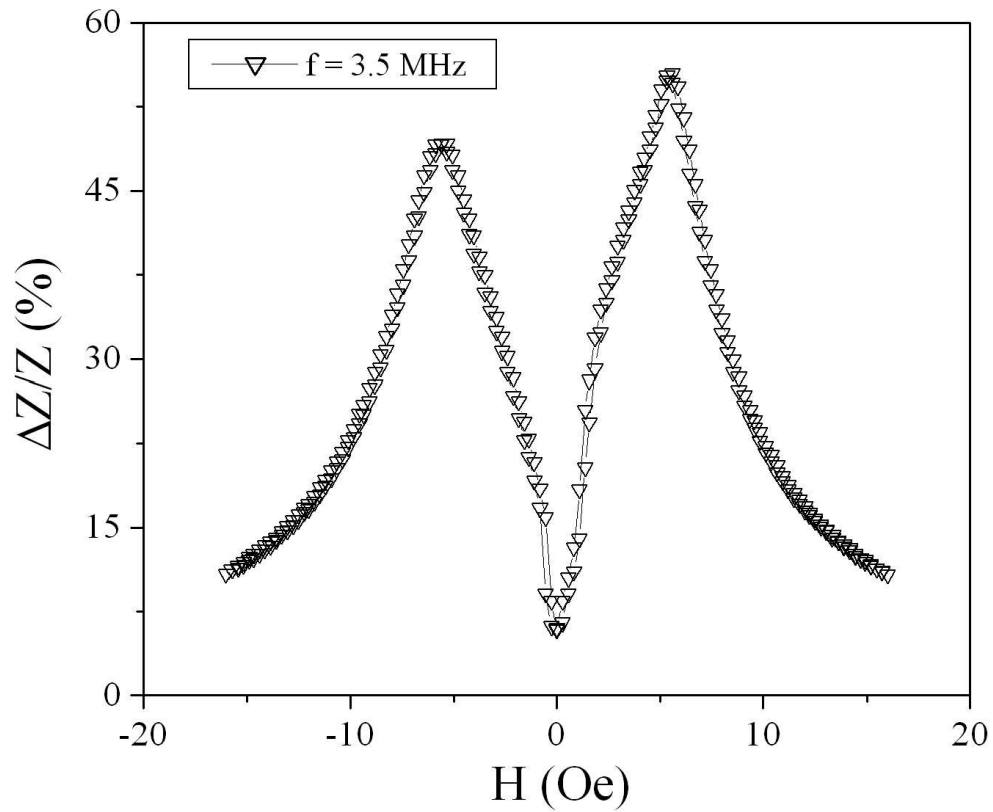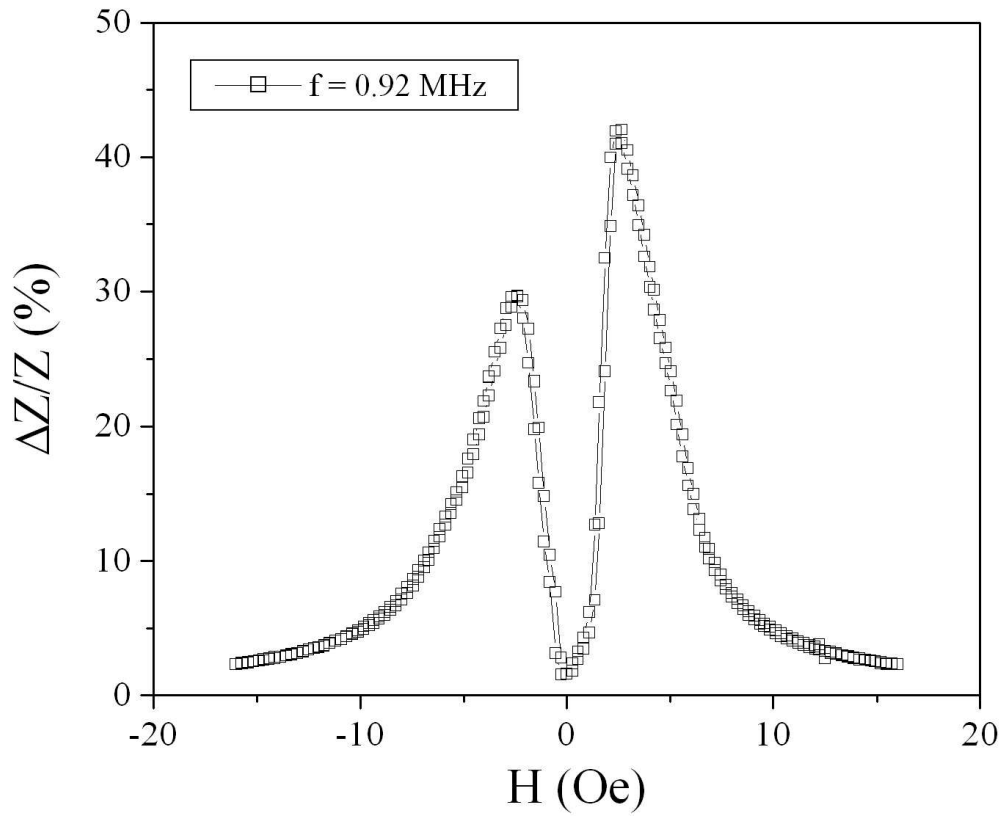
Figure 4.25: Asymmetric magnetoimpedance of glass coated amorphous $Co_{83.2}Mn_{7.6}Si_{5.8}B_{3.3}$ microwires with $I_{ac} = 1mA$ at a frquency of 0.92 MHz. Annealing was done with $I_{dc} = 2mA$ for a duration of $t_{an} = 25$ min.

Figure 4.26: Asymmetric magnetoimpedance of glass coated amorphous $Co_{83.2}Mn_{7.6}Si_{5.8}B_{3.3}$ microwires with $I_{ac} = 1mA$ at a frquency of 3.5 MHz. Annealing was done with $I_{dc} = 2mA$ for a duration of $t_{an} = 25$ min.
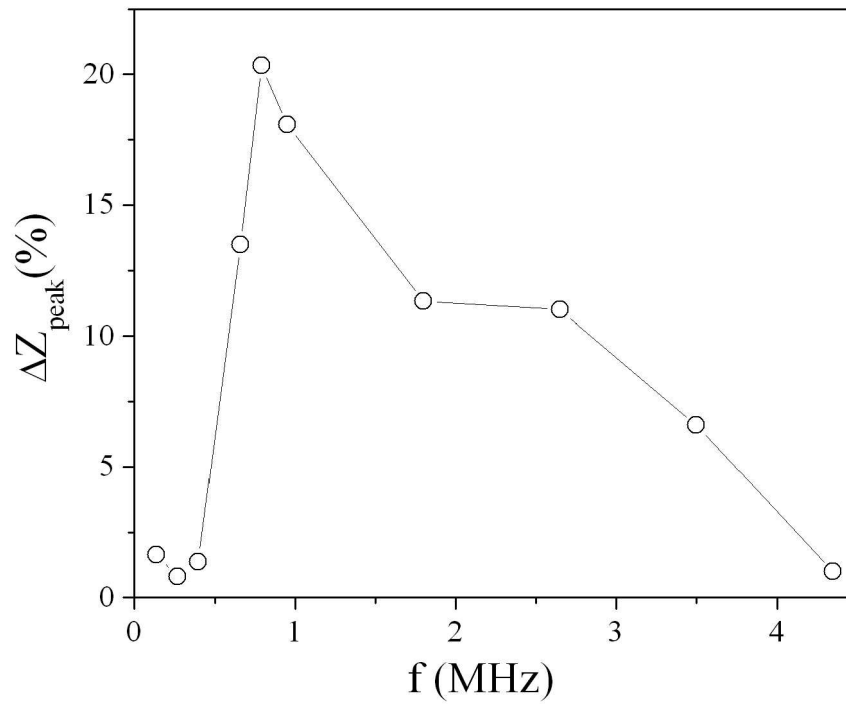
Figure 4.27: Frequency dependence of the percentage change in the difference between two MI peak heights in case of asymmetric MI of glass coated amorphous $Co_{83.2}Mn_{7.6}Si_{5.8}B_{3.3}$ microwires obtained with $I_{ac} = 1mA$ and $I_{dc} = 2mA$.
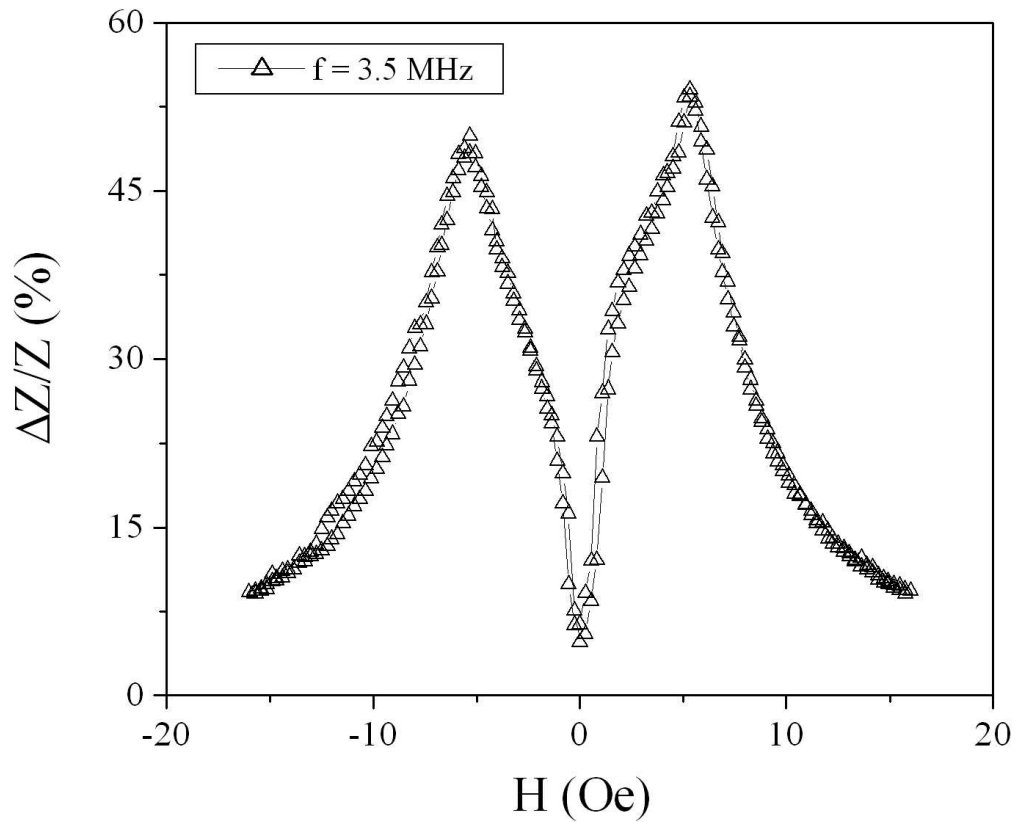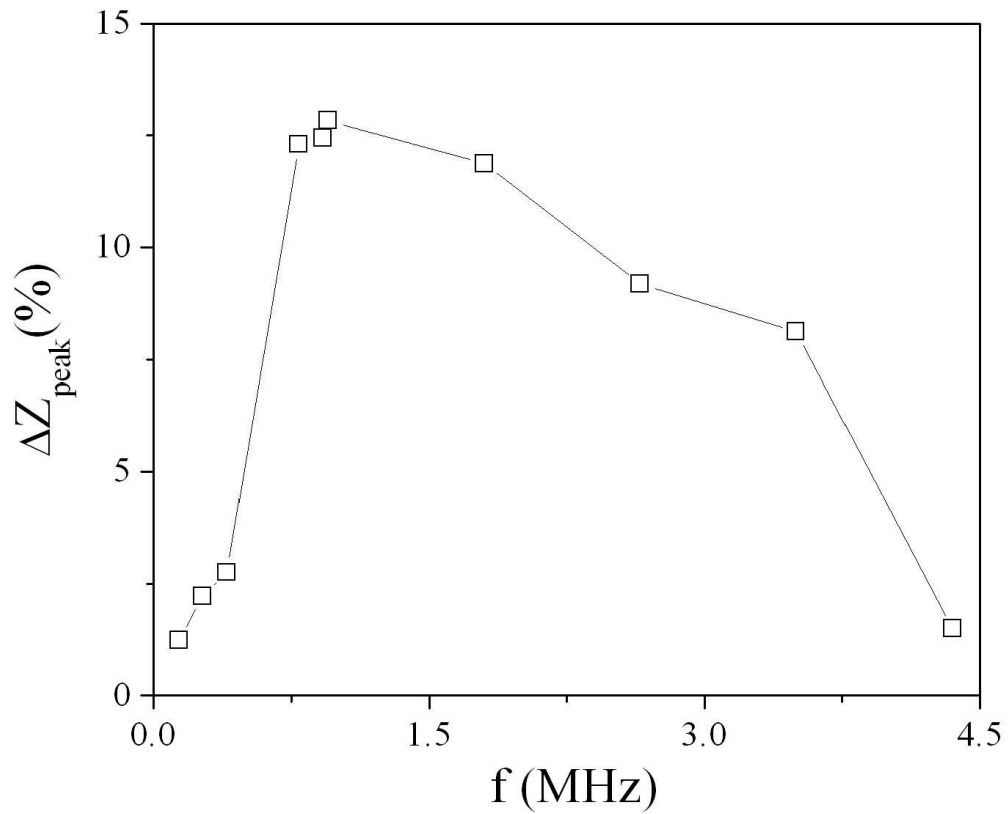
The change in MI of the microwire is dependent on the penetration depth, δ due to a change in transverse permeability, μ_ϕ by an externally applied dc magnetic field. The domain structure of this wire-shaped sample consists of an inner core (IC) domain having a magnetization direction closely parallel to the wire axis and a multi-domain outer shell (OS) with transversely oriented (radial) magnetization. There exists two permeability peaks against magnetic field, one at the switching field of IC and the other near the anisotropy field of OS. These two peaks arising from two different domain regions give two MI peaks around $H_{dc} \sim 0$ Oe. At low frequencies, the anisotopy field of these soft magnetic materials is very close to the switching field and therefore the peaks of MI originating from IC and OS coincide with each other and a single-peak GMI characteristic very close to $H_{dc} = 0$ Oe, is observed. At higher frequencies, the anisotropy field of the OS shifts more towards higher field compared to the switching field, as the domain wall displacement in OS is more affected by increase in frequency compared to the moment rotation in IC. As a result of it, a two-peak MI behaviour is observed at higher frequencies for the as-quenched as well as stress and heat treated samples.

Axial tensile stress generates a uniaxial anisotropy along the axis of the microwire and increases the inner core domain. This results in a decrease in circular permeability and hence the value of GMI decreases with increasing stress. Two-peak GMI behaviour is observed at higher frequencies because the switching and anisotropy field increases with increasing frequency (as described in the previous chapter). The applied tensile stress induces magnetoelastic anisotropy thereby increasing the magnetic softness along the axis of the microwire. This results in a decrease in switching and anisotropy field thereby reducing the value of ΔH_p with increasing stress.

Annealing the microwire by sending current pulse generates a circular magnetic field. The circular magnetic field at a distance r from the axis is given by,

$$H_c(r) = \frac{Ir}{2\pi R^2} \tag{4.3}$$

where, I is the annealing current and R is the radius of the microwire. This field induces circular magnetization of the domains in OS and therefore a transverse anisotropy is developed within the microwire. This increases the OS volume and hence the GMI value of the annealed sample (Fig. 4.13 to Fig. 4.16). In figures 4.14, 4.15 and 4.15, two peak GMI characteristic is observed for the annealed sample because on annealing in

presence of a circular field, there is an increase in the anisotropy field of the OS along the axis of the sample. This anisotropy field shifts the peak value of circumferential permeability of OS towards higher magnetic field as a result of which the MI peaks are observed at higher dc magnetic field. This is the reason for double-peak GMI of annealed sample at higher frequencies. Frequency dependent $[\Delta Z/Z(\%)]_{peak}$ (Fig. 4.17) shows an increase in GMI value with frequencies ($< \sim 5$ MHz) as the penetration depth reduces with f. For higher frequencies ($> \sim 5$ MHz) there is a decrease in GMI peak value with frequency. For sufficiently high frequency of the exciting alternating current, damping in domain-wall motion is observed due to micro-eddy current, thereby reducing the effective circular permeability so that the peak value of GMI decreases with f. The magnetization measurements indicate two kinds of domain structure within the sample, a single domain axial inner core and a multidomain outer shell. Heat treatment of the microwire with current pulses increases the outer shell volume. Since the contribution to MI from inner core is much less than that from outer shell, enhancement of GMI value by short duration annealing is due to increase in outer shell volume. Therefore short-duration heat-treatment by sending current pulses can be a useful tool to enhance the MI of wire-shaped amorphous magnetic materials.

4.3 Giant magnetoimpedance in glass coated amorphous $(Co_{0.93}Fe_{0.07})_{63}Ni_{10}Si_{11}B_{16}$ microwire

4.3.1 Experimental Details

Glass coated amorphous microwires with composition $(Co_{0.93}Fe_{0.07})_{63}Ni_{10}Si_{11}B_{16}$ of length 12cm were used in the measurement of impedance in presence of an external dc magnetic field. Fig. 4.28 shows the Scanning Electron Microscopy (SEM) image of the glass coated amorphous $(Co_{0.93}Fe_{0.07})_{63}Ni_{10}Si_{11}B_{16}$ microwire. The diameter of the metallic part of the microwire is about 14 μm (diameter including the insulating glass coating is $\sim 19\mu$m). The impedance of the sample was measured by Precision Impedance Analyzer (Agilent, 4294A, 40 Hz - 110 MHz). The frequency of the ac current was varied from 0.6 MHz to 11 MHz with its magnitude fixed at 1 mA. A Helmholtz coil system was used to apply a dc magnetic field (maximum value ~ 120 Oe) along the axis of the sample during impedance

measurement. The axis of the sample as well as that of the Helmholtz coil were kept perpendicular to the direction of the earth's magnetic field.

Here we have studied both the stress dependendence and effect of heat treatment (by sending a dc current of amplitude 50 mA for various time duration through the microwire) on GMI at various frequencies. Axial tensile stresses, σ, up to 603 MPa were applied to the wire for studying the effect of stress on magnetoimpedance. For studying the effect of heat treatment in presence of a circular magnetic field, a dc current with amplitude I_{an} = 50 mA has been passed through the samples for various time duration, T_{an}, starting from 5 minutes to 35 minutes. The percentage change of MI with applied magnetic field is calculated by using Eq.(1.7) and the maximum applied magnetic field is 120 Oe.

4.3.2   Results and Discussions

Frequency dependence of giant magnetoimpedance (GMI) in absence and in the presence of stresses 79 MPa, 210 MPa, 431 MPa, and 603 MPa was studied for glass coated amorphous $(Co_{0.93}Fe_{0.07})_{63}Ni_{10}Si_{11}B_{16}$ microwire with frequencies upto 11 MHz. Fig. 4.29 shows the field dependence of percentage change of magnetoimpedance of glass coated amorphous $(Co_{0.93}Fe_{0.07})_{63}Ni_{10}Si_{11}B_{16}$ microwire at a frequency of 2.08 MHz in absence and in the presence of stresses 79 MPa, 210 MPa, 431 MPa, and 603 MPa. The maximum of GMI value is observed at $H = 0$ Oe, thereby showing single-peak MI profile for the microwire in absence as well as in presence of axial tensile stresses. The value of $[\Delta Z/Z(\%)]_{peak}$ decreases from 3.95% at $\sigma = 0$ MPa to 1.62% at $\sigma = 603$ MPa. The value of $\Delta Z/Z(\%)$ decreass with increase of applied dc magnetic field. For a higher frequency, f = 5.05 MHz, single-peak GMI characteristic is observed for the sample in absence as well as in presence of external tensile stresses (Fig. 4.30). The maximum value of $\Delta Z/Z(\%)$ decreases from 8.85% at $\sigma = 0$ MPa to 3.92% at $\sigma = 603$ MPa. Figures Fig. 4.31 and Fig. 4.32 show the variation of percentage change of magnetoimpedance, $[\Delta Z/Z(\%)]_{peak}$ with dc magnetic field H of the microwire at frequencies 8.02 MHz and 11 MHz respectively in absence and in the presence of stresses 79 MPa, 210 MPa, 431 MPa, and 603 MPa.
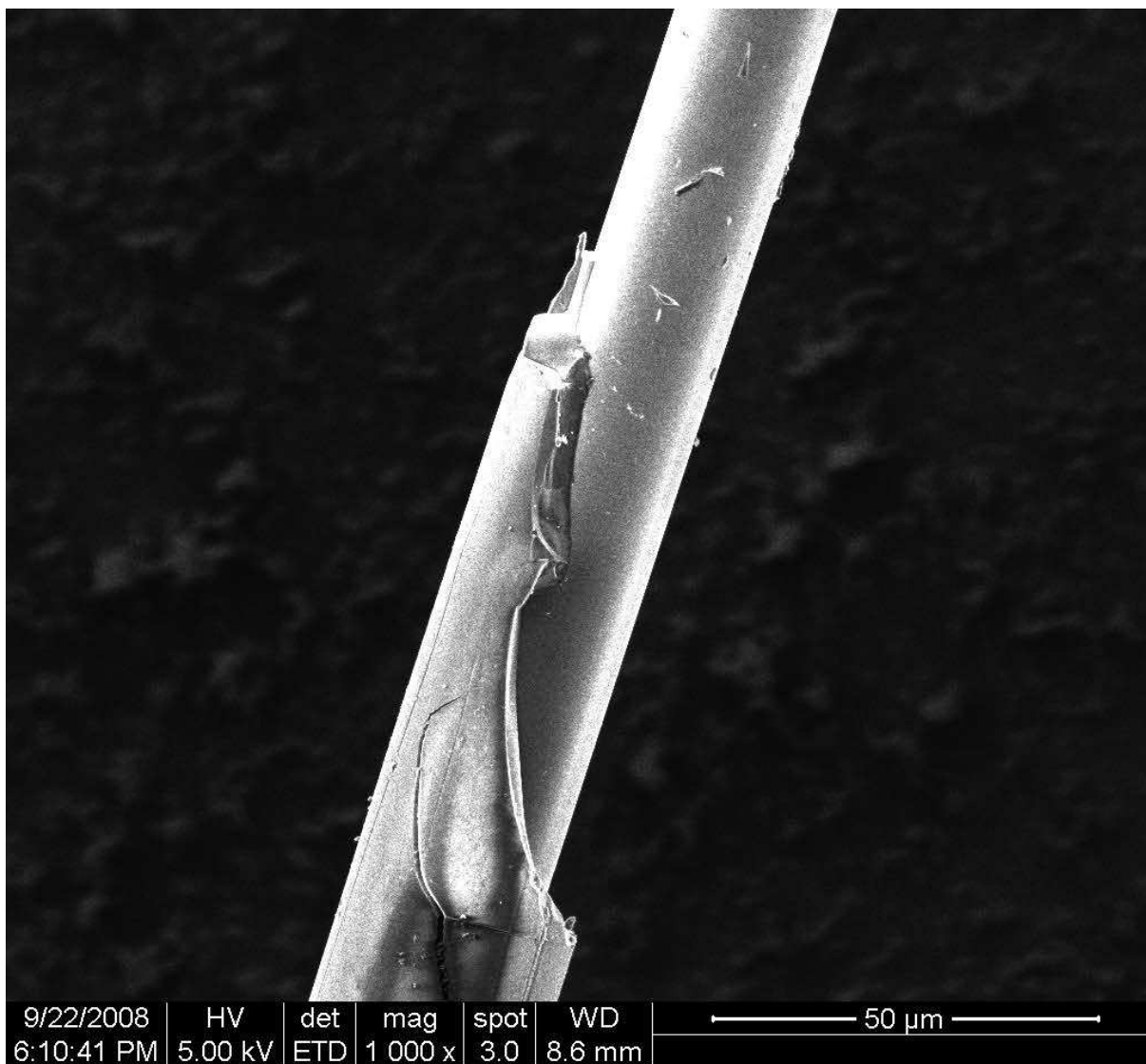
Figure 4.28: Scanning Electron Microscopy (SEM) image of glass coated amorphous $(Co_{0.93}Fe_{0.07})_{63}Ni_{10}Si_{11}B_{16}$ microwire.

Figure 4.29: The variation of percentage change of magnetoimpedance, $\Delta Z/Z(\%)$ with dc magnetic field H of glass coated amorphous $(Co_{0.93}Fe_{0.07})_{63}Ni_{10}Si_{11}B_{16}$ microwire at a frequency of 2.08 MHz in absence and in the presence of stresses 79 MPa, 210 MPa, 431 MPa, and 603 MPa.

Figure 4.30: The variation of percentage change of magnetoimpedance, $\Delta Z/Z(\%)$ with dc magnetic field H of glass coated amorphous $(Co_{0.93}Fe_{0.07})_{63}Ni_{10}Si_{11}B_{16}$ microwire at a frequency of 5.05 MHz in absence and in the presence of stresses 79 MPa, 210 MPa, 431 MPa, and 603 MPa.
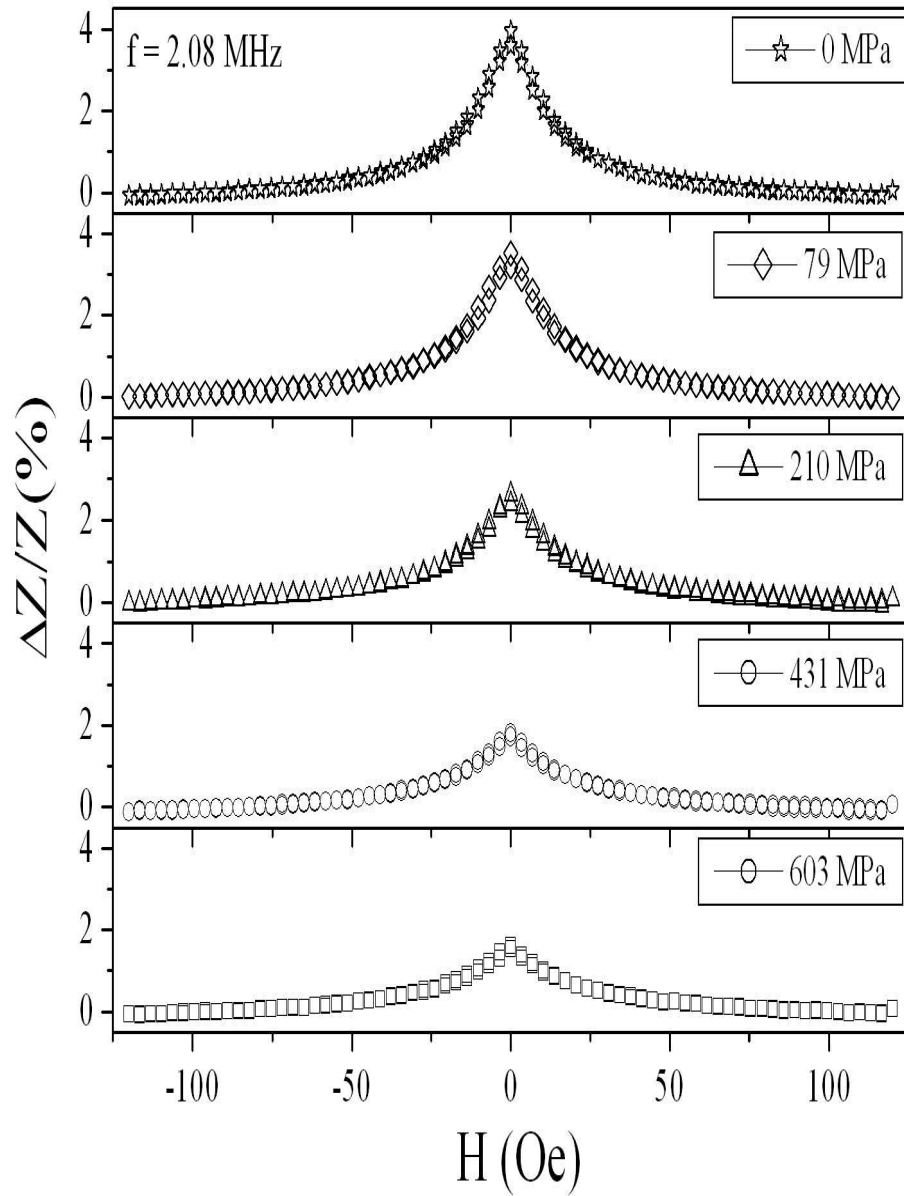
Figure 4.31: The variation of percentage change of magnetoimpedance, $\Delta Z/Z(\%)$ with dc magnetic field H of glass coated amorphous $(Co_{0.93}Fe_{0.07})_{63}Ni_{10}Si_{11}B_{16}$ microwire at a frequency of 8.02 MHz in absence and in the presence of stresses 79 MPa, 210 MPa, 431 MPa, and 603 MPa.
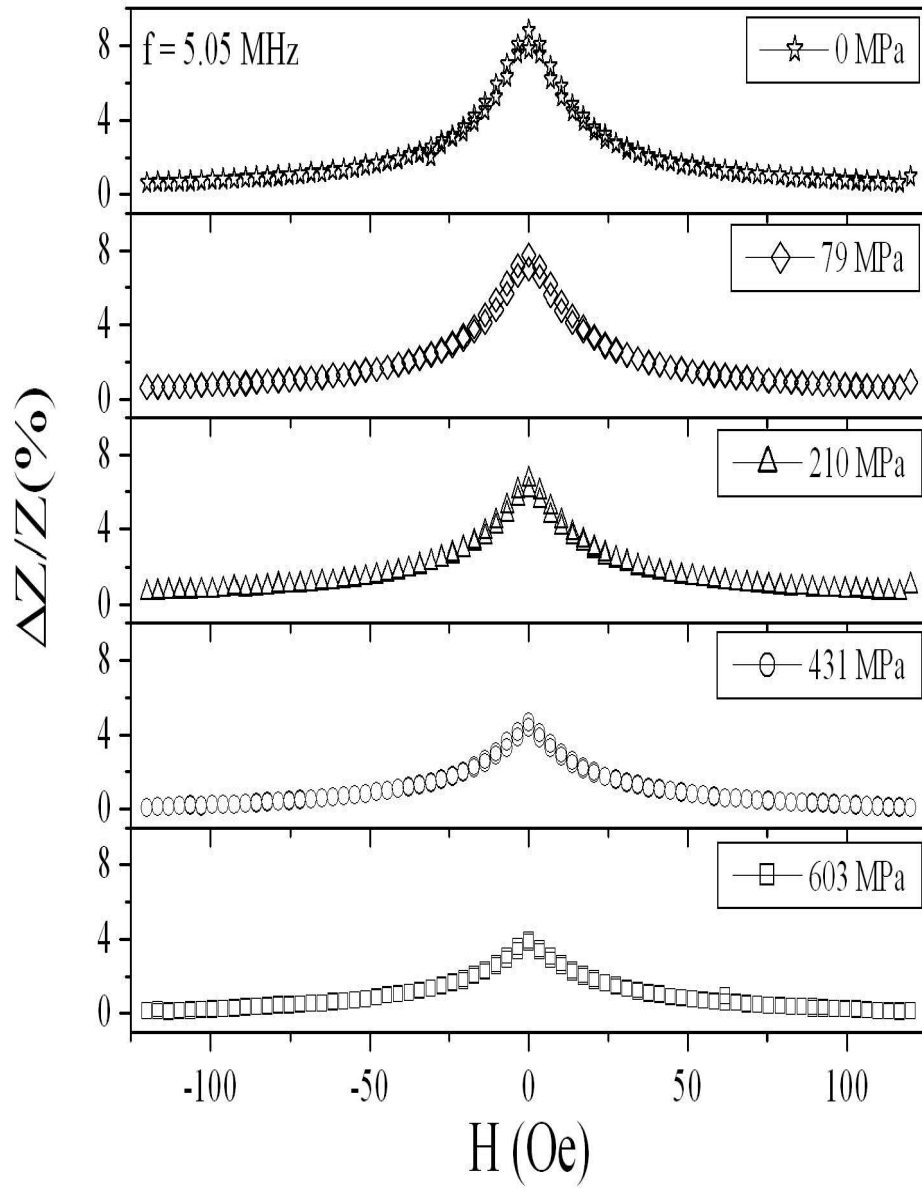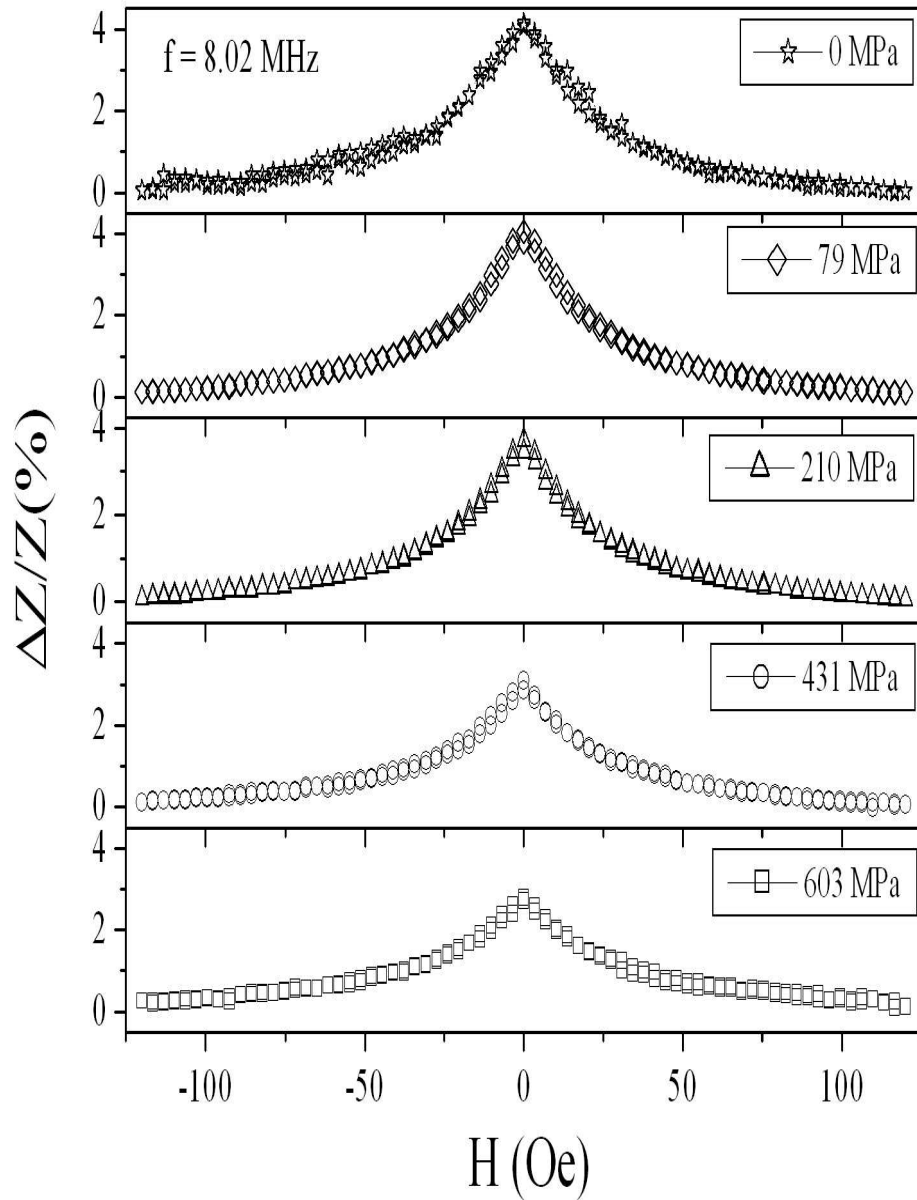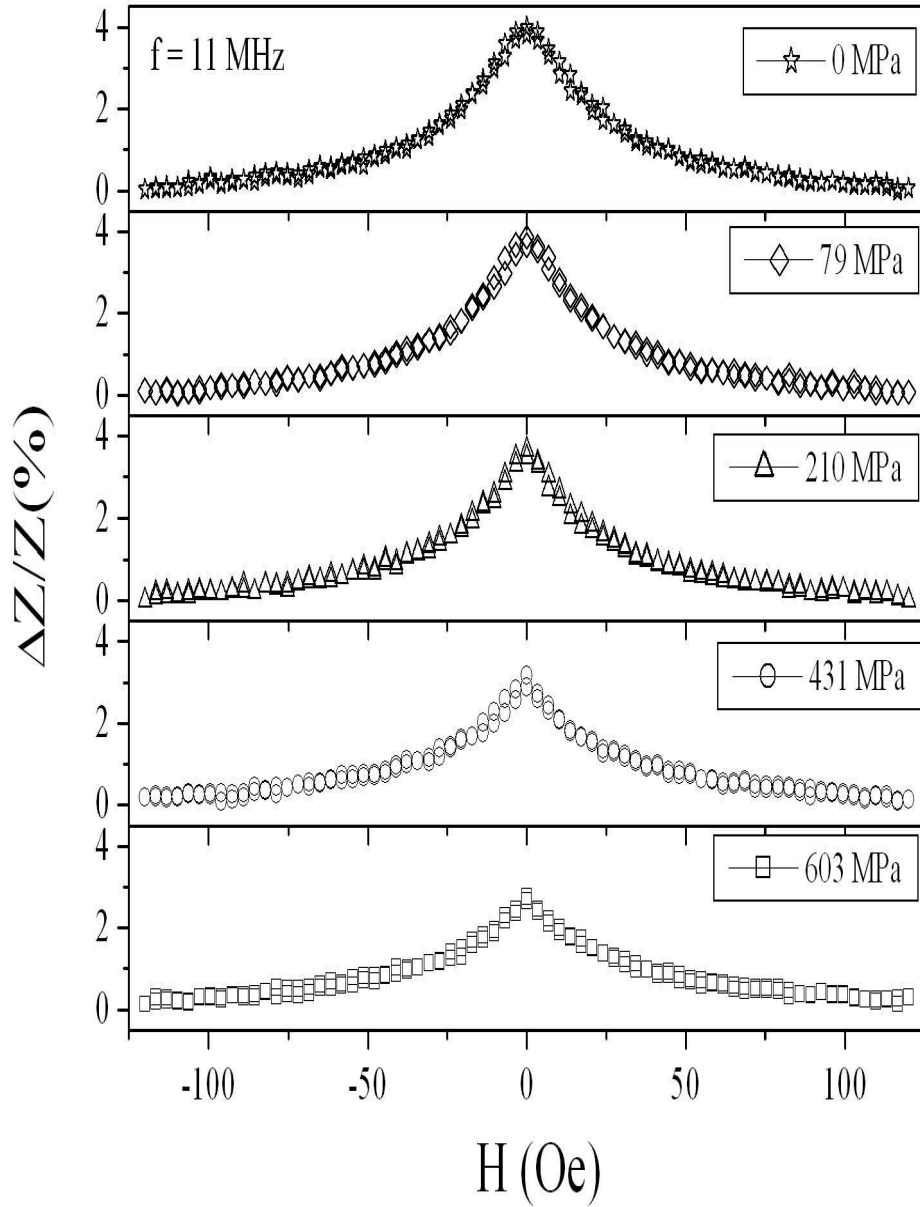
Figure 4.32: The variation of percentage change of magnetoimpedance, $\Delta Z/Z(\%)$ with dc magnetic field H of glass coated amorphous $(Co_{0.93}Fe_{0.07})_{63}Ni_{10}Si_{11}B_{16}$ microwire at a frequency of 11 MHz in absence and in the presence of stresses 79 MPa, 210 MPa, 431 MPa, and 603 MPa.

Here also we observe single-peak GMI nature for the sample at various values of stress for both the frequencies. The peak value of $\Delta Z/Z(\%)$ decreases from 4.07% at $\sigma = 0$ MPa to 2.8% at $\sigma = 603$ MPa at $f = 8.02$ MHz whereas the reduction in $[\Delta Z/Z(\%)]_{peak}$ value is from 4.0% to 2.7% on application of stress, $\sigma = 603$ MPa at $f = 11$ MHz. The variation of maximum values of percentage change in magnetoimpedance ($[\Delta Z/Z(\%)]_{peak}$) with frequency in presence of different axial tensile stresses is shown in Fig. 4.33. The peak value

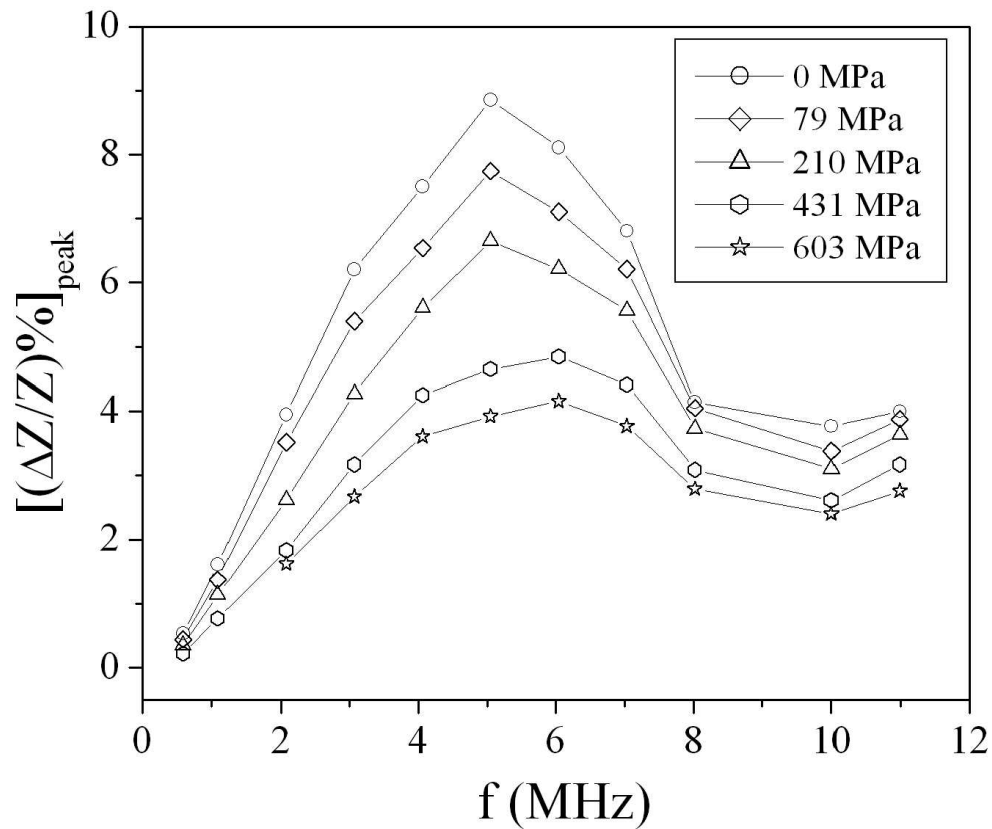Figure 4.33: The variation of maximum percentage change of magnetoimpedance, $[\Delta Z/Z(\%)]_{peak}$ with frequency under different axial tensile stresses of glass coated amorphous $(Co_{0.93}Fe_{0.07})_{63}Ni_{10}Si_{11}B_{16}$

of GMI decreases with increasing axial stress values. Maximum value of $[\Delta Z/Z(\%)]_{peak}$ = 8.85% is observed at a frequency of 5.05 MHz for the sample in absence of any stress.

The maximum value of $[\Delta Z/Z(\%)]_{peak}$ reduces to 4.16% for $\sigma = 603$ MPa at $f = 6.04$ MHz.

The variation of magnetoimpedance of the as-quenched and heat treated (annealing done by passing dc current with amplitude $I_{an} = 50$ mA for various time duration, $T_{an} = 5$ minutes, 15 minutes, 25 minutes and 35 minutes respectively) microwires as a function of dc magnetic field is shown in Fig. 4.34 for a frequency, $f = 2.08$ MHz.

Single peak GMI behaviour with maximum value $[\Delta Z/Z(\%)]_{peak}$ at $H_{dc} \sim 0$ Oe is observed for both the as-quenched and current annealed microwires. The value of $[\Delta Z/Z(\%)]_{peak}$ increases from 3.96% for the as-quenched sample to 10.94% when the microwire is current annealed with $I_{an} = 50$ mA for $T_{an} = 15$ minutes at $f = 2.08$ MHz. At a higher frequency, $f = 5.05$ MHz, the microwire shows single-peak GMI nature for both the as quenched and current annealed conditions (Fig. 4.35). Here the peak value of GMI increases from 8.84% (as-quenched sample) to 18.74% (current annealed microwire with $I_{an} = 50$ mA for $T_{an} = 25$ minutes). Figures Fig. 4.36 and Fig. 4.37 show the variation of percentage change of magnetoimpedance, $[\Delta Z/Z(\%)]_{peak}$ with dc magnetic field H of the as-quenched and current annealed microwire at frequencies 8.02 MHz and 11 MHz respectively. Single-peak GMI characteristics are observed for the as-quenched and current annealed microwires at frequencies 8.02 MHz and 11 MHz. The peak value of $\Delta Z/Z(\%)$ increases from 4.14% (as-quenched sample) to 6.09% ($I_{an} = 50$ mA for $T_{an} = 15$ minutes) at $f = 8.02$ MHz, whereas the increase in $[\Delta Z/Z(\%)]_{peak}$ value is from 3.98% to 5.77% ($I_{an} = 50$ mA for $T_{an} = 15$ minutes) at $f = 11$ MHz. The frequency dependence of $[\Delta Z/Z(\%)]_{peak}$ of the annealed microwires (annealing done with $I_{an} = 50$ mA for various durations) is shown in Fig. 4.38. The GMI value increases upto an annealing current of $I_{an} = 50$ mA for $T_{an} = 25$ minutes. The maximum value of $[\Delta Z/Z(\%)]_{peak} \sim 18.74\%$ is obtained at a frequency of 5.05 MHz when the sample is annealed for 25 minutes. The GMI value deteriorates on further annealing, and $[\Delta Z/Z(\%)]_{peak}$ decreases to $\sim 13.27\%$ at 5.05 MHz when current annealed for 35 minutes. The field sensitivity of GMI is 93%/Oe around an applied magnetic field of 5 Oe at $f = 5.05$ MHz when the sample is annealed for 25 minutes.

Figure 4.34: The variation of percentage change of magnetoimpedance, $\Delta Z/Z(\%)$ with dc magnetic field H of as-quenched and heat treated glass coated amorphous $(Co_{0.93}Fe_{0.07})_{63}Ni_{10}Si_{11}B_{16}$ microwire at a frequency of 2.08 MHz.
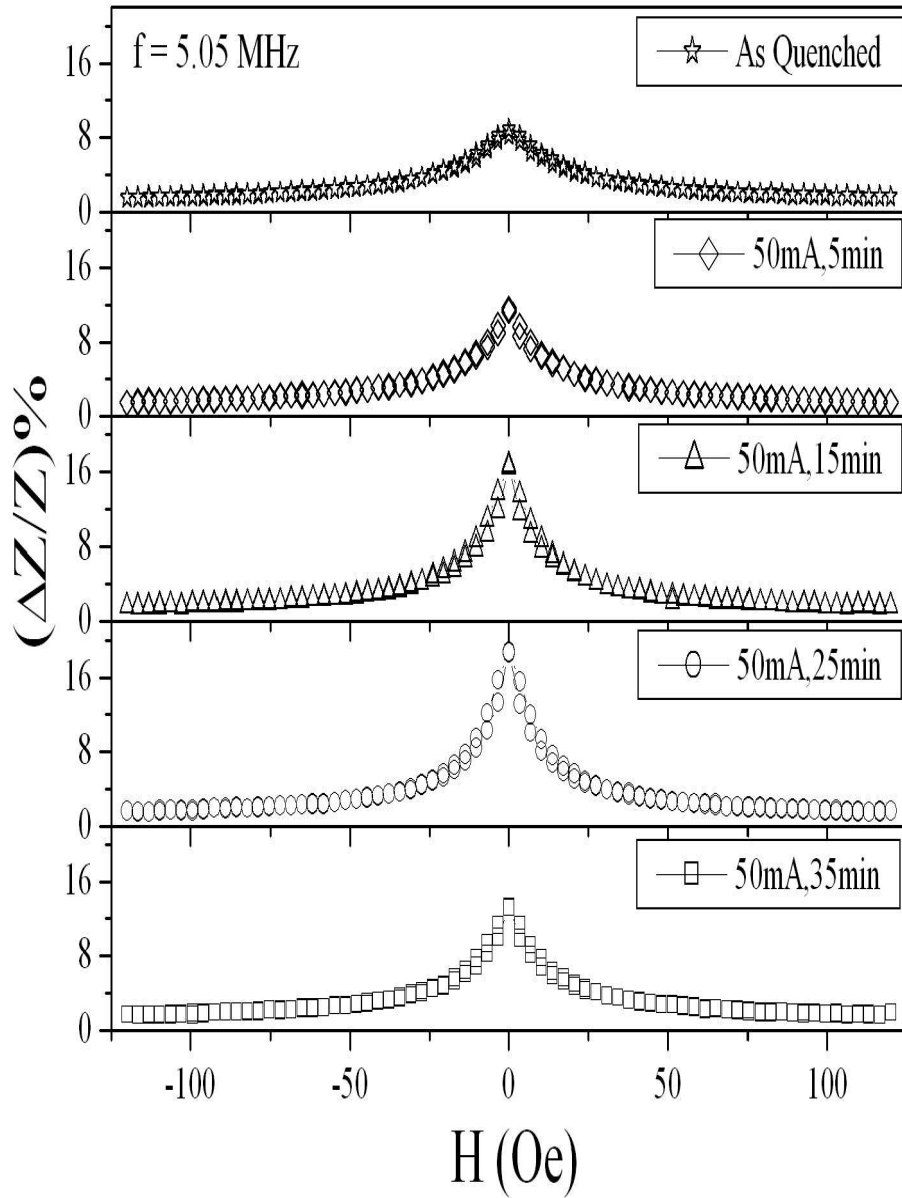
Figure 4.35: The variation of percentage change of magnetoimpedance, $\Delta Z/Z(\%)$ with dc magnetic field H of as-quenched and heat treated glass coated amorphous $(Co_{0.93}Fe_{0.07})_{63}Ni_{10}Si_{11}B_{16}$ microwire at a frequency of 5.05 MHz.
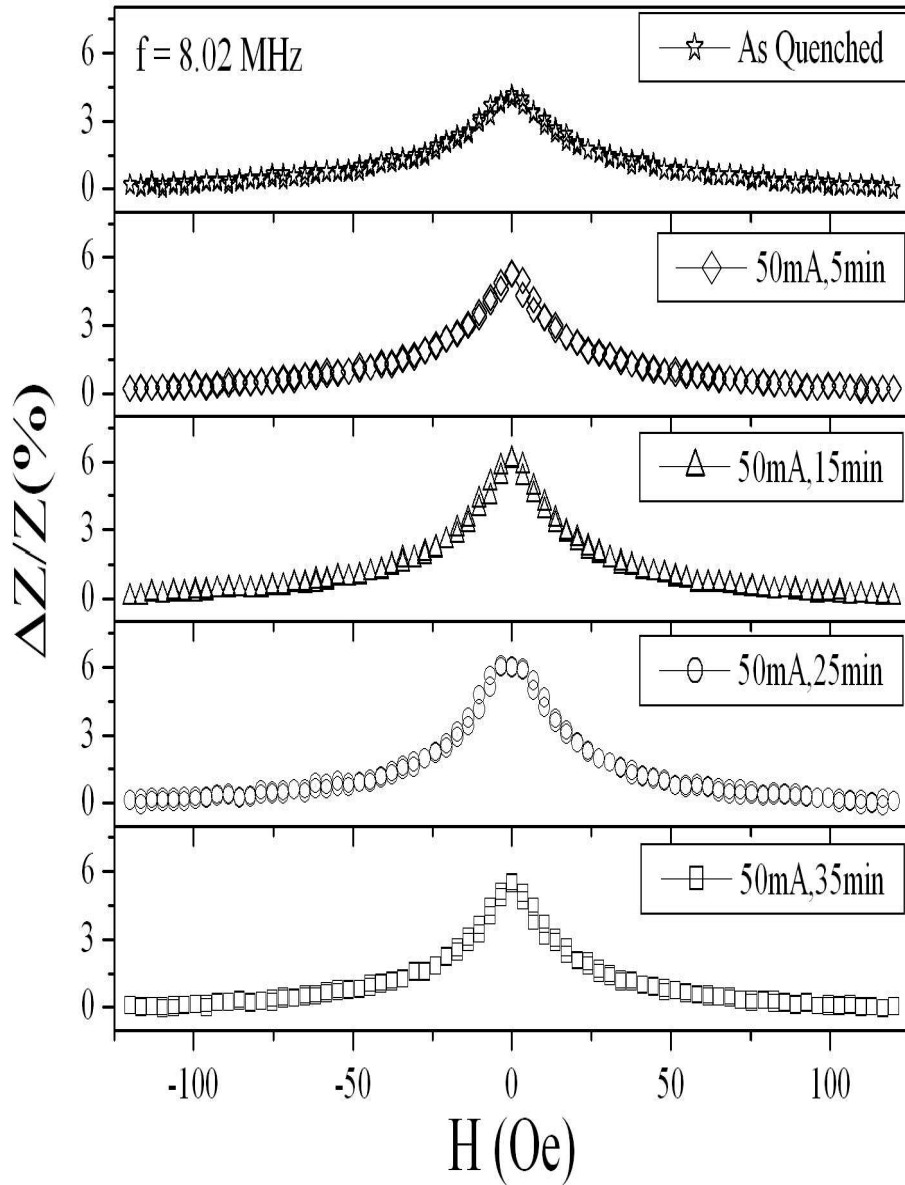
Figure 4.36: The variation of percentage change of magnetoimpedance, $\Delta Z/Z(\%)$ with dc magnetic field H of as-quenched and current annealed glass coated amorphous $(Co_{0.93}Fe_{0.07})_{63}Ni_{10}Si_{11}B_{16}$ microwire at a frequency of 8.02 MHz.
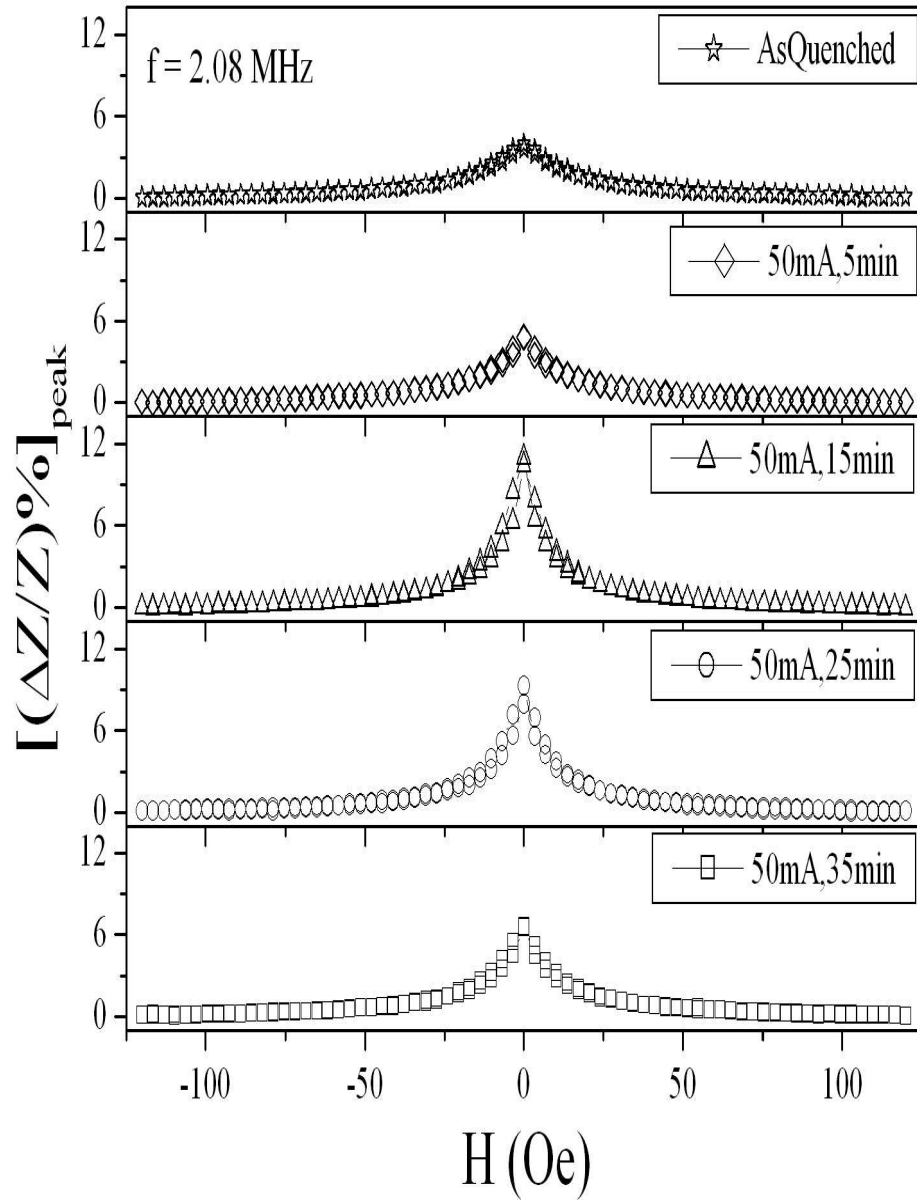
Figure 4.37: The variation of percentage change of magnetoimpedance, $\Delta Z/Z(\%)$ with dc magnetic field H of as-quenched and current annealed glass coated amorphous $(Co_{0.93}Fe_{0.07})_{63}Ni_{10}Si_{11}B_{16}$ microwire at a frequency of 11 MHz.

Figure 4.38: The variation of maximum percentage change of magnetoimpedance, $[\Delta Z/Z(\%)]_{peak}$ with frequency of the as quenched and current annealed glass coated amorphous $(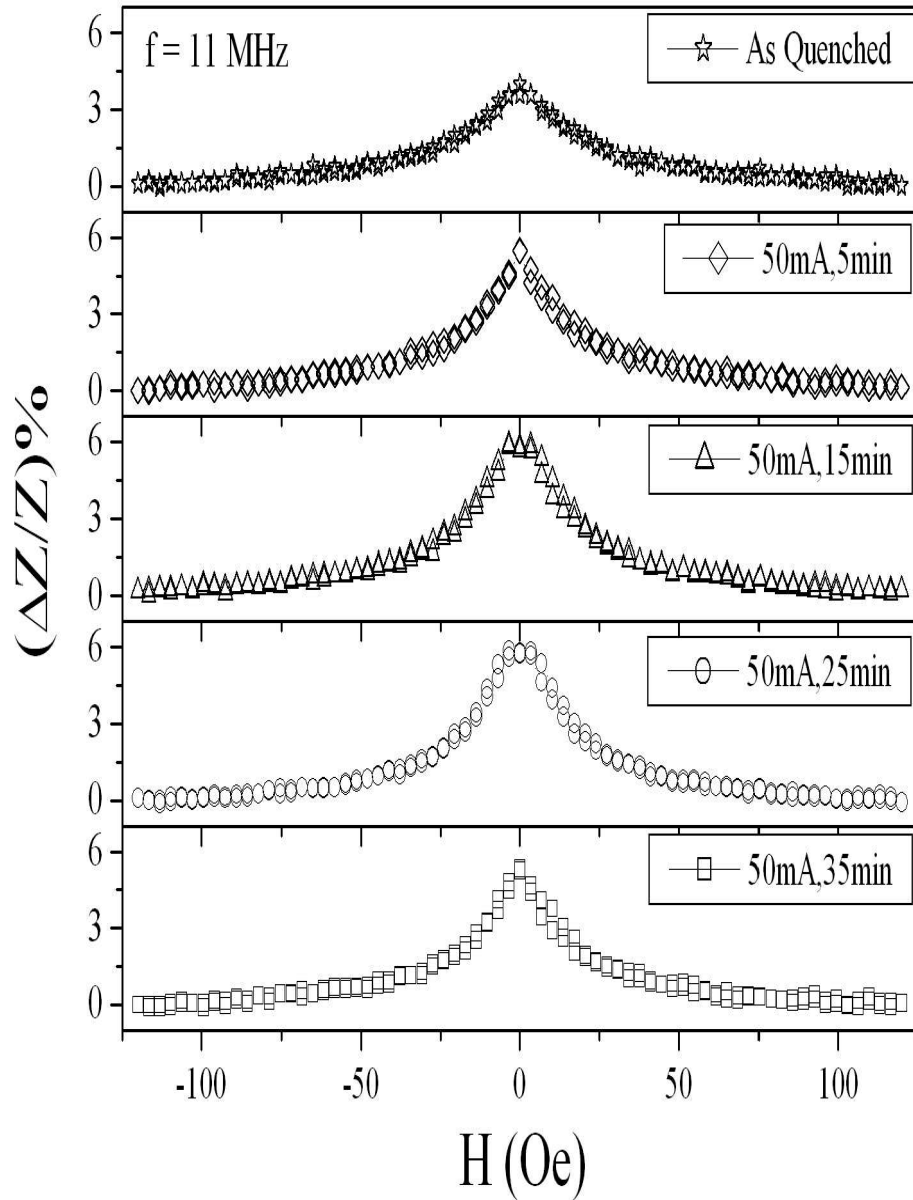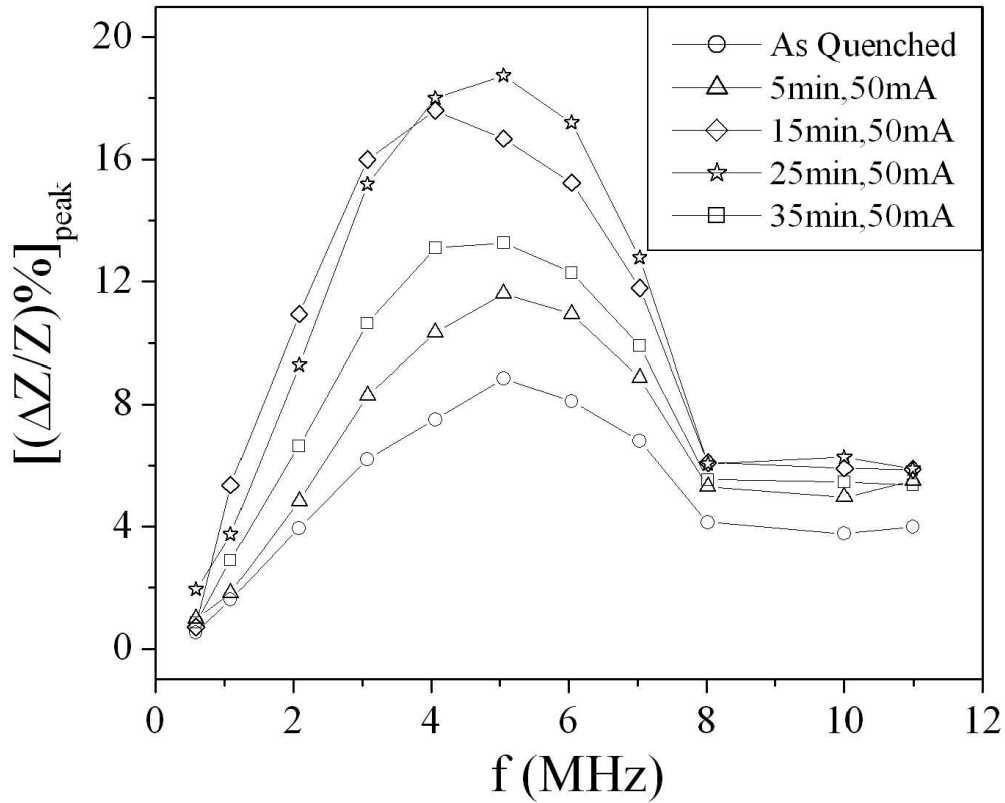Co_{0.93}Fe_{0.07})_{63}Ni_{10}Si_{11}B_{16}$ microwires (annealed with a direct current, I_{an} = 50 mA for different time durations).

The large change in MI for this low magnetostrictive amorphous microwire can be explained using Maxwell's equations of electrodynamics considering the change in skin depth, δ due to a change in transverse permeability, μ_ϕ by an externally applied dc magnetic field. The applied dc magnetic field nearly compensates the axial magnetic anisotropy when it reaches the switching field of the microwire. For this sample, the intrinsic or induced anisotropy is very small, hence most domains are large with static domain magnetizations along the wire axis at $H_{dc} = 0$ Oe, owing to shape anisotropy. In this case, circumferential permeability, μ_ϕ is large at the switching field which is very low for this sample. This results in the maximum value of GMI to be observed close to $H_{dc} = 0$ Oe. Increasing the applied magnetic field, the circumferential permeability decreases owing to the unidirectional magnetostatic anisotropy. This increases the penetration depth, δ resulting in a decrease in MI.

Neglecting other anisotropies for simplicity, domain magnetizations, M_s should be directed along the resultant of the axial field, H and the circular field, H_{cir}. For small angle rotation of domain magnetizations, M_s from the axis, we can write $M_{cir}/M_s \approx H_{cir}/H$ or $\mu_\phi/\mu_0 \approx M_{cir}/H_{cir} \approx M_s/H$. Thus $|Z|$ decreases with increasing $|H|$ as $|H|^{-1/2}$ as $Z \propto \mu_\phi^{1/2}$ at high frequency, showing a typical single-peak MI. This theoretical prediction is verified by fitting an expression,

$$|Z| = a + b|H|^{-1/2} \tag{4.4}$$

where, a and b are two constants. The fitted curve to experimental data taken at a frequency of 5.05 MHz in absence of any stress is shown in Fig. 4.39 with $a = 48.42$ and $b = 9.49$. At frequencies below 2 MHz the value of $\delta \sim 12 \ \mu m$ which is more than the radius of the microwire ($r < \delta$) and the peak value of GMI, $[\Delta Z/Z(\%)]_{peak}$, is not very large, as it mainly arises from the induced magnetoinductive voltage. At higher frequencies (f > 2 MHz) $r \gg \delta$ and higher values of GMI are obtained as a consequence of skin effect. With further increase in frequency, i.e. beyond $f = 5.05$ MHz, $[\Delta Z/Z(\%)]_{peak}$ decreases. In this frequency region, domain wall motion is strongly damped owing to eddy currents, and contributes less to the circumferential permeability resulting in small MI effect. The application of an external tensile stress generates a uniaxial anisotropy along the axis of the wire, i.e. along the axial magnetic field. This increases the volume of the IC domain since the microwire is positive magnetostrictive in nature. This results in

a decrease in the circumferential permeability and hence the value of GMI reduces with increase in stress. When the sample is annealed by passing dc current along its length,
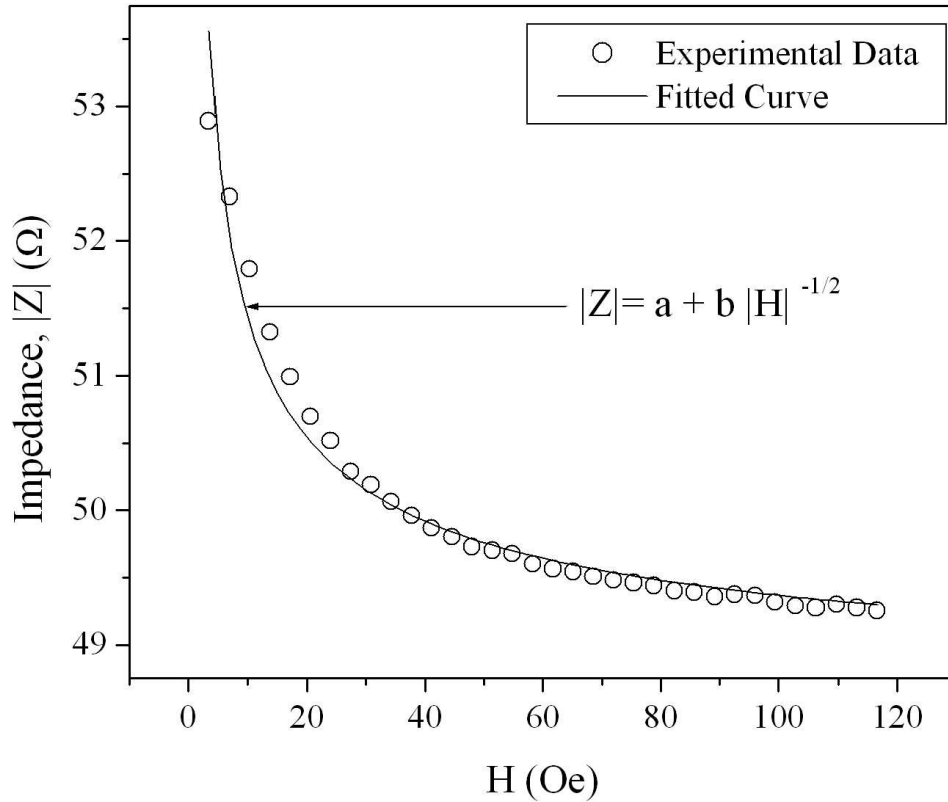
Figure 4.39: The fitting of $|Z| = a + b|H|^{-1/2}$ with $a = 48.42$ and $b = 9.49$ to the impedance, $|Z|$ versus magnetic field to experimental data taken at a frequency of 5.05 MHz in absence of any stress.

the annealing current generates a circular magnetic field during heating. As a result of it a circumferential anisotropy is developed within the sample resulting a decrease in IC and increase in OS volume resulting an increase in GMI value. The peak value of GMI, $[\Delta Z/Z(\%)]_{peak}$ increases on increasing T_{an} till 25 minutes. Annealing further for longer periods, peak value of GMI decreases due to the formation of crystallinity of the sample. Axial dc hysteresis loops of the as-quenched as well as the stressed and current annealed

samples have been studied for a better explanation of the GMI results. Fig. 4.40 shows the dc magnetic hysteresis loops of the glass coated amorphous $(Co_{0.93}Fe_{0.07})_{63}Ni_{10}Si_{11}B_{16}$ microwire in absence of any stress, in presence of a stress of 209 MPa and annealed with $I_{an} = 50$ mA for $T_{an} = 25$ minutes. The as-quenched sample shows a square-shaped hys-
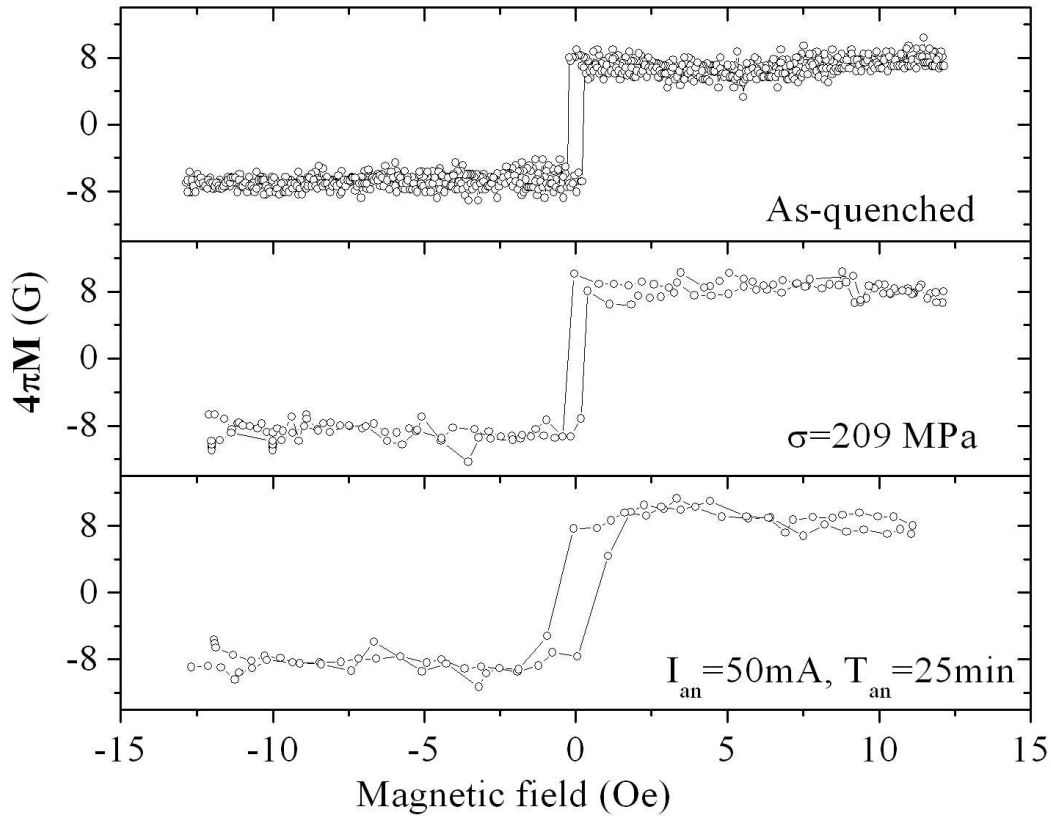
Figure 4.40: The dc magnetic hysteresis loops of the glass coated amorphous $(Co_{0.93}Fe_{0.07})_{63}Ni_{10}Si_{11}B_{16}$ microwire in absence of any stress, in presence of a stress of 209 MPa and annealed with $I_{an} = 50$ mA for $T_{an} = 25$ minutes

teresis loop with coercivity, $H_c \sim 0.25$ Oe which decreases slightly to 0.23 Oe with σ 209 MPa. The change in magnetization at coercivity and remanence also increase with stress due to the increase in volume of the IC. The coercivity of the microwire annealed with I_{an} = 50 mA for $T_{an} = 25$ minutes is higher than that of the as-quenched sample indicating

an increase in OS as a circumferential induced anisotropy is generated due to current annealing. Only a square-shaped hysteresis loop indicates that the glass coated amorphous $(Co_{0.93}Fe_{0.07})_{63}Ni_{10}Si_{11}B_{16}$ microwire mainly consists of the inner core domain.

4.4 Conclusions

Very low positive magnetostrictive glass-coated amorphous microwires with nominal composition $Co_{83.2}Mn_{7.6}Si_{5.8}B_{3.3}$ are found to show GMI effect in the range of 1-8 MHz frequency. Single-peak GMI characteristics is observed when the frequency of the ac current is below 6 MHz, beyond which double-peak behaviour is seen. GMI of this microwire is also very stress sensitive and it decreases from 53 % to 26 % due to the application of an axial tensile stress of 566 MPa. Two peaks of GMI observed at high frequency reduces to a single-peak on application of high stress. The GMI value does not change with current amplitude within the 0.2 - 5.0 mA range. On the other hand, GMI in this microwire was increased to 129 % on short-duration heat treatment by passing four current pulses of amplitude of 100 mA and each of 12 seconds duration. This increase in GMI value on short-duration annealing is due to the increase in outer shell volume of the domain structure and also inducing a transverse anisotropy.

Asymmetry in the MI peaks of the microwire was developed by passing a dc current through the sample during impedance measurement. The magnetization measurements indicated two kinds of domain structure within the sample, a single domain axial core and a multidomain outer shell with transverse magnetization. The outer shell increases on short duration heat treatment whereas the inner core domain increases when an axial tensile stress is applied.

Glass-coated amorphous microwires of nominal composition $(Co_{0.93}Fe_{0.07})_{63}Ni_{10}Si_{11}B_{16}$ showed GMI effect with a maximum change of 8.85% around a frequency of 5.05 MHz. This sample showed the GMI peaks at very low values of the applied dc field throughout the whole range of frequency studied in this experiment. On application of an axial tensile stress the GMI value reduces due to the increase in inner core domain and the development of an axial anisotropy. The decrease in impedance is found to be proportional to the

square root of the increasing applied dc magnetic field. The GMI value increases on heat treatment of the sample by passing a dc current of 50 mA through it. A maximum change of 18.74% in MI is observed on annealing the sample for 25 minutes. Almost single-peak GMI characteristics can be explained considering a square-shaped hysteresis loop of the sample.

Chapter 5

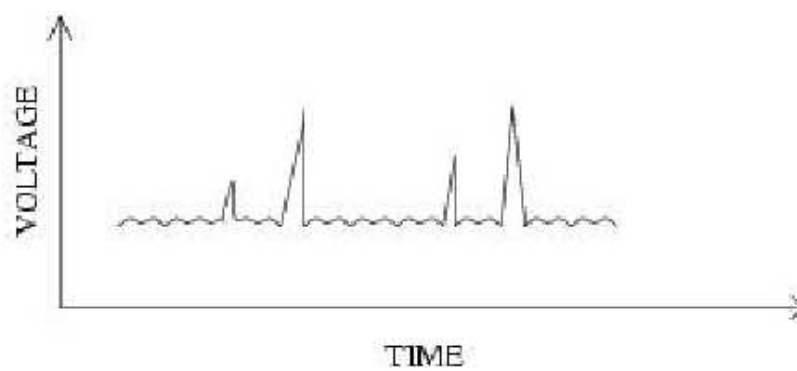# MAGNETIC BARKHAUSEN NOISE IN MAGNETIC MATERIALS

5.1   Introduction

The application of an alternating magnetic field to a ferromagnetic material induces small discontinuous changes in the magnetization of the material. These sudden localized changes in magnetization are produced by the abrupt motion of domain walls from one pinning site to the next. The corresponding voltages induced in a pick-up coil on the sample are referred to as Magnetic Barkhausen noise (MBN) [77], [78]. This effect known as Barkhausen effect was discovered by Heinrich Barkhausen in 1919 [79] and can be demonstrated with the apparatus as shown in Fig.5.1(a). A pick-up coil wound on a ferromagnetic specimen is connected through an amplifier to a an external speaker. The ferromagnetic sample is then subjected to a smoothly increasing magnetic field by an approaching hand-held magnet. Though the field is increased smoothly and continuously yet a crackling noise is heard from the speaker. Fig.5.1(b) shows the irregular spikes on the voltage time curve, which can be observed if the pick-up coil is connected to an oscilloscope.

This crackling sound (or the irregular spikes on voltage-time curve) was the result of sudden step-like discontinuous changes in magnetization of the specimen as shown in Fig.5.2. These irreversible changes occur in the steep part of the magnetization curve accounting for magnetic hysteresis in ferromagnetic materials [133]. Magnetic Barkhausen noise (MBN) is named after its discoverer, Heinrich Barkhausen. It is termed as "noise" because of the sound heard in the loudspeaker in the original experiment. The term "magnetic" is
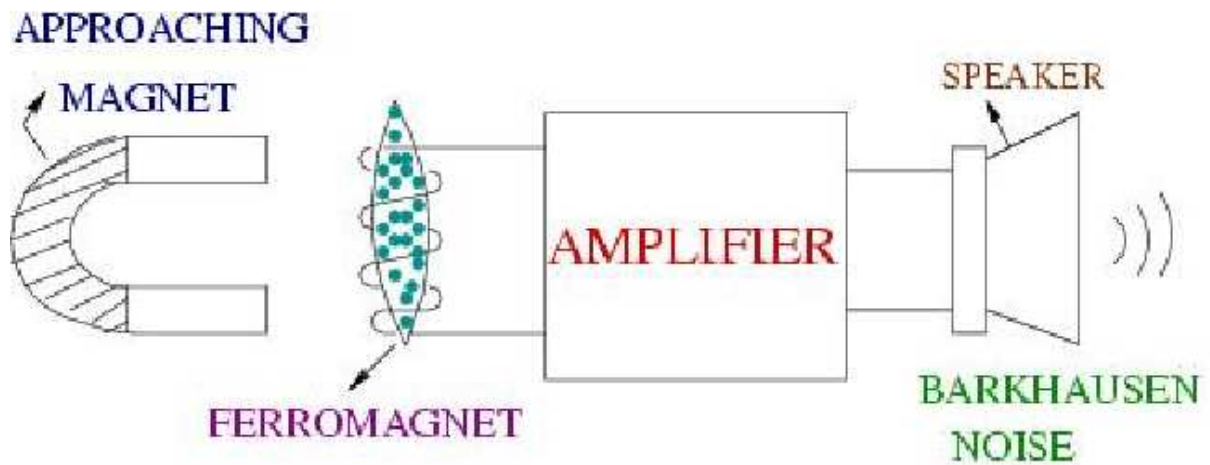
Figure 5.1: (a) Apparatus demonstrating Barkhausen effect (b) Barkhausen noise on voltage-time curve.
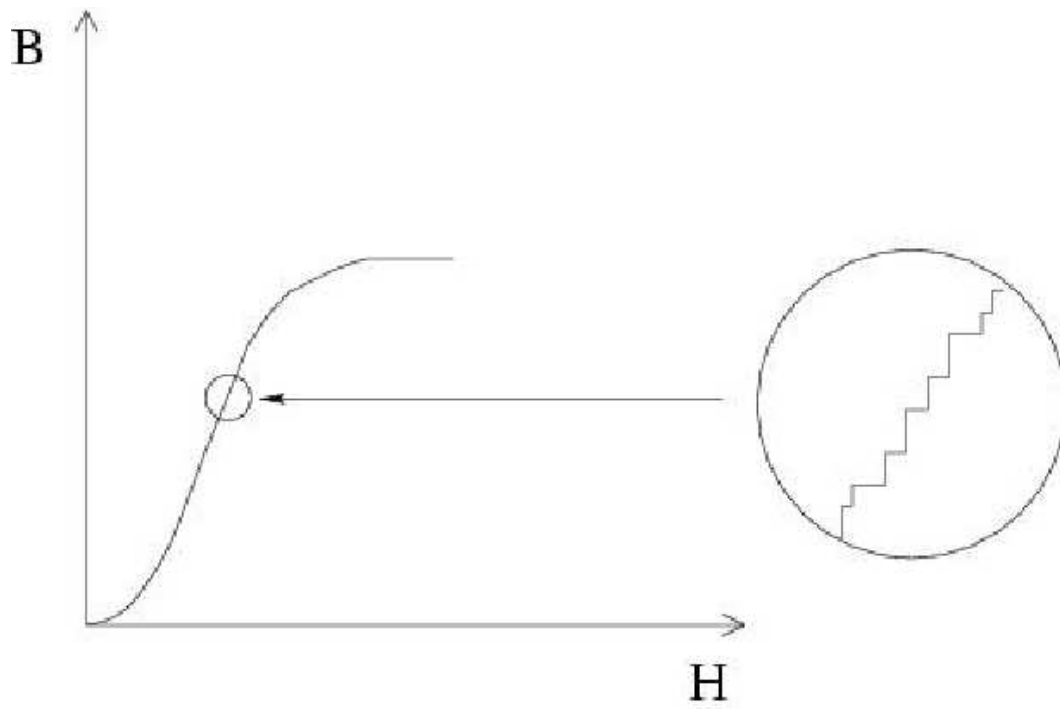
Figure 5.2: Sudden step-like discontinuous changes in magnetization.

used to distinguish it from acoustic barkhausen noise, which is based on magnetoacoustic emission [134], [135]. Magnetoacoustic emission (MAE) refers to the generation of elastic waves in ferromagnetic materials being magnetized in an alternating magnetic field [136]. Since its discovery in 1919, this effect has been investigated extensively by many researchers due to scientific and technological interest in the study of various ferromagnetic domain structure and magnetization processes [137]-[142]. Like other magnetic properties, the Barkhausen effect also depends on various physical properties of the material including the state of mechanical stress and microstructural parameters such as grain size, composition, texture etc. [143]-[145]. MBN has been studied extensively as a tool for non-destructive evaluation (NDE) of residual and applied stresses [146]-[150] leading to commercial utilization of this technique for stress-related non-destructive applications. It is also a nondestructive technique to eddy current probe sensors [151]-[152] and magnetic flux leakage [153]. MBN is also used as a successful tool to estimate carbon content, pearlite colony and lamellar spacing etc. [145],[154]-[156].

Usually two types of Barkhausen noise experiments are performed for the detection of noise [157] - [161]. In the first case, the detection coil is placed on the surface of the specimen (Fig.2.12) and the corresponding pick-up signal are termed as surface Barkhausen noise. In the other case, a pick-up coil is wrapped around the sample which detects the encircling Barkhausen noise (Fig.2.10). Considering the skin depth, the estimated depth for penetration of the magnetizing field is roughly $1mm$, whereas the depth from which the MBN signal originates is $\sim 30\mu m$.

A ferromagnetic material consists of a large number of magnetic domains, with adjacent domains being separated by Bloch walls. When the material is not magnetized, these domains are randomly oriented, so that the bulk net magnetization is zero [78], [162], [163]. Application of an external magnetic field aligns the individual magnetic moments of the domains. The domains aligned close to the field direction grow at the expense of those that are less aligned. The ferromagnetic sample becomes magnetized as the walls move between adjacent domains. This movement occurs in sudden jumps as the domain walls break away from pinning sites such as dislocations, precipitates and grain boundaries [164], also resulting in a change of magnetisation of the material.

Domain walls separating regions of opposite magnetic moment are called 180° walls,

whereas walls lying at 90° to each other are termed as 90° walls. MBN is primarily due to the 180° wall motion. The 90° domain walls have stress fields associated with them, as their magnetizations lie at right angles on either side of the wall, causing lattice spacings to be slightly larger in the direction of magnetization. The resulting strain impedes with 90° domain wall motion, making them less competitive than 180° domain walls that have a higher velocity [80]. An applied stress, jut like an applied magnetic field, changes the bulk magnetization of the sample. This is due to the fact that the magnetic domains are influenced by stress and the resulting strain inside the material. The presence of elastic stresses in the material causes the domain walls to find the direction of easiest orientation to the applied magnetic field. A tensile stress increases the value of the MBN signal and a compressive stress decreases it [165],[166].

Magnetic Barkhausen noise are characterized by several different parameters. The parameter is not limited to any particular aspect of the Barkhausen signal, but is simply a generic parameter that is calculated from a complete cycle of the Barkhausen emission. Some of the parameters that are frequently used for MBN analysis will be discussed in this section. Usually, only voltages above and below a certain threshold are considered in order to maintain the integrity of the analysis.

(i) RMS (root mean square) voltage : The RMS value of one cycle of the Barkhausen emission is calculated.

(ii) MBN energy (E_{MBN}) : E_{MBN} is calculated by integrating the square of these voltages w.r.to time i.e.,

$$E_{MBN} = \sum_{i=1}^{n} \int V_i^2 dt \tag{5.1}$$

where the time integral is over each event and the summation is taken over all N measured events.

For angular dependent MBN measurements, MBN signals are taken at small intervals (such as, $\sim 10°$) covering the entire 360° circle of the angular scan. E_{MBN} is calculated for each angle and finally the resulting angular dependent E_{MBN} is plotted on a polar graph. In absence of any magnetic anisotropy, the polar plot of E_{MBN} is a circle. In presence of any magnetic anisotropy (such as application of stress) the circle gets elongated in the direction of the magnetic anisotropy which is also the direction of the applied stress.

(iii) Pulse height distribution : The number of voltage pulses is plotted in a graph as a

function of the absolute value of the amplitude of the MBN voltages.

MBN is considered as an evaluation technique of considerable importance for microstructural and mechanical characterization of steels [167] - [170]. Angular dependent MBN measurements are very sensitive to the stress, induced in the ferromagnetic samples. There are several reports of the development of an easy axis along the direction of tensile stress and away from the compressive stress direction in steel, using this angular dependent MBN technique [137], [158] [171] - [176]. MBN is also sensitive to various parameters which affect the domain configurations that, in turn, are strongly influenced by the grain size [177] - [180], composition, ferrite, pearlite and martensite phases [154], [182] - [184]. V. Moorthy et. al. have used the MBN technique to characterize the microstructures in quenched and tempered 0.2% carbon steeland $2.25Cr - 1Mo$ steel under different tempered conditions [180] - [181]. MBN is also studied extensively in various soft amorphous magnetic materials, thin films, Finemet type materials etc. [185] - [190].

MBN has also been studied as a complex statistical phenomenon which depends on various parameters such as the kind of ferromagnetic sample, character of quenched in defects and external field driving rate [191],[192]. For an understanding of the jerky emissions of the Barkhausen noise, a model of avalanche dynamics, known as ABBM model is well studied [193], [194]. These two papers, one comprising of the development of the theory and the other to the comparison with experiments, helps in the understanding of barkhausen noise. Incorporating the concept of self-organized criticality (SOC) Bak et. al. [195] showed that dissipative dynamical systems with extended degrees of freedom can evolve towards a self-organized critical state and this concept of SOC was well supported by Meisel and Cote [197]. Critical exponents, power laws, scaling relations and data collapsing have been well studied to understand the criticality of barkhausen noise [191]-[202].

5.2 Study of Magnetic Barkhausen Noise from amorphous $Fe_{40}Ni_{40}B_{20}$ and $Fe_{70}Ni_8Si_{10}B_{12}$ ribbons

5.2.1 Introduction

Amorphous magnetic materials exhibit quite interesting magnetic properties that has made them very attractive for various technological applications. Due to the absence of crystal structure in these materials, magnetocrystalline anisotropy energy is almost negligible. These amorphous alloys present a magnetic domain structure that is chiefly determined by the magnetoelastic anisotropy developed as a result of the coupling between the magnetization and internal stresses frozen-in during the fabrication of the ribbons by rapid quenching of the molten alloy. Therefore, application of external tensile stresses affects the domain structure and magnetization process to a large extent and anisotropy can be induced in these amorphous ferromagnets by annealing under the influence of mechanical stress or a magnetic field [203],[204]. Though these materials are isotropic in the as-quenched state, a macroscopically magnetic easy axis is developed which changes direction under various conditions. Determination of this easy axis helps us understanding the direction of induced anisotropy and magnetization processes in these materials which is required for various applications.

MBN measurement is used as an important non-destructive tool to characterize various magnetic properties. In this chapter we have studied magnetization processes in ferromagnetic amorphous ribbons using Magnetic Barkhausen noise technique. A theoretical model has been developed to estimate the direction of magnetic easy axis in amorphous $Fe_{40}Ni_{40}B_{20}$ ribbon. We have also studied the effect of tensile stress on MBN in amorphous $Fe_{40}Ni_{40}B_{20}$ and $Fe_{70}Ni_8Si_{10}B_{12}$ ribbons by this home-fabricated Barkhausen noise experimental set-up. The study of MBN in presence of various external stresses helps us understanding the magnetization dynamics of amorphous magnetic materials. The hysteresis loops of amorphous $Fe_{40}Ni_{40}B_{20}$ and $Fe_{70}Ni_8Si_{10}B_{12}$ ribbons have been measured under different axial tensile stresses by induction method which gives a better understanding of the MBN results.

MBN is a direct consequence of domain wall interactions with microstructural defects and hence it can give detailed information on material structure. Microstructural characteri-

zation of materials by Non-Destructive Evaluation (NDE) techniques is essential for the assessment of initial heat treatment and subsequent degradation in microstructure and mechanical properties. Exposure to high temperature results in microstructural degradation of the sample. MBN study has been done in amorphous $Fe_{40}Ni_{40}B_{20}$ ribbon to investigate the amorphous structure changes caused by heat treatment. Here we have studued the amorphous to crystalline phase transformation by using this non- destructive technique.

5.2.2   Experimental Details

MBN measurements were performed on amorphous $Fe_{40}Ni_{40}B_{20}$ and $Fe_{70}Ni_8Si_{10}B_{12}$ ribbons by a home-fabricated Barkhausen noise experimental set-up as shown in Fig.2.12. Amorphous ribbons with composition $Fe_{40}Ni_{40}B_{20}$ and $Fe_{70}Ni_8Si_{10}B_{12}$ with dimension $40mm \times 20mm \times 25\mu m$ and $40mm \times 2mm \times 25\mu m$ respectively were used for the experiment. The instrument consists of a ferrite core sweep field magnet for applying a time varying magnetic field to the sample to generate Barkhausen noise. The signal to the ferrite core was produced by a waveform generator and amplified by a Kepco Bipolar Power Supply. The sweep field frequency was set at 12 Hz. Barkhausen noise was detected using a pick-up coil which was mounted to the ferrite core. This signal from the pick-up coil was amplified by the low-noise preamplifier (Gain = 100 and 20 for amorphous $Fe_{40}Ni_{40}B_{20}$ and $Fe_{70}Ni_8Si_{10}B_{12}$ ribbons respectively), passed through a band-pass filter $(3-300$ kHz) and then collected to a personal computer. Angular dependent MBN measurements on amorphous $Fe_{40}Ni_{40}B_{20}$ ribbon were performed by varying the orientation of the magnetic field (i.e. the ferrite core) with respect to the axis of the ribbon from $0°$ to $360°$ at intervals of $10°$. For investigating the effect of stress, tensile stresses were applied along the length of the ribbons. The tensile stress was applied to the sample by hanging various loads from one end of the sample keeping the other end fixed. To study the effect of heat treatment, the amorphous $Fe_{40}Ni_{40}B_{20}$ ribbon was isothermally annealed in presence of nitrogen atmosphere at $300°$C for various time duration.

The MBN energy denoted by E_{MBN} is calculated by integrating the square of these volt-

ages with respect to time i.e.

$$E_{MBN} = \sum_{i=1}^{n} \int V_i^2 dt \qquad (5.2)$$

where the time integral is over each event and the summation is taken over all N measured events. The MBN signal was sampled at every $25\mu s$. Four traces were taken for each measurement. Only those voltages above a certain threshold were considered in the analysis.For this purpose, a computer program has been developed.

The magnetization of amorphous $Fe_{40}Ni_{40}B_{20}$ ribbon was measured as a function of dc magnetic field in presence of various tensile stresses by induction method using an integrating fluxmeter (Walker Scientific MF-3D).

5.2.3   Results and Discussions

To check that our experimental set-up is generating real Barkhausen noise, the MBN from a polycrystalline ferromagnetic iron wire has been taken and the results have been shown in Fig.5.3. The typical MBN from the iron wire consists of a large number of usual short duration spike voltages due to 180° domain wall motion or sudden magnetization rotation and serve as a standard while comparing the other MBN signals from the amorphous samples. Fig.5.4 shows the characteristics of MBN signals for amorphous $Fe_{40}Ni_{40}B_{20}$ ribbon under different excitation field angles and under different external stresses. It is observed from the figure that maximum amplitude of MBN voltage increases with the applied stress for a particular direction of magnetic field with respect to the axis of the ribbon (here it is for 0°). However the maximum amplitude of MBN voltage decreases when the orientation of the magnetic field with respect to the ribbon axis is changed from 0° to 90° for zero stress. The angular dependence of the E_{MBN} in amorphous $Fe_{40}Ni_{40}B_{20}$ ribbon under different external stress is shown in Fig.5.5. These measurements were performed by varying the orientation of the magnetic field with respect to the axis of the ribbon from 0° to 360° at intervals of 10° considering the longitudinal axis of the ribbon as 0°. The sweep field was sufficient to achieve the saturation of magnetization of the sample. It is clear from Fig.5.5 that maximum E_{MBN} is generated along the length of the ribbon. In a particular direction, E_{MBN} is observed to increase with increasing stress.
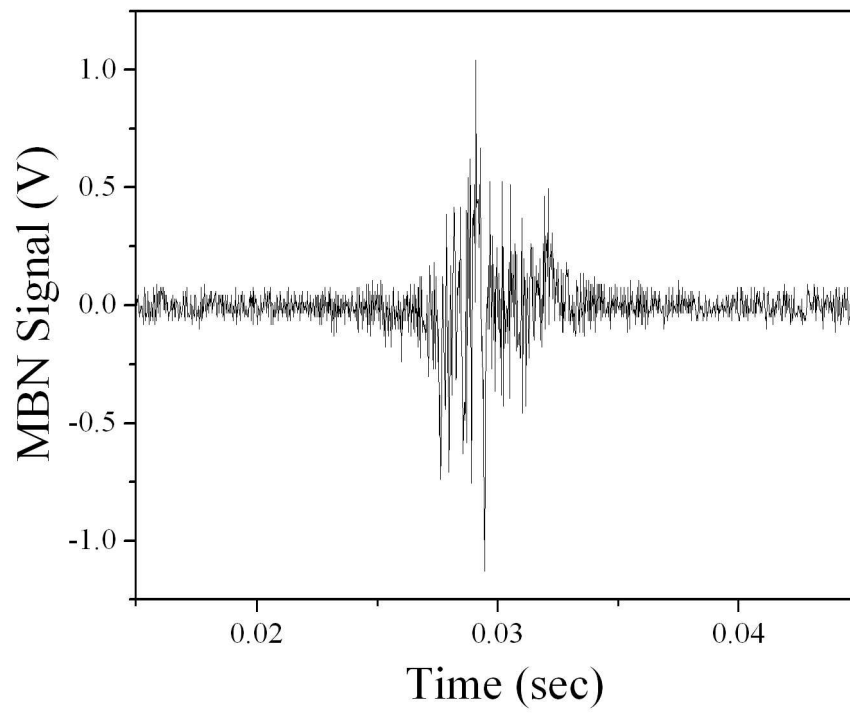
Figure 5.3: MBN signal from a polycrystalline ferromagnetic iron wire.

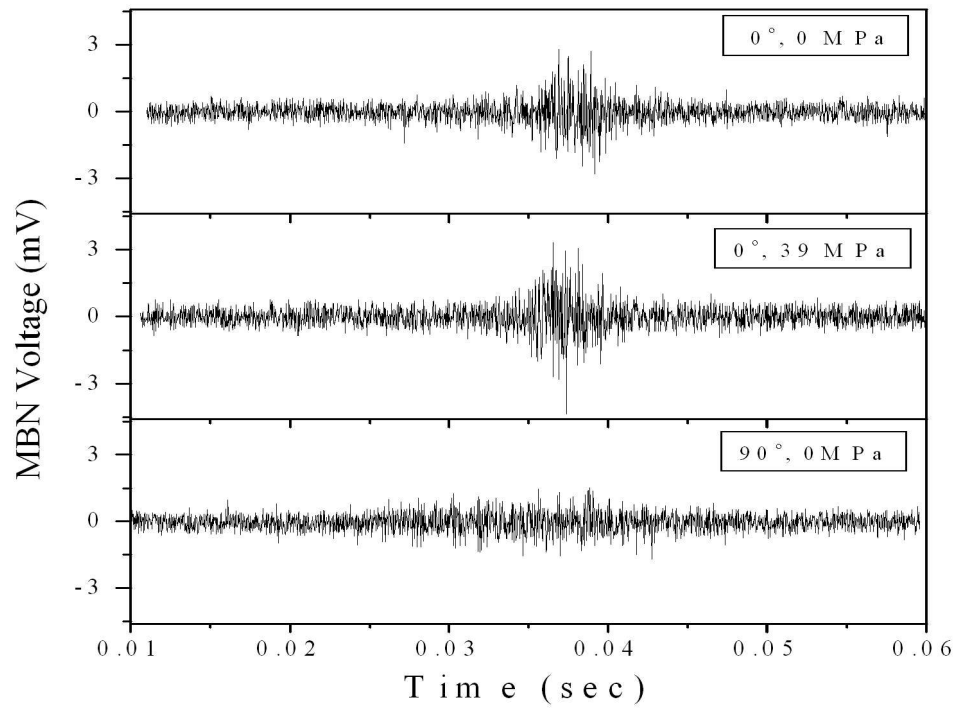Figure 5.4: MBN signal for amorphous $Fe_{40}Ni_{40}B_{20}$ ribbon under different excitation field angles and under different external stresses.
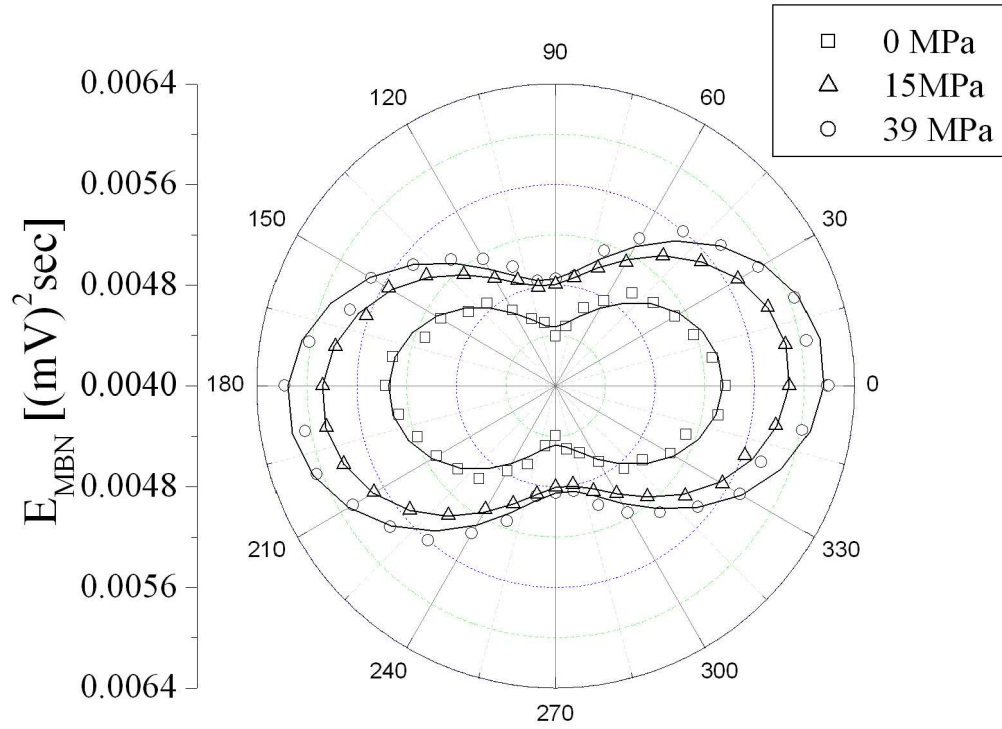
Figure 5.5: Polar plots of E_{MBN} from amorphous $Fe_{40}Ni_{40}B_{20}$ ribbon along different directions of applied field and under different external stresses of 0 MPa, 15 MPa and 33 MPa. The solid lines represent the fit of Eq. (5.18) to the experimental data.
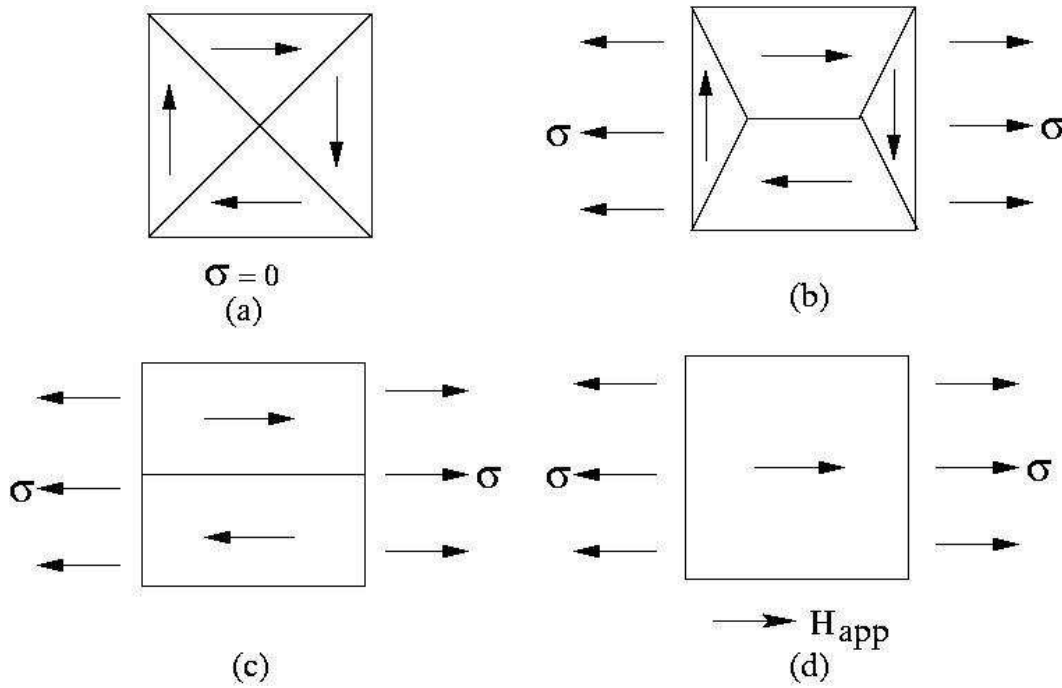
Figure 5.6: Magnetization of a positive magnetostrictive sample under tensile stress (σ).

Since $Fe_{40}Ni_{40}B_{20}$ ribbon is positive magnetostrictive in nature, therefore the application of tensile stress creates more domain walls in the stress direction. MBN is associated with the depinning of these domain walls as they move during magnetization, therefore the MBN energy is expected to increase with the increase in tensile stress.

Longitudinal internal stresses are developed within these materials during the preparation by rapid quenching from the melt. As a result, more 180° domains are developed along the length of the ribbon due to the induced anisotropy generated by the internal stresses and a bulk magnetic easy axis is developed along the length of the ribbon. The application of external tensile stress along the length of the ribbon leads to an overall increase in E_{MBN}. This is because the applied stresses further increases 180° domains as illustrated in Fig.5.6. Fig.5.6(a) represents a small portion of the demagnetized positive magnetostrictive sample comprising four domains. Application of a small tensile stress (σ) to the demagnetized sample cause domain walls to move in such a way as to decrease the volume of domains magnetized at right angles to the stress axis [Fig.5.6(b)]. The magnetoelastic energy of

an uniaxial isotropic magnetic material is given by,

$$E_{me} = 3/2\lambda\sigma\sin^2\theta \tag{5.3}$$

where λ is the magnetostriction of the sample and θ is the angle between magnetization vector and σ . These domains are completely eliminated by some higher value of stress as shown in Fig.5.6(c) to minimize E_{me}. Under this condition the application of a small magnetic field (H) along stress direction saturates the specimen completely by the process of 180° domain wall motion [Fig.5.6(d)]. Therefoe the application of a tensile stress to a positive magnetostrictive sample increases the 180° domain walls along the direction of stress, thus increasing E_{MBN} with stress.

The direction of magnetic easy axis in amorphous ribbons can be determined if MBN is considered to be generated mainly due to 180° domain wall displacements. MBN can be characterized by E_{MBN} which is the time integral of the squared voltage signal as described in Eq.(5.2). The velocity of 180° domain walls generating MBN is given by

$$v \propto (H_{\parallel} - H_c) \tag{5.4}$$

where $H_{\parallel}$ is the applied field component parallel to the domain wall and H_c is the threshold or coercive field that must be overcome by $H_{\parallel}$ for significant domain wall movement. The velocity v is proportional to the measured MBN voltage and domain wall dynamics in metallic systems may therefore be described as

$$\sigma G(\frac{d\phi}{dt}) = (H_{\parallel} - H_c) \tag{5.5}$$

where σ is the electrical conductivity of the material and G is a constant that can be obtained exactly in the limit of a wide slab and single domain wall, $(\frac{d\phi}{dt})$ is the rate of change of flux which is proportional to the domain wall velocity. Therefore the measured MBN voltage is proportional to the velocity of the domain wall. Eq.(5.5) has been modified from that proposed by Alessandro et. al[16] by incorporating the field component parallel to a particular domain wall. Substituting Eq.(5.4) and Eq.(5.5) in Eq. (5.2) and providing a constant A_i to absorb all the proportionality factors, the expression of E_{MBN} is obtained as,

$$E_{MBN} = \sum_{i=1}^{n} A_i \int (\frac{d\phi}{dt})^2 dt \tag{5.6}$$

Let us consider a ferromagnetic sample having a magnetic easy axis (E.A.) at an angle φ with respect to a particular direction along which an external stress (σ) is applied. Magnetic fied (H_{app}) is applied to the sample along a direction θ with respect to the externally applied stress. Then the induced anisotropy energy due to external stress, σ is,

$$E_{ani} = -K_1 \cos^2 \varphi \tag{5.7}$$

The constant of uniaxial anisotropy K_1 is given by $(3/2)\lambda\sigma$, where λ is the magnetostriction of the sample. Therefore, we can consider an equivalent field H_σ, derived from the induced anisotropy energy E_{ani} due to external stress (σ) as

$$H_\sigma = K \cos^2 \varphi \tag{5.8}$$

where K is a constant. Therefore the components of the two magnetic fields i.e. H_σ and H_{app} along the easy axis of the sample are $H_\sigma \cos\varphi$ and $H_{app} \cos(\theta - \varphi)$ respectively. We can therefore write the effective field component aligned with the domain magnetization vector or the easy axis of the sample that induces the 180° domain wall to move as

$$H_{eff} = H_\sigma \cos\varphi + H_{app} \cos(\theta - \varphi) \tag{5.9}$$

Applying Eq.(5.4) and allowing the constants to be absorbed into a constant A, Eq.(5.6) becomes,

$$E_{MBN} = \sum_{i=1}^{n} A \int (H_{eff} - H_c) d\phi \tag{5.10}$$

For this sample with a macroscopic magnetic easy axis, the majority of 180° domain walls may be considered to be aligned in the easy axis direction, while the remaining 180° domain walls are isotropically oriented. Therefore, Eq.(5.10) is separable into two components, (i) the first component is due to those domains that contribute to the net magnetic easy axis and (ii) the second one from those domains that are isotropically aligned and form a net angular independent background. If MBN is peaked up from an area S, then $\phi = B.S = \mu.H.S$, and we can write Eq.(5.10) as,

$$E_{MBN} = \sum_{easyaxis} [A_e \int \mu_e [H^e_{eff} - H^e_c] dH^e_{eff}] + \sum_{j} [A_j \int \mu_j (H^j_{eff} - H^j_c) dH^j_{eff}] \tag{5.11}$$

where A_e and A_j are constants that refer to those domains contributing to the net magnetic easy axis and to those that contribute to the background MBN, respectively. μ_e and

μ_j are the permeability for events occuring due to the irreversible motion of domains that contribute to the net magnetic easy axis and for those occuring due to MBN background respectively. Integrating Eq.(5.11) we have,

$$E_{MBN} = \sum_{easyaxis} A_e\mu_e[\frac{(H^e_{eff})^2}{2} - H^e_cH^e_{eff}] + \sum_j A_j\mu_j[\frac{(H^j_{eff})^2}{2} - H^j_cH^j_{eff}] \quad (5.12)$$

Substituting the expression of H_{eff} from Eq. (5.9) in Eq.(5.12) we have,

$$
\begin{aligned}
E_{MBN} &= \sum_{easyaxis} \frac{A_e\mu_e}{2}[H_\sigma{}^2\cos^2\varphi + 2H_\sigma\cos\varphi H_{app}\cos(\theta-\varphi) + H_{app}{}^2\cos^2(\theta-\varphi)] \\
&\quad -2H^e_c(H_\sigma\cos\varphi + H_{app}\cos(\theta-\varphi))] \\
&\quad +\sum_j A_j\mu_j[\frac{(H^j_{eff})^2}{2} - H^j_cH^j_{eff}]
\end{aligned}
\quad (5.13)
$$

Therefore,

$$E_{MBN} = \alpha\cos^2(\theta-\varphi) + \alpha' + \beta \quad (5.14)$$

where we have set

$$\alpha = \sum_{easyaxis} \frac{A_e\mu_e}{2}H_{app}{}^2 \quad (5.15)$$

$$\alpha' = \sum_{easyaxis} \frac{A_e\mu_e}{2}[H_\sigma{}^2\cos^2\varphi + 2H_\sigma\cos\varphi H_{app}\cos(\theta-\varphi) - 2H^e_c(H_\sigma\cos\varphi + H_{app}\cos(\theta-\varphi))]$$

$$(5.16)$$

$$\beta = \sum_j A_j\mu_j[\frac{(H^j_{eff})^2}{2} - H^j_cH^j_{eff}] \quad (5.17)$$

Considering negligible variation of the parameter α' in Eq. 5.14 compared to α and β as observed earlier, Eq. 5.14 can be modified as,

$$E_{MBN} = \alpha\cos^2(\theta-\varphi) + \beta \quad (5.18)$$

which can be used as the final expression for fitting the experimental data of the angular dependent E_{MBN} in amorphous magnetic materials.

Here α is the MBN signal produced by the irreversible motion of 180° domain walls contributing to the direction of magnetic easy axis and β is the background MBN signal due to the isotropically oriented 180° domains. The maximum in E_{MBN} at an angle

φ obtained from angular dependent MBN measurements indicates the direction of the macroscopic magnetic easy axis of the sample.

The variation of the direction of the magnetic easy axis with respect to the applied stress is shown in Fig.5.7. It is evident from Fig.5.7 that the direction of magnetic easy axis is almost constant and it is close to the direction of the length of the ribbon i.e. along the direction of applied stress. The behaviour of the angular averaged MBN energy signal (i.e. the energy averaged over $180°$) $< E_{MBN} >= (\alpha/2 + \beta)$ as a function of increasing tensile stress is also shown in Fig.5.7. The results indicate an increase of the overall MBN energy signal with increasing tensile stress.

As $Fe_{40}Ni_{40}B_{20}$ is a positive magnetostrictive sample, the applied axial tensile stress develops an anisotropy along the length of the ribbon, i.e., close to the easy axis. From Fig.5.7 we observe that there is a negligible variation of the direction of magnetic easy axis with applied tensile stress and it is within $10°$ of the direction of applied stress. Increase of E_{MBN} under applied tensile stress reflects the orientation of the magnetic easy axis towards the direction of applied stress. The application of an external stress modifies the direction of the easy axis by inducing a magnetoelstic anisotropy energy along the direction of stress. The direction of easy axis is then determined by the minimization of magnetoelstic anisotropy energy. In the case of positive magnetostrictive $Fe_{40}Ni_{40}B_{20}$ ribbon the presence of an external tensile stress increases the $180°$ domains along the direction of stress. This reduces its magnetoelastic energy and enhances the MBN activity. $< E_{MBN} >$ parameter actually reflects the change in the number of $180°$ domain walls within interaction regions under condition of applied stress. Increase of $< E_{MBN} >$ value with increasing stress indicates the increase in population of $180°$ domain walls i.e. an increase of the overall MBN activity with increasing stress applied along the magnetic easy axis of the ribbon.

Since the above results reveal that the MBN is most stress sensitive along the length of the ribbon, we have studied the field dependence of MBN along the ribbon length in presence of various tensile stresses to understand the magnetization processes in amorphous ribbons. MBN measurements were performed by varying the magnetic field upto 29 Oe and in presence of tensile stresses upto 33 MPa stress. Fig.5.8 shows the field dependence of E_{MBN} in amorphous $Fe_{40}Ni_{40}B_{20}$ ribbon at different values of tensile stress. E_{MBN}
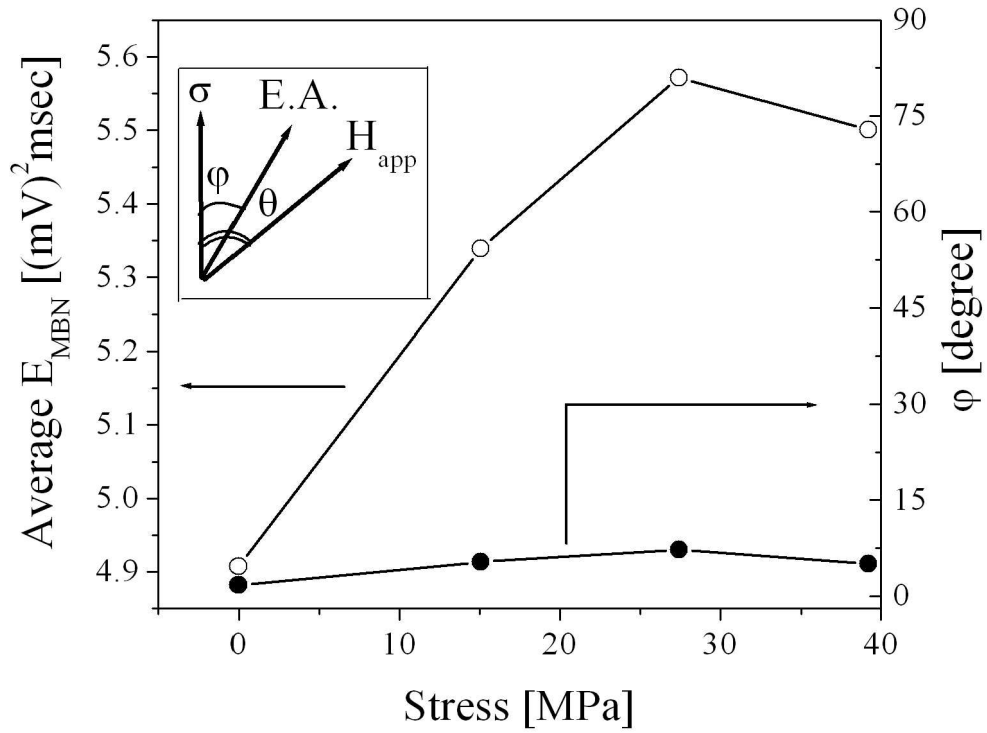
Figure 5.7: Variation of the average MBN energy, $< Energy >$ and the direction of magnetic easy axis (solid line is a guide to the eye) with respect to the tensile stress applied along the length of the amorphous $Fe_{40}Ni_{40}B_{20}$ ribbon. Inset shows the magnetic easy axis (E.A.) at an angle φ with respect to a particular direction along which an external stress (σ) is applied and it also makes an angle ($\theta - \varphi$) with the applied magnetic field, H_{app}.
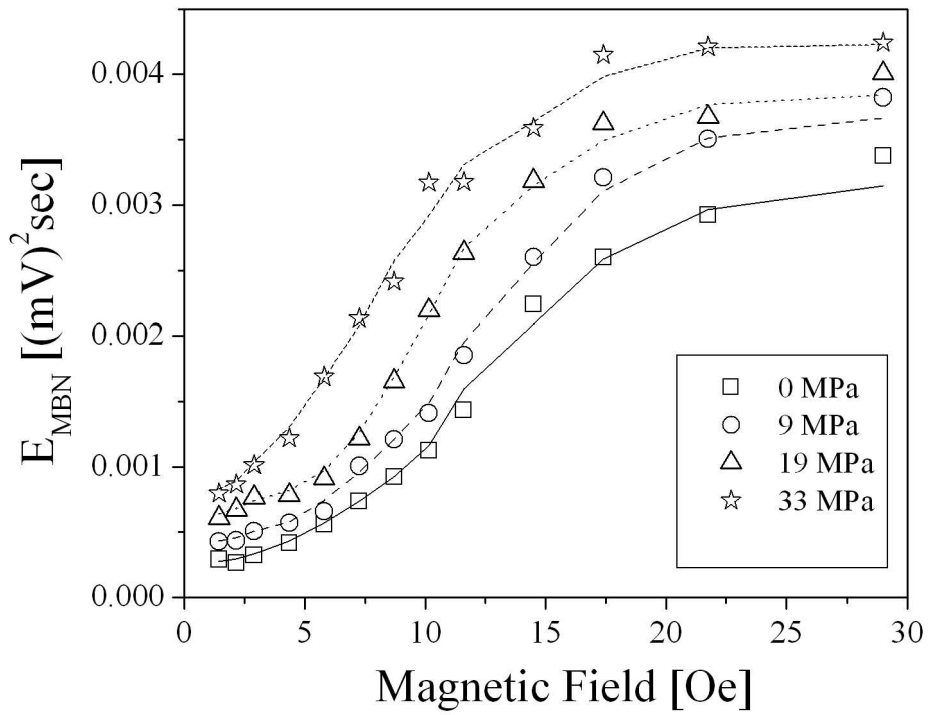
Figure 5.8: E_{MBN} as a function of magnetic field in amorphous $Fe_{40}Ni_{40}B_{20}$ ribbon at 0 MPa, 9 MPa, 19 MPa and 33 MPa stresses.
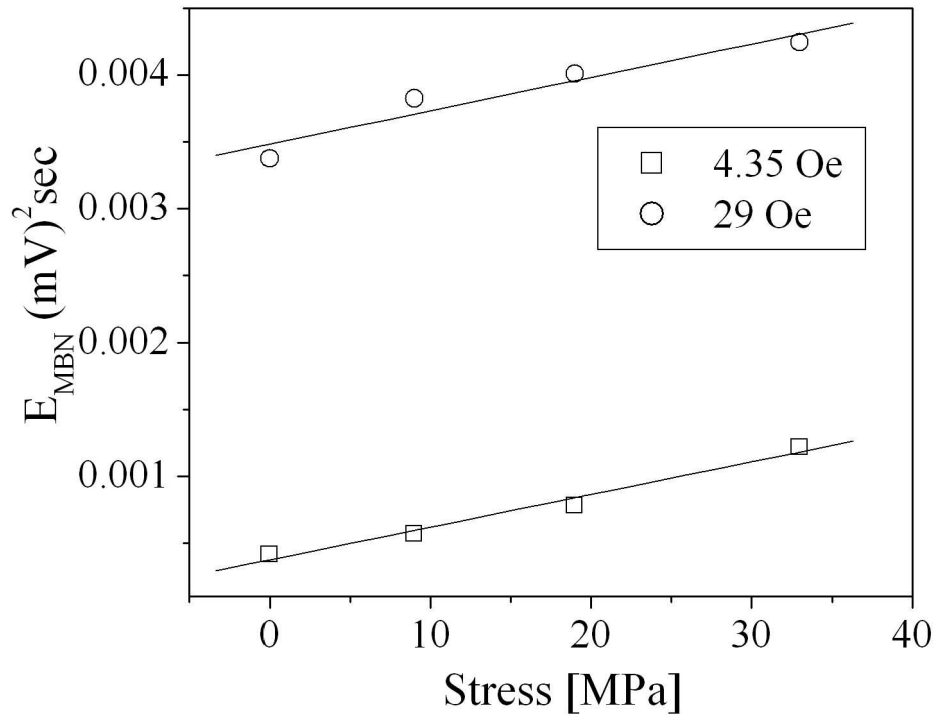
Figure 5.9: Stress dependence of E_{MBN} in amorphous $Fe_{40}Ni_{40}B_{20}$ ribbon at magnetic fields of 4.35 Oe and 29 Oe.

initially increases with magnetic field and finally gets saturated at higher fields for both without stress as well as in presence of 9MPa, 19MPa and 33MPa stresses. It is clear from Fig.5.8 that there is an increase in E_{MBN} with increasing tensile stress. Fig.5.9 shows the dependence of E_{MBN} on applied tensile stress for two different values of magnetic field, $H = 4.35Oe$ and $H = 29Oe$.

The variation of the magnetization, M of amorphous $Fe_{40}Ni_{40}B_{20}$ ribbon as a function of magnetic field, H is shown in Fig.5.10 for different tensile stresses, $\sigma = 0$MPa, 47MPa and 94MPa. The magnetization increases very steeply at low field and attains a saturation value around a field of ~ 100 Oe . In presence of a tensile stress the magnetization process is enhanced and the saturation is obtained at lower field. The variation of the coercive field H_c of the ribbon with external tensile stress, σ is shown in Fig.5.11. It is
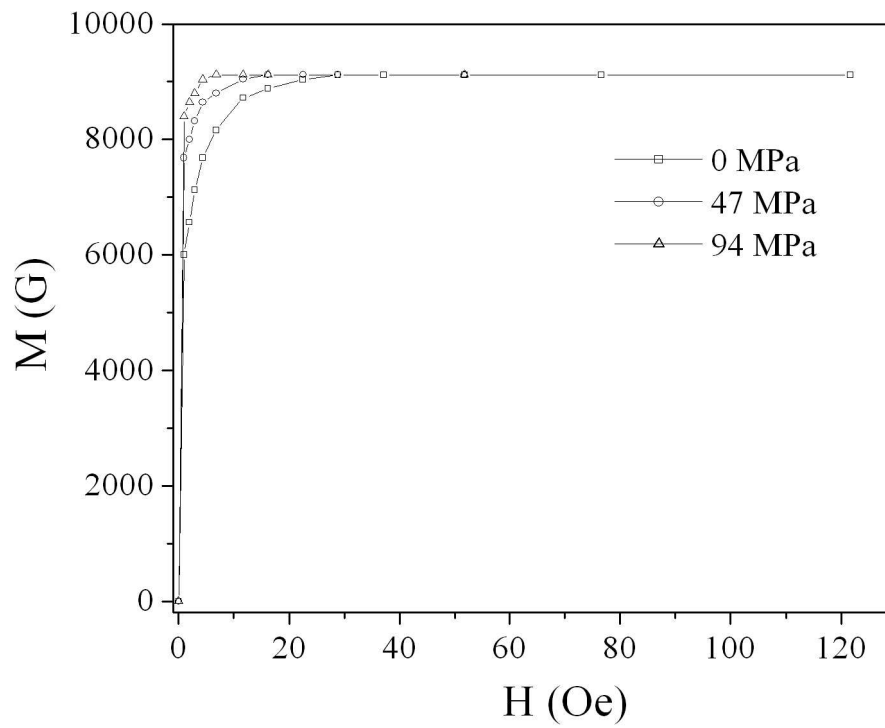
Figure 5.10: Variation of magnetization of amorphous $Fe_{40}Ni_{40}B_{20}$ ribbon as a function of magnetic field under different tensile stresses.
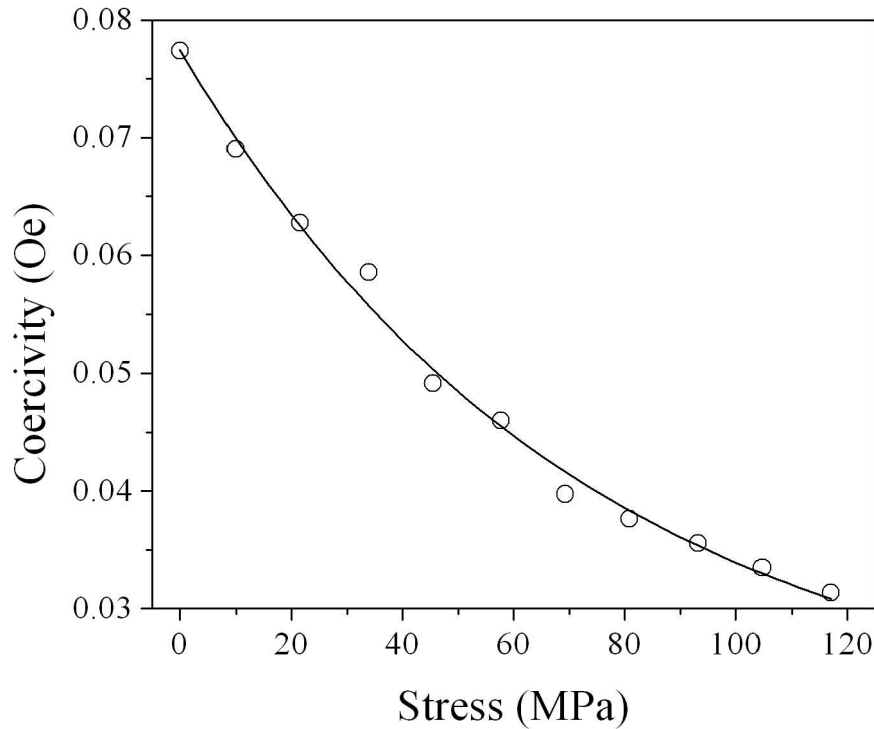
Figure 5.11: Variation of coercive field with tensile stress in amorphous $Fe_{40}Ni_{40}B_{20}$ ribbon.

observed that the coercive field decreases with applied tensile stress.

From Fig.5.8 it is evident that E_{MBN} initially increases sharply with magnetic field and eventually gets saturated at higher magnetic field for both under stress and without stress condition. As the magnetic field is increased from low values, the domain walls overcome higher energy pinning sites, thus increasing the Barkhausen noise. Though the atoms are oriented randomly in amorphous magnetic materials, a magnetic easy axis is developed along the length of the ribbon as a stress induced anisotropy is generated along the length during preparation of the samples. Fig.5.9 shows that at a particular magnetic field E_{MBN} increases with increasing stress. Therefore when the stress is applied along the length of the ribbon and as the stress is increased, more 180° domains are developed along the direction of tensile stress which contributes more inthe magnetization process.

Thus E_{MBN} increases with increasing stress resulting in the steeper magnetization curves and reduction in coercivity in presence of stress.

The effect of stress on MBN in amorphous $Fe_{70}Ni_8Si_{10}B_{12}$ ribbon has also been studied along its length in presence of tensile stresses up to 38 MPa. The MBN measurements were performed by varying the magnetic field from 0.7 Oe to 29 Oe in presence of different tensile stresses. Here the magnetic field (H) is parallel to the applied stress (σ) direction. Fig.5.12 shows the MBN signal for a magnetic field of 29 Oe at different applied stress conditions.

Fig.5.13 shows the field dependence of E_{MBN} in the sample at different values of tensile stress, σ. Fig.5.14 shows the dependence of E_{MBN} on applied tensile stress for two different values of magnetic field, H=5.8 Oe and H=29 Oe. It is clear from Fig.5.13 that the E_{MBN} initially increases sharply with magnetic field and eventually gets saturated for higher magnetic field. This behaviour is observed in the sample for both under stress and without stress condition. As the magnetic field is increased from low values, the domain walls overcome higher energy pinning sites, thus increasing the Barkhausen noise. Though the atoms are oriented randomly in amorphous magnetic materials, a magnetic easy axis is developed along the length of the ribbon as a stress induced anisotropy is generated along the length during the preparation of the samples. The 180^0 magnetic domains are preferentially oriented along a particular direction called the easy axis of magnetization. Fig.5.14 shows that at a particular magnetic field the E_{MBN} increases with increasing stress. Therefore when the stress is applied along the length of the sample, as the stress is increased, more and more 180^0 domains are oriented along the direction of tensile stress, which is the direction of the applied field also. Thus the E_{MBN} increases with increasing stress.

Amorphous magnetic materials gradually change from amorphous to crystalline phase on heat treatment around their crystallization temperature. To check whether MBN can be used to detect this structural transition, amorphous $Fe_{40}Ni_{40}B_{20}$ ribbon was isothermally heated in a furnace at 300°C in presence of nitrogen atmosphere for various time durations. Fig. 5.15 shows the field dependence of E_{MBN} in amorphous $Fe_{40}Ni_{40}B_{20}$ ribbon of the as-quenched and annealed samples.
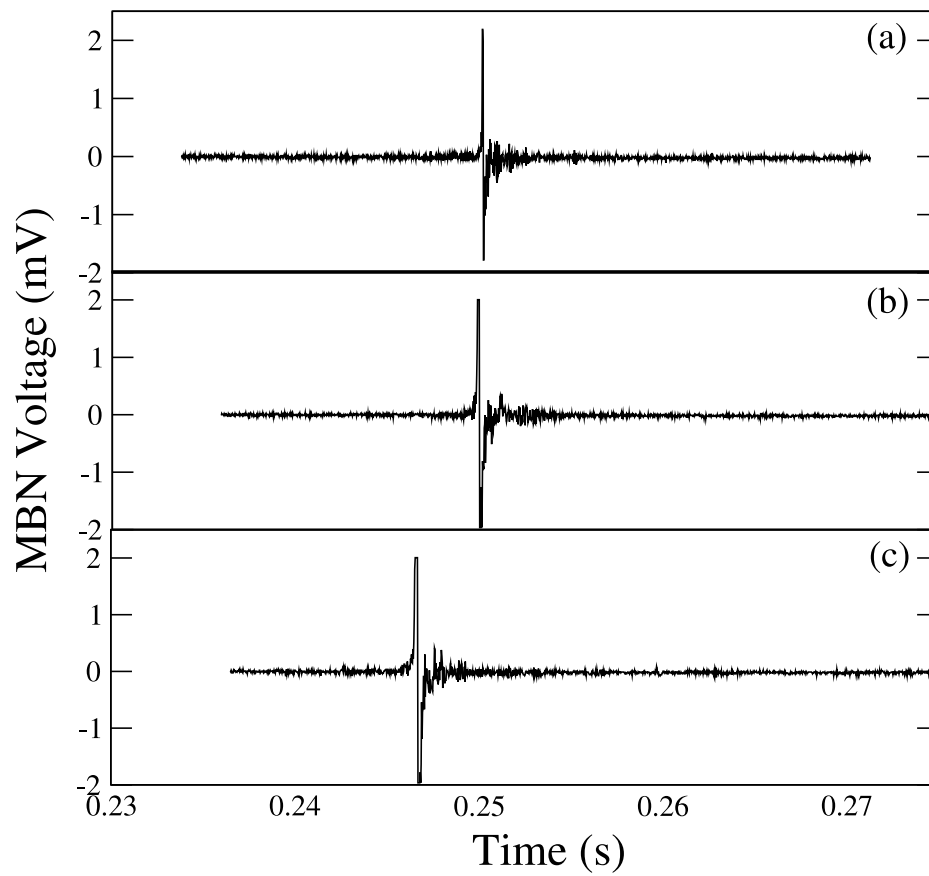
Figure 5.12: MBN from amorphous $Fe_{70}Ni_8Si_{10}B_{12}$ ribbon with (a) H=29 Oe , σ=0 MPa,(b) H=29 Oe , σ=26 MPa,(c) H=29 Oe , σ=38 MPa.
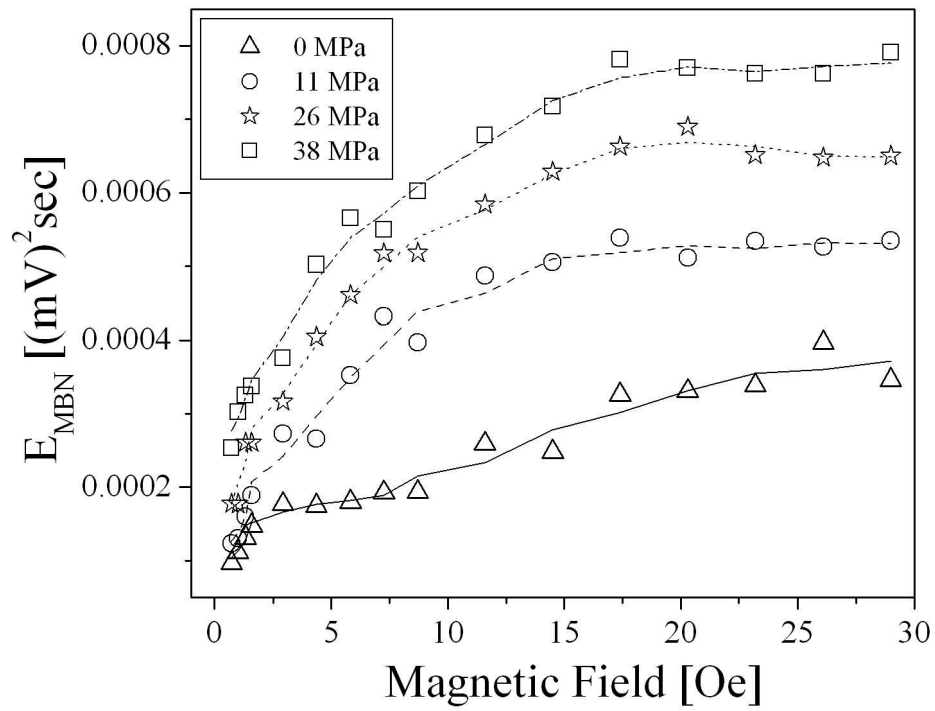
Figure 5.13: E_{MBN} as a function of magnetic field in amorphous $Fe_{70}Ni_8Si_{10}B_{12}$ ribbon at 0 MPa, 11 MPa, 26 MPa and 38 MPa stresses.
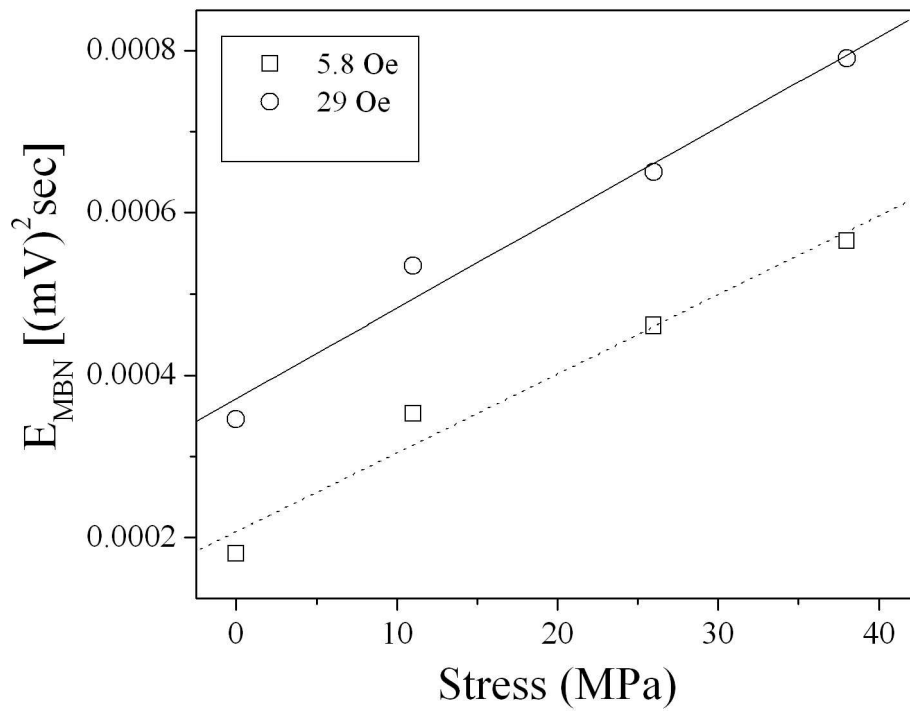
Figure 5.14: Stress dependence of E_{MBN} in amorphous $Fe_{70}Ni_8Si_{10}B_{12}$ ribbon at magnetic fields of 5.8 Oe and 29 Oe .
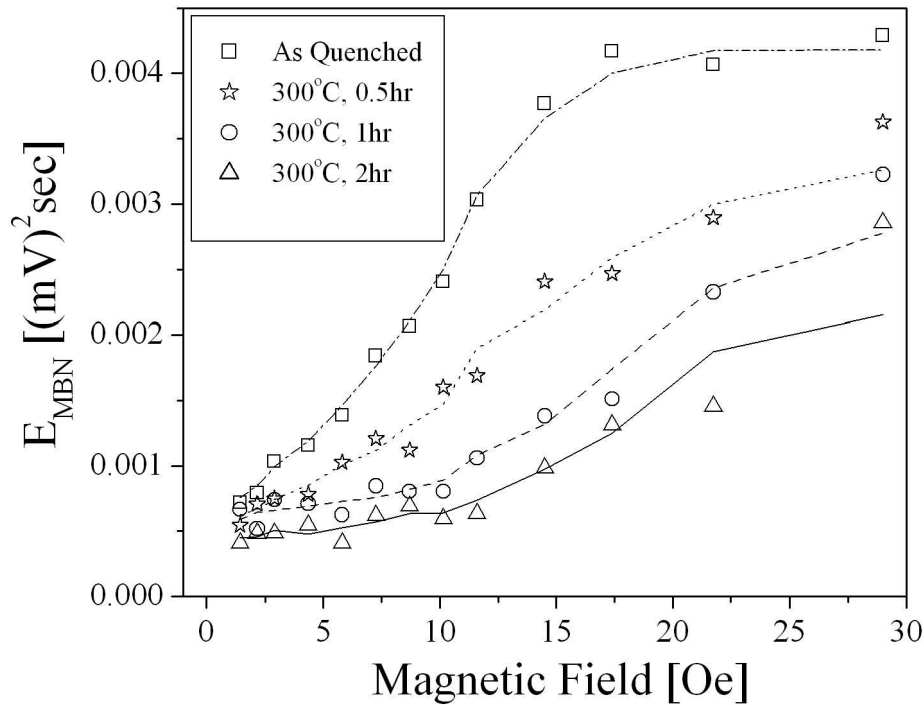
Figure 5.15: Variation of E_{MBN} with magnetic field of the as quenched and annealed (annealed at 300°C for 0.5 hour, 1 hour and 2 hour) amorphous $Fe_{40}Ni_{40}B_{20}$ ribbons.

From Fig. 5.15 it is clear that E_{MBN} initially increases sharply with magnetic field and eventually gets saturated at higher magnetic field. It is also observed that the E_{MBN} decreases with increasing duration of heat treatment. This decrease in E_{MBN} with increasing duration of heat treatment at 300°C has been connected with the crystallization process that has formed crystalline grains. The gradual decrease in E_{MBN} in the amorphous $Fe_{40}Ni_{40}B_{20}$ ribbon with increasing duration of heat treatment indicates a gradual transformation from amorphous to crystalline phase. Fig. 5.16 shows the variation of root mean square voltage (of the MBN voltage) with time in amorphous $Fe_{40}Ni_{40}B_{20}$ ribbon of the as-quenched and annealed samples (annealed in presence of nitrogen atmosphere at 300°C for different time durations). In Fig. 5.16, the as-quenched sample shows a broad peak. After annealing for 1 hour at 300°C, two distinct peaks corresponding to amorphous
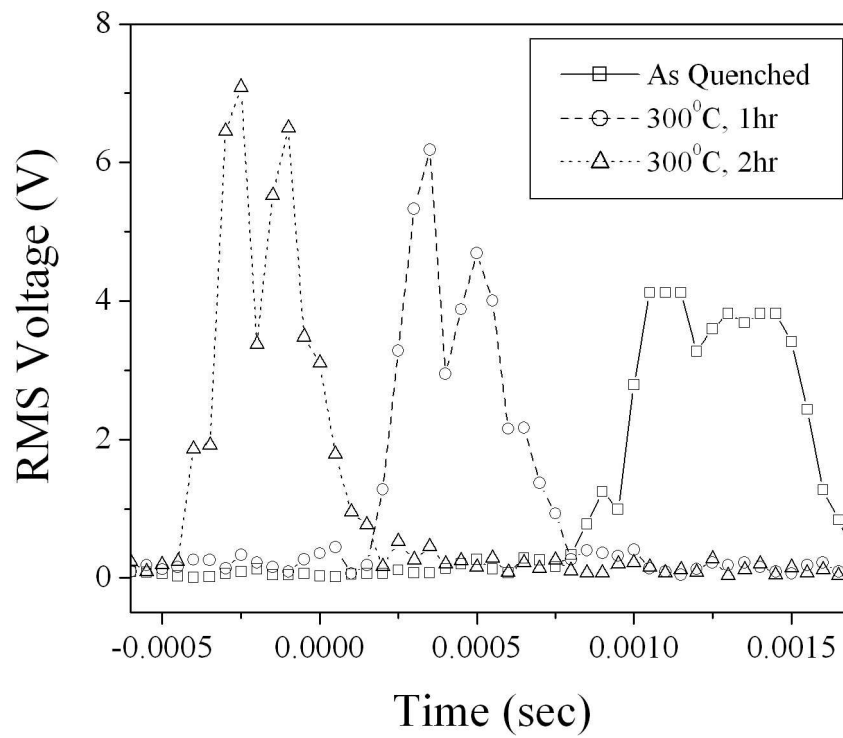
Figure 5.16: The variation of root mean square voltage (of the MBN voltage) with time of the as quenched and annealed (annealed at 300°C for 1 hour and 2 hour) amorphous $Fe_{40}Ni_{40}B_{20}$ ribbons.

and crystalline phase are observed. The two peaks become more prominent with the increase in annealing time. On further annealing (2.0 hour) a distinct two-peak behaviour in root mean square voltage is observed. This development of two-peak characteristics with annealing is a consequence of amorphous to crystalline phase transformation in the amorphous $Fe_{40}Ni_{40}B_{20}$ ribbon.

5.3   Study of Magnetic Barkhausen Noise in Amorphous $Fe_{73.5}Cu_1Nb_3Si_{13.5}B_9$ nanocrystalline ribbons

5.3.1   Results and Discussions

The sample used in the present study was an amorphous ribbon (known under its commercial name FINEMET) with nominal composition $Fe_{73.5}Cu_1Nb_3Si_{13.5}B_9$ having dimensions $40mm$ x $4mm$ x $25\mu m$. It is a conventional nanocrystalline material composed of ultrafine bcc FeSi grains embedded in a residual amorphous matrix. These amorphous materials gradually change from amorphous to nanocrystalline phase on heat treatment around their crystallization temperature. In this section we have studied this phase transformation using MBN technique. The $Fe_{73.5}Cu_1Nb_3Si_{13.5}B_9$ ribbon was isothermally heated in a furnace in nitrogen atmosphere at 540°C for 1 hour. MBN was then studied from both the as-quenched and the annealed samples.

A magnetic field is generated by passing a low frequency (4Hz) sinusoidal current through the Helmholtz coil. A small pick-up coil with 100 turns, around the sample was used to detect the MBN signals. The MBN signal was sampled at the intervals of 25 μs and eight traces were taken for each measurement. The signal from the coil was amplified by 1000 times using a low-noise pre-amplifier, passed through a band-pass filter (3 kHz 300 kHz) and then collected in a personal computer. Only those voltage signals having amplitudes higher than a selected threshold were considered for analysis. The MBN activity was characterized by $MBN_{envelope}$, which represents the locus of the absolute values of MBN signal as a function of time. The axial hysteresis loops of the samples were measured by a vibrating sample magnetometer (Lakeshore) up to a maximum field of 2000 Oe. The phase structure of both as-quenched and annealed samples was verified by X-ray diffractometer (XRD, X'Pert Pro, Panalytic).
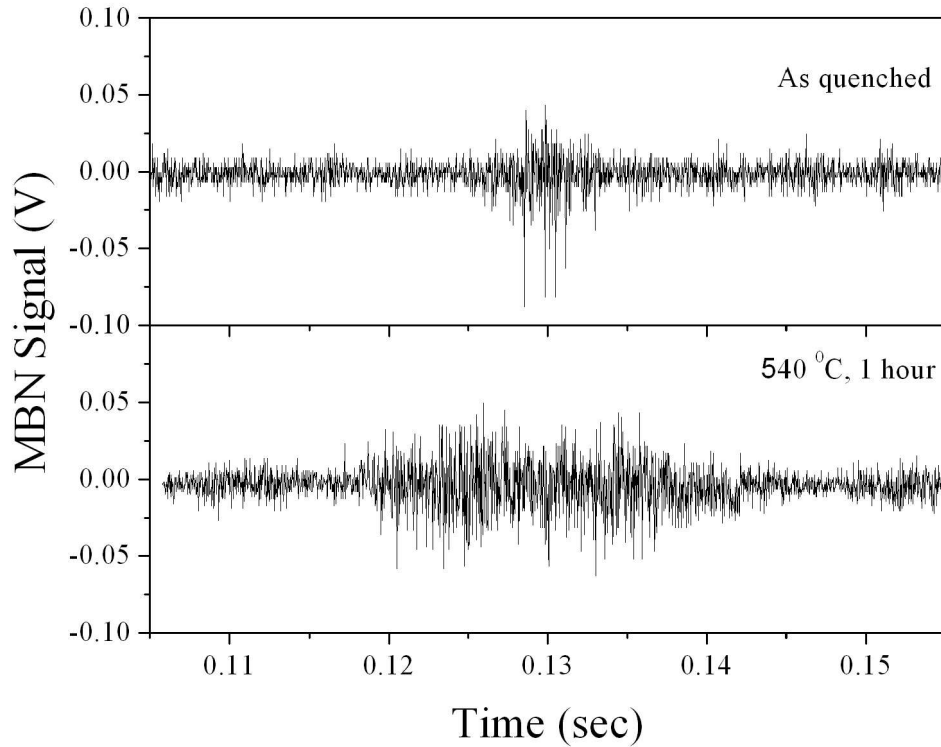
Figure 5.17: MBN signal from the as-quenched and annealed (heated at 540°C for 1 hour) $Fe_{73.5}Cu_1Nb_3Si_{13.5}B_9$ ribbon.

Fig. 5.17 shows signal from the as-quenched and annealed (heated at 540°C for 1 hour) $Fe_{73.5}Cu_1Nb_3Si_{13.5}B_9$ ribbon. MBN envelope from the as-quenched and annealed (heated at 540°C for 1 hour) $Fe_{73.5}Cu_1Nb_3Si_{13.5}B_9$ ribbons are shown in Fig. 5.18. It is observed from the figure that the $MBN_{envelope}$ show a single-peak and a double-peak for the as-quenched and annealed samples respectively. The single-peak can be attributed to the single amorphous phase of the ribbon. On annealing at 540°C for 1 hour, nanocrystalline α FeSi phase is formed in the amorphous matrix. Therefore, the two-peaks of the $MBN_{envelope}$ (for the annealed sample) correspond to the nanocrystalline and the amorphous phases.

The variation of the normalized magnetization as a function of the magnetic field of the as-quenched and annealed (heated at 540°C for 1 hour) $Fe_{73.5}Cu_1Nb_3Si_{13.5}B_9$ ribbon
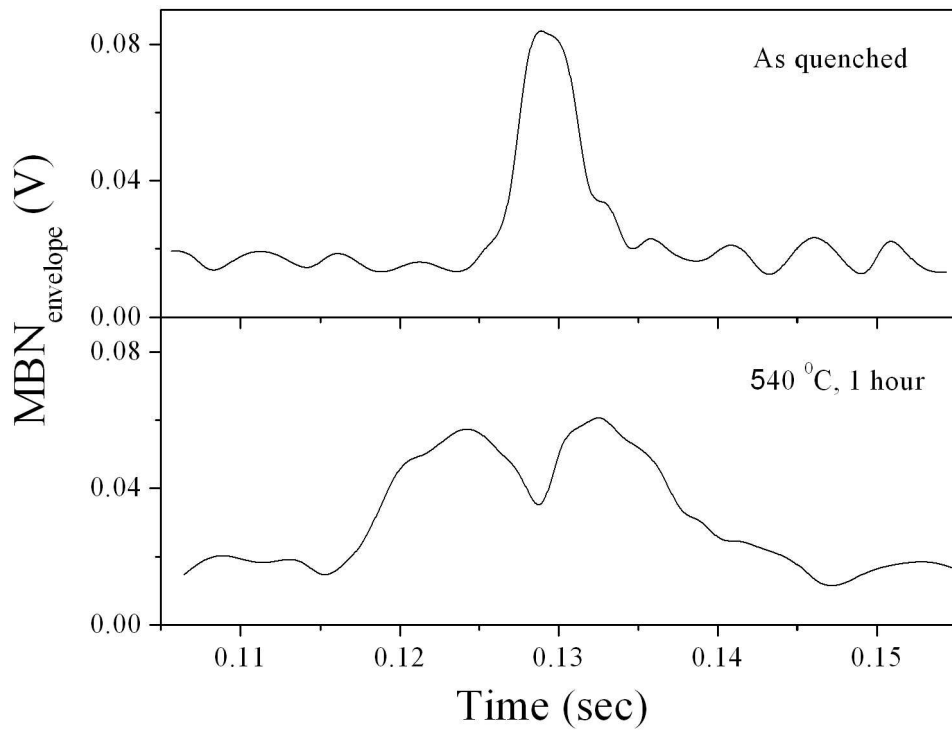
Figure 5.18: MBN envelope from the as-quenched and annealed (heated at 540°C for 1 hour) $Fe_{73.5}Cu_1Nb_3Si_{13.5}B_9$ ribbon.
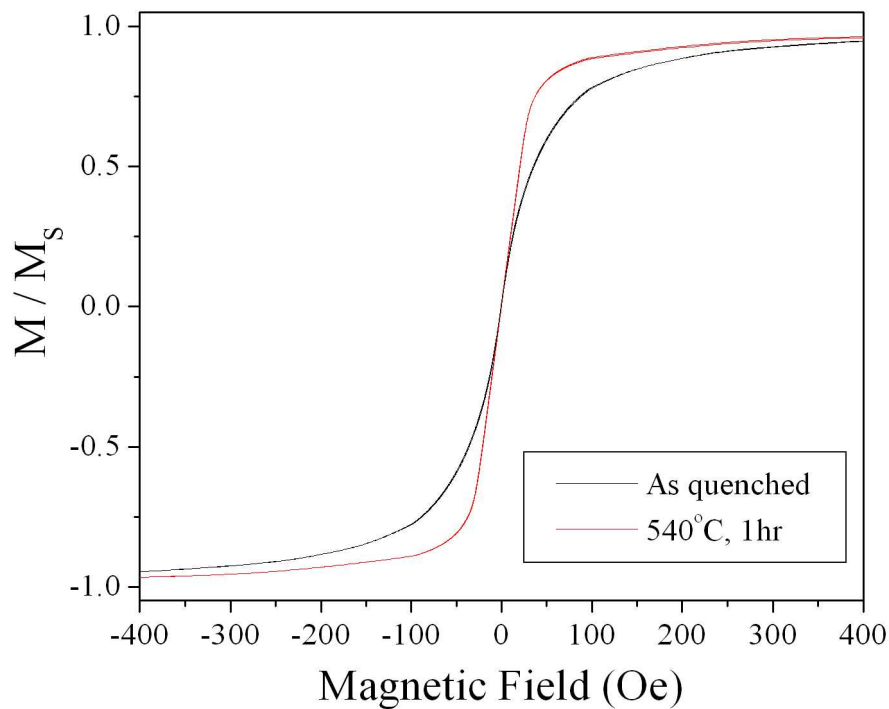
Figure 5.19: Variation of the normalized magnetization as a function of the magnetic field of the as-quenched and annealed (heated at 540°C for 1 hour) $Fe_{73.5}Cu_1Nb_3Si_{13.5}B_9$ ribbon.

are shown in Fig.5.19. On annealing the sample, there is jump in magnetization at low magnetic field as compared to the as-quenched sample. The X-ray diffraction patterns for the as-quenched and annealed (heated at 540°C for 1 hour) $Fe_{73.5}Cu_1Nb_3Si_{13.5}B_9$ ribbon are shown in Fig.5.20. The XRD pattern for the as-quenched ribbon exhibited only one very broad peak around $2\theta = 45°$ (often known as diffuse halo) indicating that the ribbon is amorphous. XRD patterns of the annealed sample show two peaks at around $2\theta = 45°$ and $2\theta = 68°$ corresponding to α FeSi phase and Fe_3Si phase respectively. Therefore the XRD results indicated that α FeSi phase was detected on annealing the sample at 540°C for 1 hour and verified our MBN results.

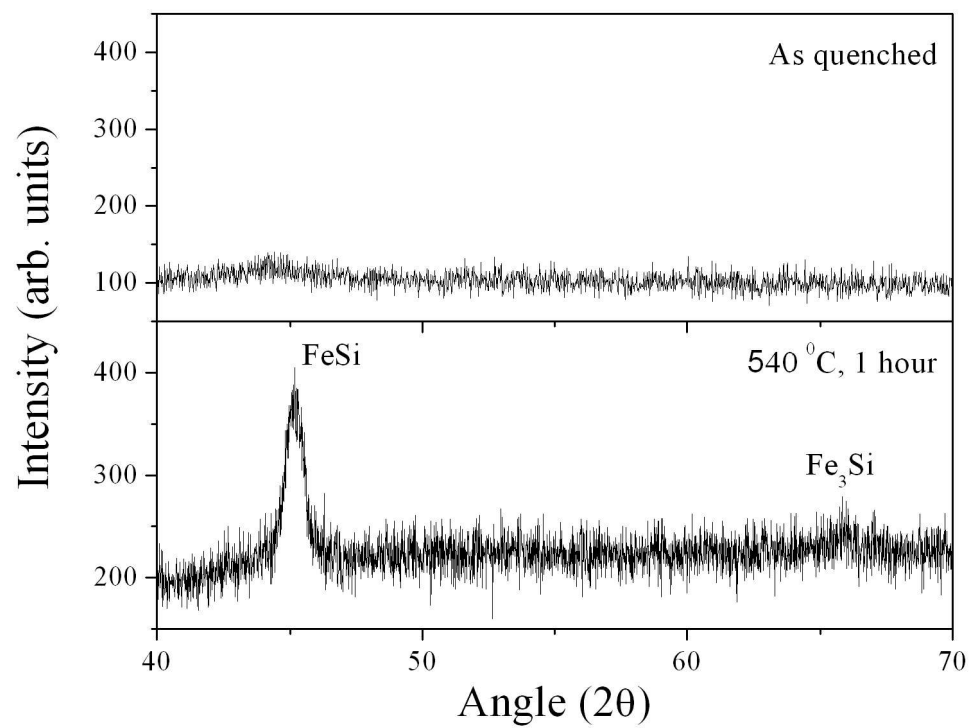Therefore, MBN technique was successfully employed to study the phase transforma-

Figure 5.20: X-ray diffraction patterns for the as-quenched and annealed (heated at 540°C for 1 hour) $Fe_{73.5}Cu_1Nb_3Si_{13.5}B_9$ ribbon.

tion in amorphous $Fe_{73.5}Cu_1Nb_3Si_{13.5}B_9$ nanocrystalline ribbons. The amorphous as-quenched state transformed into bcc nanograins with excellent soft magnetic properties.

5.4 Effect of Tensile Stress on the Magnetic Barkhausen Noise in Amorphous $Co_{68.15}Fe_{4.35}Si_{12.5}B_{15}$ wire

5.4.1 Results and Discussions

The sample used in the present study was an amorphous wire with nominal composition $Co_{68.15}Fe_{4.35}Si_{12.5}B_{15}$ having a diameter 125 μm and length 12 cm. MBN from this amorphous wire were studied in presence of various tensile stresses using a home-fabricated sensitive experimental setup. A magnetic field, which is sufficient for the technical saturation of the sample, is generated by passing a low frequency (4Hz) sinusoidal current through the Helmholtz coil. A small pick-up coil with 10,000 turns, around the sample is used to detect the MBN signals. The MBN signal was sampled at the intervals of 25 μs and eight traces are taken for each measurement. The signal from the coil is amplified by 1000 times using a low-noise pre-amplifier, passed through a band-pass filter (10 kHz 1 MHz) and then collected in a personal computer. Only those voltage signals having amplitudes higher than a selected threshold are considered for analysis. We have characterized MBN by MBN Energy denoted as E_{MBN} which is calculated by integrating the square of these voltages with respect to time.

To get a clear understanding of the domain structure and magnetization processes in wire-shaped amorphous magnetic materials, we have studied stress dependent MBN on $Co_{68.15}Fe_{4.35}Si_{12.5}B_{15}$ amorphous wire. Fig. 5.21 shows the MBN from $Co_{68.15}Fe_{4.35}Si_{12.5}B_{15}$ amorphous wire in the presence of 0 MPa, 23 MPa and 69 MPa tensile stress. MBN decreases with increasing stress applied along the length of the sample. Stress dependence of MBN energy (E_{MBN}) of the wire is shown in Fig.5.22. It is seen that E_{MBN} reduces with increasing stress.

Increasing longitudinal tensile stress, induces a transverse anisotropy within the sample. MBN in this negative magnetostrictive sample takes place by 180° domain wall motion in the IC. Application of stress along the length of the wire reduces the fractional volume of IC domain as well as the differential permeability of the hysteresis loop. Since
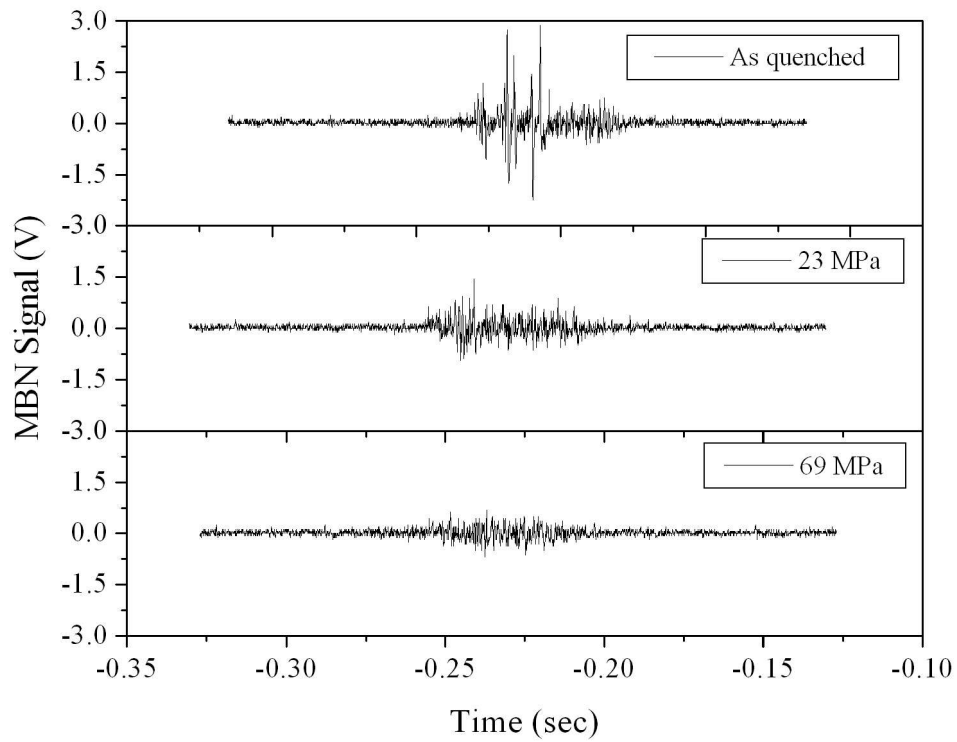
Figure 5.21: MBN signal from amorphous $Co_{68.15}Fe_{4.35}Si_{12.5}B_{15}$ wire in absence and in presence of 23 MPa and 69 MPa stress.
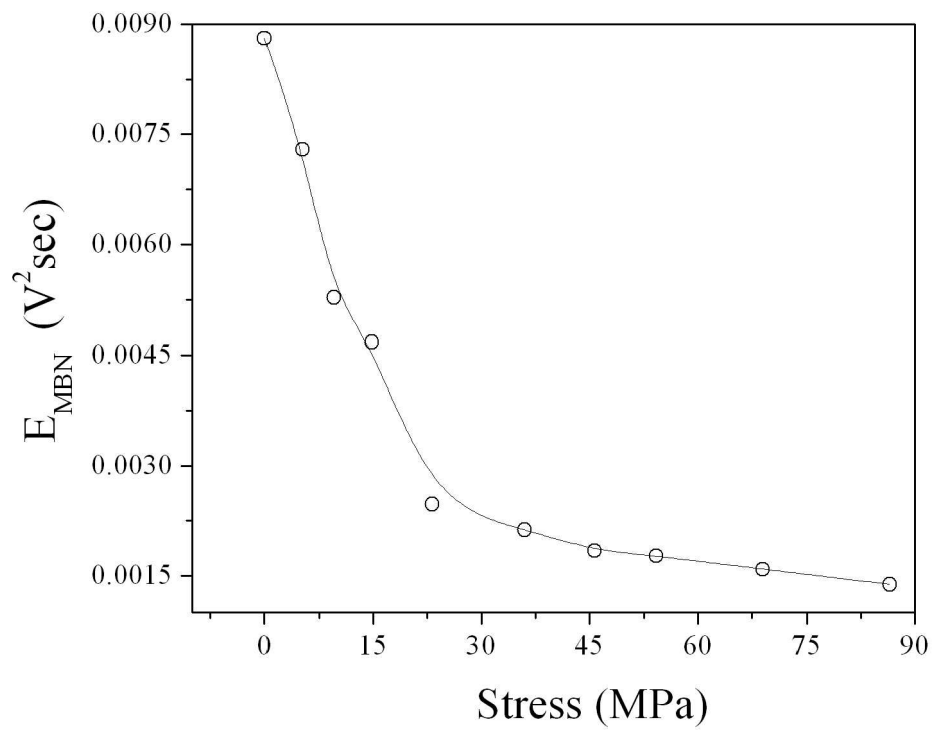
Figure 5.22: Stress dependence of MBN energy of amorphous $Co_{68.15}Fe_{4.35}Si_{12.5}B_{15}$ wire.
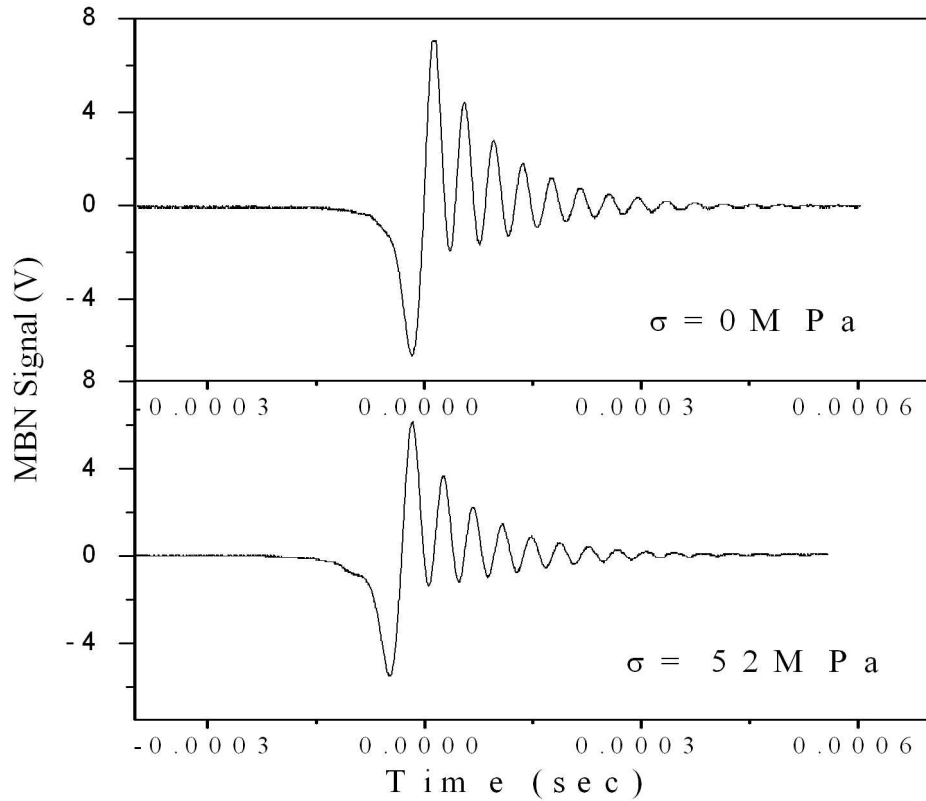
Figure 5.23: MBN from amorphous $Co_{68.15}Fe_{4.35}Si_{12.5}B_{15}$ wire in the absence and in presence of 52 MPa stress for maximum possible applied magnetic field.

the Barkhausen voltage (hence E_{MBN}) is proportional to the differential irreversible susceptibility, therefore MBN decreases with stress along the direction of applied field.

We have also studied the magnetic field dependence of MBN from amorphous $Co_{68.15}Fe_{4.35}Si_{12.5}B_{15}$ wire. Here we have reported only the results of MBN for maximum magnetic field ($\sim$ 2 Oe) applied . Fig.5.23 shows the MBN from amorphous $Co_{68.15}Fe_{4.35}Si_{12.5}B_{15}$ wire in the absence and in presence of 52 MPa stress at the highest magnetic field applied. The stress dependence of E_{MBN} of amorphous $Co_{68.15}Fe_{4.35}Si_{12.5}B_{15}$ wire at highest magnetic field is shown in Fig.5.24. On application of high magnetic field, only the inner core domain of the wire exists with a single magnetization vector nearly parallel to the wire axis. This magnetization vector actually spirals in to equilibrium position parallel to the magnetic field. The magnetization undergoes precession (untill it

Figure 5.24: Stress dependence of E_{MBN} of amorphous $Co_{68.15}Fe_{4.35}Si_{12.5}B_{15}$ wire for maximum possible applied magnetic field.

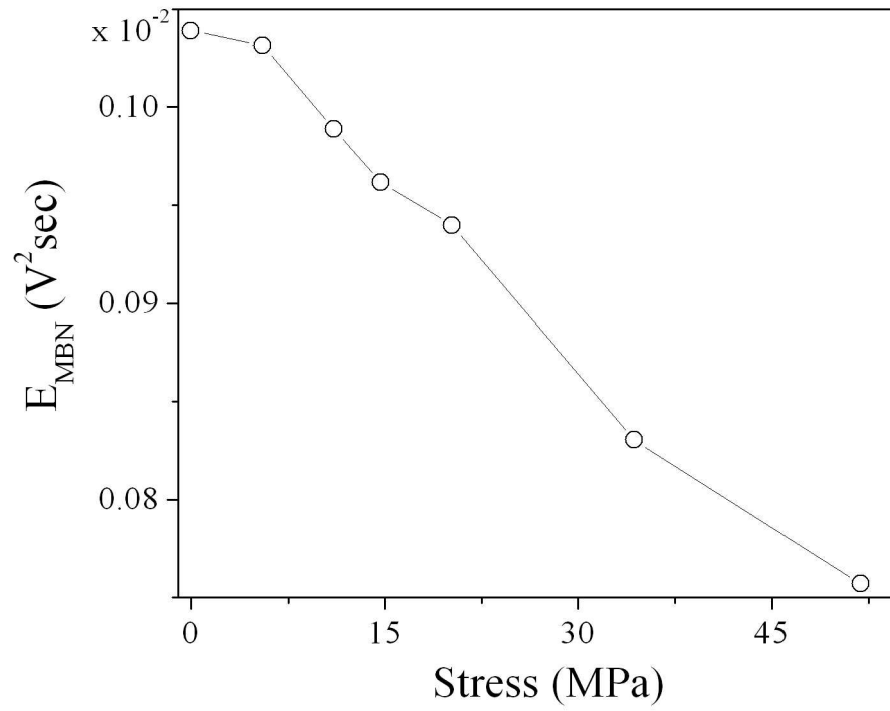alligns along the wire axis), as a result of the torque exerted on the magnetization by the external magnetic field, which is reflected in our MBN results.

5.5 Conclusions

Magnetic Barkhausen Noise (MBN) measurements were performed on amorphous $Fe_{40}Ni_{40}B_{20}$ and $Fe_{70}Ni_8Si_{10}B_{12}$ ribbons under different tensile stress conditions. Experimental results show that there is an increase of MBN with increasing tensile stress applied along the length of the sample. The dependence of MBN on stress is influenced by the parameters such as the orientations of magnetic easy axis of the sample, the direction and magnitude of applied stress and magnetic field. Therefore using this technique, these parameters can be estimated. Magnetization measurement in amorphous $Fe_{40}Ni_{40}B_{20}$ ribbon reveals a decrease in coercivity with increasing tensile stress applied along the length of the ribbon. Temperature dependent MBN study has been done in amorphous $Fe_{40}Ni_{40}B_{20}$ ribbon. It is observed that there is a decrease of MBN with increased duration of heat treatment at 300°C. Gradual development of a two-peak behaviour with increased duration of heating indicates an amorphous to crystalline phase transformation in amorphous $Fe_{40}Ni_{40}B_{20}$ ribbon. This study shows that the MBN measurement could be used to evaluate the different structural phases of ferromagnetic samples. Angular dependence of MBN has been studied to estimate the magnetic easy axis in amorphous $Fe_{40}Ni_{40}B_{20}$ ribbon. Angular dependent E_{MBN} was fitted by an expression $E_{MBN} = \alpha \cos^2(\theta - \varphi) + \beta$. Here α and β are fitting parameters and φ and θ are the directions of applied magnetic field and magnetic easy axis respectively with respect to the sample axis. MBN study from the as-quenched and annealed (heated at 540°C for 1 hour) $Fe_{73.5}Cu_1Nb_3Si_{13.5}B_9$ ribbon showed the amorphous to crysatlline phase transformation. Stress dependent MBN on $Co_{68.15}Fe_{4.35}Si_{12.5}B_{15}$ amorphous wire gives a better understanding of the domain structure and magnetization processes in wire-shaped amorphous magnetic materials.

Bibliography

[1] A. I. Gubanov, Fiz. Tver. Tel. *2*, 502 (1960).

[2] A. Brenner, D. E. Couch and E. K. Williams, J. Res. Nat. Bureau Standards *44*, 109 (1950).

[3] P. Duwez, R. H. Willens and W. Klement Jr., J. Appl. Phys. *31*, 1136 (1960).

[4] P. Duwez and S. C. H. Lin, J. Appl. Phys. *38*, 4096 (1967).

[5] F. E. Luborsky, J. J. Becker and R. O. McCary, IEEE Trans. Mag. *MAG-11*, 1644 (1975).

[6] T. Mizoguchi, IBM Research report RC, 6054 (1976).

[7] G. S. Cargill III, Solid State Physics, Vol. 30 Ed. Ehrenreich et. al. Academic Press. New York (1975).

[8] T. Masumoto, S. Ohnuma, K. Shirakawa, M. Nose and K. Kobeyshi, Int. Conf. on liquid and amorphous metals, Grenoble, France (1980).

[9] J. J. Gilman and H. J. Leamy, eds., Metallic Glasses (ASM, Metals Prak, OH, 1978).

[10] F. E. Luborsky, ed., Amorphous Metallic alloys (Butterworths, London, 1983).

[11] H. J. Guntherodt and H. Beck, ed. Glassy Metals, Vol-I (Springer, Berlin, 1981).

[12] H. Beck and H. J. Guntherodt, ed. Glassy Metals, Vol-II (Springer, Berlin, 1983).

[13] R. Hasegawa, ed., Metallic Glasses : Magnetic Chemical and Structural Properties (CRC, Boca Ratan, FL, 1983).

[14] K. Moorjani and J. M. D. Coey, Magnetic Glasses (Elsevier, Amsterdam, 1984).

[15] H. O. Hooper and A. M. de Graaf, eds. Amorphous Magnetism I (Plenum, New York, 1973).

[16] R. Hasegawa and R. A. Levy, eds. Amorphous Magnetism II (Plenum, New York, 1977).

[17] R. C. O'Handley, J. Appl. Phys. *62*, R15 (1987).

[18] R. Roy, B. C. Giessen and N. J. Grant, Scripta Met. *2*, 357 (1968).

[19] H. A. Davies and B. G. Lewis, Scripta Met. *9*, 1107 (1975).

[20] F. E. Luborsky, Ferromagnetism Vol. I, ed. by E. P. Wohlfarth (North Holland, Amsterdam, 1980) p. 451.

[21] E. M. Breinan, B. H. Kear and C. M. Banas, Phys. Today *29* 45 (1976).

[22] R. Clampitt, M. G. Scott, K. L. Aithen, L. Gowland, Rapidly Quenched Metals III, ed. by B. Cantor (The Metals Society, London, 1978).

[23] A. E. Berkowitz and J. L. Walter, Rapid Solidification Proc. II, ed. R. Mehraban, B. H. Kear and M. Cohen (Claitor's Pub. Div. Louisiana, 1980) p. 294.

[24] Manuel Vazquez, Handbook of Magnetism and Advanced Magnetic Materials, Ed. Helmut Kronmuller and Stuart Perkin, John Wiley and Sons. Ltd. 2007, p.2193.

[25] A. Zhukov, J. Gonzalez and M. Vazquez, Encyclopedia of Nanoscience and Nanotechnology, Ed. H. S. Nalwa, American Scientific Publishers 2003, Vol. X p. 1.

[26] S. Kavesh, Apparatus for liquid quenching of free jet spun metal. US Patent 3 960 200 (1976).

[27] I. Ohnaka, T. Fukusako, T. Ohmichi et al., Proceedings of the 4th International Conference Rapidly Quenched Metals, Ed. T. Masumoto and K. Suzuki : The Japan Institute of Metals, Sendai, p. 31 (1982).

[28] T. Masumoto, I. Ohnaka, A. Inoue and M. Hagiwara, Scripta Materialia *15* 293 (1981).

[29] G. F. Taylor, Phys. Rev. *23* 655 (1924).

[30] G. F. Taylor, Process and apparatus for making filaments, Patented February 24, 1931, United States Patent Office, 1, 793, 529.

[31] A. V. Ulitovsky, Micro-Technology in Design of Electric Devices, Vol. 7, Leningrad, p. 6 (1951).

[32] A. V. Ulitovsky and N. M. Avernin, Method of fabrication of metallic microwire, Patent No. 161325 (USSR) 19.03.64, Bulletin No. 7, p. 14.

[33] A. V. Ulitovsky, I. M. Maianski and A. I. Avramenco, Method of continuous casting of glass coated microwire, Patent No. 128427 (USSR), 15.05.60, Bulletin No. 10, p. 14.

[34] M. Vazquez, Physica B, *299* 302 (2001).

[35] M. Vazquez and A. Hernando, J. Phys. D : Appl. Phys. *29*, 939 (1996).

[36] V. S. Larin, A. V. Torcunov, A. Zhukov, J. Gonzalez, M. Vazquez and L. Panina, J. Magn. Magn. Mater. *249*, 39 (2002).

[37] A. Zhukov, M. Ipatov, J. Gonzalez, J. M. Blanco and V. Zhukova, J. Magn. Magn. Mater. *321*, 822 (2009).

[38] J. Durand, J. Physique *41* c8-609 (1980).

[39] A. Lienard, Thesis, Grenoble (1981).

[40] G. S. Cargill III, Solid State Phys. *30* 227 (1975).

[41] R. W. Cochrane, R. Harris, J. O. Strom Olson and M. J. Zuckermann, Phys. Rev. Lett. *35* 676 (1975).

[42] R. C. O'Handley and D. S. Boudreaux, Phys. Status Solidi A *45* 607 (1978).

[43] V. Jaccarino and L. R. Walker, Phys. Rev. Lett. *15*, 259 (1965).

[44] K. H. J. Buschow, M. Brouha, J. W. M. Biesterbos, A. G. Dirks, Physica B *91*, 261 (1977).

[45] W. Heisenberg, Z. Phys. *49*, 619 (1928).

[46] D. C. Mattis, Theory of Magnetism, Harper and Row, New York (1965).

[47] G. T. Rado and H. Suhl (Eds.), Magnetism, 5 Vols., (Academic Press, New York, 1963).

[48] M. A. Ruderman and C. Kittel, Phys. Rev. *96*, 99 (1954).

[49] T. Kasuya, Prog. Theo. Phys. *16*, 45 (1956).

[50] K. Yosida, Phys. Rev. *106*, 893 (1957).

[51] C. Herring, Magnetism Vol. IV ed. by G. T. Rado and H. Suhl, (Academic Press, New York, 1963).

[52] S. Crane and H. Claus, Phys. Rev. Lett. *46* 1693 (1981).

[53] G. J. Nieuwenhyys, B. H. Verbeeck and J. A. Mydosh, J. Appl. Phys. *50*, 1685 (1979).

[54] G. J. Nieuwenhyys, H. Stocker, B. H. Verbeeck and J. A. Mydosh, Solid State Comm. *27* 197 (1978).

[55] M. Vazquez, W. Fernegel andH. Kronmuller, Phys. Stat. Solidi *80* 513 (1983).

[56] A. Oguchi, Progress of Theoretical Phys. *56* 1442 (1976).

[57] Giselher Herzer, Handbook of Magnetism and Advanced Magnetic Materials, Ed. Helmut Kronmuller and Stuart Perkin, John Wiley and Sons. Ltd. 2007, p.1882.

[58] Akihisa Inoue, Akihiro Makino and Teruo Bitoh, Handbook of Magnetism and Advanced Magnetic Materials, Ed. Helmut Kronmuller and Stuart Perkin, John Wiley and Sons. Ltd. 2007, p.1909.

[59] Y. Yoshizawa, S. Oguma and K. Yamauchi, J. Appl. Phys. em64 6044 (1988).

[60] G. Herzer, IEEE Trans. Magn. *25* 3327 (1989).

[61] G. Herzer, IEEE Trans. Magn. *26* 1397 (1990).

[62] B. Hofmann and H. Kronmuller, J. Magn. Magn. Mater. *152* 91 (1996).

[63] $FINEMET^R$, (2006). www.hitachi-metals.co.jp.

[64] $VITROPERM^R$, (2006). www.vacuumschmelze.de.

[65] K. Hono, K. Hiraga, Q. Wang, A. Inoue and T. Sakurai, Acta Metall. Mater. *40(9)* 2137 (1992).

[66] J. D. Ayers, V. G. Harris, J. A. Sprague, W. T. Elam and H. N. Jones, Acta Mater. *46(6)* 1861 (1998).

[67] A. C. Hsiao, M. E. McHenry, D. E. Laughlin, M. R. Tamoria and V. G. Harris, IEEE Trans. Magn. *37(4)* 2236 (2001).

[68] E. P. Harrison, G. L. Turney and H. Rowe, Nature *135*, 961 (1935).

[69] E. P. Harrison, G. L. Turney, H. Rowe and H. Gallop, Proc. Royal Soc. *157*, 651 (1937).

[70] L. V. Panina, K. Mohri, K. Bushida and M. Noda, J. Appl. Phys. *76*, 6198 (1994).

[71] L. V. Panina and K. Mohri, Appl. Phys. Lett. *65*, 1189 (1994).

[72] R. S. Beach and A. E. Berkowitz, J. Appl. Phys. *76*, 6209 (1994).

[73] R. S. Beach and A. E. Berkowitz, Appl. Phys. Lett. *64*, 3652 (1994).

[74] M. Vazquez, J. Magn. Magn. Mater. *226*, 693 (2001).

[75] M. Knobel and K. R. Pirota, J. Magn. Magn. Mater. *242*, 33 (2002).

[76] M. Knobel, M. Vazquez and L. Krauss, Handbook of Magnetic Materials, Ed. K. H. J. Buschow (Elsevier, 2003) Vol. 15, p. 497.

[77] S. Chikazumi, Physics of ferromagnetism, (Oxford University Press, 1997) p. 387.

[78] B. D. Cullity, Introduction to Magnetic Materials (Addison-Wesley Publishing Company, 1972) p. 287.

[79] H. Barkhausen, Phys. Z *20* 401 (1919).

[80] C.-G. Stefanita, From Bulk to Nano : The Many Sides of Magnetism, 2008.

[81] K. Mandal and S. K. Ghatak, Phys. Rev. B *47*, 233 (1993).

[82] F. L. Machado, B. L. da Silva, S. M. Rezende and C. S. Martins, J. Appl. Phys. *75*, 6563 (1994).

[83] M. Knobel, M. L. Sánchez, J. Velázquez and M. Vázquez, J. Phys.: Condens. Matter *7*, L115 (1995).

[84] M. Vazquez, M. Knobel, M. L. Sanchez, R. Valenzuela and A. P. Zhukov, Sens. Act. A *59*, 20 (1997).

[85] M. Knobel,M. Vázquez, M. L. Sánchez, and A. Hernando, J. Magn. Magn. Mater. *169*, 89 (1997).

[86] D. X. Chen, J. L. Munoz, A. Hernando and M. Vazquez, Phys. Rev. B *57*, 10699 (1998).

[87] K. Mandal, S. Sinha and P. Anil Kumar, J. Appl. Phys. *99*, 033901 (2006).

[88] K. Mandal, S. Pan Mandal, M. Vazquez, S. Puerta and A. Hernando, Phys. Rev. B *65*, 064402 (2002).

[89] S. Sinha, K. Mandal and M. Vazquez, J. Magn. Magn. Mater. *302*, 223 (2006).

[90] S. Sinha, B. Das and K. Mandal, J. Appl. Phys. *105* 07A311 (2009).

[91] V. Zhukova, M. Ipatov, J. Gonzalez, J. M. Blanco and A. Zhukov, J. Appl. Phys. *103*, 07E714 (2008).

[92] L. V. Panina and K. Mohri, J. Magn. Magn. Mater. *157*, 137 (1996).

[93] R. L. Sommer and C. L. Chien, Appl. Phys. Lett. *67*, 3346 (1995).

[94] K. C. Mendes, F. L. A. Machado, L. G. Pereira, S. M. Rezende, F. C. Montenegro, M. V. P. Altoe and F. P. Missell, J. Appl. Phys. *79*, 6555 (1996).

[95] F. L. A. Machado, C. S. Martins and S. M. Rezende, Phys. Rev. B *51*, 3926 (1995).

[96] A. N. Medina, M. Knobel, S. Salem-Sugui Jr. and F. G. Gandra, J. Appl. Phys. *79*, 5462 (1996).

[97] S. Q. Xiao, Y. H. Liu, Y. Y. Dai, L. Zhang, S. X. Zhou and G. D. Liu, J. Appl. Phys. *85*, 4127 (1999).

[98] Y. Zhou, J. Yu, X. Zhao and B. Cai, IEEE Trans. Magn. *36*, 2960 (2000).

[99] M. Knobel, M. L. Sanchez, C. Gomez Polo, A. Hernando, P. Marin and M. Vazquez, J. Appl. Phys. *79*, 1646 (1995).

[100] H. Q. Guo, H. Kronmuller, T. Dragon, Z. H. Cheng and B. G. Shen, J. Appl. Phys. *89*, 514 (2001).

[101] H. B. Nie, A. B. Pakhomov, X. Yan, X. X. Zhang and M. Knobel, Solid State Commun. *112*, 285 (1999).

[102] J. Velazquez, M. Vazquez, D. X. Chen and A. Hernando, Phys. Rev. B *50*, 16737 (1994).

[103] R. L. Sommer and C. L. Chien, J. Appl. Phys. *79*, 5139 (1996).

[104] K. Mandal, S. Puerta, M. Vazquez and A. Hernando, Phys. Rev. B *62*, 6598 (2000).

[105] L. D. Landau, E. M. Lifshitz and L. P. Pitaevskii, Electrodynamics of Continuous Media (Pergamon Press, 1984) p. 210.

[106] A. Yelon, D. Menard, M. Britel and P. Ciureanu, Appl. Phys. Lett. *69*, 3084 (1996).

[107] M. R. Britel, D. Menard, L. G. Melo, P. Ciureanu, A. Yelon, R. W. Cochrane, M. Rouabhi and B. Cornut, Appl. Phys. Lett. *77*, 2737 (2000).

[108] P. Ciureanu, M. Britel, D. Menard, A. Yelon, C. Akyel, M. Rouabhi, R. W. Cochrane, P. Rudkowski and J. O. Strom-Olsen, J. Appl. Phys. *83*, 6563 (1998).

[109] L. D. Landau, E. M. Lifshitz and L. P. Pitaevskii, Electrodynamics of Continuous Media (Pergamon Press, 1984) p. 300.

[110] S. E. Lofland, S. M. Bhagat, M. Dominguez, J. M. garcia Beneytez, F. Guerrero and M. Vazquez J. Appl. Phys. *85*, 4442 (1999).

[111] C. Chiriac, C. N. Colesnuic and A. T. Ovari, IEEE Trans. Magn. *35*, 3841 (1999).

[112] F. Vinai, M. Coisson and P. Tiberto, J. Magn. Magn. Mater. *300*, e82 (2006).

[113] S. Chikazumi and S. H. Charap, Physics of Magnetism (Krieger, Malabar, FL, 1978) p. 50.

[114] Manh-Huong Phan, Seong-Cho Yu, Cheol Gi Kim and M. Vazquez, Appl. Phys. Lett. *83*, 2871 (2003).

[115] T. Kitoh, K. Mohri and T. Ushiyama, IEEE Trans. Magn. *31*, 3137 (1995).

[116] C. Gomez-Polo, M. Vazquez and M. Knobel, Appl. Phys. Lett. *78*, 246 (2001).

[117] S. H. Song, K. S. Kim, S. C. Yu, C. G. Kim and M. Vazquez, J. Magn. Magn. Mater. *215*, 532 (2000).

[118] J. Velazquez, M. Vazquez and A. P. Zhukov, J. Mater. Res. *11*, 2499 (1996).

[119] D. Atkinson and P. T. Squire, J. Appl. Phys. *83*, 6569 (1998).

[120] F. L. A. Machado and S. M. Rezende, J. Appl. Phys. *79*, 6558 (1996).

[121] N. Usov, J. Magn. Magn. Mater. *185*, 159 (1998).

[122] C. Gomez-Polo, M. Knobel, K. R. Pirota and M. Vzquez, Physica B *299*, 322 (2001).

[123] D.P. Makhnovskiy, L.V. Panina and D.J. Mapps, Phys. Rev. B *63*, 144424 (2001).

[124] L. V. Panina, K. Mohri and D. P. Makhnovskiy, J. Appl. Phys. *85*, 5444 (1999).

[125] D. P. Makhnovskiy, L. V. Panina and D. J. Mapps, Appl. Phys. Lett. *77*, 121 (2000).

[126] A. Mitra, M. Vazquez, K. Mandal and S. K. Ghatak, J. Appl. Phys. *70*, 4455 (1991).

[127] A. Zhukov, M. Vazquez, J. Velazquez, A. Hernando and V. Larin, J. Magn. Magn. Mater. *170*, 323 (1997).

[128] D. C. Jiles, Acta Mater. *51*, 5907 (2003).

[129] A. Zhukov, M. Vazquez, J. Velazquez, C. Garcia R. Valenzuela and B. Ponomarev, Mater. Sci. Eng., A *226-228*, 753 (1997).

[130] B. D. Cullity, Introduction to Magnetic Materials (Addison-Wesley Publishing Company, 1972) p. 248.

[131] D. Menard, D. Frankland, P. Ciureanu, A. Yelon, M. Rouabhi, R. W. Cochrane, H. Chiriac and T. A. Ovari, J. Appl. Phys. *83*, 6566 (1998).

[132] J. Nowak, J. Appl. Phys. *72*, 1490 (1992).

[133] R. Beckerand W. Döring, Ferromagnetismus, (Springer Verlag, Berlin, 1939).

[134] A. E. Lord, Acoustic Emission, ed. by W. P. Mason and R. N. Thurston, Physics Acoustics, vol. 9 (Academic Press, New York, 1975).

[135] Y. H. Xu, L. Ma, F. M. Du, X. Y. Ma and D. H. L. Ng, J. Magn. Magn. Mater. *219* 166 (2000).

[136] K. Ono, Progress in Acoustic Emission III, The Japanese Society of NDT p.200 (1986).

[137] T. W. Krause, L. Clapham, A. Pattantyus and D. L. Atherton, J. Appl. Phys. *79* 4242 (1996).

[138] S. Sinha, K. Mandal and B. Das, J. Phys. D : Appl. Phys. *40* 2710 (2007).

[139] T. W. Krause, K. Mandal and D. L. Atherton, J. Magn. Magn. Mater. *195* 193 (1999).

[140] M. Birsan, J. A. Szpunar, T. W. Krause, and D. L. Atherton, IEEE Trans. Magn. *32(2)* 527 (1996).

[141] Onuttom Narayan, Phys. Rev. Lett. *77(18)* 3855 (1996).

[142] Pierre Cizeau, Stefano Zapperi, Gianfranco Durin and H. Eugene Stanley, Phys. Rev. Lett. *79(23)* 4669 (1997).

[143] H. Kwun, J. Magn. Magn. Mater. *49* 235 (1985).

[144] T. W. Krause, N. Pulfer, P.Weyman and D. L. Atherton, IEEE Trans. Magn. *32(5)* 4764 (1996).

[145] A. Dhar and D. L. Atherton, Nondestr. Test. Eval. *10* 287 (1993).

[146] C. G. Gardner, G. A. Matzkanin and D. L. Davidson, Int. J. Nondes. Test. *3* 131 (1971).

[147] S. Sinha and K. Mandal, Journal of Nondestructive Testing and Evaluation *5* 49 (2006).

[148] S. Sinha and K. Mandal, Indian Journal of Physics *79* 991 (2005).

[149] R. Rautioaho, P. Karjalainen and M. Moilanen, J. Magn. Magn. Mater. *73* 96 (1988).

[150] K. Tiitto, Nondest. Test. *26* 36 (1989).

[151] S. Nath, B. Wincheski, J. P. Fulton and M. Namkung, IEEE Trans. Magn. *30(6)* 4644 (1994).

[152] B. Wincheski, J. P. Fulton, S. Nath, M. Namkung and J. W. Simpson, Mat. Eval. *52(1)* 22 (1994).

[153] V. Babbar, B. Shiari and L. Clapham, IEEE Trans. Magn. *40(1)* 43 (2004).

[154] L. Clapham, C. Jagadish and D. L. Atherton, *Acta. Metal. Mater.* **39(7)** 1555 (1991).

[155] B. D. Cullity, Introduction to Magnetic Materials (Addison-Wesley Publishing Company, 1972) p. 207.

[156] D. C. Jiles, *Acta. Mater.* **51** 5907 (2003).

[157] Thomas W. Krause, J. M. Makar and D. L. Atherton, J. Magn. Magn. Mater. *137* 25 (1994).

[158] L. Clapham, C. Heald, T. Krause,and D. L. Atherton, J. Appl. Phys. *86(3)* 1574 (1999).

[159] C.-G. Stefanita, D. L. Atherton and L. Clapham, Acta. Mater. *48* 3545 (2000).

[160] K. Tiito, Nondestructive Evaluation : Application to Materials Processing, Ed. by O. Buck and S. M. Wolf (ASM, Materials Park, Ohio, 1984) p. 161.

[161] X. Kleber and A. Vincent, NDT&E Int. *37* 439 (2004).

[162] S. Chikazumi, Physics of Magnetism, (Wiley, New York, 1964).

[163] D. C. Jiles, Introduction to Magnetism and Magnetic Materials, (Chapman and Hall, New York, 1991).

[164] D. M. Stewart, K. J. Stevens and A. B. Kaiser, Current Applied Physics *4* 308 (2004).

[165] H. K. Tonshoff, B. Karpuschewski and I. Oberbeck-Spintig, 1st International Conference on Barkhausen and Micromagnetic Testing (1998), Hannover : Stresstech Oy., p. 141.

[166] B. Karpuschewski, 1st International Conference on Barkhausen and Micromagnetic Testing (1998), Hannover : Stresstech Oy., p. 85.

[167] D. G. Hwang and H. C. Kim, J. Phys. D : Appl. Phys. *21* 1807 (1988).

[168] K. Mandal, Th. Cramer and D. L. Atherton, J. Magn. Magn. Mater. *212* 231 (2000).

[169] K. Mandal, T. W. Krause and D. L. Atherton, Indian J. Phys. *77A(2)* 93 (2003).

[170] O. Stupakov, J. Pal'a, V. Yurchenko, I. Tomas and J. Bydzovsky, J. Magn. Magn. Mater. *320* 204 (2008).

[171] C. Jagadish, L. Clapham, D. L. Atherton, IEEE Trans. Magn. *25(5)* 3452 (1989).

[172] C. Jagadish, L. Clapham, D. L. Atherton, NDT Int. *22(5)* 297 (1989).

[173] C. Jagadish, L. Clapham, D. L. Atherton, IEEE Trans. Magn. *26(1)* 262 (1990).

[174] C. Jagadish, L. Clapham, D. L. Atherton, J. Phys. D : Appl. Phys. *23* 443 (1990).

[175] K. Mandal, D. Dufour, R. Sabet-Sharghi, B. Sijgers, D. Micke, T. W. Krause, L. Clapham and D. L. Atherton, J. Appl. Phys. *80(11)* 6391 (1996).

[176] T. W. Krause, K. Mandal, C. Hauge, P. Weyman, B. Sijgers, D. L. Atherton, J. Magn. Magn. Mater. *169* 207 (1997).

[177] R. Ranjan, D. C. Jiles and P. K. Rastogi, IEEE Trans. Magn. MAG. *23* 1869 (1987).

[178] C. Gatelier-Rothea, J. Chiocio, R. Fougeres, P. Fleischman, Acta mater. *46* 4873 (1998).

[179] J. Anglada-Rivera, L. R. Padovese and J. Capo-Sanchez, J. Magn. Magn. Mater. *231* 299 (2001).

[180] V. Moorthy, S. Vaidyanathan, T. Jayakumar and Baldev Raj, J. Magn. Magn. Mater. *171* 179 (1997).

[181] V. Moorthy, S. Vaidyanathan, T. Jayakumar, B. Raj and B. P. Kashyap, Acta Mater. *47(6)* 1869 (1999).

[182] O. Saquet, J. Chicois and A. Vincent, Mater. Sci. Eng. A *269* 73 (1999).

[183] J. Kameda and R. Ranjan, Acta Metall. *35* 1515 (1987).

[184] J. Kameda and R. Ranjan, Acta Metall. *35* 1527 (1987).

[185] G. Durin, A. Magni and G. Bertotti, J. Magn. Magn. Mater. *160* 299 (1996).

[186] Gianfranco Durin and Stefano Zapperi, J. Appl. Phys. *85(8)* 5196 (1999).

[187] Maurizio Zani and Ezio Puppin, J. Appl. Phys. *94(9)* 5901 (2003).

[188] Ezio Puppin and Maurizio Zani, J. Phys.: Condens Matter. *16* 1183 (2004).

[189] Luca Callegaro, Ezio Puppin and Simona Ricci, J. Appl. Phys. *90(5)* 2416 (2001).

[190] L. Santi, A. D. C. Viegas, A. M. H. deandrade, R. L. Sommer, R. Grossinger and R. Sato Turtelli, J. Magn. Magn. Mater. *226* 1484 (2001).

[191] E. Puppin, Phys. Rev. Lett. *84* 5415 (2000).

[192] G. Durin and S. Zapperi, Phys. Rev. Lett. *84* 4705 (2000).

[193] B. Alessandro, C. Beatrice, G. Bertotti and A. Montorsi, J. Appl. Phys. *68* 2901 (1990).

[194] B. Alessandro, C. Beatrice, G. Bertotti and A. Montorsi, J. Appl. Phys. *68* 2908 (1990).

[195] P. Bak, C. Tang and K. Wiesenfeld, Phys. Rev. Lett. *59* 381 (1987).

[196] P. Bak, C. Tang and K. Wiesenfeld, Phys. Rev. A *38* 364 (1998).

[197] L. V. Meisel and P. J. Cote, Phys. Rev. B *46* 10822 (1992).

[198] D. Spasojevic, S. Bukvic, S. Milosevic and H. E. Stanley, Phys. Rev. E *54* 2531 (1996).

[199] E. Vives, J. Goicoechea, J. Ortin and A. Planes, Phys. Rev. E *52* R5 (1995).

[200] Olga Perkovic, Karin Dahmen and James P. Sethna, Phys. Rev. Lett. *75(24)* 4528 (1995).

[201] Amit P. Mehta, Andrea C. Mills, Karin A. Dahmen and James P. Sethna, Phys. Rev. E *65* 046139 (2002).

[202] B. Tadic, Phys. Rev. Lett. *77* 3843 (1996).

[203] M. Vazquez, E. Ascasibar, A. Hernando and O. V. Nielsen, J. Magn. Magn. Mater. *66* 37 (1987).

[204] B. Hofmann and H. Kronmuller, J. Magn. Magn. Mater. *152* 91 (1996).